Summer 2012

Heterogeneous chemistry and photochemistry of metal-containing aerosols and their impacts on atmospheric chemistry, metal mobilization, biogeochemical cycles and human health

Haihan Chen
University of Iowa

HETEROGENEOUS CHEMISTRY AND PHOTOCHEMISTRY OF METAL-CONTAINING AEROSOLS AND THEIR IMPACTS ON ATMOSPHERIC CHEMISTRY, METAL MOBILIZATION, BIOGEOCHEMICAL CYCLES AND HUMAN HEALTH

by

Haihan Chen

An Abstract

Of a thesis submitted in partial fulfillment
of the requirements for the Doctor of
Philosophy degree in Chemical and Biochemical Engineering
in the Graduate College of
The University of Iowa

July 2012

Thesis Supervisor: Professor Vicki H. Grassian

ABSTRACT

Atmospheric aerosols have significant impact on the chemical balance of the atmosphere, biogeochemical cycles, the Earth's climate and human health. Although extensive studies have been performed to explore these effects, there is still considerable uncertainty.

For example, understanding of heterogeneous photochemistry on aerosols may be crucial to accurately predict the impact of aerosol loadings on atmospheric chemistry, yet few studies have been conducted. In this dissertation research, laboratory studies were performed to investigate heterogeneous photoreactions of HNO_3 and O_3 on typical components of metal containing aerosols. Results indicate that irradiation can change the reaction mechanism, kinetics, reaction extent, products, and product partitioning. The presence of water at different relative humidity also plays a key role in the rates of these reactions and the product distribution.

Increasing evidence has suggested that anthropogenic aerosols play a more important role in supplying soluble iron into open ocean water compared with mineral dust. Dissolution experiments to simulate atmospheric processing were performed to compare iron mobilization abilities of coal fly ash with Arizona test dust, a model for mineral dust aerosol. Results indicate that coal fly ash can release more iron into water compared with Arizona test dust. The iron solubility strongly depends on the source material, surface pH, types of acidic media, and the presence of solar irradiation.

A study on Pb mobilization from PbO particles following exposure to NO_2 shows interaction of PbO particles with NO_2 leads to an increase in Pb dissolution. Collaboration work indicates that size and surface area of iron nanoparticles play a role in affecting bacteria growth, pathogenicity, and impairing the AMP activity. Nanoparticles, especially the smaller particles with large surface areas, may be harmful to human health as it relates to individuals susceptible to bacterial infections and/or colonization.

This thesis summarizes the above studies in Chapter 3 to Chapter 7. The research described herein provides a number of important issues where further studies are warranted. The last chapter suggests future directions for laboratory studies that have the potential to make an important contribution on understand the global impacts of atmospheric aerosols and heterogeneous chemistry.

Abstract Approved: _____
Thesis Supervisor

_____
Title and Department

_____
Date

HETEROGENEOUS CHEMISTRY AND PHOTOCHEMISTRY OF METAL-CONTAINING AEROSOLS AND THEIR IMPACTS ON ATMOSPHERIC CHEMISTRY, METAL MOBILIZATION, BIOGEOCHEMICAL CYCLES AND HUMAN HEALTH

by

Haihan Chen

A thesis submitted in partial fulfillment
of the requirements for the Doctor of
Philosophy degree in Chemical and Biochemical Engineering
in the Graduate College of
The University of Iowa

July 2012

Thesis Supervisor: Professor Vicki H. Grassian

Graduate College
The University of Iowa
Iowa City, Iowa

CERTIFICATE OF APPROVAL

_____

PH.D. THESIS

_____

This is to certify that the Ph.D. thesis of

Haihan Chen

has been approved by the Examining Committee for the thesis requirement for the Doctor of Philosophy degree in Chemical and Biochemical Engineering at the July 2012 graduation.

Thesis Committee: _____
Vicki H. Grassian, Thesis Supervisor

_____
Gregory R. Carmichael

_____
C. Allan Guymon

_____
Charles O. Stanier

_____
David M. Cwiertny

ACKNOWLEDGEMENTS

The work in this thesis would not have been possible without the aid of a great many people, most importantly my research advisor, Professor Vicki Grassian. When I applied for graduate study more than four years ago, Vicki showed her great kindness and patience by answering all of my questions regarding the application and the graduate program. It was her kindness and patience that made me decide to come to the University of Iowa and be her student. I am grateful that she gave me this opportunity to work with her. During my Ph.D. study, Vicki encouraged me to work on several projects at the same time and always trusted me to be able to take on the challenges. With her help and encouragement, I have learned to think critically and work independently. Vicki willingly assisted me with my projects whenever I needed help. She has a talent in science. Discussion with her always generated new thoughts. This work would not have been accomplished without Vicki's tremendous support and invaluable insight.

I have also been privileged to work closely with Professor Mark Young. His door was always open for me. He provided insight, advice, and he consistently shared his time to help me out in the lab. Thank you Mark for all of your support. I would also like to thank Dr. Alex Laskin at Pacific Northwest National Laboratory (PNNL) for his support and instruction during my time at PNNL. I admire him for his critical thinking, rigorous scientific attitude, and superior editorial skills. The things I learned from him will benefit me for the rest of my entire academic career. I also appreciate the help from Professor Charles Stanier, who gave me valuable comments on the KPP model. Many thanks also go to my other past and present committee members, Professor Gregory Carmichael, Michelle Scherer, Allan Guymon, and David Cwiertny, for all of your support, advice, and discussions to help me accomplish my Ph.D. study.

A couple members (past and present) of the Grassian research group deserve recognition. I would specially thank Dr. Juan Navea, who guided me through the

chamber study step by step, shared his experience with the chamber, and allowed me the freedom to learn from my mistakes. Additional thanks to Dr. Jonas Baltrusaitis for his patience and time to help me with the data collection and analysis. I would also like to thank all of the members of the Grassian research group for their help and friendship.

In addition, I would like to express my gratitude to several staff members at the University of Iowa, including Jackie Jensen, Linda Wheatley, Natalie Potter, and Frank Turner. They always encouraged me to seek out their assistance and were very accommodating when I did. As staff members, they are more than excellent. I appreciate their help, patience, and support.

My sincere thanks go to all of my friends and family. I would like to specially thank to some friends I met in Iowa, including Weichen Gao, Wen Zhang, Zheng Zhang, Xiayu Xu, Bo Chen, Chichi Choi, Wei He, Yuwei Li, Ning Zhao, Cheng Wang, Rui Zhang, Weipeng Bian, Xue Mei, Shunzhen Huo, Zenggang Yao, Qi Zhao, Pengfei Du, Li Teng, Lijuan Liu Sujit Mohanty, and Andrew Hirsh. They never hesitated to assist me when I needed help. Their ceaseless encouragement has been a great source of energy and they often gave me much needed laughter. Their friendship has been a tremendous source of comfort.

Finally, my greatest thanks go to my parents, Yaning Chen and Xiaoyan Huang who have never limited my ambitions and have always had absolute confidence in me. Their character has, and continues to, inspire me. I know no matter what mistakes I make, they will always be supportive and proud of me. Words cannot express how much I love them and how grateful I am to them for bringing me into this world, loving me continuously, and being fully supportive of every single step I made in my life. I feel so honored to be the first Ph.D. student in our family. It is not only my dream but also theirs. I am proud of myself for not letting either of you down.

ABSTRACT

Atmospheric aerosols have significant impact on the chemical balance of the atmosphere, biogeochemical cycles, the Earth's climate and human health. Although extensive studies have been performed to explore these effects, there is still considerable uncertainty.

For example, understanding of heterogeneous photochemistry on aerosols may be crucial to accurately predict the impact of aerosol loadings on atmospheric chemistry, yet few studies have been conducted. In this dissertation research, laboratory studies were performed to investigate heterogeneous photoreactions of HNO_3 and O_3 on typical components of metal containing aerosols. Results indicate that irradiation can change the reaction mechanism, kinetics, reaction extent, products, and product partitioning. The presence of water at different relative humidity also plays a key role in the rates of these reactions and the product distribution.

Increasing evidence has suggested that anthropogenic aerosols play a more important role in supplying soluble iron into open ocean water compared with mineral dust. Dissolution experiments to simulate atmospheric processing were performed to compare iron mobilization abilities of coal fly ash with Arizona test dust, a model for mineral dust aerosol. Results indicate that coal fly ash can release more iron into water compared with Arizona test dust. The iron solubility strongly depends on the source material, surface pH, types of acidic media, and the presence of solar irradiation.

A study on Pb mobilization from PbO particles following exposure to NO_2 shows interaction of PbO particles with NO_2 leads to an increase in Pb dissolution. Collaboration work indicates that size and surface area of iron nanoparticles play a role in affecting bacteria growth, pathogenicity, and impairing the AMP activity. Nanoparticles, especially the smaller particles with large surface areas, may be harmful to human health as it relates to individuals susceptible to bacterial infections and/or colonization.

This thesis summarizes the above studies in Chapter 3 to Chapter 7. The research described herein provides a number of important issues where further studies are warranted. The last chapter suggests future directions for laboratory studies that have the potential to make an important contribution on understand the global impacts of atmospheric aerosols and heterogeneous chemistry.

TABLE OF CONTENTS

LIST OF TABLES x

LIST OF FIGURES xi

CHAPTER

1 INTRODUCTION 1

1.1 Atmospheric Aerosol 2
1.1.1 Mineral Dust Aerosol 5
1.1.2 Anthropogenic Aerosol 10
1.2 Impacts of Aerosol 12
1.2.1 Heterogeneous Chemistry and Photochemistry of Aerosol 12
1.2.2 Water Adsorption and Its Effects on Heterogeneous Reactions 14
1.2.3 Photochemistry of Nitrate 16
1.2.4 Climate Effect of Aerosol 16
1.2.5 Aerosol in Biogeochemical Cycles 17
1.2.6 The Effect of Aerosol on Human Health 20
1.3 Specific Objectives and Significance 22
1.4 Synopsis of Dissertation Chapters 25

2 EXPERIMENTAL APPARATUS AND PROCEDURES 29

2.1 Experimental Design for Studies of Heterogeneous Reactions 29
2.1.1 Environmental Aerosol Chamber 29
2.1.2 Solar Simulator 31
2.1.3 FTIR Spectroscopy 37
2.1.4 Aerosol Generation 39
2.1.5 Humidity Controlled Flow System 40
2.1.6 Ozone Generator 40
2.1.7 Sample Line 42
2.1.8 Experimental Protocol 42
2.2 Data Analysis for Studies of Heterogeneous Reactions 44
2.2.1 Infrared Spectral Analysis 44
2.2.2 Kinetic Analysis 45
2.3 Quantitative Iron Dissolution Measurements 45
2.3.1 Dissolution Apparatus 46
2.3.2 Simulated Cloud Processing 46
2.3.3 Analytical Methods for Dissolved Iron Determination 48
2.4 Complementary Physicochemical Characterization Techniques and Methods 49
2.4.1 Scanning Electron Microscopy with Energy Dispersive X-ray Spectroscopy 49
2.4.2 Computer-Controlled Scanning Electron Microscopy 50
2.4.3 Transmission Electron Microscopy 51

2.4.4 Powder X-ray Diffraction 51
2.4.5 BET Surface Area Measurement 52
2.4.6 X-ray Photoelectron Spectroscopy....53
2.4.7 Inductively Coupled Plasma Optical Emission Spectroscopy 55
2.4.8 ^{57}Fe Mössbauer Spectroscopy....55
2.5 Reagents and Materials 56
2.5.1 Particle Samples....56
2.5.2 Liquid and Gas Reagents 57

3 HETEROGENEOUS CHEMISTRY AND PHOTOCHEMISTRY OF HNO_3 ON TYPICAL COMPONENTS OF MINERAL DUST AEROSOL 58

3.1 Abstract 58
3.2 Introduction....59
3.3 Experimental Methods 61
3.4 Results and Discussions....62
3.4.1 Comparison of Adsorption Cross-section of HNO_3 with Irradiance Spectrum of the Solar Simulator....62
3.4.2 Heterogeneous Photoreaction of HNO_3 with Al_2O_3....64
3.4.3 RH Effect on the HNO_3 Heterogeneous Photochemistry with Al_2O_3....75
3.5 Conclusions and Atmospheric Implications 78
3.6 Acknowledgments....79

4 HETEROGENEOUS CHEMISTRY AND PHOTOCHEMISTRY OF OZONE ON TYPICAL COMPONENTS OF MINERAL DUST AEROSOL 80

4.1 Abstract 80
4.2 Introduction....81
4.3 Experimental Methods 84
4.3.1 Experimental Apparatus and Procedures 84
4.3.2 Kinetic Analysis....85
4.4 Results....91
4.4.1 Ozone Decomposition on Oxide Particle Surfaces 91
4.4.2 Kinetic Analysis....94
4.5 Discussions....96
4.5.1 Comparison of Ozone Decomposition on Different Oxides under Dry Conditions 96
4.5.2 Effect of Relative Humidity on the Kinetics of Ozone Decomposition on Oxide Surfaces 103
4.6 Conclusions and Atmospheric Implications 105
4.7 Acknowledgements....107

5 CHARACTERIZATION OF ANTHROPOGENIC AEROSOLS AND IRON DISSOLUTION OF ANTHROPOGENIC AEROSOLS DURING SIMULATED ATMOSPHERIC PROCESSING 109

5.1 Abstract 109
5.2 Introduction....110
5.3 Experimental Methods 115
5.3.1 Reagents and Materials 115

5.3.2 Traditional Characterization Methods....115
5.3.3 FIB/SEM Analysis....116
5.3.4 Dissolution Measurements....117
5.3.5 Simulated Cloud Processing with and without Solar Radiation....118
5.4 Results and Discussions....119
5.4.1 Characteristics of Fly Ash and Arizona Test Dust....119
5.4.2 Interior Structure of Fly Ash SRM 2689 Particles....128
5.4.3 Comparing Iron Dissolution between FA and AZTD at Low pH....135
5.4.4 Morphology and Chemical Composition Change of Fly Ash and Arizona Test Dust during Simulated Atmospheric Processing....142
5.4.5 Simulated Cloud Processing of Iron Dissolution in FA....150
5.4.6 Solar Radiation Enhances Iron Dissolution during Simulated Cloud Processing. 157
5.4.7 Influence of Different Acids on Iron Dissolution 157
5.4.8 Influence of pH of Organic Solution on Iron Dissolution and Dissolved Iron Speciation....164
5.4.9 Influence of Solar Radiation on Iron Dissolution and Dissolved Iron Speciation in Organic Solution....166
5.5 Atmospheric Implications....171
5.6 Acknowledgements....174

6 HETEROGENEOUS CHEMISTYR OF NITROGEN DIOXIDE ON LEAD OXIDE PARTICLES AND ITS IMPACT ON LEAD DISSOLUTION....176

6.1 Abstract....176
6.2 Introduction....176
6.3 Experimental Methods....180
6.3.1 Materials....180
6.3.2 Particle Characterization....180
6.3.3 Dissolution Measurements....180
6.3.4 Surface Analysis....181
6.4 Results and Discussions....181
6.4.1 Particle Characterization....181
6.4.2 XPS Analysis of NO_2 Exposed PbO Particles under Various Environmental Conditions....183
6.4.3 Effect of NO_2 Exposure on the Dissolution of PbO Particles....191
6.5 Environmental and Health Implications....193
6.6 Acknowledgments....194

7 A COLLABORATIVE STUDY ON THE IMPACT OF IRON-CONTAINING PARTICLES ON HUMAN HEALTH....195

7.1 Abstract....195
7.2 Introduction....195
7.3 Experimental Methods....197
7.3.1 Synthesis of α-Fe_2O_3 Nanoparticles....197
7.3.2 Characterization of α-Fe_2O_3 Nanoparticles....198

7.3.3 α-Fe_2O_3 Nanoparticle Bacterial Exposure Experiments....198
7.4 Results and Discussions....199
7.4.1 Characterization of Nanoscale α-Fe_2O_3....199
7.4.2 Growth and Pathogenicity of PAO1 in the Presence of α-Fe_2O_3 Nanoparticles....205
7.5 Conclusions....212
7.6 Acknowledgements....212

8 CONCLUSIONS AND FUTURE WORK....214

APPENDIX A WINFIRST MACROS USED FOR INFRARED SPECTRAL COLLECTION AND ANALYSIS....221

APPENDIX B INPUT FOR KINETIC PREPROCESSER....226

REFERENCES....231

LIST OF TABLES

Table

1.1 Global Emission Estimated for Major Aerosol Classes....6

1.2 Abundance of Major Oxides in the Continental Crust....8

4.1 Commercial Sources and Physical Properties of the Oxide Powder Samples Used in the Current Study....85

4.2 Reactions and Their Corresponding Rate Constants Used in the KPP Modeling Simulation of Heterogeneous Photoreaction of Ozone with Oxides....89

4.3 Surface Rate Constants and Uptake Coefficients for Ozone Uptake on Oxides Under a Variety of Conditions (%RH and Light)....99

5.1 Physical Properties and Elemental Analysis of Fly Ash Particles Including FA 2689, 2690, and 2691....120

5.2 Correlation Coefficients between Different Parameters of Fly Ash SRMs 2689, 2690, and 2691....153

6.1 XPS Binding Energy Assignments....187

6.2 Tabulated Solubility Products of Lead Compounds....193

7.1 Summary of TEM Particle Size, BET and Manufacturer Data of α-Fe_2O_3 Nanoparticles Used....200

7.2 Elemental Composition of α-Fe_2O_3 Nanoparticles as Determined from XPS Analysis....205

LIST OF FIGURES

Figure

1.1 Schematic of aerosol sources, composition, transport, deposition, and impacts on climate and biogeochemistry. Adapted from Ref. 7. 4

1.2 Dust images were captured using Moderate Resolution Imaging Spectroradiometer (MODIS) on NASA's Terra satellite. (a) Dust plume is transported off of the west coast of Africa and over the Atlantic Ocean in late September 2011. (b) Dust from the Gobi desert is transported eastward as shown in late April 2011 raised from both north and south sources of the Mongolia-China border. [Reprinted with permission from Visible Earth (http://visibleearth.nasa.gov). Copyright 2012 NASA] 7

1.3 Relative elemental concentrations of major constituents in mineral aerosol from various source locations. Adapted from Ref. 18. 9

1.4 Solar radiation spectrum for direct light at both the top of the Earth's atmosphere and at sea level. The sun produces light with a distribution similar to what would be expected from a 5525 K (5250 ℃) blackbody, which is approximately the sun's surface temperature. As light passes through the atmosphere, some is absorbed by gases with specific absorption bands. Adapted from http://www.globalwarmingart.com/wiki/File:Solar_Spectrum _png. Image was created by Robert A. Rohde / Global Warming Art. 15

1.5 Global average radiative forcing (RF) in 2005 (best estimates and 5 to 95% uncertainty ranges) with respect to 1750 for CO_2, CH_4, N_2O and other important agents and mechanisms, together with the typical geographical extent (spatial scale) of the forcing and the assessed level of scientific understanding (LOSU). Adapted from Ref. 62....19

2.1 Schematic diagram of environmental aerosol chamber and simulated solar system: (A) aerosol inlet valve and antechamber, (V) water bubbler for relative humidity experiments, (B) flow meters, (RH) relative humidity sensor, (FT-IR) FT-IR spectrophotometer, (M) mirrors for the external beam path, (MCT) midband HgCdTe IR detector, (PB) purge boxes for the external beam path; (SS) solar simulator, (WF) water filter, (UVT) borofloat 33 glass window. Thermocouples and pressure transducers are also connected to the chamber. Adapted from Ref. 105....30

2.2 Picture of solar simulator S13-575. 32

2.3 Transmittance of Borofloat 33 window used in the current study.....34

2.4 Schematic diagram of solar simulator S13-575 showing the positions of the occulting spots on the Teflon surface window. The occulting spots are represented as squares on the right side of the figure. The bottom of the map corresponds to the side with electric fan component on the solar simulator. 35

2.5 Solar simulator spectral irradiance at the bottom of the environmental aerosol chamber. The insert shows the solar constant profile in the environmental aerosol chamber. 36

2.6 Mirror system used to direct the external IR beam from FTIR instrument to get through the environmental aerosol chamber and then focus on the MCT detector. 38

2.7 The left side of the figure is a picture of the partial impactor system. The right side is a schematic with critical dimensions labeled....41

2.8 Schematic of the custom glass vessel used for quantitative iron dissolution measurement. 47

3.1 Solar simulator spectral irradiance (blue line) at the bottom of the environmental aerosol chamber compared to the absorption cross section of nitric acid (red line)....63

3.2 (A) FTIR spectra of gaseous species in the environmental aerosol chamber collected at <1% RH (a) prior to Al_2O_3 introduction in the dark; (b) prior to Al_2O_3 introduction after 60 minutes of irradiation; (c) after Al_2O_3 introduction for 200 minutes with irradiation; (d) after Al_2O_3 introduction for 400 minutes with irradiation; (e) turned off radiation and post-irradiation. (B) A magnified view of the spectral region from 1000 to 2000 cm-1. A decrease of HNO_3 bands is evident, as well as the growth of NO and NO_2 bands....65

3.3 A typical concentration-time profile of gaseous HNO_3 (○), NO_2 (□), and NO (◊) during the heterogeneous photoreaction of HNO_3 with Al_2O_3 at <1% RH in the environmental aerosol chamber. Negative reaction time represents the passivation period (t < -100 min), and irradiation period (t = -100 min-0 min) before Al_2O_3 introduction at time t = 0 min, followed by the period of heterogeneous photoreaction. The solar simulator was turned off at time t = 550 min, followed by the post-irradiation period. 66

3.4 A typical concentration-time profile of gaseous HNO_3 in the presence of Al_2O_3 under dark and <1% RH conditions in the environmental aerosol chamber. The saturation uptake of HNO_3 on Al_2O_3 is rapidly attained after the introduction of Al_2O_3 at t = 0 min. 72

3.5 A typical concentration-time profile of gaseous HNO_3 (○) and NO_2 (□) during the heterogeneous photoreaction of HNO_3 with Al_2O_3 at 20% RH in the environmental aerosol chamber. 76

4.1 Solar simulator spectral irradiance (blue line) at the bottom of the environmental aerosol chamber compared to the absorption cross section of ozone (red line) and hydrogen peroxide (black line). 88

4.2 Ozone decay on oxides in the environmental aerosol chamber under dry, <2% RH, conditions for both dark and irradiation experiments: (a) α-Fe_2O_3, (b) α-FeOOH, (c) TiO_2 and (d) α-Al_2O_3. Aerosol introduction into the chamber occurred at time, t = 0 min. The effect of irradiation on the ozone uptake depends on the nature of the specific....93

4.3 Comparison of ozone decay obtained from laboratory measurements and model calculations at 18% RH and 30% RH in the absence of oxides. Open symbols represent the experimental data, while the solid line depicts the results of the model calculation. 95

4.4 Comparison of ozone decay obtained from laboratory measurements and model calculations in the presence of α-Fe_2O_3 under a variety of conditions: (a) dark and dry, <2% RH, (b) dark and 21% RH, (c) irradiated and dry,<2% RH, and (c) irradiated and 25% RH. Open symbols represent the experimental data, while the solid line depicts the results of the model calculation. Aerosol introduction into the chamber occurred at time, t = 0 min. 97

4.5 Comparison of ozone decay obtained from laboratory measurements and model calculations in the presence of TiO_2 under a variety of conditions: (a) irradiated and dry, <2% RH, (b) irradiated and 12% RH, (c) irradiated and 22% RH, and (c) irradiated and 39% RH. Open symbols represent the experimental data, while the solid line depicts the results of the model calculation. Aerosol introduction into the chamber occurred at time, t = 0 min. 98

4.6 A schematic showing the comparison of daytime and nighttime chemistry of ozone on various atmospherically relevant oxides. 108

5.1 Representative secondary electron images and corresponding Al, Si, and Fe elemental maps obtained from SEM/EDX analyses of (a) fly ash SRM 2689, (b) fly ash SRM 2690, and (c) fly ash SRM 2691. The fly ash particles are mainly spherical with a heterogeneous distribution of iron.....121

5.2 Mössbauer spectra of fly ash particles SRMs 2689, 2690, and 2691collected at 13 K. Each spectrum has been least-squares fitted to a model based on three distinct iron-bearing components, including Fe(III) in oxides (a), and Fe(III) (b) and Fe(II) (c) in aluminosilicate glass, respectively, as indicated by the line diagrams above the spectra. 123

5.3 Fitting results of Mössbauer spectra of fly ash SRMs 2689, 2690, and 2691.(a) the fitting Mössbauer spectra; (b) the partitioning of iron speciation. 124

5.4 Ternary diagrams indicating the relative amounts of Fe-Si-Al and Fe-Si-O obtained by CCSEM/EDX analysis in (a) fresh fly ash SRM 2689 particles, and (b) processed fly ash SRM 2689 particles after dissolution in pH 2 H_2SO_4 for 50 hours. 126

5.5 Ternary diagrams indicating the relative amounts of Fe-Si-Al and Fe-Si-O obtained by CCSEM/EDX analysis in (a) fresh Arizona test dust particles, and (b) processed Arizona test dust particles after dissolution in pH 2 H_2SO_4 for 50 hours. 127

5.6 Preparation of a cross-section FA particles, (a) lift-out of particles from substrate; (b) a high-magnification view of a cluster of fly-ash particles electrostatically attached to the probe tip. 130

5.7 Elemental maps obtained from EDX analysis of the cross-section fly ash particles in Figure 5.6. 131

5.8 Side-view (a) and top-view (b) secondary electron images of fly ash particles cut by a 30-kV Ga focused ion beam across selected boundary. The cross sections are highlighted with open red circles in the top-view image. (c) Elemental maps obtained from EDX analysis of the cross-section fly ash particles in (b). 133

5.9 Side-view (a) and top-view (b) secondary electron images of fly ash particles cut by a 30-kV Ga focused ion beam across selected boundary. The cross sections are highlighted with open red circles in the top-view image. (c) Elemental maps obtained from EDX analysis of the cross-section fly ash particles in (b). 134

5.10 Secondary electron images and elemental maps of fly ash particles cut by a 30-kV Ga focused ion beam across selected boundary. Elemental maps obtained from EDX analysis of the cross-section fly ash particles. 136

5.11 Secondary electron images and elemental maps of fly ash particles cut by a 30-kV Ga focused ion beam across selected boundary. Elemental maps were obtained from EDX analysis of the cross-section fly ash particles. 137

5.12 Dissolution of fly ash SRM 2689 and Arizona test dust in pH 1 and pH 2 H_2SO_4 over time. Calculated solubilities are shown for (a) dissolved Fe(II), (b) dissolved Fe(III), (c) total dissolved iron, and (d) the fraction of total dissolved Fe present as Fe(II) for each sample. Reactors contained a solids loading of 2 g L^{-1}. When present, uncertainties represent one standard deviation from triplicate experiments. 138

5.13 Representative secondary electron images of (a) fresh fly ash SRM 2689, and (b) processed fly ash SRM 2689 after dissolution in pH 2 H_2SO_4 for 50 hours.....140

5.14 Representative secondary electron images of (a) fresh Arizona test dust, and (b) processed Arizona test dust after dissolution in pH 2 H_2SO_4 for 50 hours.....141

5.15 Elemental maps of processed fly ash SRM 2689 particles after dissolution in pH 2 H_2SO_4 for 50 hours. The Fe-rich and Si-rich particles are clearly distinguished, further verifying the enrichment of Fe or Si in individual particles. 143

5.16 Elemental maps of processed fly ash SRM 2689 particles after dissolution in pH 2 H_2SO_4 for 50 hours. The Fe-rich and Si-rich particles are clearly distinguished, further verifying the enrichment of Fe or Si in individual particles. 144

5.17 Elemental maps of processed fly ash SRM 2689 particles after dissolution in pH 2 H_2SO_4 for 50 hours. 145

5.18 Elemental maps of fresh Arizona test dust particles. 147

5.19 Elemental maps of processed Arizona test dust particles after dissolution in pH 2 H_2SO_4 for 50 hours. 148

5.20 Dissolution of iron over time in simulated cloud processing of fly ash SRM 2689 particles: (a) the imposed pH cycle, (b) the corresponding total Fe solubility, (c) the fraction of total dissolved Fe present as Fe(II), and (d) the dissolved Fe(II) and Fe(III).....151

5.21 Dissolution of iron over time in simulated cloud processing of fly ash SRM 2690 particles: (a) the imposed pH cycle, (b) the corresponding total Fe solubility, (c) the fraction of total dissolved Fe present as Fe(II), and (d) the dissolved Fe(II) and Fe(III).....155

5.22 Dissolution of iron over time in simulated cloud processing of fly ash SRM 2691 particles: (a) the imposed pH cycle, (b) the corresponding total Fe solubility, (c) the fraction of total dissolved Fe present as Fe(II), and (d) the dissolved Fe(II) and Fe(III).....156

5.23 Comparison of iron dissolution under dark and irradiated conditions at different sampling points during the pH cycling from fly ash SRM 2689 particles. Irradiation enhances both the total dissolved Fe and the fraction of total dissolved Fe present as Fe(II).....158

5.24 Dissolution of fly ash SRM 2689 as a function of time in pH 2 solutions acidified by H_2SO_4, acetic acid and oxalic acid, respectively. Measured dissolved iron is shown as (a) dissolved Fe(II), (b) dissolved Fe(III), (c) total dissolved iron, and (d) the fraction of total dissolved iron present as Fe(II). Reactors contained a solid loading of 2 g L^{-1}. When present, error bars represent one standard deviation from triplicate experiments.....159

5.25 Dissolution of Arizona test dust as a function of time in pH 2 solutions acidified by H_2SO_4, acetic acid and oxalic acid, respectively. Measured dissolved iron is shown as (a) total dissolved iron and (b) the fraction of total dissolved iron present as Fe(II). Reactors contained a solid loading of 2 g L^{-1}. When present, error bars represent one standard deviation from triplicate experiments.....163

5.26 Influence of pH on iron dissolution of fly ash SRM 2689 at a function of time in solutions acidified by acetic acid and oxalic acid, respectively. Measure dissolved iron is shown as (a) total dissolved iron and (b) the fraction of total dissolved iron present as Fe(II). Reactors contained a solid loading of 2 g L^{-1}. When present, error bars represent one standard deviation from triplicate experiments.....165

5.27 Influence of irradiation on iron dissolution of fly ash SRM 2689 at a function of time in solutions pacified by acetic acid and oxalic acid, respectively. Measure dissolved iron is shown as (a) total dissolved iron and (b) the fraction of total dissolved iron present as Fe(II). Reactors contained a solid loading of 2 g L^{-1}. When present, error bars represent one standard deviation from triplicate experiments.....168

5.28 Dissolution profile of fly ash SRM 2689 as a function of time in pH 2 oxalic acid under dark and irradiation conditions, respectively. The results are showed the evolution of (a) pH, (b) the concentration of oxalic acid, (c) total dissolved iron, and (d) the fraction of total dissolved iron present as Fe(II).....169

5.29 Schematic showing disintegration of spherical coal fly ash particles into small irregular fragments during atmospheric transport and processing. 173

6.1 National inventory of lead emissions in U.S. in 2008 179

6.2 SEM image and XRD pattern PbO particles used in the current study. For comparison, XRD patterns of lead containing compounds and minerals, including PbO (massicot), Pb metal, PbO (litharge), PbO_2 (plattnerite), Pb_3O_4 (minium), $PbCO_3$ (cerussite) and $Pb_3(CO_3)_2(OH)_2$ (hydrocerussite) are shown. ...182

6.3 Survey spectra of unreacted PbO and after reactions with 100 mTorr NO_2. Inset: N1s region with a peak due to the adsorbed nitrate, NO_3^-, species. Standard deviation was calculated from three independent 30 min NO_2 adsorption experiments. 185

6.4 High resolution XPS O1s, N1s, C1s and Pb4f spectra of unreacted and reacted PbO under various environmental conditions, as well as $Pb(NO_3)_2$ standard. 186

6.5 (Filled circles) Quantification of nitrogen reaction product adsorbed on PbO after six consecutive exposures to 100 mTorr NO_2 for 30 min. For comparison, separate set of data is shown in filled squares of consecutive 100 mTorr NO_2 exposures at various RH. 190

6.6 ICP-OES measured Pb amounts in solution from unreacted PbO and reacted with 100 mTorr NO_2 for 24 h, as well as 100 mTorr NO_2 and 8 Torr H_2O mixture for 24 h. Reactors contained a solids loading of 50 g L^{-1}. Uncertainties represent one standard deviation from triplicate experiments. 192

7.1 Powder X-ray diffraction (XRD) patterns of α-Fe_2O_3 nanoparticles used in this study. 201

7.2 TEM images of α-Fe_2O_3 nanoparticles of different size. Analysis of over two hundred particles yield an average size of 2 ± 1, 43 ± 6, 85 ± 25, and 540 ± 90 nm for the four different samples used (see Table 7.1). 203

7.3 XPS high resolution spectra in the Fe2p, O1s and C1s regions for α-Fe_2O_3 nanoparticles. The O1s region was peak-fit using four Gaussian-Lorentzian synthetic components. The black solid line represents experimental data and the green line with circular markers represents the total calculated fit. The other curves represent components used to curve fit the spectra. Ratios for different peak areas are given in Table 7.2 204

7.4 PAO1 grown overnight in M9 media were subcultured and exposed to four α-Fe_2O_3 particles (10 μg/mL) of different size and surface area (Table 7.1). Growth was recorded over nine hours. PAO1 exposed to the smaller particles with a larger surface area had the largest growth effect. Non-linear regression (curve-fit) with variable slope from three independent experiments was used for statistical analysis. Data were compared for all parameters of the growth curve using the extra sum of squares F-test to detect differences throughout the entire growth curve. n = 3 in triplicates. SEM reported * $p<0.0001$. 206

7.5 Iron oxide nanoparticles increase biofilm formation. PAO1 grown in the presence of 10µg/mL α-Fe_2O_3 (2 nm and 540 nm) or $FeCl_3$ for 24 hours and crystal violet staining was used to determine biofilm formation. 2 nm and 540 nm α-Fe_2O_3 as well as $FeCl_3$ increased biofilm formation more than control (*p<0.0001), however there were no differences between 2 nm and 540 nm biofilm formation. N=7 in triplicates. T-test used to compare 2 nm and 540 nm conditions. SEM reported. 208

7.6 Iron oxide nanoparticles inhibit antimicrobial peptide activity. Panel a. PAO1 growth in the presence of $FeCl_3$ with and without AMP cocktail in sodium phosphate buffer. After eighteen hours, $FeCl_3$ increased PAO1 growth. (-AMP) In the presence of $FeCl_3$, AMPs (600 µg/mL Lysozyme, 200 µg/mL Lactoferrin and 100ng/mL β-Defensin 1&2) are inhibited with and without incubating for one hour. (+AMP and Inc. AMPs) Panel b. α-Fe_2O_3 particles (2 nm and 540 nm) were added to PAO1 culture in the presence and absence of AMPs. PAO1 growth in the presence of 2 nm induces more growth than 540 nm particles (-AMP) * p=0.011. 2 nm α-Fe_2O_3 appears to inhibit AMP activity (+AMP) when compared with 540 nm **p=0.0061. When particles are removed after incubating with AMPs for one hour, the size dependent effect of AMP inhibition is lost (Inc. AMPs). N=3 in triplicates. T-test used to compare 2 nm and 540 nm conditions. SEM reported. 211

CHAPTER 1

INTRODUCTION

The atmosphere is composed of 78% nitrogen (N_2), 21% oxygen (O_2), a variable amount of water vapor (H_2O), argon (Ar), carbon dioxide (CO_2), and traces of other "noble" gases.[1] Although the composition of the atmosphere changes slowly from the perspective of the Earth's evolution, the trace gas abundances have changed rapidly and remarkably over the last two centuries due to the dramatic growth of population and the great development of industry.

Comparison of current levels with those of the distant part suggested that CO_2 and CH_4 are two typical extreme examples of recent increases of atmospheric trace gases.[1] The comparison can be achieved by measuring the concentration of CO_2 and CH_4 in the bubble air trapped in the ice core in perpetually cold places such as Antarctica and Greenland. With extensive measurements, CO_2 and CH_4 concentrations are believed to stay relative stable at 260 and 0.7 ppm, respectively, from the end of the last ice age some 10,000 years ago until approximately 300 years ago. After that, the CO_2 and CH_4 concentrations have been built up continually, reaching to a current mixing ratio of approximately 390 and 1.8 ppm, respectively. Human activities account for most of the rapid changes in trace gases over the past 200 years due to combustion of fossil fuels for transportation and energy, biomass burning, industrial activities, agricultural activities and deforestation.

Although trace gases only account for approximately 1% abundance in the atmosphere, they play a crucial role in regulating the Earth's climate, and have a great influence on human health. CO_2 and CH_4 are two typical greenhouse gases in the atmosphere. Increases of these gases in the atmosphere potentially elevate the Earth's temperature, cause sea levels to rise, and eventually lead to climate change.

Another representative example of change in trace gas concentrations that impose great environmental concerns is that of ozone (O_3). Ozone in the stratosphere acts as a UV filter to absorb biologically harmful ultraviolet (UV) light to prevent UV radiation reaching the Earth's surface. The emission of large quantities of chlorofluorocarbons (CFCs) and halons are extremely stable and can therefore reach the stratosphere, where it can be photolyzed to form atomic Cl and F radicals and catalytically deplete the ozone layer. Due to the ozone depletion, more UV radiation would penetrate the atmosphere and reach the Earth's surface, causing a deleterious effect on the vegetations, animals, ecosystem and human health.

Local scale air pollution around industrial areas and big cities also causes great environmental and health problems. Photochemical smog, for example, is resulted from the interaction of nitrogen oxides and hydrocarbons, two common pollutants emitted from combustion of fossil fuel, under solar radiation to form highly oxidizing species including ozone and peroxyaceyl nitrate.[2, 3] It causes severe eye irritation, respiratory irritation and poor visibility. Sulfur dioxide, which is emitted from coal and heavy oil burning, can form industrial smog in winter. It was first discovered in 1952 in London that had approximately one million coal-fired stoves in addition to the emissions from local industry.[4, 5] The city experienced an extended period of extremely high particulate levels, which were 5-19 times greater than modern regulatory standards and led to the deaths of more than 4000 people during the two week episode and over 12,000 in the following 3 months.

1.1 Atmospheric Aerosol

The photochemical smog and industrial smog are both characteristic of aerosol formation. Aerosol, which is defined as a suspension of fine solid or liquid particles in the atmosphere, has gained enormous interest in the research of atmospheric chemistry.

Atmospheric aerosol particles originate from both natural and anthropogenic sources. Primary particles are emitted directly from the sources, like wind-blown soils, incomplete combustion of fossil fuel, biomass burning, sea spray, volcanic eruption and biological materials (plant debris, pollen, etc.) as shown in Figure 1.1. Secondary particles are formed by gas-to-particle conversion in the atmosphere and/or condensation of gas species on aerosol particles. Aerosols contain sulfate, ammonium, nitrate, sodium chloride, trace metals, carbonaceous material, crustal elements, and waters. While natural emissions contribute the background level of aerosol in the atmosphere, anthropogenic emissions leading to atmospheric aerosol have increased dramatically over the past century and have been implicated in human health effects, in visibility reduction in urban and regional areas, in acid deposition, and in perturbing the Earth's radiation balance.

Aerosol undergoes a variety of physical and chemical interactions and transformation in the atmosphere, during which the size, morphology, and chemical composition of aerosol would change (Figure 1.1). The interaction of trace gases and aerosols, which is termed "heterogeneous reaction", is especially of considerable significance. For example, ozone depletion in the stratosphere is driven by heterogeneous reactions between aerosol in the form of ice particulates and inactive chlorine compounds. The aerosol surface acts as a medium to promote the conversion of inactive chlorine reservoir species to chlorine gas that can then be photolyzed to produce chlorine atoms, and participate in the ozone depletion chemical cycles. Aerosols can undergo cloud processing by acting as cloud condensation nuclei, on which water vapor in the atmosphere can condense to form cloud droplets. When the clouds re-evaporate, aerosol particles are again released from the evaporating cloud droplets. Given the dramatical change of water content and hence pH on the surfaces of aerosol particles during cloud condensation and evaporation, the sizes, morphologies and chemical compositions of aerosol particles would be modified.[6]

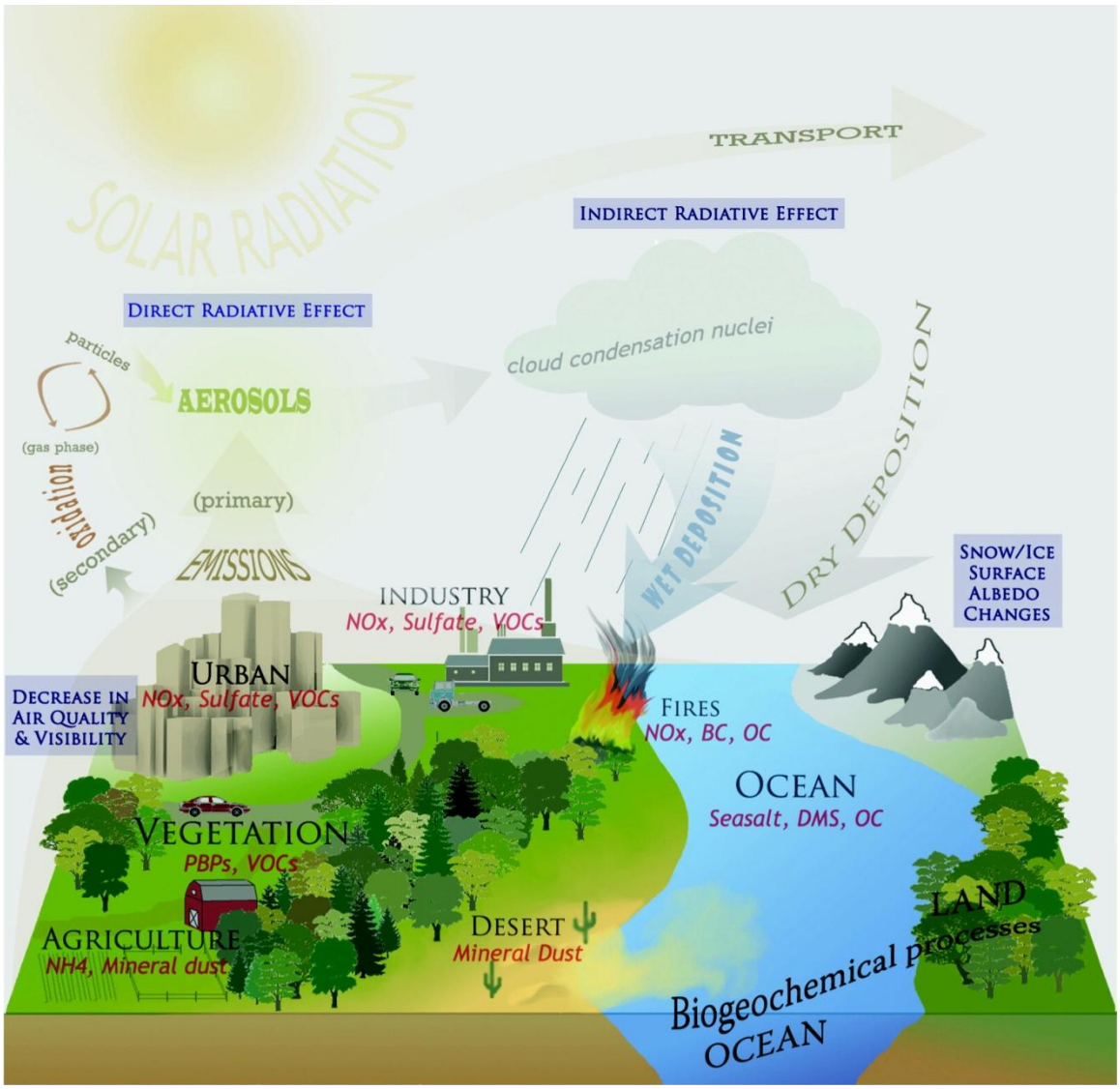

Figure 1.1 Schematic of aerosol sources, composition, transport, deposition, and impacts on climate and biogeochemistry. Adapted from Ref. 7.

If, however, cloud droplets form precipitation and reach the Earth's surface, aerosol particles are scavenged to the surface and removed from the atmosphere. This process, termed "wet deposition", is the primary sink of aerosol particles in the accumulation mode (e.g. 0.1-1 μm). Beside wet deposition, particle deposition without precipitation of airborne water particles, that is, "dry deposition" by convective transport, diffusion, and adhesion to the Earth's surface, is less important but the primary sink for large aerosol particles (Figure 1.1). Depending on the aerosol properties and the meteorological conditions, the characteristic residence time (lifetime) of aerosol particles in the atmosphere range from hours to weeks.

An overview of major type, sources, and inventories of atmospheric aerosol is given in Table in 1.1. This thesis mainly focuses on mineral dust and anthropogenic aerosol from coal combustion, biomass burning and industrial processes. These different types of aerosol are discussed in detail below.

1.1.1 Mineral Dust Aerosol

As one of the most mass abundant types of aerosol emitted into the atmosphere, wind-blown mineral dust aerosol accounts for one third to one half of the mass of the total aerosol budget. It is estimated that between 1600 and 2000 Tg of mineral dust is uplifted into the atmosphere annually.[8] Wind-blown soil is the main source of mineral dust.[9] The arid and semiarid areas of the world, which cover one third of the global continental area, are where the majority of mineral dust is originated. Saharan-Sahel region of northern Africa is the largest global source, and central Asia is the second largest dust source. Figure 1.2 shows images of Saharan and Gobi desert regions during dust storm events captured by NASA's Terra satellite. In addition, human activities, such as improper agricultural and grazing practices, contribute to 20-50% of the atmospheric dust loadings.[10, 11] The improper agricultural and grazing practices have resulted in

Table 1.1 Global Emission Estimated for Major Aerosol Classes

Source			Estimated Flux ($Tg\ yr^{-1}$)
Natural	Primary	Mineral dust 0.1-1.0 μm	48
		Mineral dust 1.0-2.5 μm	260
		Mineral dust 2.5-5.0 μm	609
		Mineral dust 5.0-10.0 μm	573
		Mineral dust 0.1-10 μm	1490
		Seasalt	10,100
		Volcanic dust	30
		Biological debris	50
	Secondary	Sulfates from DMS	12.4
		Sulfate from volcanic SO_2	20
		Organic aerosol from biogenic VOC	11.2
Anthropogenic	Primary	Industrial dust (except black carbon)	100
		Black carbon	12
		Organic aerosol	81
	Secondary	Sulfate from SO_2	48.6
		Nitrates from NO_x	21.3

Source: Seinfeld, J. H.; Pandis, S. N., *Atmospheric Chemistry and Physics: From Air Pollution to Climate Change*. 2 ed.; John Wiley: New York, 2006.

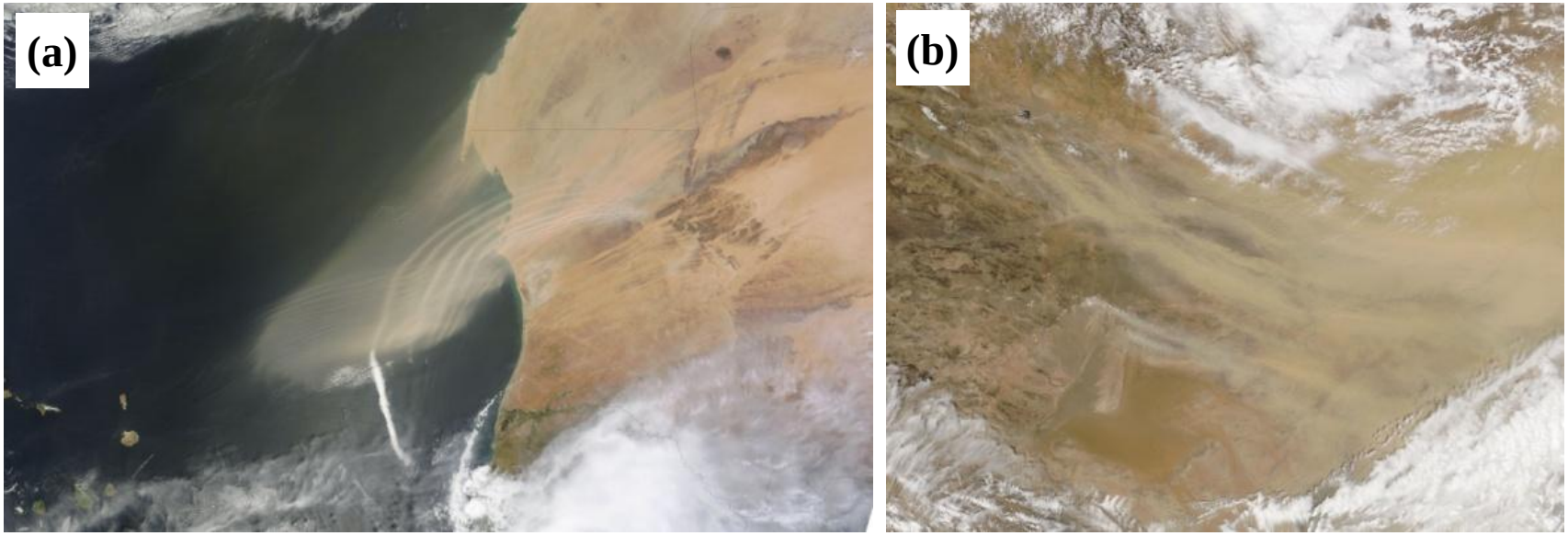

Figure 1.2 Dust images were captured using Moderate Resolution Imaging Spectroradiometer (MODIS) on NASA's Terra satellite. (a) Dust plume is transported off of the west coast of Africa and over the Atlantic Ocean in late September 2011. (b) Dust from the Gobi desert is transported eastward as shown in late April 2011 raised from both north and south sources of the Mongolia-China border. [Reprinted with permission from Visible Earth (http://visibleearth.nasa.gov). Copyright 2012 NASA]

desertification of land throughout the globe.[12] The estimated budget of mineral dust is therefore likely to increase due to the predicted increase of human activities as well as the expansion of arid regions.[12] Gravitational settling and wet deposition are the major removal pathways for mineral dust from the atmosphere. The average lifetime of mineral dust particles is approximately 2 weeks, during which dust can be transported thousands of miles. Saharan dust plumes frequently reach the Caribbean, and plumes of dust from central Asia can be detected on the west coast of North America.[1, 13-17] Fine Asian dust (<2.5 μm) is a regular component of the troposphere over the eastern Pacific and western North America.[16]

Given that mineral dust aerosol is from wind-blown eroded soils, the chemical composition is thought to be similar to that of the continental crust which is in part composed of a number of mineral oxide phases. The exact percentage of each phase varies and depends on the exact mineral dust source region from which it orginates.[18] Typical abundances of different major oxides in the continental crust are given in Table 1.1. Mineral dust is approximately composed of 60% SiO_2 and 10-15% Al_2O_3. The percentages of other oxides, such as Fe_2O_3, MgO, and CaO are slightly more varied and dependent on source location.

Table 1.2 Abundance of Major Oxides in the Continental Crust[18]

Oxide	SiO_2	Al_2O_3	Fe_2O_3	CaO	Na_2O	MgO	K_2O	TiO_2	BaO	MnO
%	61.5	15.1	6.28	5.5	3.2	3.7	2.4	0.68	0.0584	0.1

Source: Usher, C. R.; Michel, A. E.; Grassian, V. H. Reactions on mineral dust. *Chemical Reviews* **2003,** *103*(*12*), 4883-4939.

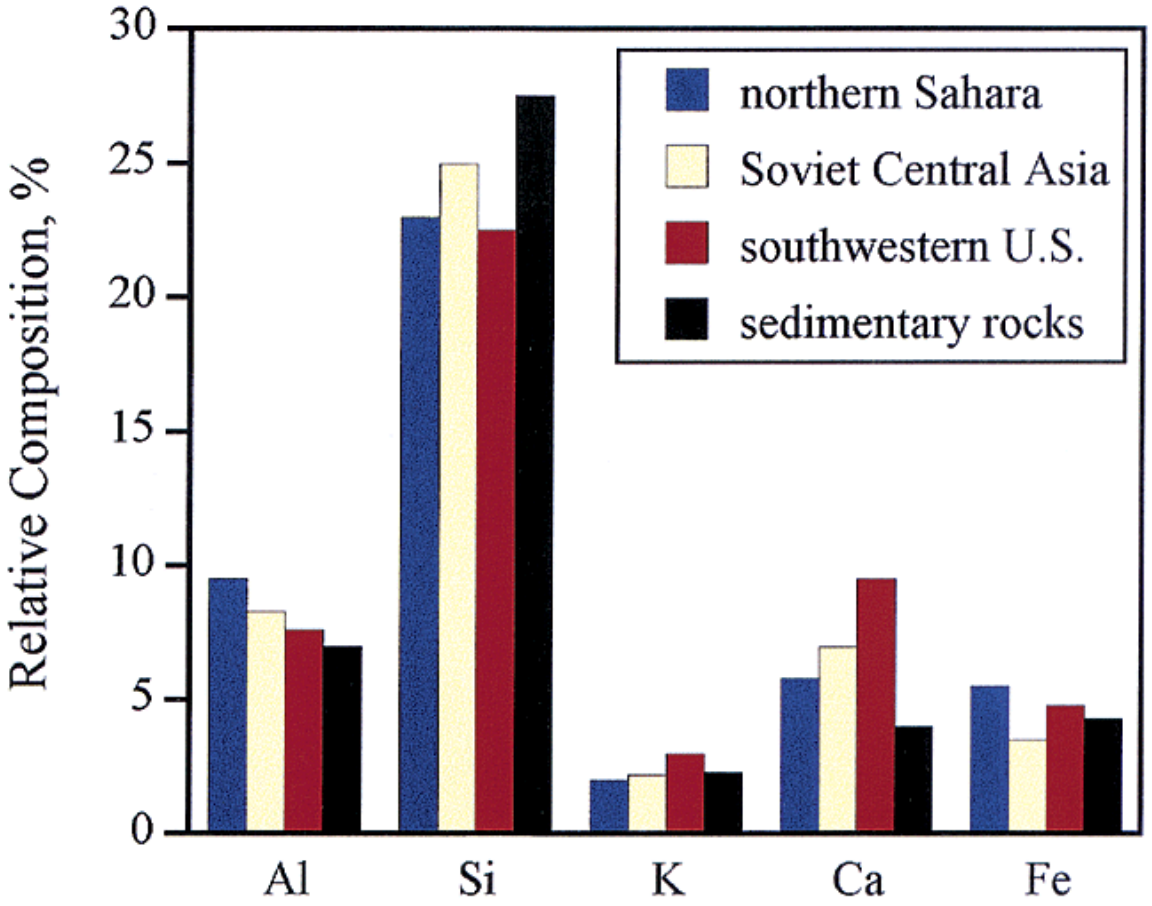

Figure 1.3 Relative elemental concentrations of major constituents in mineral aerosol from various source locations. Adapted from Ref. 18.

Analyses of the composition of airborne mineral dust collected from various source locations show that mineral dust around the globe has fairly small variations in elemental content as shown in Figure 1.3.[19] As a general rule, most of analyzed elements are found to be enriched in the aerosol compared with elemental percentages in sedimentary rocks. Only Si has higher concentration in bulk soils and rocks. Large grains of wind-blown mineral dust commonly contain higher abundance of quartz (SiO_2) and rapidly fall out of the atmosphere due to the large size and high settling velocity.

While oxide minerals represent the majority of mineral dust, reactive oxide components, such as alumina oxide, iron oxide, and titanium oxide have gained even more interest. Extensive studies have been carried out using these oxide components as models of mineral dust.[18]

1.1.2 Anthropogenic Aerosol

With the intensification of human activity, aerosols are estimated to have been increased by 10-40%[20, 21] since the preindustrial era. Human activities such as biomass burning and incomplete combustion of fossil fuels create an enormous continuous input of aerosol into the atmosphere with an estimation of 270 Tg $year^{-1}$.[1] These anthropogenic aerosols are typically in the submicrometer- to micrometer-size range and are composed of numerous inorganic and organic species.[22, 23]

Fly ash which originates from coal combustion is one of the typical metal-containing anthropogenic aerosols. Even equipped with highly efficient gas cleaning devices, a considerable portion of finely sized fraction of fly ash may escape from the combustion stack into the atmosphere with the exhaust gas, resulting in air pollution on both urban and regional scale.[24] With increasing legislative pressure to reduce nitrogen oxides and mercury emission, operators are tending to run at lower temperature and with an adsorbent present.[25] These changes in operating conditions unfortunately increase the fly ash production. Fly ash particles contain high levels of toxic metals, such as Pb, Co,

Cr, Ni, Se, Mo, As, Sb, and Cd, which potentially impose negative effects on human health. In addition, the expanding utilization of engineered nanomaterials releases nanoparticles, especially environmentally damaging and toxic metal,[26] into the atmosphere, representing another significant yet unknown source.

Although a number of natural processes, such as forest fires and volcano eruptions, can bring nanoparticles to the atmosphere, the exposure of humans to nanoparticles has increased dramatically in the last century because of anthropogenic sources such as internal combustion engines and power plants.[27-29] While considerable progress has been made in engine combustion technologies, the size of primary black carbon soot particles in vehicle exhaust has decreased substantially from micrometer into nanometer size range, increasing the emission of nanoparticles in the atmosphere. In addition, nanoparticles are not only emitted directly from various sources but also formed in the atmosphere from precursors through complex pathways, like gas-to-particle conversion. Photochemical reactions of volatile organic compounds, for example, lead to the formation of low molecular weight organic compounds, which may condense to form secondary organic aerosol through gas-to-particle conversion.[30]

The rapidly developing field of nanotechnology is likely to become another significant source of engineered nanomaterials in the atmosphere.[27-29] Engineered nanomaterials can enter the environments from manufacturing effluent or from spillage during shipping and handling.[28] Personal-care products such as cosmetics and sunscreens, mostly contain nanomaterials, which can enter the environment from wearing and washing off.[28] Nanomaterials are used in electronics, tires, fuel cells, and many other products. It is unknown whether some of these materials may leak out or be worn off over the period of use. Nanomaterials have been also applied in disposable materials such as filters and electronics and may therefore reach the environment through landfills and other methods of disposal.

Due to the ineffectiveness of aerosol sampling methods in collecting nanoscale particles, atmospheric nanoparticles remain relatively unknown and difficult to detect.[30-33] In a study by Bang et al.,[26] ultrafine or nanoparticulates (<10-100 nm) that were collected on transmission electron microscope (TEM) carbon-coated formvar grids in a thermal precipitator (TP) exhibited a propensity (>50%) of non-biological material. Most of the collected, non-biological particles were crystalline, or aggregates of individual, inorganic, and crystal grains. This seems to be an especially important feature since large crystal surface/volume ratios are catalytically active.

Besides the direct emission, naturally occurring aerosols can be modified by human activity as well. For instance, with the high industrial emission of sulfur dioxide and nitrogen oxides into the atmosphere, airborne mineral dust was found to be coated with sulfate and nitrate during the long-range transport and exhibit higher hydroscopic and more efficient as cloud condensation nuclei (CCN).[18, 34] Such a large perturbation of the global aerosol by human activity is currently a major environmental concern. Relevant questions are how the perturbation of aerosol by human activity would affect chemical balance of atmosphere, biogeochemical cycle, climate and human health *and,* what are the differences between the global impact of anthropogenic aerosols and naturally occurring ones?

1.2 Impacts of Aerosol

Long-range transport of atmospheric aerosols indicates that these particles interact with many atmospheric, terrestrial, and ocean systems. It has been well established that aerosols can greatly affect atmospheric chemistry, global climate, human health, and biogeochemical cycle, which are discussed in more detail below.

1.2.1 Heterogeneous Chemistry and Photochemistry of Aerosol

The interaction of aerosol with gas species, as one typical heterogeneous reactio, is evident in the atmosphere. For example, in-situ airborne measurements of trace gases, aerosol size distribution, chemistry and optical properties over Mexico and the Eastern North Pacific during MILAGRO and INTEX-B campaigns indicate that heterogeneous reactions between trace gases and mineral dust. During transport across the North Pacific, ~5-30% $CaCO_3$ is converted to $CaSO_4$ or $Ca(NO_3)_2$ with an additional ~4% consumed through reactions with HCl.[35]

By providing surfaces that facilitate heterogeneous chemistry, aerosols can alter the chemical composition of the troposphere and therefore act as sinks for some trace gases, as well as sources of others. When interacting with atmospheric species, the composition, hydroscopicity, and even morphology of the aerosol will change, which in turn affects its subsequent reactivity with other atmospheric species.[18]

Since 1996, much work in field, laboratory, and modeling studies have been done to investigate heterogeneous chemistry of aerosols, bringing an increasingly clear understanding to this issue. The seasalt aerosols present in the marine boundary layer are highly concentrated solution of halides. Uptake of reactive species, such as HOBr, $ClONO_2$, HNO_3 and N_2O_5, can lead to the liberation of halogens.[36-40] The release of halogens from seasalts have far-reaching significance given that halogens are potent oxidants in the atmosphere. Trace atmospheric gases, such as SO_2, HNO_3, and O_3, can react with mineral dust surfaces with formation of gaseous or/and surface adsorbed species.[18] For example, mineral dust containing $CaCO_3$ removes effectively nitric acid to form CO_2, representing an important scavenger for nitric acid in the atmosphere.[41] Ozone was reported to decompose on typical components of aerosol.[42, 43]

Research over the last decade focuses on the nighttime chemistry of aerosol. Little is known about heterogeneous chemical processes activated by light and surface photocatalysis. Indeed, although short-wavelength radiation is absorbed in the

stratosphere and upper troposphere, solar radiation with wavelength >300 nm can reach the Earth's surface. The atmospheric penetrating flux of solar photons is enormous. At sunny noon, for example, the density of the solar radiation with wavelengths of the near UV region of 300-400 nm corresponds to approximately 10^{13} quanta cm^{-2} s^{-1}.[44] Various atmospherically relevant metal oxides such as TiO_2, ZnO and Fe_2O_3, as well as light absorbing coatings associated with the aerosol particle surface experience absorption of quanta with wavelengths radiation <400 nm and even of visible light. Solar radiation in this region has sufficient energy to initiate heterogeneous photoreactions in the atmosphere. Relevant questions, then, are what is the role of heterogeneous photochemistry in the troposphere *and,* how does the daytime chemistry of aerosol differ from its nighttime chemistry?

1.2.2 Water Adsorption and Its Effects on Heterogeneous Reactions

Water is one of the most important and pervasive chemicals in the Earth's atmosphere. Mostly, atmospheric aerosols are covered by dense layers of water molecules in ambient pressure environments, and even in ultrahigh vacuum (UHV) conditions. The surface adsorbed water is in a dynamic balance with water vapor. Depending on the system, adsorbed water can be present as a molecule or it may dissociate on the surface. Atmospheric water vapor readily adsorbs to aerosol particles and dissociates resulting a pair of hydroxyl groups terminated on the aerosol particle surface. Adsorbed water is then hydrogen bonded to these hydroxyl groups in equilibrium with water vapor forming a thin water layer over the particle surface, causing a potential modification of surface properties of aerosol particles.[45, 46] Previous work has shown that surface adsorbed water can either inhibit or enhance heterogeneous reactions depending on the relative humidity, the physicochemical properties of aerosols and the specific reactions explored. The potential effects of surface adsorbed water include: (i) altering reaction pathways and product speciation; (ii)

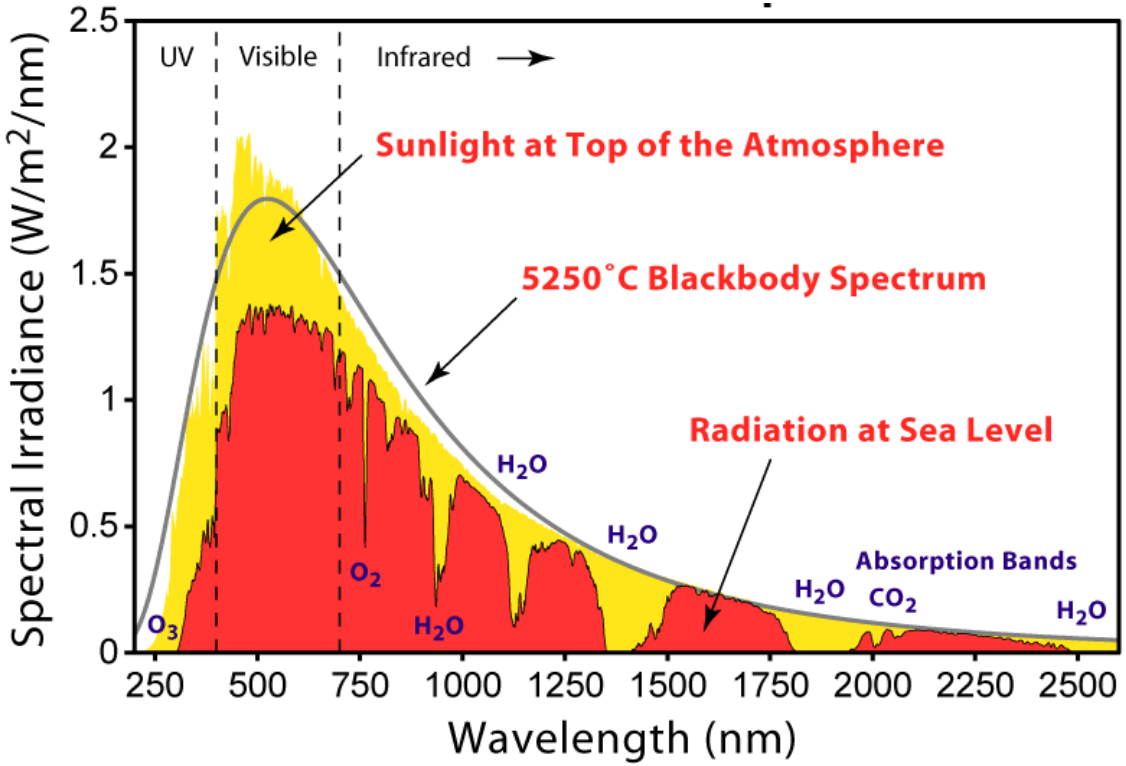

Figure 1.4 Solar radiation spectrum for direct light at both the top of the Earth's atmosphere and at sea level. The sun produces light with a distribution similar to what would be expected from a 5525 K (5250 ℃) blackbody, which is approximately the sun's surface temperature. As light passes through the atmosphere, some is absorbed by gases with specific absorption bands. Adapted from http://www.globalwarmingart.com/wiki/File:Solar_Spectrum_png. Image was created by Robert A. Rohde / Global Warming Art.

coordinating with surface species; (iii) enhancing the reactions by increasing ion mobility; and (iv) inhibiting the reactions by blocking surface active sites.[18, 47, 48] An interesting yet unknown aspect is the interaction between surface adsorbed water and heterogeneous photochemistry.

1.2.3 Photochemistry of Nitrate

While it has been well established from field studies that nitrate exists on the surface of mineral dust,[49-51] nitrate was believed to be the end-product of NO_x (NO_x = NO + NO_2) oxidation, with removal via wet and dry deposition. However, with the observation of active photochemistry of nitrate in snow packs,[52, 53] and the subsequent studies on the reactive oxides of nitrogen such as HONO, NO and NO_2 generated in this process,[54-59] particulate nitrate may, in fact, be a reservoir rather than a sink for gas-phase nitrogen oxides in the atmosphere. Additionally, recent model calculations predicted nitrate aerosols to become more important in the future atmosphere due to the expected increase in nitrate precursor emissions and the decline of ammonium-sulphate aerosols.[60] Surface nitrate has a huge influence on the global ozone budget.[1] All of the aforementioned factors together make an understanding of all the relevant processes involving nitric acid, nitrogen oxides and ozone, including photochemistry, even more important.

1.2.4 Climate Effect of Aerosol

Aerosols have substantially different optical properties than atmospheric gases and can absorb and scatter solar radiation. This feature results in a direct modification to the radiative budget of the atmosphere and the surface below, known as a direct radiative effect. The magnitude and sign of the direct radiative effect for a specific aerosol is strongly dependent on its optical properties, which dictate the fractions of light aerosols absorb or reflect as a function of wavelength. Aerosol can also affect the global radiation

balance indirectly through their interaction with clouds by acting as cloud nucleation nuclei (CCN). Aerosols can change the size distribution, residence time, and optical properties of clouds, influencing radiative transfer and causing an unexpected global climate change.[61] In addition, aerosols can provide a surface site for heterogeneous reactions of atmospheric gases as discussed in the previous subsection, causing the change of atmospheric balance. The modifications of optical constants and thermodynamic properties of aerosol surfaces as well as the change of atmospheric gas phase compositions, have an effect on the radiative forcing, and eventually lead to climate change. Very small concentrations of absorbing aerosols deposited onto snow and sea ice can reduce albedo of snow. Small change of snow albedo can exert a large influence on climate by altering the timing of snow melt and triggering snow/ice-albedo feedback.

Currently, researchers have a low level of scientific understanding about the effect of aerosols on radiative budget of the atmosphere, according to the latest report by the Intergovernmental Panel on Climate Change (ICPP).The scientific understanding are designated as "medium - low" and "low" for direct and indirect climate forcing, respectively, as shown in Figure 1.5.[1, 62] Moreover, the IPCC AR4 report (2007) concluded that uncertainties associated with changes in Earth's radiation budget due to anthropogenic aerosols make the largest contribution to the overall uncertainty in radiative forcing of climate changes among the factors assessed over the industrial period.[62]

1.2.5 Aerosol in Biogeochemical Cycles

Aerosol has significant effects on biogeochemical cycles through the transport and deposition of aerosols in the open ocean water. The deposition of aerosol in the open ocean water can release various nutrients including iron, nitrogen, and phosphorus to ocean microorganisms. The most important nutrient for the ocean biogeochemistry

appears to be iron given that soluble iron serves as a limiting nutrient for various organisms in the ocean. The relief of iron stress triggers the growth of various organisms, affecting ocean biogeochemical cycles which in turn has a large-scale feedback on global climate through atmospheric CO_2 consumption and dust production.[63] Iron enrichment in the extensive regions of the ocean referred to as high nutrient low chlorophyll (HNLC) regions leads to elevated phytoplankton biomass and rates of photosynthesis in surface water, causing a large drawdown of carbon dioxide, an increase of dimethyl sulfide levels, and eventually a potential feedback effect on the Earth climate system.[63-67] Due to the complexity of the aerosol-Earth system and the lack of data, considerable uncertainties in these interactions still remain, requiring more comprehensive research.

It is generally believed that soluble iron is mainly derived from the transport and deposition of mineral dust.[63, 68-71] While the solubility of iron in soil is relative low, the atmospheric chemical processing of dust particles was suggested to increases iron solubility.[69, 72-79] Indeed, some field studies fail to demonstrate apparent change in the solubility of iron particles as they move downwind from the North African source, indicating that the hypothesis of atmospheric chemical processing sole is insufficient to explain the high iron solubility observed in field studies.[80]

More recent evidence from field, laboratory and modeling studies suggest that anthropogenic aerosol produced from fossil fuel combustion and biomass burning may represent a significant source of soluble iron.[70, 81-85] The high correlation between soluble iron and combustion-derived black carbon observed at Cheju, Korea[85] strongly highlights the anthropogenic combustion source of iron. A modeling study by Luo[81] further supports this hypothesis by predicting that combustion-derived aerosols supply a source of highly-soluble iron to the surface ocean. Schroth[83] also reported high solubility of iron (~80%) from oil fly ash, in which iron mainly presents as ferric sulfate salts.

The contribution of bioavailable iron from anthropogenic emission relative to mineral dust deposition still remains controversial. Laboratory experiments to explore the

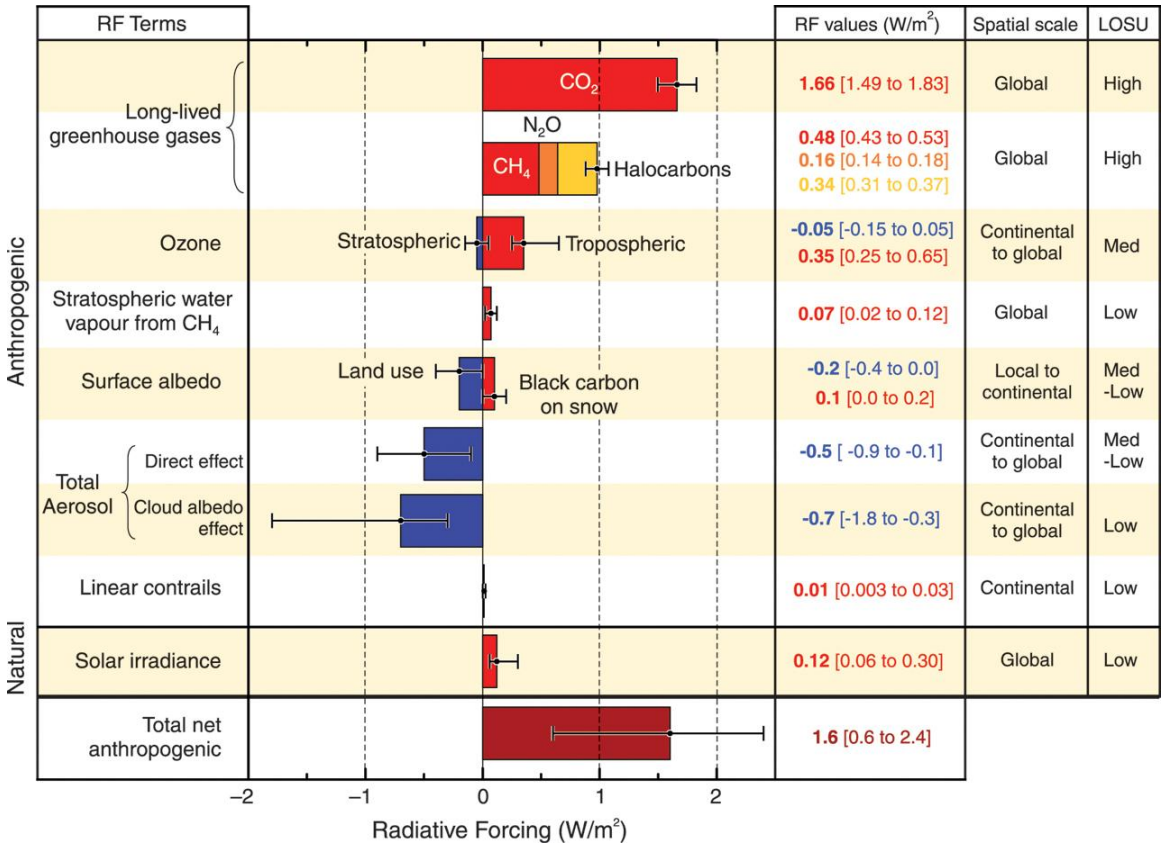

Figure 1.5 Global average radiative forcing (RF) in 2005 (best estimates and 5 to 95% uncertainty ranges) with respect to 1750 for CO_2, CH_4, N_2O and other important agents and mechanisms, together with the typical geographical extent (spatial scale) of the forcing and the assessed level of scientific understanding (LOSU). Adapted from Ref. 62.

iron dissolution behavior of anthropogenic aerosols are highly desirable for better understanding the effects of aerosols on biogeochemical cycles and climate.

1.2.6 The Effect of Aerosol on Human Health

Long-term exposure to a large amounts of aerosol can lead to damage of the human respiratory system since fine particulates can penetrate into and deposit on lung tissue, producing scarring and pulmonary disorders.[86] Numerous epidemiological studies have shown that fine particles in the atmosphere are correlated with severe health effects, including enhanced mortality, cardiovascular, respiratory, and allergic diseases.[87] The effects of aerosols on human health have been reviewed in detail.[88-90] Toxicological investigation in vivo and in vitro have demonstrated substantial pulmonary toxicity of model and real environmental aerosol particles, but the biochemical mechanisms and molecular processes that cause the toxicological effects such as oxidative stress and inflammatory response have not yet been resolved. Parameters that are potentially relevant to aerosol health effects include particle size and morphology, durability of particles, and surface chemistry. An example of particles affecting the human health is "World Trade Center cough". The collapse of the World Trade Center towers in New York City on September 11, 2011, released aerosols containing a wide range of dust and other particulate into the atmosphere.[91, 92] Besides the initial release, settled particles were also re-suspended into the atmosphere during the rescue and clean-up efforts. The emergency works at ground zero, and even the residents live nearby have shown symptoms that have been correlated with particulates they inhales.[93, 94]

In 1997, the U.S. Environmental Protection Agency established the "PM (particulate matter) 2.5" standard, which recognizes the importance of aerosols with size <2.5 μm in causing health problems. Long exposure to or large doses of particles below this size can cause respiratory damage because they penetrate deep into the lung tissues, produce scarring, and potentially lead to conditions such as emphysema.

Particles with size <100 nm, termed as "ultrafine particle" are suspected to be particularly hazardous to human health, given that they can transfer into the human body through inhalation, ingestion, and skin uptake.[28, 95] The effect of nanoparticles on human health has been extensively reviewed previously.[28, 29, 96] They can penetrate the membranes of the respiratory tract and enter the blood circulation or be transported along olfactory nerves into the brain. A study by Zhiqiang et al. has shown that suspended ultrafine particles act as vehicles transporting toxic chemicals into human respiratory system.[27] A large portion of the ultrafine particles is engineered nanoparticles, whose release keeps rising due to the expanding applications in various areas including electronic components, cosmetics, cigarette filters, antimicrobial and stain-resistant fabrics and sprays, sunscreens, cleaning products, ski waxes, and self-cleaning window. The association between human health effects and engineered nanoparticles in the atmosphere is another issue awaiting for resolution.

Heavy metals are a major health threat to humans at increased concentrations in the blood stream.[97] Those of highest concern include As, Cd, Co, Cr, Cu, Hg, Mn, Ni, Pb, Sn, and Tl, whose emissions are regulated. Some of these elements are carcinogenic or toxic, affecting, among other areas, the central nervous system (Hg, Pb, As), the kidneys or liver (Hg, Pb, Cd, Cu), skin, bones, or teeth (Ni, Cd, Cu, Cr).[98] Emissions of heavy metals to the atmosphere occur *via* a wide range of processes and pathways, including combustion, extraction and processing.[97] Thus, there is the potential for humans to be exposed to these potentially harmful chemical, physical and biological agents in air, water, soil and/or food. One primary concern regarding the aerosol-induced adverse health effects is lead-containing aerosols, which have been increased by a factor of 10-100 by human activity.[99] Geochemical studies have indicated that the majority of lead in ecosystems was originated from industrial operations. Considerable research has been previously made to assess lead bioavailability of Pb-bearing particles.[5, 100-102] Given that atmospheric chemical processing modifies the physiochemical properties of aerosols in

long-range transport, the solubility of lead from aerosols is also likely to be modified, potentially affecting the lead distribution between different compartments of the Earth's system.

In addition, transition metals in aerosol have a significant effect on human health as well. Among all the transition metals, iron is almost always the most abundant one. Accumulation of iron represents an important factor promoting oxidative stress and inflammation. In addition, nanoparticles have large specific surface area and high biological activity, allowing them to affect a greater epithelial surface area in the lung and deposit in the lower airways and alveolar space. Research on biological response to iron-containing particles is therefore highly desirable.

1.3 Specific Objectives and Significance

As discussed above, the effect of aerosols on atmospheric chemistry, biogeochemical cycles and human health has not been explored to any great extent. The overall aim of this thesis is to better evaluate global impact of metal-containing aerosols. Specifically, laboratory studies were performed to investigate heterogeneous photochemistry, iron release, lead mobilization, and biological toxicity of metal-containing aerosols. The thesis focuses on the following four objectives.

(I) To perform laboratory studies that provide insights into the role of heterogeneous photochemistry of trace atmospheric gases on components of mineral dust aerosols

Given that aerosols can contain a variety of photoactive semiconductor metal oxides, such as TiO_2 and Fe_2O_3, as well as light absorbing coatings associated with the aerosol surface, it is worthwhile to examine heterogeneous photochemistry of mineral dust aerosols. Particulate nitrate as a chromophore was found to convert into NO and NO_2 under sunlight.[52, 53, 56-59] For example, it was reported that irradiation of nitrate-

coated Al_2O_3 at 310 nm results in a loss of adsorbed nitrate with the concomitant formation of several gaseous products including NO_2, NO and N_2O.[58, 59] The product yields and branching ratios change with relative humidity. Previous work was performed with particles in the powder form under single-wavelength irradiation. In the proposed studies, an environmental aerosol chamber coupled with a solar simulator will allow heterogeneous photoreactions under more atmospherically relevant conditions, i.e. with suspended aerosols under broadband irradiation. Typical components of metal-containing aerosols including Fe_2O_3, Al_2O_3 and TiO_2 will be used to investigate their photoreactions with trace atmospheric gases such as HNO_3 and O_3. Reaction kinetics and mechanism under irradiation will be explored in detail. The effect of relative humidity on photochemical reactions will be also studied. In addition, a simple model built with Kinetic PrePocessor (KPP) will be incorporated with laboratory data to obtain kinetic information. The studies unravel new and unidentified reactions activated by sunlight. The studies help us further understand daytime heterogeneous chemistry, and better evaluate the role of solar radiation plays in the atmosphere.

(II) To perform laboratory studies that better define the role of anthropogenic aerosols in supplying bioavailable iron to the open ocean

Recent studies have been revealed the significance of anthropogenic aerosols in supplying soluble iron into the open ocean. However, few studies have focused on measuring iron solubilities from anthropogenic aerosols. In addition, as atmospheric chemical processing, including the reduction of Fe(III) to Fe(II), the interaction with inorganic and organic acid (e.g. SO_2 and its oxidation products), and the exposure to sunlight during cycles of cloud water condensation and evaporation, were reported to elevate the iron solubility of aerosol, fundamental studies are necessary to clarify the relevant mechanism. Thus typical iron-containing anthropogenic aerosols, coal fly ash particles, were characterized to identify their physiochemical properties. Dissolution experiments were performed to investigate iron mobilization of those particles.

Experiments were carried out to examine the effect of various factors, including composition, solution pH, radiation, atmospheric acid processing, and atmospheric cloud processing, on controlling the rate, extent, and speciation of iron dissolution. A commercially available material, Arizona test dust (AZTD) will be included as a proxy of mineral dust for comparison. The studies help us better understand the impact of anthropogenic aerosols on atmospheric iron cycling and marine ecosystem.

(III) To perform laboratory studies of the gas-phase and aqueous phase chemistry of heavy metal-containing aerosols such as lead to better understand the mobility and bioavailability of these metals in the environment

The environmental risk of lead in aerosols is related to its bioavailability. As stated above, atmospheric processing modifies the physiochemical properties of particles dispersed in the atmosphere, and may subsequently affect their lead solubility. The influence of aerosol aging process on lead solubility was explored in this thesis. Dissolution experiments were performed to explore how atmospheric acid processing controls the extent of lead dissolution. X-ray photoelectron spectroscopy was used to detect adsorbed species following the adsorption of NO_2 on lead-containing particles. Dissolution experiments of reacted lead-containing of particles were performed. The studies provide some insights into the migration and bioavailability of lead in the environment. The data can also serve as basis of regulations for lead control.

(IV) Through collaborative studies, perform laboratory studies, on well-characterized particles, to better understand the effect of iron-containing aerosols on human health

Iron is the most abundant transition metal in the troposphere. As a transition metal, it is capable of generating reactive oxygen species (ROS) and contributing to oxidative stress. In collaboration with Dr. Alejandro Comellas' laboratory in the Department of Internal Medicine, we explored the biological response of iron-containing particles. Specifically, , *Pseudomonas aeruginosa* (PAO1) was grown in the presence of

α-Fe_2O_3 nanoparticles of different size and antimicrobial peptides (AMPs). The proposed studies lead to a better understanding of the mechanisms involved in iron-induced oxidative damage and lung inflammation, allowing us to design better strategies to protect individuals, especially those with chronic lung disease, exposed to high particulate matter levels.

1.4 Synopsis of Dissertation Chapters

The research presented herein focuses on understanding the global impact of metal-containing aerosols. Specifically, laboratory studies are presented which investigate heterogeneous photochemistry, iron dissolution, lead mobilization, and biological toxicity of metal-containing aerosols.

Multiple experimental techniques were used. The main analytical tool for probing heterogeneous reactions on atmospherically relevant interfaces is Fourier transform infrared spectroscopy (FTIR). Heterogeneous reactions in the atmosphere were simulated in an environmental aerosol chamber that has been equipped with a solar simulator. Both reactions under dark and irradiation conditions were investigated to explore the differences between daytime chemistry and nighttime chemistry. Solid particles used in the current study were characterized by a variety of techniques, including X-ray diffraction (XRD), X-ray photoelectron spectroscopy (XPS), scanning electron microscopy coupled with energy dispersive X-ray spectroscopy (SEM/EDX), computer controlled scanning electron microscopy coupled with energy dispersive X-ray spectroscopy (CCSEM/EDX), transmission electron microscopy (TEM), 57Fe Mössbauer spectroscopy and BET surface area analysis. These characterization techniques provide useful information regarding physicochemical properties of the atmospherically relevant particles used. The experimental methods and procedures are discussed in detail in Chapter 2.

In Chapter 3, we investigate heterogeneous chemistry and photochemistry of trace atmospheric gas HNO_3 with components of mineral dust aerosol using an environmental aerosol. For reaction of HNO_3 with aluminum oxide, broadband irradiation initiates photoreactions to form gaseous NO and NO_2. A complex dynamic balance between surface adsorbed nitrate, and gaseous nitrogen oxide products including NO and NO_2 is observed. Furthermore, the role of relative humidity and, thus, adsorbed water, on heterogeneous photochemistry has been explored. The atmospheric implications of these results are discussed.

Chapter 4 describes an investigation of heterogeneous chemistry and photochemistry of ozone on oxide components of mineral dust aerosol, including α-Fe_2O_3, α-FeOOH, TiO_2, and α-Al_2O_3, at different relative humidity using an environmental aerosol chamber. The rate and extent of O_3 decomposition on these oxide surfaces are found to be a function of the nature of the surface as well as the presence of light and relative humidity. Under dark and dry conditions, only α-Fe_2O_3 and α-FeOOH exhibit catalytic decomposition toward O_3, while the reactivity of TiO_2 and α-Al_2O_3 is rapidly quenched upon ozone exposure. However, upon irradiation, TiO_2 is active toward O_3 decomposition, and α-Al_2O_3 remains inactive. In the presence of relative humidity, ozone decay on α-Fe_2O_3 subject to irradiation or under dark conditions is found to decrease. In contrast, ozone decomposition is enhanced for irradiated TiO_2 as relative humidity initially increases but then begins to decrease at even higher relative humidity levels. A kinetic model was used to obtain heterogeneous reaction rates for different homogeneous and heterogeneous reaction pathways taking place in the environmental aerosol chamber. Atmospheric implications of these results are discussed.

Chapter 5 reports an investigation of iron dissolution for three fly ash samples in acidic aqueous solutions and compares the solubilities with that of Arizona test dust, a reference material for mineral dust. The effects of iron speciation, pH, type of acid anion, simulated cloud processing, and solar radiation on iron solubility were explored. Similar

to previously reported results on mineral dust, iron in aluminosilicate phases provides the predominant component of dissolved iron. Iron solubility of FA is substantially higher than of the crystalline minerals comprising AZTD. Simulated atmospheric processing elevates iron solubility due to significant changes in the morphology of aluminosilicate glass, a dominant material in FA particles. Iron is continuously released into the aqueous solution as FA particles break up into smaller fragments. Proton-promoted and ligand-promoted dissolutions are two main mechanisms in mobilizing iron under our experimental conditions. Oxalate can form bidentate ligand with Lewis acid iron center, and therefore displayed the highest rate of iron dissolution. Solar irradiation shows a considerable enhancement on iron dissolution. The assessment of dissolved atmospheric iron deposition fluxes and their effect on the biogeochemistry at the ocean surface should be constrained by the source, environmental pH, type of acid anion, iron speciation, and solar radiation.

Chapter 6 discusses heterogeneous chemistry of nitrogen dioxide with lead-containing particles for better understanding heavy metal mobilization in the environment. In particular, PbO aerosol, a model lead-containing compound due to its widespread presence as a component of lead paint and as a naturally occurring minerals, massicot and litharge, are exposed to nitrogen dioxide at different relative humidity. Exposed particles are found to increase the amount of lead that dissolves in aqueous suspensions at pH 7 compared to unreacted particles. X-ray photoelectron spectroscopy shows that upon exposure to nitrogen dioxide, PbO surfaces form adsorbed nitrates with the surface coverage and extent of formation of adsorbed nitrate relative humidity dependent. Although powder X-ray diffraction analysis shows no bulk formation of $Pb(NO_3)_2$, surface adsorbed nitrate increases the amount of dissolved lead. These results point to the potential importance and impact that heterogeneous chemistry with trace gases can have on increasing solubility and therefore the mobilization of heavy metals such as lead in the environment. This study also show that surface intermediates, such as

adsorbed nitrates, that form can yield higher concentrations of lead in water systems including drinking water systems, ground water systems, estuaries and lakes.

Chapter 7 presents a collaboration work for better understanding the mechanisms of iron-containing particle induced bacterial growth and virulence. Specifically, *Pseudomonas aeruginosa* (PAO1) was grown in the presence of iron oxide nanoparticles of different size and AMPs. We report that PAO1 utilizes iron from particles for growth and virulence and inhibits AMPs. Furthermore, nanoparticle surface area and size correlate with bacteria growth.

General conclusions are given in Chapter 9 along with the future directions. Collectively, the results presented herein provide insight into the global impact of metal-containing aerosols on atmospheric chemistry, human health, climate change and biogeochemical cycles.

CHAPTER 2

EXPERIMENTAL APPARATUS AND PROCEDURES

A variety of experimental methods and techniques were used in this study for better understanding the global impacts of metal-containing aerosols. Laboratory experiments to simulate atmospheric processing coupled with particle characterization techniques can provide comprehensive information regarding the chemistry and photochemistry of gas species on atmospherically relevant surfaces. The details of the experimental apparatus and methods are described below.

2.1 Experimental Design for Studies of Heterogeneous Reactions

Heterogeneous reactions were mainly explored using a custom environmental aerosol chamber that incorporates with a solar simulator. Various assemblies are attached to the chamber to achieve an in-situ investigation of reactions in the chamber, including an aerosol generation part, a sample line system to introduce gas species of interest, instrumental probes, a humidity controlled flow system to adjust the relative humidity in the chamber.

2.1.1 Environmental Aerosol Chamber

An environmental aerosol chamber was fabricated to study heterogeneous reactions between trace atmospheric gases of interest and model atmospheric aerosols.[103, 104] A schematic diagram of the environmental aerosol chamber is shown in Figure 2.1.[105] The chamber is a stainless steel cylinder that has a height of 0.83 m and a diameter of 0.56 m. It has a total volume of 0.151 m^3 with a volume to surface ratio of 10.7 m^{-1}. Six sets of side arms located at different heights and positions of the chamber allow access to the chamber interior. Through these ports, connections are made several different instrumental probes, vacuum pumps, a sample line, pressure transducers and an aerosol

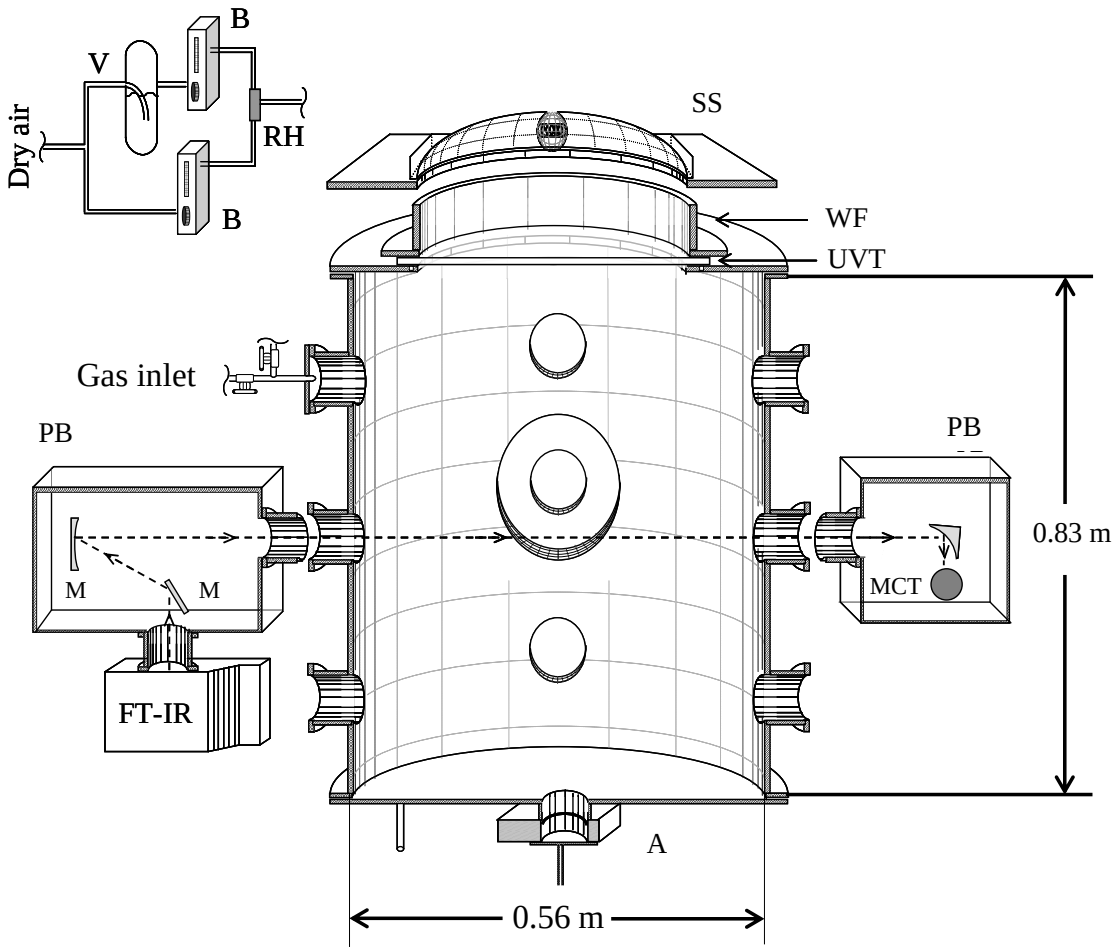

Figure 2.1 Schematic diagram of environmental aerosol chamber and simulated solar system: (A) aerosol inlet valve and antechamber, (V) water bubbler for relative humidity experiments, (B) flow meters, (RH) relative humidity sensor, (FT-IR) FT-IR spectrophotometer, (M) mirrors for the external beam path, (MCT) midband HgCdTe IR detector, (PB) purge boxes for the external beam path; (SS) solar simulator, (WF) water filter, (UVT) borofloat 33 glass window. Thermocouples and pressure transducers are also connected to the chamber. Adapted from Ref. 105.

inlet. All chamber interior surfaces and surfaces in contact with gases have been either coated with a 3 mm layer of FEP (fluorinated ethylene propylene) Teflon or were fabricated from glass or Teflon to provide a chemically inert surface. Large mating flanges fabricated by stainless steel for the top and the bottom of the chamber can be removed to allow access to the chamber interior. The top mating flange can also be replaced by a same size glass window attached with a water filter to allow irradiation getting through into the chamber from the top during irradiation experiments.

The chamber is mounted in a steel frame, holding the chamber approximately 70 cm off the floor, to allow people access into the chamber from below for cleaning. The frame was fabricated from lengths of 1 ¾" square and 1 ½" square, 12 gauge steel tubing that allows the chamber height to be adjusted. The chamber can be positioned at three different heights, aligning one of three sets of the side arms with the tops of the nearby optical tables. The chamber height may be finely adjusted via leveling feet, one under each corner of the chamber mount. These feet also serve as vibration dampers.

2.1.2 Solar Simulator

A commercial solar simulator (Optical Energy Technologies Inc., S13-575) sits on the top of the environmental aerosol chamber to allow for studies of heterogeneous reactions under irradiation. The picture of the solar simulator is shown in Figure 2.2. It is a 575 W metal halide arc lamp with a continuum spectral response close to 6000 K. The lamp situates at the focus of a parabolic reflector to produce 13" diameter beam. Light from the solar simulator, mounted on top of the chamber, passes through a circulating water filter to remove infrared radiation and prevent a temperature rise in the chamber. The base of the water filter is a glass transmission window (Borofloat 33, 1.3 cm thick), which also provides the seal to the chamber and removes radiation below about 280 nm. Contact with the filter caused the temperature to increase to about 303 K, measured in the

Figure 2.2 Picture of solar simulator S13-575.

middle of the chamber, and a temperature gradient of about 10 K to develop over the height of the chamber. The transmittance of Borofloat 33 window was measured using a UV/vis spectrometer and the measurement result is shown in Figure 2.3. Irradiance below 280 nm is completely blocked by the Borofloat window. In contrast, the window is relative transparent for irradiance above 340 nm, with a transmittance of approximately 90%.

Testing with a calibrated solar cell showed that the beam is relatively uniform with an average intensity of 1 AM0 (air mass zero, the integrated solar spectral irradiance at the top of the Earth's atmosphere, an average of ~1.4 kW m^{-2}). In order to obtain homogeneous irradiance, five occulting spots were placed on the Teflon film window of the solar simulator, and their positions are shown in Figure 2.4. The occulting spots improve the homogeneity of the irradiance profile for the solar simulator as shown in the inset of Figure 2.5, which represents the spatial distribution of the simulator beam after 1 m measured using a calibrated photocell. The data show that there is a central obscuration effect, due to the lamp bulb, where the irradiance is about 50% lower than the maximum value recorded. With the Borofloat window placed on the top, the irradiance averaged over the diameter of the simulator beam is approximately 1.2 of AM1 (air mass one, the integrated solar spectral irradiance reached the Earth's surface, an average of ~1.1 kW m^{-2}), which is close to the irradiance at the top of the Earth's atmosphere.

The spectral absolute irradiance from the solar simulator was determined by placing a calibrated radiometer at the bottom of the chamber, a distance of approximately 1 m from the solar simulator. The results for the chemically relevant near UV and visible region of the spectrum are shown in Figure 2.5. As noted above, the Borofloat window effectively blocks radiation below about 280 nm.

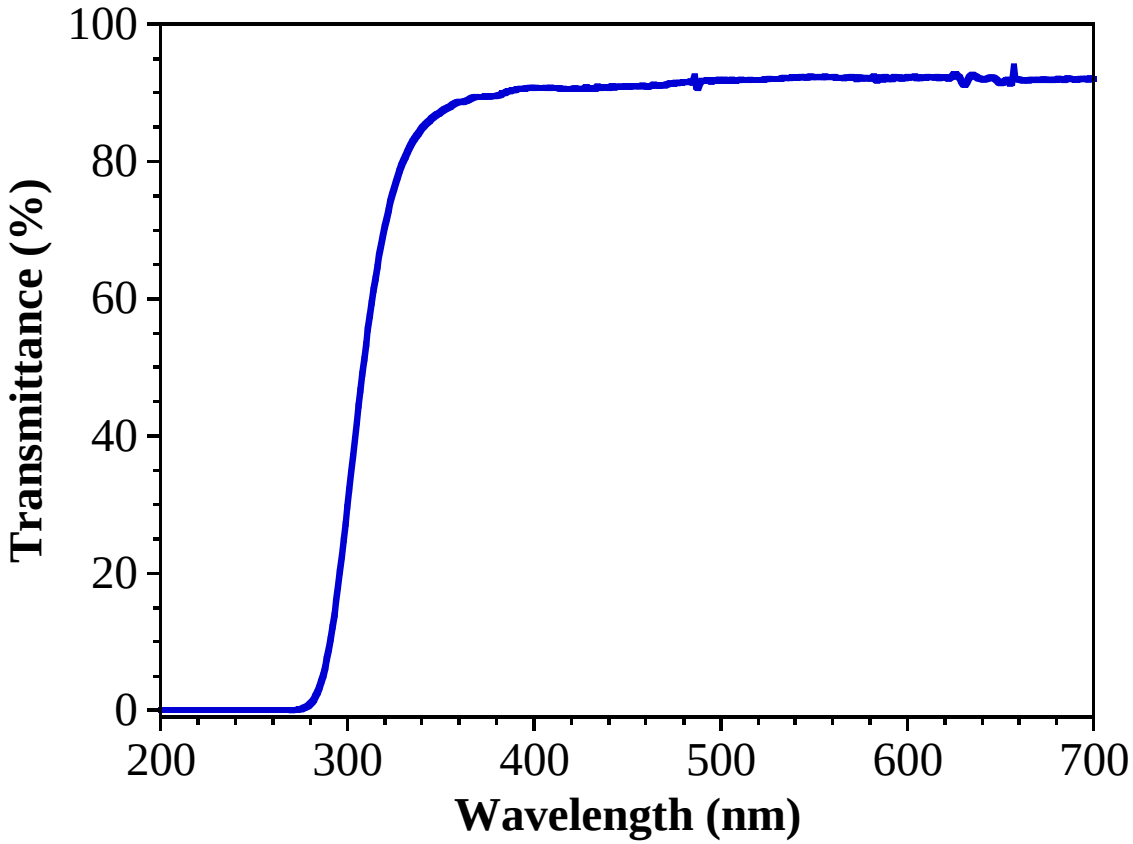

Figure 2.3 Transmittance of Borofloat 33 window used in the current study.

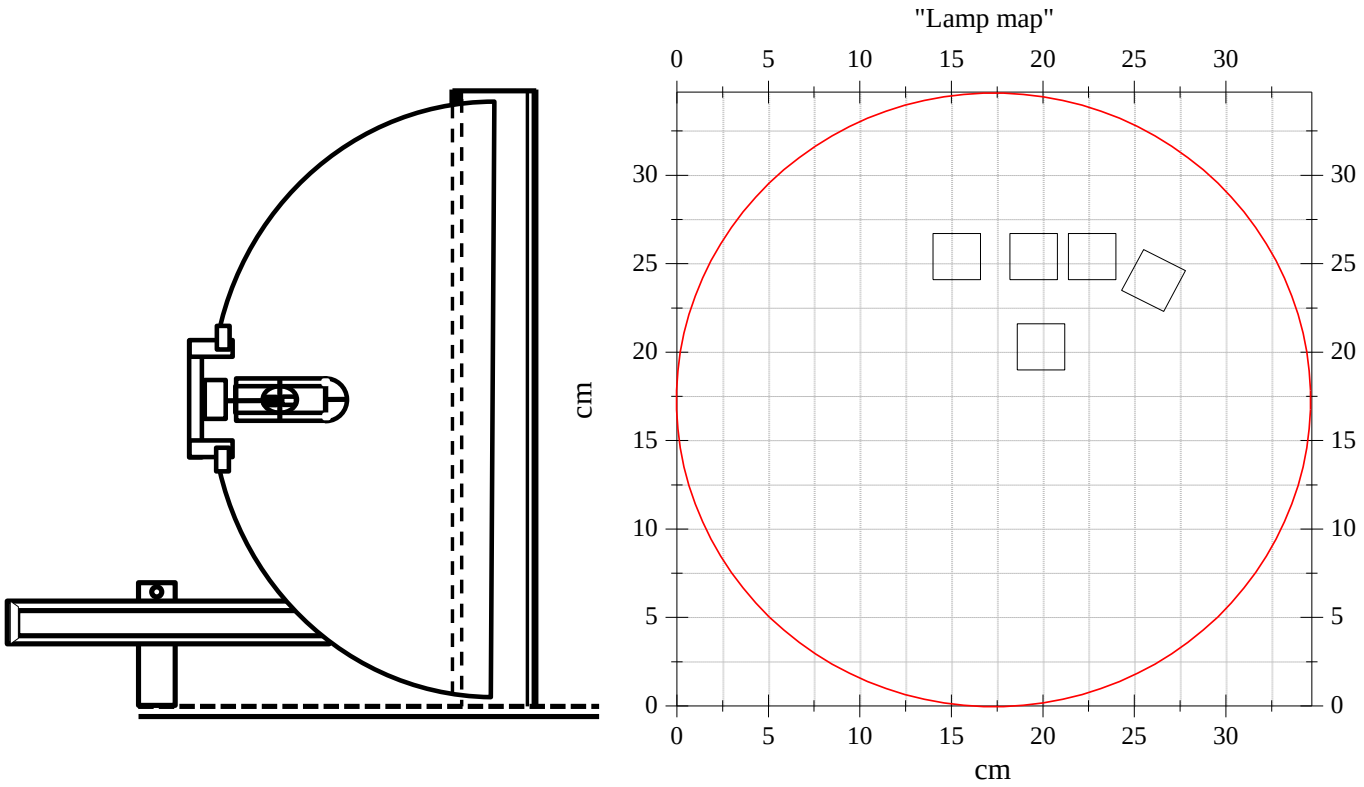

Figure 2.4 Schematic diagram of solar simulator S13-575 showing the positions of the occulting spots on the Teflon surface window. The occulting spots are represented as squares on the right side of the figure. The bottom of the map corresponds to the side with electric fan component on the solar simulator.

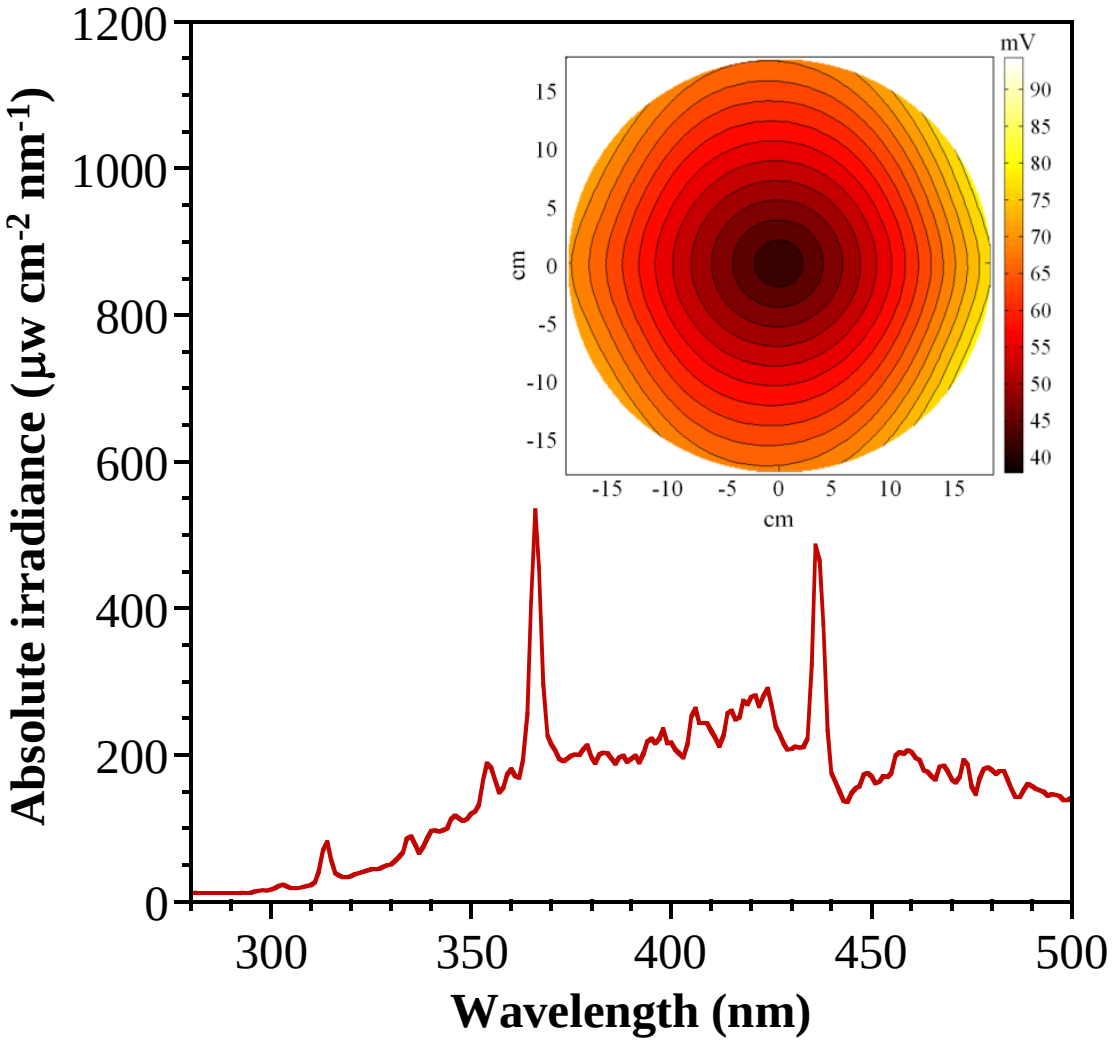

Figure 2.5 Solar simulator spectral irradiance at the bottom of the environmental aerosol chamber. The insert shows the solar constant profile in the environmental aerosol chamber.

2.1.3 FTIR Spectroscopy

The decay and/or growth of gas phase species in the environmental aerosol chamber were monitored using a Fourier transform infrared spectrometer (FTIR, Mattson, Infinity 60AR). Spectra were collected in the range of 650-5000 cm^{-1} at a resolution of 8 cm^{-1}, and 256 scans were averaged for each spectrum resulting in a time resolution of ~52 seconds. A mirror system is used to align the IR beam to get through the chamber and then focus on to an IR detector. A schematic diagram of the mirror system is shown in Figure 2.6. The IR beam is directed out of FTIR instrument by a computer controlled mirror inside the spectrometer. Two gold-coated mirrors are used to keep the beam collimated and send it through the central set of side arms on the chamber. The first mirror is 3"square flat mirror which directs the diverging beam onto a 6 inch spherical mirror which has a focal length of 60 inches (Edmund Scientific, A32-846). The IR beam is focused through the chamber and is again diverging as it exits the chamber. After exiting, the beam is directed onto a gold-coated, off-axis parabolic mirror (Janos Technology, A803730), and then focus onto a liquid-cooled, mid-band, mercury-cadmium-telluride (MCT) detector. The focal region of the parabolic mirror is 90^0 off-axis from the incident IR beam (4 inch focal length), allowing the previously diverging beam to be easily focused on the 1 mm^2 detection element. The detector is mounted on a 5 inch square linear stage that is capable of 0.5 inch of travel in both the x and y directions and can be adjusted with micrometer (Newport, 401-SM-13).

The IR beam has a diameter of approximately 2 cm at the center of the chamber. The chamber side arms are sealed with optical quality, 2" diameter, germanium window (Janos Technology, A1305W658) to reduce complications associated with the reactivity of salt windows. Wedged (30') Ge were used to diminish fringing and unwanted reflections that occur when plane parallel germanium windows are used. The external IR beam path is continuously purged with dry air for stability. The partial pressures of gas

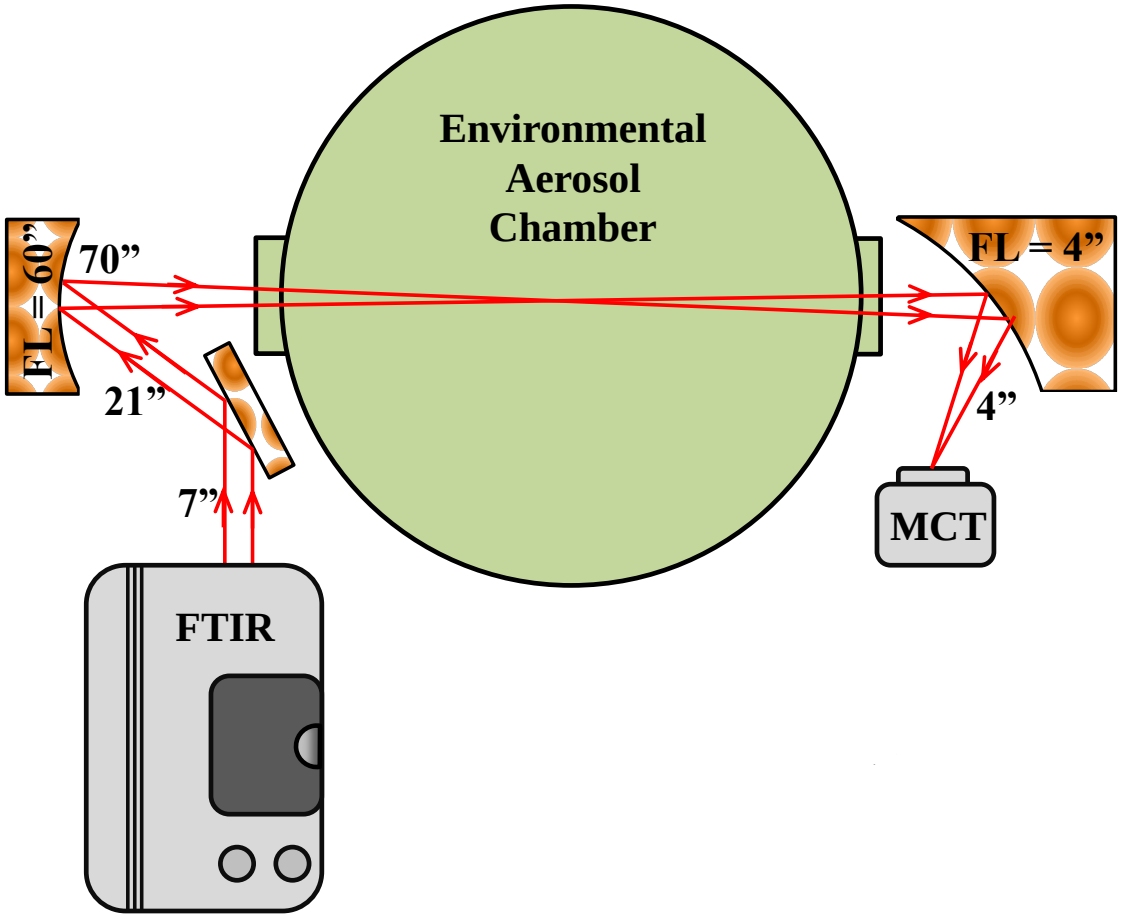

Figure 2.6 Mirror system used to direct the external IR beam from FTIR instrument to get through the environmental aerosol chamber and then focus on the MCT detector.

phase species including water vapor, as well as gaseous reactants and products, were determined using a Beer's law calibration.

A pair of capacitance manometers (MKS, 62611TBE, 626A13TBE, range 0.000 to 10.000 Torr and 0.0 to 1000.0 Torr, respectively) allows the pressure inside the chamber to be continuously measured.

2.1.4 Aerosol Generation

Aerosol samples are introduced using a cartridge sample holder connected to the chamber through stainless steel tubing and terminated by a partial impactor plate. The assembly previously was on the top of the environmental aerosol chamber but was relocated to the bottom to accommodate the solar simulator. The sample was held under vacuum for several hours before introduction to remove surface adsorbed water from the sample. To initiate aerosol introduction, the valve connected the sample cartridge to the chamber was opened and a short pulse of Ar pressurized at the cartridge, rapidly forcing the powder past the impactor and into the chamber. Typical operating conditions include a backing pressure of ~90 psig and a pulse width (length of time the valve is opened) of 1.0 seconds. The pulse width can be adjusted from 10 milliseconds to 10 seconds using a custom built circuit that supplies the normally closed valve with 120 VAC for the specified duration. The impactor ensures efficient deagglomeration of the particles and quick mixing of the aerosol with the reactant gases. Typical particle sample loading was approximately 500 mg.

A picture of the actual partial impactor system is shown in Figure 2.7. It was fabricated from stainless steel and electropolished, stainless steel tubing. The impaction plate and muzzle were mechanically polished to a mirror finish. Also shown in Figure 2.7 is a schematic of the partial impactor system, depicted from a cross sectional view. The nozzle diameter, W, is 2.0 mm, the muzzle throat length, T, is 5.0 mm and S, the nozzle-to-plate distance, is 3.2 mm.

2.1.5 Humidity Controlled Flow System

The relative humidity inside the environmental aerosol chamber is controlled by a flow system located adjacent to the chamber on a ring stand. A schematic of the system is shown in the upper left panel of Figure 2.1. The flow system's gas supply is provided from the purge gas generator. The gas line is split into a dry flow and a humidified flow. The humidified flow passes through a 50 cm, cylindrical glass bubbler filled with water (Fisher, Optimal grade). The bubble has an estimated volume of 1.4 L, and is approximately half-filled with glass beads in 6 mm diameter. The glass beads maximize the gas-water interact area and help the flow reach saturation water vapor pressure at the bubbler exit. Rotameters are placed on both the dry and humidified flows to control the flow rate in both the dry and humidified flow line. After passing through the dry and humidified lines, the split gas lines are recombined and get into the chamber. The combined gas flow passes by an in-line relative humidity sensor (HyCal Sensing Product, HIH-3602L-CP), and then couples to the environmental aerosol chamber via a series of Teflon ball valves. The relative humidity of the combined gas can be controlled by adjusting the rotameters on the individual lines.

If dry gas is desirable, the humidified line can be shut off, providing buffer gas with <1% relative humidity, as determined by IR adsorption measurement. Conversely, the maximum relative humidity gas can be achieve by shutting off the dry line, which will result in humidified gas with >90% relative humidity. The flow rate into the chamber is typically 25 L min^{-1}.

2.1.6 Ozone Generator

An OREC electric discharge generator (Model O3V5-O) is used to generate ozone in studies of ozone decomposition. Oxygen gets through the high voltage electric discharger to generate ozone. Water is circulated continuously in the generator to avoid

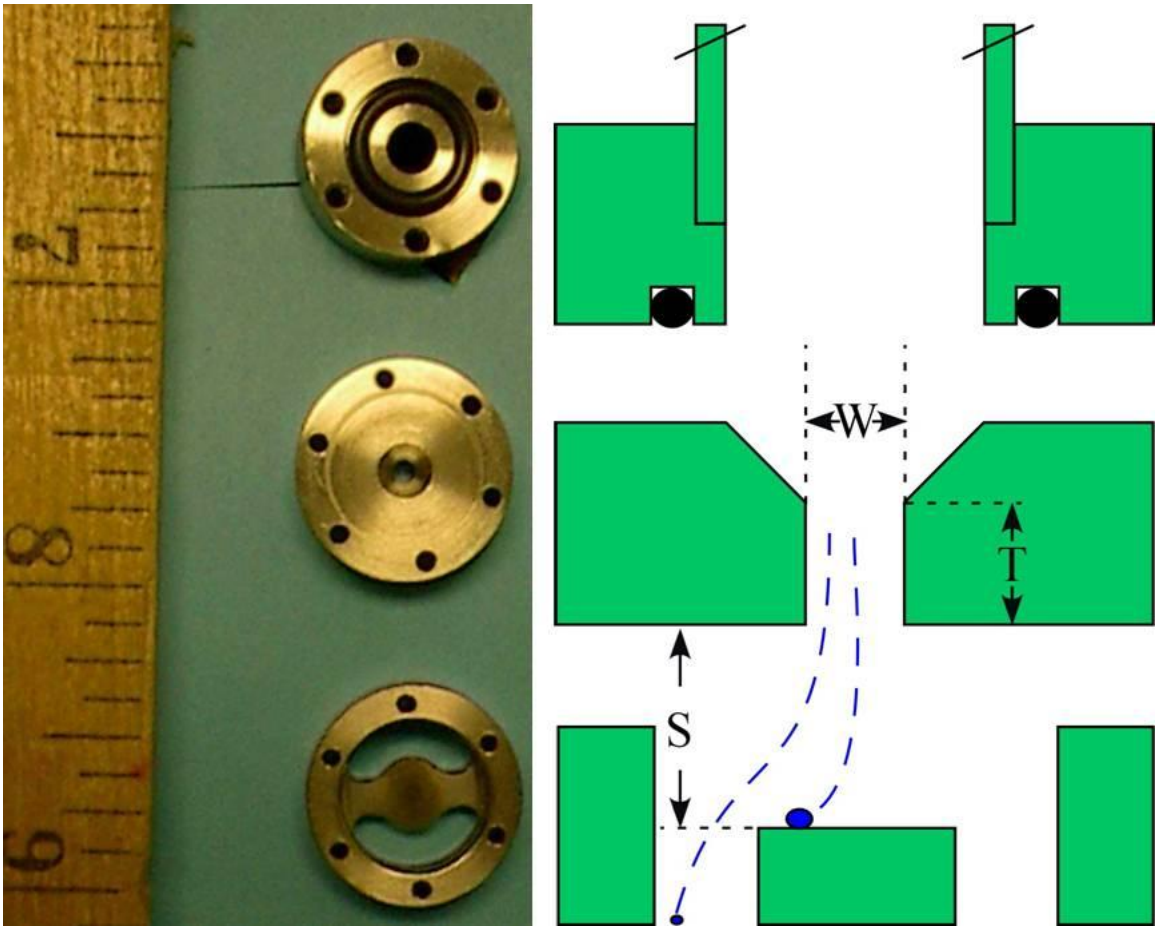

Figure 2.7 The left side of the figure is a picture of the partial impactor system. The right side is a schematic with critical dimensions labeled.

temperature rising in the electric discharger. The generated ozone/oxygen mixture then flows into the environmental aerosol chamber through the sample line. The mixing ratio of ozone in the ozone/oxygen mixture is dependent on the flow rate of oxygen getting into the generator and the voltage applied. Generally, a voltage of 3.4 Volts, and an oxygen flow rate of 10 L min^{-1} were used.

2.1.7 Sample Line

A glass vacuum line is used to introduce the reagent gas samples into the chamber. The sample line consists of a glass manifold equipped with a liquid nitrogen trapper mechanical pump (Edwards 8). A capacitance manometer (MKS, 121A-12204) with a measured range from 0.0 to 1000.0 Torr measures the pressure inside the glass manifold. The manifold has several Teflon valves to which gas cylinders or sample line can be attached and is connected to the chamber through a length Teflon tubing that is sealed at the chamber with a Teflon ball valve.

2.1.8 Experimental Protocol

In a typical experiment, the environmental aerosol chamber is purged overnight with dry air to remove water and other impurities. Several IR spectra are collected. The spectra are ratioed to each other and the peak-to-peak noise is calculated over the range 2500-2800 cm^{-1}. The value is monitored in a daily base as check of IR transmittance arising from possible difficulties such as window misalignment or loss of source power. Typical noise values range from 1-3 $\times 10^{-4}$ absorbance units. Then the chamber was evacuated to low pressure (e.g. 680 Torr), filled with the reagent gas at a certain RH, and brought up to near atmospheric pressure with dry air. The reactant gases were allowed to sit in the chamber for about one hour for passivation and quantification of wall losses. For dark experiments, s precisely weighed powder sample was then introduced from the aerosol-introduced system to initiate heterogeneous reactions involving the gas phase

species. For experiments under irradiation, the solar simulator was turned on before aerosol introduction for 100 minutes to further quantify additional wall losses and photolysis reactions induced by the solar simulator. The powder sample was then introduced into the chamber to allow heterogeneous reactions under irradiation. The solar simulator was turned off after approximately 500 minutes of reaction to yield a post-irradiation period. Gas phase concentrations, as well as RH, temperature and total pressure in the chamber, were monitored during the entire experiment.

Upon completion of each experiment, the chamber is purged with dry air for several hours to remove gas phase residual reactants and products. The side arm mating flanges holding the germanium IR windows are removed. The large bottom flange on the chamber cylinder is unattached from the chamber and lowed with the help of a custom large lab jack. The chamber interior surfaces are then carefully cleaned with deionized water and lab tissues (Kimberly-Clark, Kimwipes). The germanium windows are carefully removed from the side arm mating flanges and cleaned with methanol for at least three times. Gloves and optical papers should be used when cleaned the germanium window to avoid possible scratches on germanium window. The windows are then replaced in their mounts, and all the flanges that have been removed are reattached to the chamber for next experimental running. Marks have been made on the germanium windows and holder so that they may be reproducibly positioned after removal. Care is taken when replacing these windows to ensure alignment of the IR beam with the detector. When reattaching the bottom flange on the chamber it is necessary to lubricate the sealing O-ring to aid in position. A non-reactive lubricant is used for this purpose (Dupont, Krytox). The chamber is typically cleaned after each experiment involving a powder sample.

The top large flange or glass window is also removed for cleaning after several experimental runnings. For irradiated experiments when glass window is used, it is necessary to lubricate the sealing O-ring in the water filter to aid in position and help

sealing. Given that the temperature of water in the water filter is raised during irradiated experiment, a heat-resistant lubricant (Dow Corning, 3145 RTV) is used.

2.2 Data Analysis for Studies of Heterogeneous Reactions

Methods to analyze data for studies of heterogeneous reactions are described in the section below.

2.2.1 Infrared Spectral Analysis

The FTIR spectra were continually collected during a typical experiment. The gases of interest in the environmental aerosol chamber were monitored by following the adsorption intensity in the infrared spectral as a function of time. Typical, the most prominent adsorption feature for each specific gas was chosen. Depending on the specific gas species, either the integrated area in a certain region or the peak height at certain wavelength is examined. The integrated area or the peak height is then compared to a previously determined Beer's law calibration and the exact partial pressure of reagent gas or product species is assessed. The instrumental software, Winfirst, was used to analyze the infrared spectra. The macros used for data collection and analyses are given in Appendix A.

In an idea experiment, all adsorption bands of gases of interest are well separated. When band overlapping for different species occurs, it is possible to isolate the band of interest using a serious of well-controlled spectral subtractions. A macro program used to subtract water adsorption bands is given in Appendix A. Unless experiments under dry conditions, the subtraction of water adsorption bands were applied to each spectrum. A gas phase water spectra was taken before each experiments to be used as a reference.

2.2.2 Kinetic Analysis

Heterogeneous reaction of a gaseous species on a model aerosol surface can be described by a simple mechanism in equation (2-1),

$$R + S \xrightarrow{k_s} P + S \tag{2-1}$$

where R is the reagent gas, S represents the available reactive sites, and P represents product species. The kinetics can be made pseudo-first order when the number of surface sites is in excess relative to the concentration of gas phase species.

The surface rate constants, k_s, obtained by fitting the experimental kinetic data to a first order exponential decay or obtained from the model calculations under various conditions. Uptake coefficients, γ, normalized to the specific surface areas can be determined using k_s. The heterogeneous uptake coefficient, which is defined as the fraction of gas-surface collisions that lead to gas loss, is determined from[42]

$$\gamma = \frac{4k_s}{\bar{c} S_{BET} [C_{mass}]} \tag{2-2}$$

where $\bar{c}$ is the mean speed of gas phase species in m s^{-1}, S_{BET} is the specific surface area of the particle sample in m^2 g^{-1}, and C_{mass} is the mass concentration of the particle sample in the chamber in g m^{-3}.

2.3 Quantitative Iron Dissolution Measurements

In order to compare the contributions of atmospherically relevant aerosols in providing soluble iron into open ocean water, dissolution experiments to simulate

atmospheric processing were carried out as described in detail in the following subsections.

2.3.1 Dissolution Apparatus

The dissolution measurement setup is shown in Figure 2.8. Briefly, dissolution experiments were carried out in a 70 mL glass vessel containing 50 mL of an appropriate aqueous solution. As suggested in previous work,[106] the minor variations in ionic strength did not significantly influence the results of the dissolution studies. Thus the ionic strength was not controlled. All solutions were stirred under oxygen exposure, and kept at 298 K using a water jacket integrated to the reaction vessel. The typical solid loading was 2 g L^{-1}. All dissolution experiments were conducted in triplicate and results represent the averages and standard deviation of three measurements. After addition of the particles into the solution, an appropriate volume of suspension was periodically withdrawn from the vessel using a disposable syringe. The aqueous samples were passed through a 0.2 μm PTFE filter and immediately acidified to a final concentration of approximately 0.2 N HCl to preserve the samples for iron analysis. For each sampling event, sufficient solution was taken out to allow for determinations of both dissolved Fe(II) and total dissolved iron. The explore the effect of irradiation, a solar simulator with a 150 W xenon lamp (Oriel Corp.) was mounted on the top of the vessels to allow irradiated experiments. For comparison, dissolution experiments in the dark were conducted with the vessels wrapped in aluminum foil.

2.3.2 Simulated Cloud Processing

Cloud processing involves radical fluctuations in pH and has been suggested to increase the solubility of iron.[74, 77, 79, 107-109] To determine the effect of varying pH cycles on iron solubility, solutions were cycled between highly and slightly acid conditions over periods of 24 hours in separate experiments to simulate cloud processing. Milli-Q water

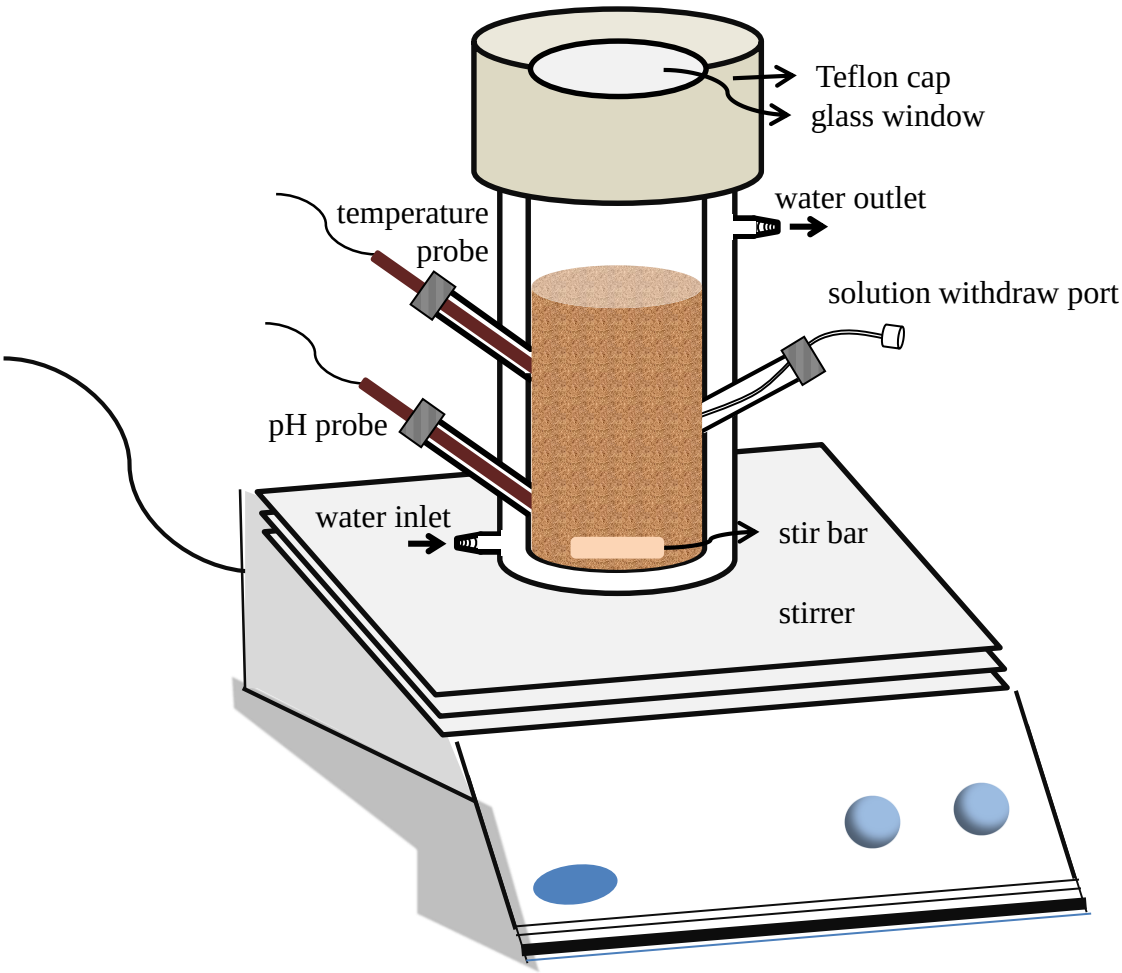

Figure 2.8 Schematic of the custom glass vessel used for quantitative iron dissolution measurement.

was used instead of acid media. After approximately 24 hours of dissolution, the suspension was acidified to pH ≈ 2, a pH value the deliquescent layer on the aerosol particle could have,[75] with concentrated H_2SO_4. The system was allowed for dissolution for a further 24 hours before being restored to pH ≈ 5 with concentrated NH_4OH. After a further 24 hours, the suspension was lower to pH ≈ 2 again. The varying pH cycle repeated up to 3 times. Sufficient solution was periodically withdrawn for both Fe(II) and total dissolved Fe analyses during the entire experiment. To explore the effect of irradiation, a solar simulator with a 150 W xenon lamp (Oriel Corp.) was mounted on the top of the vessels to allow irradiated experiments. For comparison, dissolution experiments in the dark were conducted with the vessels wrapped in aluminum foil.

2.3.3 Analytical Methods for Dissolved Iron Determination

Ferrous iron was measured calorimetrically with 1, 10-phenanthroline as described previously.[106] For Fe(II) analysis, 20 μL of a 5 mM 1, 10-phenanthroline solution and 200 μL of an ammonium acetate buffer were added to 1 mL of sample. To avoid possible interference from Fe(III), which can also form a complex with 1, 10-phenanthroline when present at high concentrations, 50 μL of 0.43 M ammonium fluoride was added to the sample prior to 1, 10-phenanthroline. The mixture was allowed to sit in the dark for 30 min prior to UV-vis analysis, during which time a reddish-orange color developed if Fe(II) was present. Total dissolved iron was determined via the same protocol, except that 20 μL of 1.5 M hydroquinone, which reduces Fe(III) to Fe(II), was added to the aqueous sample instead of ammonium fluoride.

Absorbance measured at 510 nm was converted to concentrations using aqueous standards prepared from anhydrous beads of ferrous chloride (Sigma Aldrich). Standards were prepared in each acid used in dissolution studies, and no matrix effects were observed. The determination of iron using UV-vis spectroscopy is in a detection limit of 1 μM. The concentrations of dissolved Fe(III) was calculated from the difference in

experimentally measured concentrations of total dissolved iron and dissolved Fe(II). It is operationally defined the dissolved Fe(III) concentrations as the summed concentrations of aqueous Fe(III) and all colloidal Fe(III) particles less than 0.2 μM present in our systems.

2.4 Complementary Physicochemical Characterization Techniques and Methods

A variety of characterization techniques were applied to the samples used in this study to explore their physicochemical properties. The different techniques and the corresponding principles are described in the following paragraphs.

2.4.1 Scanning Electron Microscopy with Energy Dispersive X-ray Spectroscopy

The morphology and composition of particles were examined using a Hitachi S-3400 N scanning electron microscopy (SEM) coupled with energy dispersive X-ray spectroscopy (EDX) system. In SEM analysis, a demagnified, focused spot of electrons is generated to scan over the surface of an electrically conductive specimen. These impinging electrons strike the specimen, producing signals that contain information about the morphology, composition and other properties of the specimen. Typical signals produced by a SEM include secondary electron, backscattered electron, characteristic X-rays, light, specimen current and transmitted electrons. Secondary/backscattered electrons escaped from the uppermost layer of the specimen can be collected, processed, and eventually translated to a series of pixels. The brightness of the pixels is directly proportional to the number of secondary/backscattered electrons generated from the specimen surface. Since the electron beam is scanned rapidly over the specimen, the numerous points appear to blend into a continuous-tone image composed of many density levels or shades of gray, giving the information about the morphology of the specimen.

Characteristic X-rays are emitted from the surface when an impinging electron removes the core electron of an atom, causing a higher energy level electron to fill the shell and releasing X-rays. These characteristic X-rays are used to identify the element composition of the specimen.

Particles in SEM/EDX analysis were dispersed onto carbon tape that had been mounted on an aluminum stub and were subsequently carbon coated. Elemental analyses used an integrated Bruker XFlash. X-ray microanalysis system that used an accelerating voltage of 10 kV and had a detection limit of 1 wt%. A resolution of 256 × 200 pixels and a dwell time of 1 second were used.

2.4.2 Computer-Controlled Scanning Electron Microscopy

Computer-controlled scanning electron microscopy with energy dispersive X-ray analysis (CCSEM/EDX)[110] was also applied to examine the morphology and elemental composition of particles of interest. The system allows automated measurement of size, aspect ratio and elemental composition for a large number of individual particles.

Particle samples for CCSEM/EDX analysis were prepared in the same manner for all tested particles. Dry particles were mechanically dispersed infront of the inlet of the Multi Orifice Uniform Deposition Impactor (MOUDI), model 110-R (MSP, Inc) and then were deposited onto TEM grids placed on the 5th stage (cut-off size, D_{50} = 1 μm) of the impactor. A dual-beam FIB/SEM FEI Quanta instrument was used in this work. The instrument is equipped with an EDX spectrometer with a Si(Li) detector with an active area of 10 mm^2 and an ATW2 window. In CCSEM/EDX operation mode, selected sample areas are imaged and particle features in the images are recognized by an increase of the detector signal above a pre-set threshold level. Then, X-ray spectra are acquired for all detected features. In this work, particles with an equivalent circle diameter within a range of 0.2-5 μm were measured. A magnification of ×2000-10000, a beam current of 400-600 pA, and an accelerating voltage of 20 kV were used, and X-ray spectra were

acquired for 10 seconds. Additional details of the CCSEM/EDX analysis of particles can be found elsewhere.[110]

A focused Ga-ion beam was used to cross-section agglomerates of individual particle lifted from the substrate using an AutoProbe^{TM} 300 nanomanipulator (Omniproble, Inc.). During cross-sectioning of particles the ion beam energy and current were set at 30 kV and 3 nA, respectively, for initial milling, and then final cleaning was performed at 1 nA beam current. Cross sectioned particles were imaged by SEM from normal direction to the cross section plane. Additional ion-beam induced SEM images were acquired from direction parallel to the cross-section, using non-destructive ion beam current of 0.5 pA. Elemental mapping of sectioned particles was performed at the standard positioning geometry of the EDX detector at the takeoff angle of 45 ° with respect to the cross-section plane, over the sample positioned at 10 mm working distance.

2.4.3 Transmission Electron Microscopy

Transmission electron microscopy (TEM) is a powerful technique for imaging the fine specimen at a significantly higher resolution than conventional light microscopy. In TEM system, a beam of electrons is transmitted through an ultra thin specimen, interacting with the specimen as it passed through. The electrons transmitted through the specimen are collected, and then translated to form a TEM image.

JEOL 2100F TEM, operating at 200 kV accelerating voltage, was used to determine an average particle size and morphology. Particles were prepared for TEM imaging by suspending and sonicating in methanol for 5 minutes and then depositing them onto 200 mesh Cu grids (Ted Pella) and drying in air.

2.4.4 Powder X-ray Diffraction

Bulk crystalline phase analysis was performed using powder X-ray diffraction (XRD) utilizing Rigaku MiniFlex II spectrometer with a filtered cobalt source. In XRD

analysis, the specimen is illuminated with X-rays at a fixed wavelength, and the intensity of the reflected radiation as a function of angle is recorded using a goniometer. The intensities of reflection at different angles yield information about the crystalline compounds of the specimen.

In XRD analysis, dry powder samples were placed in the XRD sample holder, and powder sample was smoothed with a razor until flush with the rim of the holder before XRD analysis. Two theta angles ranged from 20 to 80 degree at a 0.02 degree step with a step dwell time of 0.6 seconds.

2.4.5 BET Surface Area Measurement

Surface area measurements for all samples used a seven-point N_2-BET adsorption isotherm that was acquired with a Quantachrome Nova 1200 surface area analyzer. The method is based on a theory developed by Stephen Brunauer, Paul Hugh Emmett, and Edward Teller. In a BET surface area measurement, an inert gas, N_2 in the current research, is introduced into a calibrated sample cell that allows the adsorption of the inert gas on the powder sample of interest. The adsorption can be expressed by the BET equation as follows,

$$\frac{1}{W[(P_0/P)-1)]} = \frac{C-1}{W_m C}\left(\frac{P}{P_0}\right) + \frac{1}{W_m C} \qquad (2\text{-}3)$$

where P and P_0 are the equilibrium and the saturation pressures of adsorbates at the temperature of adsorption, W is the weight of adsorbate at a given P/P_0, W_m is the weight of adsorbate in monolayer coverage, C is the BET constant. The linear relationship between $1/W[(P_0/P)-1)$ and P/P_0 is used to determine W_m. While the cross section of N_2 is known, the total surface area can be obtained. Prior to analysis, samples were

evacuated overnight to remove surface adsorbed water at temperatures that would not change the properties of the materials.

2.4.6 X-ray Photoelectron Spectroscopy

X-ray photoelectron spectroscopy (XPS) is a powerful surface sensitive technique that not only can identify surface compositions of a sample but also can determine quantitatively the composition. XPS spectra are obtained by irradiating a material with X-ray beams while simultaneously measuring the kinetic energy and the number of electrons that escape. The X-ray beams can eject core electron, an electron from a higher energy level, then relaxes down to a lower energy state and simultaneously releases a photoelectron which has a characteristic binding energy. Because the energy of the X-ray at particular wavelength is known, the electron binding energy of each electron emitted from surface can be determined by,

$$E_B = h\nu - E_k \tag{2-4}$$

where E_B is the electron binding energy referenced to vacuum level and E_K is the kinetic energy of the electron. XPS only can detect electrons that have actually escaped into the vacuum of the instrument. The mean free path of electrons in the material is 10-12 nm, thus XPS inherently probes the surface and near-surface regions of the material, making it a powerful surface sensitive technique. The electron binding energy values are used to directly identify each element on the surface of the material being analyzed. It can also provide information regarding to the oxidation state of the elements and surface functional group present.

A custom-designed Kratos Axis Ultra X-ray photoelectron spectroscopy system (Manchester, UK) was used in the current study. The powder samples were pressed onto

indium foil which was placed on either a stainless bar or copper stub for analysis. The sample was placed into the XPS analysis chamber, which had a pressure that was maintained in the 10^{-9} Torr range during analysis. Charging was prevented by using low energy electrons to neutralize the samples. Wide energy range survey scans were acquired using the following instrumental parameters: energy range from 1200 to -5 eV, pass energy of 160 eV, step size of 1 eV, dwell time of 200 ms, and an x-ray spot size of ~ 700 × 300 μm. High resolution spectra in the region of interest were acquired using the following instrumental parameters: 20-40 eV energy window; pass energy of 20 eV; step size of 0.1 eV and dwell time of 1000 ms.

In addition, for heterogeneous reactions explored using XPS, a reaction chamber that connects to sample transfer antechamber is used. The transfer antechamber connects both the reaction chamber and the analysis chamber to allow the sample holder be transferred between two chambers. Two sample transfer rods were used for transferring. The reaction chamber was fabricated with stainless steel. The chamber contains a leak valve, a pressure transducer (BOC Edwards WRG-S-NW35), a pumping system (BOX Edwards TIC) and two Pyrex glass windows. The pumping system consists of a rotary pump, a foreline trap (both BOC Edwards) and an EXT75DX turbomolecular pump with 60 L s^{-1} pumping capacity. The pumping system is separated from the reaction chamber by a hand valve (Granvile-Philips Co.).

All spectra were calibrated using the adventitious C1s peak at 285.0 eV. A Shirley-type background was subtracted from each spectrum to account for inelastically scattered electrons that contribute to the broad background. CasaXPS software was used to process the XPS data. Transmission corrected relative sensitivity factor (RSF) values from the Kratos library were used for elemental quantification. The components of the peaks contain a Gaussian/Lorentzian product with 30% Lorentzian and 70% Gaussian character. An error of ±0.2 eV is reported for all peak binding energies.

2.4.7 Inductively Coupled Plasma Optical Emission Spectroscopy

Inductively coupled plasma optical emission spectrometry (ICP/OES, Varian 720-ES, Walnut Creek, CA) is a powerful tool for trace metal analysis. ICP can produce excited atoms and ions that emit electromagnetic radiation at wavelengths characteristic of a particular element. The intensity of the emission is indicative of the concentration of the element within the sample. Argon gas is used to create the plasma. The solutions were passed through a 0.2 μm PTFE filter to remove particles, and then centrifuged at 20,000 rpm for 20 minutes. The supernatant liquid was taken out to remove residual nanoscale particles precipitated at the bottom of centrifuge tube. The obtained solution is then analyzed by ICP/OES. Approximately 3 mL solution is needed for each ICP/OES analysis. Instrument response was converted to aqueous phase concentrations using standard stock solutions that were prepared daily in an appropriate aqueous solution.

2.4.8 ^{57}Fe Mössbauer Spectroscopy

Information regarding the oxidation state of iron in the source materials was examined with ^{57}Fe Mössbauer spectroscopy. The Mössbauer spectroscopy uses the Mössbauer effect, which is described the resonant absorption and recoil-free emission of nuclear γ–rays in solid, to probe the hyperfine interactions of an atom nucleus and its surroundings. When a free nucleus absorbs or emits a γ–ray to conserve momentum the nucleus must recoil, in terms of energy:

$$E_{\gamma\text{–ray}} = E_{\text{nuclear transition}} - E_{\text{recoil}} \quad (2\text{-}5)$$

where $E_{\gamma\text{–ray}}$, $E_{\text{nuclear transition}}$ and E_{recoil} represent the energies of γ–ray, nuclear transition and recoil respectively. When in a solid matrix the recoil energy goes to zero because the

effective mass of the nucleus is extremely large and momentum can be conserved with negligible movement of nucles. So equation (2-5) can be simplified to

$$E_{\gamma-ray} = E_{nuclear\ transition} \quad (2\text{-}6)$$

In this way, the resonant absorption/emission of γ-rays occurs. In Mössbauer absorption spectroscopy, a solid sample is exposed to a beam of gamma radiation, and detector measures the intensity of the beam transmitted through the samples. The ^{57}Fe Mössbauer spectra were collected as previously described.[106, 111] Briefly, Mössbauer spectra were collected in transmission mode with a constant acceleration drive system and a ^{57}Co source. ^{57}Fe Mössbauer spectra were collected on dry samples at T = 13 K, with an attempt made to randomly orient the powder prior to analysis. Spectral fitting was done using Recoil software (University of Ottawa; Ottawa, Canada) with Voigt-based modeling. Phase identification was done based on center shift, quadrupole splitting, hyperfine field values, and temperature-dependent magnetic ordering.

2.5 Reagents and Materials

2.5.1 Particle Samples

Commercially available metal oxides, including α-Fe_2O_3 (Aldrich), α-Fe_2O_3 (Alfa Asar), α-Fe_2O_3 (Nanostructured & Amorphous Materials), TiO_2 (Degussa), γ-Al_2O_3 (Degussa), α-Al_2O_3 (Alfa Aesar), PbO (Acros Organics), and $Pb(NO_3)_2$ (Acro Organics), were used as received. Three FA samples (SRMs 2689, 2690, and 2691, National Institute of Standards & Technology), and Arizona fine test dust (ISO 12103-1 A2 test dust, Power Technology Inc.) were used as well. The specific surface areas of the particle samples were measured by BET analysis (Quantachrome Nova 4200) and the mineralogy was confirmed by powder X-ray diffraction.

2.5.2 Liquid and Gas Reagents

Distilled H_2O (Optimal grade) was purchased from Fisher Scientific and was degassed prior to use. Gaseous HNO_3 was introduced from a bubbler using a mixed solution of H_2SO_4 (96.0%, Fisher) and HNO_3 (79.5%, Fisher) in a 3:1 ratio. The solution was purified by several freeze-pump-thaw cycles prior to use. Measurements of dissolved Fe(II) and total dissolved iron were performed with 1,10-phenanthroline (≥99%) and hydroxylamine hydrochloride (98%) which were purchased from Sigma Aldrich and ammonium acetate (98.5%, Fisher) and glacial acetic acid (99.7%, EMD).

Ozone was produced by flowing oxygen (Air products, USP grade) through an electric discharge generator (OREC, Model O3V5-O).

CHAPTER 3

HETEROGENEOUS CHEMISTRY AND PHOTOCHEMISTRY OF HNO_3 ON TYPICAL COMPONENTS OF MINERAL DUST AEROSOL

3.1 Abstract

Mineral dust aerosol is known to provide a reactive surface in the troposphere for heterogeneous chemistry to occur. Certain components of mineral dust aerosol, such as semiconductor metal oxides, as well as light absorbing coatings associated with the dust particle surface can act as chromophores that initiate chemical reactions, while adsorbed organic and inorganic species may also be photoactive. However, relatively little is known about the impact of heterogeneous photochemistry of mineral dust aerosol in the atmosphere. This study investigates the heterogeneous photochemistry of trace atmospheric gas HNO_3 with aluminum oxide, a typical component of mineral dust aerosol using an environmental aerosol chamber that incorporates a solar simulator. For reaction of HNO_3 with aluminum oxide, broadband irradiation initiates photoreactions to form gaseous NO and NO_2. A complex dynamic balance between surface adsorbed nitrate, and gaseous nitrogen oxide products including NO and NO_2 is observed. The role of relative humidity and, thus, adsorbed water, on heterogeneous photochemistry has also been explored. Results show that the presence of water has a significant influence on the reaction extent, the decay rate of HNO_3, the product partitioning and even the reaction mechanism. NO was barely observed at 20%, indicating that NO formation is not kinetically favored under humid conditions. The study indicates that irradiation of surface adsorbed nitrate can result in renoxification of HNO_3 back into the gas phase in the form of NO_x product species. The NO_x levels in the troposphere may, therefore, be affected by the continued reactions of adsorbed nitrate initiated by solar radiation.

3.2 Introduction

Of the estimated annual emission of 3000-5000 Tg of particulate matter in the form of mineral dust, sea salt, sulfate aerosols, organic compounds and soot,[112] components of mineral dust aerosol are particularly reactive with trace atmospheric gases.[18] Convincing evidence from field, laboratory and modeling studies has shown that heterogeneous reactions with mineral dust alter the chemical composition of the atmosphere. It is also well established that mineral dust aerosol impacts solar radiation and can influence radiative transfer by absorption and scattering of solar radiation (direct effect), and by changing the size distribution, optical properties and lifetimes of cloud (indirect effects).[18, 112, 113] Atmospheric processing through heterogeneous reactions can alter the physicochemical properties of mineral dust aerosol itself, as well.[18, 34]

While mineral dust can contain various photoactive semiconductor metal oxides, as well as light absorbing coatings associated with the dust particle surface, little is known about heterogeneous chemical processes activated by light and surface photocatalysis. Although heterogeneous reactions of trace atmospheric gases, such as SO_2, HNO_3, and O_3, with mineral dust have been previously well established, possible heterogeneous photochemistry of mineral dust has not yet been as widely considered. Relevant questions, then, are what is the role of heterogeneous photochemistry in the troposphere *and*, how does the daytime chemistry of mineral dust aerosol differ from nighttime chemistry?

Short wavelength (<290 nm) radiation is absorbed in the stratosphere and the upper troposphere[1] but a significant solar actinic flux reaches the Earth's surface. The actinic flux in the lower troposphere in the near UV region, 300-400 nm, is on the order of 10^{13} quanta cm^{-2} s^{-1}.[44] Photon energies in this region (300-400 kJ/mole) are sufficient to initiate a number of direct photochemical processes involving adsorbates on dust surfaces or indirect processes mediated by the absorption of the dust particle itself, for instance in the case of semiconductor metal oxides. In addition, cooperative excitations

involving charge-transfer between an adsorbate and the particle may also occur. Photochemistry involving photoactive adsorbate species may play an important role in the daytime chemistry of the atmosphere.

Nitrogen oxides including NO and NO_2, are important atmospheric pollutants which are mainly introduced into the atmosphere by human activities, such as coal and fuel combustion, biomass burning and vehicle exhaust. Nitrogen oxides along with volatile organic compounds are precursors of photochemical smog, which was first discovered in Los Angeles in the late 1940s.[2, 114] The non-linear reactions of nitrogen oxides and volatile organic compounds under solar radiation initiate a series of chain radical reactions, and represent as the sources of ozone in the troposphere. The atmospheric chemistry involved nitrogen oxides is therefore important to accurately estimate the formation of tropospheric ozone.

HNO_3 is general believed to be the product of oxidation of nitrogen oxides. Adsorption of HNO_3 on mineral dust has been observed in field studies with formation of nitrates, and is suggested to be a potential pathway for HNO_3 removal in the atmosphere.[49-51] For example, Wu and Okada[50] found that both sea-salt and mineral dust particles collected in Japan during a "Kosa" sandstorm event contained a certain amount of nitrate along with Si, Al, Fe, and Ca containing species. It was concluded that heterogeneous reaction of HNO_3 on the surface of dust particles is the main source of surface nitrate. Subsequent laboratory experiments conducted by Mamane further bolstered this conclusion.[115] Through a number of laboratory studies, the mechanism of nitric acid reaction with mineral dust is now[116-120] fairly well understood.

For decades, it was thought that nitrate is the end-product of NO_x (NO_x = NO + NO_2) oxidation, with removal via wet and dry deposition. However, with the observation of active photochemistry of nitrate in snow packs,[52, 53] and the subsequent studies on the reactive oxides of nitrogen such as HONO, NO and NO_2 generated in this process,[54-59, 121]

particulate nitrate may, in fact, be a reservoir rather than a sink for gas-phase nitrogen oxides in the atmosphere.

Further evidence has been reported in several field, laboratory and modeling studies. For example, the ratio of $[HNO_3]/[NO_x]$, in the free troposphere is measured at ~1 to 9 (averaging ~5), which is consistently lower than the value of 12-100 predicted by modeling calculation. Chatfield attributed the discrepancy to reaction of HCHO with HNO_3 in aerosols and cloud droplets.[122] Study on heterogeneous reaction of HNO_3 on amorphous carbon observed the conversion of HNO_3 to NO, NO_3 and H_2O.[123] HNO_3 has also been identified as a precursor to HONO formation in the atmosphere.[55, 56]

In earlier publications, it has been studied the photochemistry of adsorbed nitrate on aluminum oxide where nitrogen-containing species, including NO_2, NO and N_2O,[58, 59] are produced. Additionally, nitric acid uptake on mineral dust has a large influence on the global ozone budget, making an understanding of all the relevant processes involving nitric acid, including photochemistry, even more important.

This study expands on some of initial studies of heterogeneous photochemistry using an environmental aerosol chamber recently redesigned to include a solar simulator. This study investigates the heterogeneous photochemistry of nitric acid with aluminum oxide, a typical component of mineral dust aerosol. Comparison was made for the nighttime and daytime chemistry of these species in the presence and absence of dust aerosol. From these results, the influence of heterogeneous photoreactions on tropospheric chemistry is discussed.

3.3 Experimental Methods

Experiment was conducted using the environmental aerosol chamber. In a typical experiment, the chamber was purged overnight with dry air to remove water and other impurities. Then the chamber was evacuated to low pressure (e.g. 680 Torr), filled with

the reagent gas, HNO_3 in the current study, at a certain RH, and brought up to near atmospheric pressure with dry air. The reactant gases were allowed to sit in the chamber for about one hour for passivation and quantification of wall losses. The solar simulator then was turned on before aerosol introduction for 100 minutes to further quantify additional wall losses and photolysis reactions induced by the simulator. A precisely weighed powder sample was then introduced to initiate heterogeneous reactions involving the gas phase species. The solar simulator was turned off after approximately 500 minutes of reaction to yield a post-irradiation period. Gas phase concentrations, as well as RH, temperature and total pressure in the chamber, were monitored during the entire experiment.

Gaseous HNO_3 was introduced from a bubbler using a mixed solution of H_2SO_4 (96.0%) and HNO_3 (79.5%) in a 3:1 ratio. The solution was purified by several freeze-pump-thaw cycles prior to use. Commercially available γ-Al_2O_3 (Degussa, Aluminum oxide C) with a surface area of 101 $\pm$ 4 m^2 g^{-1} was used as received. Surface area measurements were performed by using a Quantachrome Nova 4200e multipoint BET apparatus.

3.4 Results and Discussions

3.4.1 Comparison of Adsorption Cross-section of HNO_3 with Irradiance Spectrum of the Solar Simulator

Figure 3.1 shows the comparison of adsorption cross-section of HNO_3 with irradiance spectrum of the solar simulator in the environmental aerosol chamber. The spectral absolute irradiance from the solar simulator was determined by placing a calibrated radiometer at the bottom of the chamber, a distance of approximately 1 m from the solar simulator. There is small overlap between the simulator irradiance and the absorption profile of nitric acid.

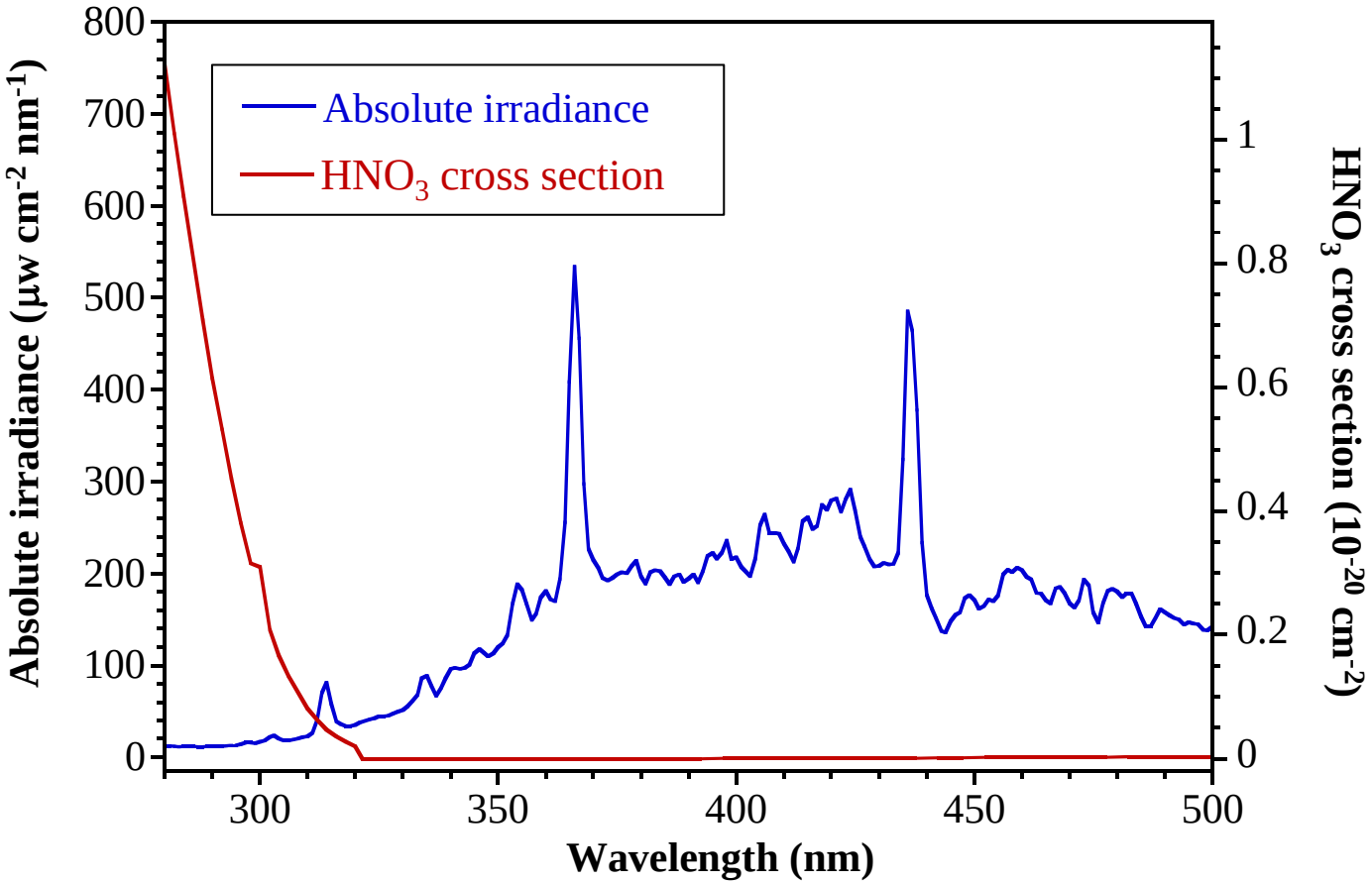

Figure 3.1 Solar simulator spectral irradiance (blue line) at the bottom of the environmental aerosol chamber compared to the absorption cross section of nitric acid (red line).

3.4.2 Heterogeneous Photoreaction of HNO_3 with Al_2O_3

The heterogeneous photoreaction of HNO_3 with Al_2O_3 under dry conditions (<2% RH) was investigated in the environmental aerosol chamber. Typical initial concentrations of HNO_3 were approximately 160 ppm and the Al_2O_3 mass loadings about were 500 mg. Figure 3.2 displays representative FTIR spectra of the chamber contents collected at various times over the course of the experiment. The spectrum collected before irradiation, Figure 3.2(a), shows three main absorption bands at 1719, 1315 and 893 cm^{-1}, which are attributed to gaseous HNO_3.[124] These features are observed to decrease as the reaction proceeds, especially after the aerosol sample is introduced, corresponding to positive reaction times. Small, but observable, bands centered at 1875 cm^{-1} and 1616 cm^{-1}, corresponding to NO and NO_2 respectively,[59] grow in during nitric acid decay indicating that both NO and NO_2 are produced in the reaction. The appearance of a sloping spectral baseline after introduction of Al_2O_3 into the environmental aerosol chamber is characteristic of Mie scattering.

To assess the time dependent behavior of the gas phase components, infrared spectra were collected throughout the course of the experiment. The various absorbance features were integrated and converted to mixing ratios (ppm) using previously determined Beer's law calibrations in order to quantify the gas phase concentrations. Typical concentration-time profiles for the reactant, HNO_3, and product species, NO_2 and NO, are shown in Figure 3.3. Negative reaction times represent the passivation period (t < -100 minutes) and irradiation period (t = -100-0 minutes) before introduction of the alumina dust sample (t = 0 minutes). The heterogeneous reaction was allowed to proceed under irradiation until the simulator was turned off (t = 550 minutes) and the post-irradiation period was monitored.

Analysis of the HNO_3 profile shows that there is a small decay during the passivation and initial irradiation period that can be ascribed to wall loss. The decay of HNO_3 slows slightly when the simulator is turned on, suggesting that nitric acid is

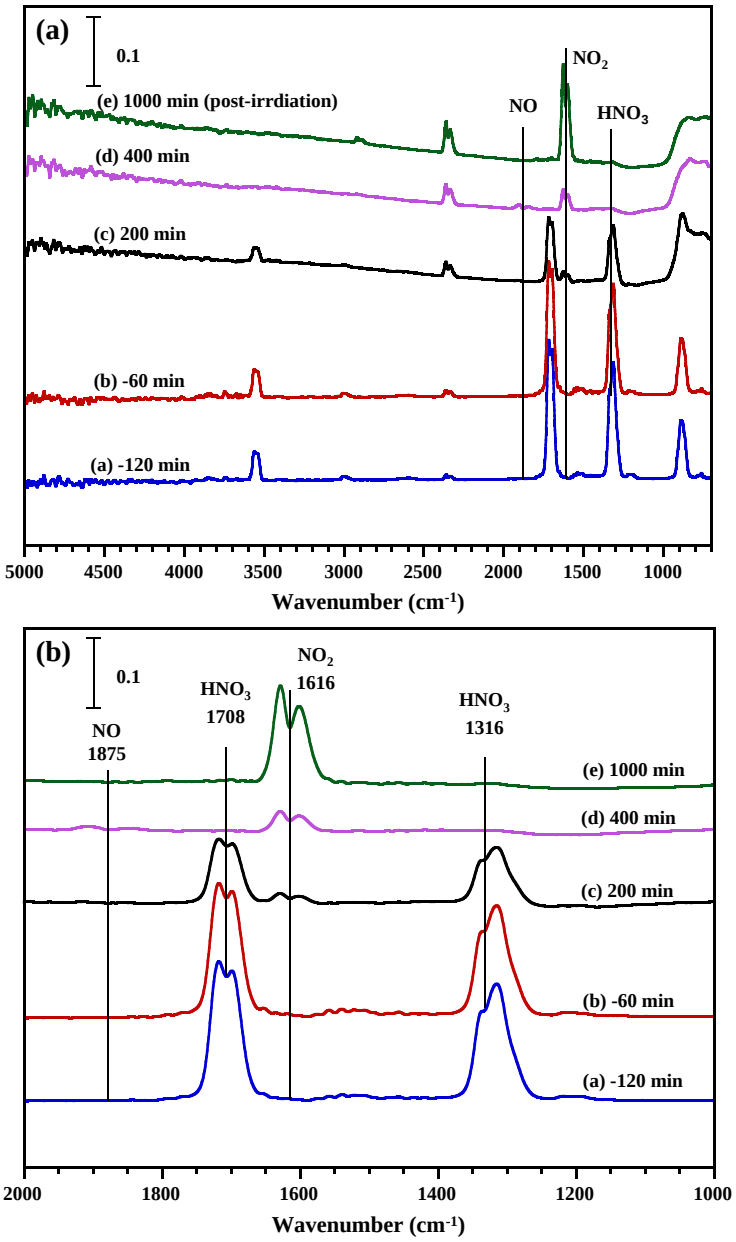

Figure 3.2 (A) FTIR spectra of gaseous species in the environmental aerosol chamber collected at <1% RH (a) prior to Al_2O_3 introduction in the dark; (b) prior to Al_2O_3 introduction after 60 minutes of irradiation; (c) after Al_2O_3 introduction for 200 minutes with irradiation; (d) after Al_2O_3 introduction for 400 minutes with irradiation; (e) turned off radiation and post-irradiation. (B) A magnified view of the spectral region from 1000 to 2000 cm-1. A decrease of HNO_3 bands is evident, as well as the growth of NO and NO_2 bands.

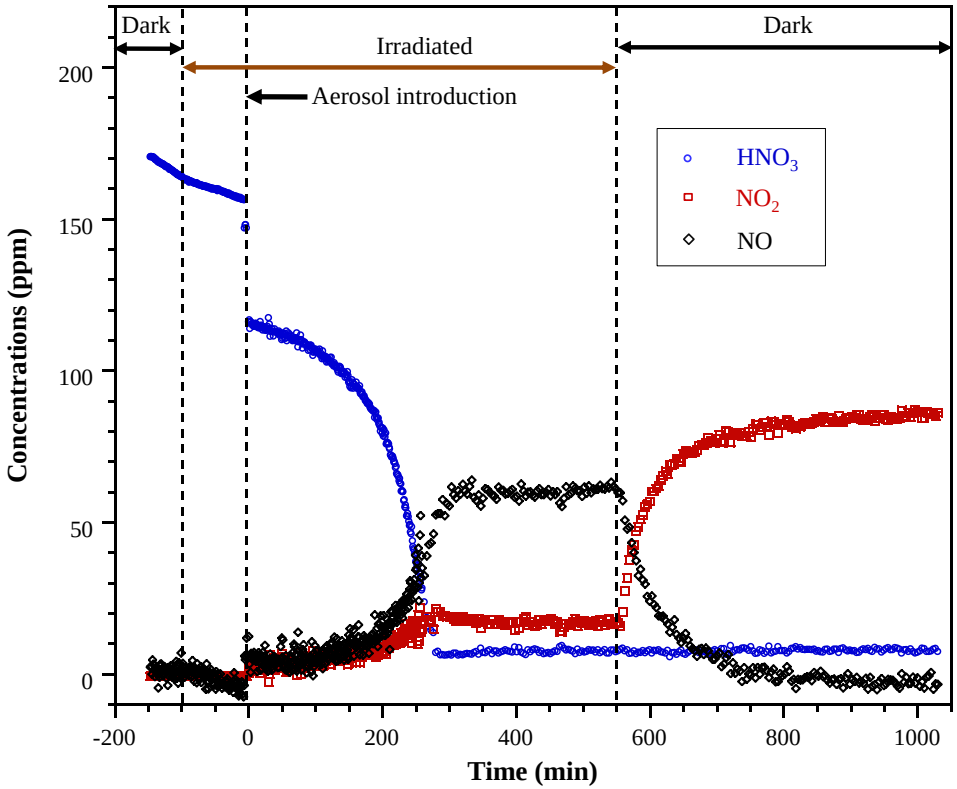

Figure 3.3 A typical concentration-time profile of gaseous HNO_3 (○), NO_2 (□), and NO (◊) during the heterogeneous photoreaction of HNO3 with Al_2O_3 at <1% RH in the environmental aerosol chamber. Negative reaction time represents the passivation period (t < -100 min), and irradiation period (t = -100 min-0 min) before Al_2O_3 introduction at time t = 0 min, followed by the period of heterogeneous photoreaction. The solar simulator was turned off at time t = 550 min, followed by the post-irradiation period.

reversibly desorbed from the chamber walls due to the small increase in temperature. Significantly, no gaseous products are observed with the simulator on but prior to Al_2O_3 introduction. A separate experiment, prolonged irradiation of nitric acid in the absence of alumina for a period of up to 500 minutes failed to yield detectable levels of gas phase products. Despite overlap between the tail of the HNO_3 absorption spectrum and the simulator output, homogeneous photolysis of the HNO_3 is negligible under the current experimental conditions.

Upon introduction of the aerosol, the HNO_3 concentration exhibits a rapid initial drop due to uptake by the Al_2O_3 particles on time scale faster than the current experimental resolution. Subsequently, a non-exponential decay of HNO_3 is observed. The rate of nitric acid consumption increases until all of the HNO_3 has been consumed by a reaction time of $t \approx 270$ minutes. Concomitant with HNO_3 loss, growth of NO and NO_2 is also observed. In dark experiments reported here and in previous work,[41,125] NO_x products were not observed from HNO_3 reaction with alumina surfaces, indicating the important role of photoinduced processes. The NO_x product species increase in concentration at a similar rate until all of the gas phase HNO_3 has been lost whereupon they rapidly reach a photostationary state with $[NO] > [NO_2]$. The steady state persists until the simulator is extinguished and all of the NO is converted to NO_2 and the reaction appears to be complete; no further change in the product nitrogen dioxide concentration is observed.

In separate experiments,[126] not shown here, NO_2 was found to irreversibly and rapidly uptake to the surface of Al_2O_3. The lack of further reaction of NO_2 in the post-irradiation period at the end of the experiment suggests that the surface of the aerosol is saturated. The amount of product NO_2 at the end of the experiment, 85 ppm, represents a reaction yield of about 50% of the HNO_3 initially present in the chamber when the dust sample is introduced, ≈ 157 ppm. Subtracted the wall loss, the amount of reacted HNO_3,

63 ppm, is presumably adsorbed as nitrate to the surface of the alumina. The nitrate coverage, $n_{NO_3^-}$, can be calculated as,

$$n_{NO_3^-} = \frac{X_{HNO_3,rxn} P_\tau VN}{RTC_{mass} S_{BET}} \quad (3\text{-}1)$$

where $X_{HNO_3,rxn}$ = 63 ppm is the mixing ratio for the reacted nitric acid, P_T is the total chamber pressure, V is the chamber volume, N_A is Avogadro's number, C_{mass} is the mass loading of Al_2O_3, and S_{BET} is the BET surface area of the commercial mineral dust sample. A coverage of 4.5×10^{14} cm^{-2}, ≈ 1 monolayer, is calculated. The approximate monolayer coverage of nitrate indicates that the surface does become saturated and the alumina sample is no longer reactive towards NO_2.

In the atmosphere, NO can be rapidly converted to NO_2 via oxidation by O_3 in the reaction,

$$NO + O_3 \xrightarrow{k_1} NO_2 + O_2 \quad (3\text{-}2)$$

However, in the chamber experiments, the NO concentration is large and the reaction with molecular oxygen is also possible, even though it is a termolecular process,

$$2NO + O_2 \xrightarrow{k_2} 2NO_2 \quad (3\text{-}3)$$

In the post-irradiation period, the quantitative conversion of NO to form NO_2 would require 60 ppm of O_3, well within the detection limits of the current FTIR probe method. No detectable ozone indicates that the conversion of NO to form NO_2 is mainly through equation (3-3). Since oxygen, with a mixing ratio of 21%, is in excess in the

chamber, equation (3-3) is pseudo-second order and the half-life, $\tau_{½}$, can be calculated as,

$$\tau_{1/2} = \frac{1}{k_2[O_2][NO]_0} \tag{3-4}$$

where $[NO]_0 \approx 60$ ppm, is the nitric oxide concentration at the start of the post-irradiation period. The calculated half-life of approximately 100 minutes is in accordance with the observed decay/growth curves for NO/NO_2 observed in Figure 3.3 after the simulator is turned off and confirms the importance of equation (3-3) in the post-irradiation period.

In the photostationary period, t ≈ 280-550 minutes, the concentrations of NO and NO_2 remain constant. There are no irreversible heterogeneous source or sink reactions involving NO or NO_2 during this period, although there may be reversible processes, perhaps induced by radiation from the simulator. This is unlikely, however, as the total product NO_x, $[NO] + [NO_2] \approx 85$ ppm, is equivalent to the NO_2 yield at the end of the experiment. Thus, the nitrate coverage is the same, $\theta \approx 1$ monolayer, as the post-irradiation period, and the alumina surface is saturated. The production of NO_2 is governed by the equation of (3-2) and (3-3), and the most likely loss mechanism is via photolysis,

$$NO_2 + h\nu \xrightarrow{J_{NO2},+O_2} NO + O_3 \tag{3-5}$$

where the O atom product is rapidly converted to ozone through the O_2 association reaction. The NO_2 photolysis rate constant, J_{NO_2}, can be calculated from the overlap of the measured solar simulator irradiance with the known NO_2 absorption spectrum using the equation,

$$J_{NO_2} = \int_{\lambda} \sigma_{NO_2} \phi_{NO_2} I_S d\lambda \tag{3-6}$$

where σ_{NO_2} and ϕ_{NO_2} are the wavelength dependent absorption cross-section and dissociation quantum yield, respectively,[127] for NO_2, and I_S is the spectral actinic flux for the simulator determined from the data of Figure 3.1. The rate constant calculated from equation (3-6) is $\approx 0.013\ s^{-1}$.

By setting up the production and loss rates of NO_2 to be equal,

$$[O_3] = \frac{J_{NO_2}[NO_2] - 2k_2[O_2][NO]^2}{k_1[NO]} \tag{3-7}$$

and substituting the calculated J_{NO_2} and the observed concentrations of the NO_x species and the known rate constants for reactions of (3-2) and (3-3),[128] the ozone concentration under photosationary conditions is calculated to be ≈ 8.3 ppb, and lower than the detection limits of the current FTIR probe method. The NO oxidation with O_3 through reaction (3-2) represented 92% of total NO_2 production, is therefore the main way to recycle NO back to NO_2 under photosationary conditions in the current experimental system.

The initial reaction period from the time of aerosol introduction until the establishment of photostationary conditions, t ≈ 0-280 minutes, is characterized by the loss of HNO_3 at an exponentially increasing rate and the steady growth of NO_x product species. The HNO_3 loss can be compared to the results of a dark experiment carried out under similar conditions of nitric acid pressure and alumina powder mass loading but in the absence of irradiation. The HNO_3 concentration profile for that experiment, shown in Figure 3.4, indicates that after correcting for wall loss (for t > 0, after powder introduction), the alumina surface becomes saturated and no further reaction with HNO_3 is observed. In

addition, neither NO nor NO_2 are observed. The total surface coverage is calculated to be $n_{NO_3^-} \approx 4.0 \times 10^{14}$ cm^{-2}, or $\theta \approx 1$ monolayer, assuming that this level of coverage corresponds to the effective reactive surface site density for the Al_2O_3 sample used. The final nitrate coverage, 4.5×10^{14} cm^{-2}, in the solar simulator experiment is slightly higher than experiment performed in the dark, and the saturated surface also exhibits no reactivity towards NO_x, indicating that higher nitrate coverage is required to maintain the balance between surface adsorbed nitrate and gaseous NO_x. However, in the presence of irradiation, all of the nitric acid is consumed and the effective nitrate coverage is calculated to be greater than two monolayers. This suggests that the loss of gas phase HNO_3 is continuous in the presence of Al_2O_3 and irradiation.

The product NO and NO_2 species appear immediately upon introduction of the aerosol and in the presence of irradiation along with a large initial loss of HNO_3. Furthermore, the concentrations of NO and NO_2 track each other over most of the initial reaction period, only diverging when the nitric acid is nearly gone. The concentration of NO_2 is about 5 ppm initially, corresponding to an NO production rate of about 0.4 ppm $minute^{-1}$ under the current experimental conditions. However, no induction period is observed for the NO product. It appears, then, that the formation and/or loss reactions for the NO_x species are closely tied together and that heterogeneous processes are probably involved. Most interestingly, the photostationary state is not achieved until the HNO_3 has been totally consumed, suggesting that gas phase nitric acid is important to the reaction mechanism.

Finally, as previously noted, the rate of nitric acid disappearance increases exponentially. Surface nitrate species formed on the alumina may act as effective chromophore that absorb solar radiation.[59] By analogy with nitrate photolysis in solutions and in ice and snowpack,[52, 53] NO_2 and NO formation may ensue from the following reactions,

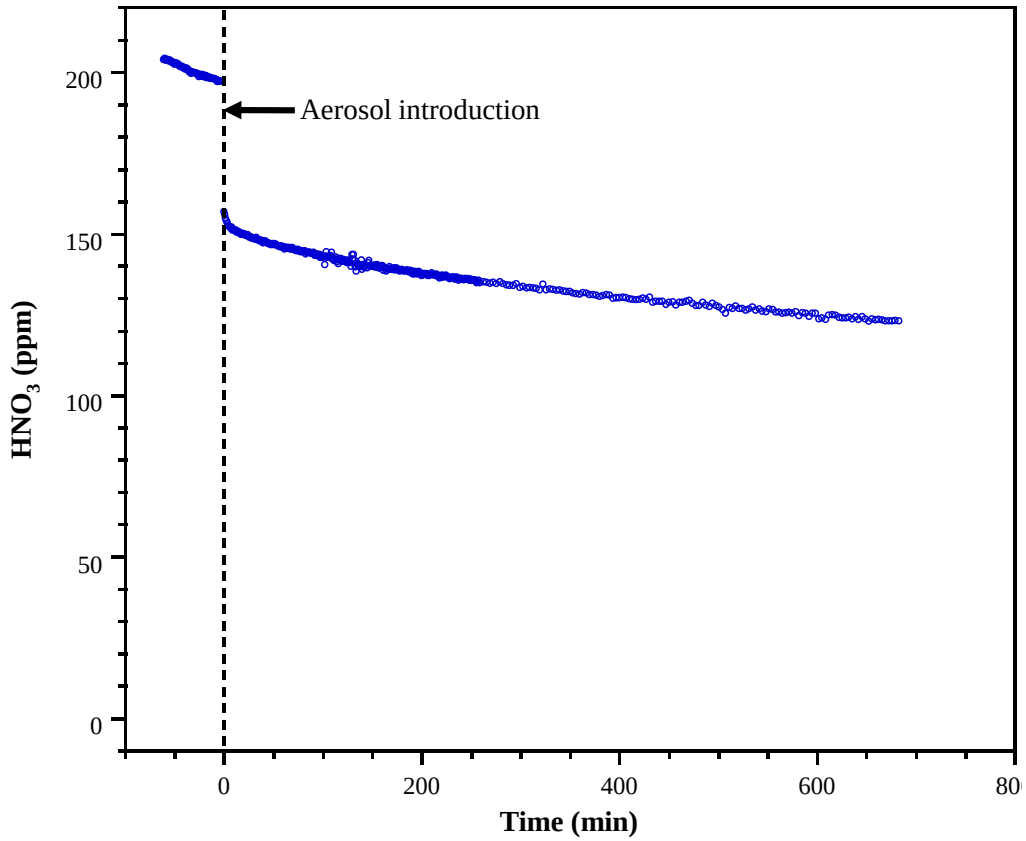

Figure 3.4 A typical concentration-time profile of gaseous HNO3 in the presence of Al_2O_3 under dark and <1% RH conditions in the environmental aerosol chamber. The saturation uptake of HNO3 on Al_2O_3 is rapidly attained after the introduction of Al_2O_3 at t = 0 min.

$$NO_3^- + H + h\nu \rightarrow NO_2 + OH \quad (3\text{-}8)$$

$$NO_3^- + h\nu \rightarrow NO_2^- + O \quad (3\text{-}9)$$

$$NO_2^- + H^+ + h\nu \rightarrow NO + OH \quad (3\text{-}10)$$

where NO_2 and NO would then interconvert via the photochemical cycle described by equations (3-2), (3-3) and (3-5), above. In studies of heterogeneous photolysis of HNO_3 on silica (glass) surfaces, Zhou et al.[56] also detected the production of NO and NO_2, although the nitric oxide was produced in much smaller amounts. Their study reported a heterogeneous photolysis rate constant for NO_x production of $J = 6 \times 10^{-5}$ s^{-1} for noontime sun under dry conditions. From a comparison of the current calculated NO_2 photolysis rate, 0.013 s^{-1}, to the atmospheric photolysis rate of $\approx$ 0.015 s^{-1},[1] a NO_x production rate constant of 5×10^{-5} s^{-1} might be expected from the alumina surfaces if a similar mechanism to that elucidated by Zhou et al. is applicable. From the known Al_2O_3 mass loading in the chamber and assuming the reactive nitrate surface density is 4.5×10^{14} cm^{-2} from the measured HNO_3 saturation, the NO_x production rate was calculated to be $\approx$ 0.18 ppm min^{-1}. Such a formation rate is reasonable based on the time scale of the current experimental measurements.

The low concentration of NO relative to NO_2 during the initial reaction period suggests there may be other sinks for NO. In studies of heterogeneous reactions of HNO_3 with silica surfaces, molecularly adsorbed nitric acid was detected via its IR signature.[129] The nitric acid adsorbate is thought to facilitate a heterogeneous reaction with NO,

$$NO(g) + HNO_3(a) \rightarrow HONO(a) + NO_2(g) \quad (3\text{-}11)$$

followed by,

$$HONO(a) + HNO_3(a) \rightarrow 2NO_2(g) + H_2O \quad (3\text{-}12)$$

The effect of equations (3-11) and (3-12) may be to enhance the rate of HNO_3 loss as the NO concentration, and NO precursors such as NO_2, build up in the chamber, leading to the observed exponential increase in the nitric acid reaction rate. The nitrous acid intermediate, HONO, may also desorb into the gas phase. This study detected no HONO in the current experiments but the photolysis rate would be quite large in the chamber experiment, with a HONO lifetime with respect to photodissociation of 1-2 minutes. Zhou et al.[56] also detected very little HONO in their photolysis experiments under dry conditions. A reaction similar to (3-11) with surface nitrate could yield nitrite,

$$NO(g) + NO_3^-(a) \rightarrow NO_2^-(a) + NO_2(g) \quad (3\text{-}13)$$

which could then photodissociate on the surface to yield NO, as in equation (3-10), and in analogy to the solution phase mechanism for NO_3^- photodissociation.[130]

Hydroxyl radicals may also play a role in the photochemical reaction mechanism. Hydroxyl radicals could be formed from HONO photodissociation or from O_3 photolysis,

$$O_3 + h\nu \rightarrow O_2 + O^* \quad (3\text{-}14)$$

$$O^* + H_2O \rightarrow 2OH \quad (3\text{-}15)$$

where hydrogen sources could be from water adsorbed to the chamber walls, residual surface water, or hydroxyl groups terminating the alumina surface. Two potentially important radical reactions would be,

$$OH + NO_2 \xrightarrow{M} HNO_3 \quad (3\text{-}16)$$

$$OH + HNO_3 \rightarrow NO_3 + H_2O \quad (3\text{-}17)$$

The nitrate radical, NO_3, would have a short lifetime due to photolysis, 1-2 minutes, returning to NO_2 and NO. Equation (3-17) could contribute to the exponential increase in the observed rate of HNO_3 loss as OH precursor species build up in the chamber. However, the loss reaction, (3-17), is generally slower than the HNO_3 formation reaction, (3-16). The relative rate depends on the ratio of nitric acid to nitrogen dioxide and the loss reaction is only faster for a ratio of $[HNO_3]/[NO_2] > 160$, conditions not achieved during the entire experimental course. Other, as yet unidentified, processes that are facilitated by the simulated solar irradiation may also play important roles.

3.4.3 RH Effect on the HNO_3 Heterogeneous Photochemistry with Al_2O_3

In order to investigate the role of relative humidity (RH) and adsorbed water on the heterogeneous photoreaction of HNO_3 with Al_2O_3, a similar experiment was performed at 20% RH. Figure 3.5 displays the loss of HNO_3 and the evolution NO_2 in the environmental aerosol chamber. In contrast to the dry experiments, NO is not detected. The initial, rapid loss of HNO_3 upon aerosol introduction is approximately the same as in the dry experiment. However, compared to dry conditions, the subsequent decay of HNO_3 appears to be linear and does not manifest an exponential rate increase. When the solar simulator is turned off at time t = 500 min, the HNO_3 resumes an exponential decay. The loss of HNO_3 with and without irradiation present is likely dominated by wall loss processes and the data are difficult to interpret. The product NO_2 appears immediately after aerosol introduction and remains approximately constant at ≈ 5-10 ppm during the irradiation period. In the post-irradiation period, the concentration increase exponentially

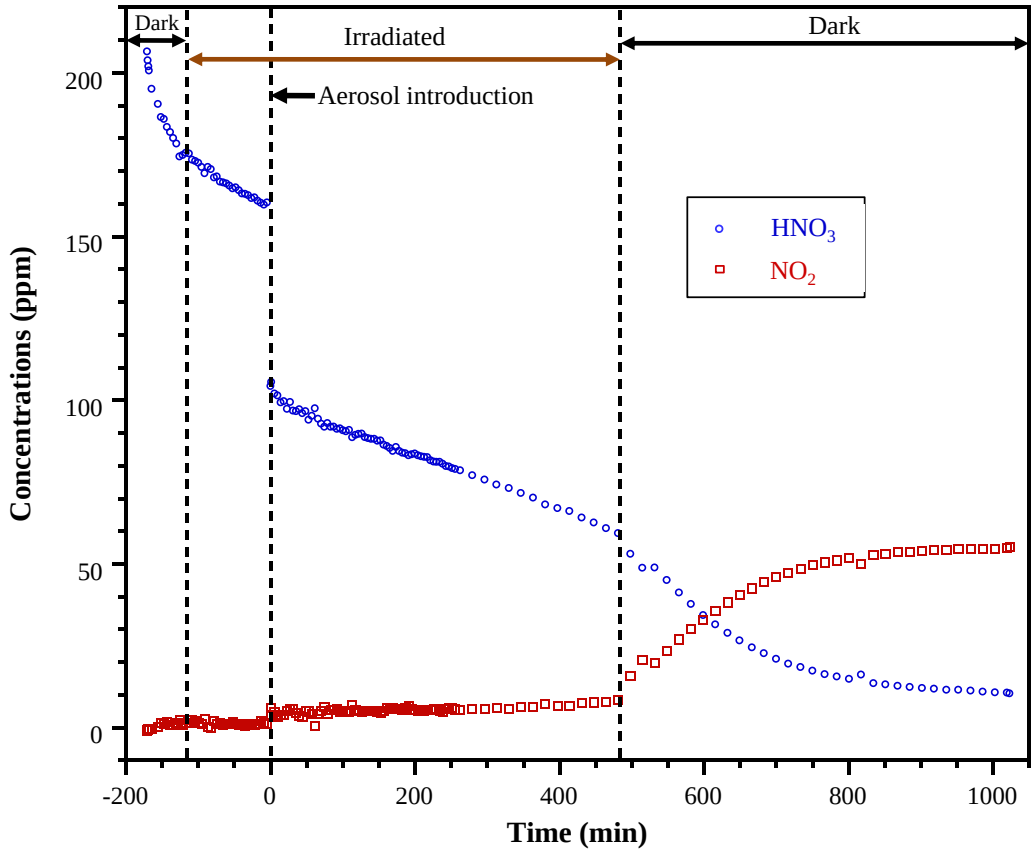

Figure 3.5 A typical concentration-time profile of gaseous HNO_3 (○) and NO_2 (□) during the heterogeneous photoreaction of HNO_3 with Al_2O_3 at 20% RH in the environmental aerosol chamber.

to a final value of 60 ppm, corresponding to a reaction yield of approximately 38%, less than the 50% yield in the dry experiments.

The lack of detectable NO is consistent with the previous work which showed that NO formation is not kinetically favored under humid conditions.[58] It is proposed that photolysis of nitrite, NO_2^-, to yield NO, reaction (3-10), is suppressed in the presence of adsorbed water due to the formation of $[NO_2^- \cdot H_2O]$ on the surface and the lower acidity of the wet particle. Zhou et al.[56] also reported a decrease in the total photolysis rate of nitric acid adsorbed on silica in the presence of water. The product yield for HONO increased with RH but the NO_x yield decreased with NO_2 representing almost all of the NO_x product.

The slower HNO_3 loss can also be partially attributed to heterogeneous hydrolysis of NO_2, one of the gaseous products of surface nitrate photochemistry. As discussed in detail in previous reports,[54, 131] heterogeneous hydrolysis of NO_2 can occur in the presence of water:

$$2NO_2 + H_2O \xrightarrow{\text{surface}} HONO + HNO_3 \qquad (3\text{-}18)$$

Equation (3-18) recycles product NO_2 back into surface adsorbed nitric and nitrous acids, potentially blocking further absorption of HNO_3 on the alumina surface. A photoenhancement of the heterogeneous hydrolysis of NO_2 along with an increased generation of HONO has been reported in several previous studies.[132, 133] The HONO formed in equation (3-18) may be more likely to stay adsorbed on the surface at this intermediate RH, 20%. At higher RH, surface adsorbed water can displace the HONO to the gas phase.[134] As noted above, any HONO that does desorb would photolyze rapidly and may not be detected in the current experiment. Once the solar simulator is turned off,

the adsorbed HONO reacts with HNO_3 to reform NO_2 (the reverse of reaction (3-18)), resulting in the loss of nitrate and the formation of NO_2.

3.5 Conclusions and Atmospheric Implications

This study has incorporated a solar simulator into an existing environmental aerosol chamber to investigate the heterogeneous photochemistry of HNO_3 on mineral dust proxies, single chemical components of mineral dust, to better understand the differences between daytime and nighttime chemistry. It is shown the dynamic balance between surface adsorbed nitrate, and gaseous HNO_3, NO_2, and NO. Irradiation of surface adsorbed nitrate can result in renoxification of HNO_3 back into the gas phase in the form of NO_x product species. The NO_x levels in the troposphere may, therefore, be affected by the continued reactions of adsorbed nitrate initiated by solar radiation. Furthermore, as discussed, the concentration of a number of important atmospheric species, including tropospheric ozone, can be affected by heterogeneous photochemical processes as well. As a consequence of photochemistry, uptake of HNO_3 on mineral dust represents a part of the active nitrogen oxide cycle rather than acting as a permanent sink. The presence of water has a significant influence on the reaction extent, the decay rate of HNO_3 and even the reaction mechanism. Although the photoinduced conversion between surface adsorbed and gaseous nitrogen oxide species appears to be rather complex, such renoxification processes may need to be taken into account in future field studies and modeling work.

The current study shows that heterogeneous photochemistry of trace atmospheric gases with mineral dust aerosol surfaces can potentially play an important role in the troposphere. Solar radiation may change the product distribution, the reaction extent, the reaction rate, and the reaction mechanism of trace atmospheric gases on the surface of mineral dust. Since the surfaces on which such processes may occur include not only

airborne particles but also soils, rock formations, buildings, and vegetation, the relevant heterogeneous photoreactions might be widespread and globally impact the chemical state of the troposphere. Although heterogeneous photochemistry should be incorporated into atmospheric chemical models to improve the prediction accuracy of the model results, much work remains to fully understand these processes. For example, the role of aerosol composition in promoting heterogeneous photochemistry needs to be further explored. In addition, the concentrations of the relevant gases in the environmental aerosol chamber used in this work are considerably greater than the ambient tropospheric concentrations. Experiments carried out under more atmospherically relevant conditions will be important to pursue.

3.6 Acknowledgments

This material is based upon work supported by the National Science Foundation under Grant No. CHE-0952605. Any opinions, findings, and conclusions or recommendations expressed in this material are those of the author and do not necessarily reflect the views of the National Science Foundation. I would like to acknowledge Professor Mark A. Young who gave me valuable suggestions on the work, and Dr. Juan G. Navea who helped me with the data collection and analysis.

CHAPTER 4

HETEROGENEOUS CHEMISTRY AND PHOTOCHEMISTRY OF OZONE ON TYPICAL COMPONENTS OF MINERAL DUST AEROSOL

4.1 Abstract

A number of field, laboratory and modeling studies have suggested that ozone decomposition on mineral dust surfaces is effectively to present as a sink of tropospheric ozone. While previous laboratory experiments are mainly performed under dark condition, the impact of solar radiation on ozone decomposition has not explored to any greater extent. Indeed, mineral dust aerosol contains semiconductor oxides such as hematite and titanium oxide as well as insulator such as aluminum oxide and silicon oxides. The energy of solar radiation is sufficient to activate the semiconductors and therefore initiate photo-induced reactions that would affect the reaction mechanism, reaction extent and even product partitioning. In order to explore the role of solar radiation plays in ozone decomposition on mineral dust aerosol, the heterogeneous chemistry and photochemistry of ozone on oxide components of mineral dust aerosol, including α-Fe_2O_3, α-FeOOH, TiO_2, and α-Al_2O_3, at different relative humidity have been investigated using an environmental aerosol chamber. The rate and extent of O_3 decomposition on these oxide surfaces are found to be a function of the nature of the surface as well as the presence of light and relative humidity. Under dark and dry conditions, only α-Fe_2O_3 and α-FeOOH exhibit catalytic decomposition toward O_3, while the reactivity of TiO_2 and α-Al_2O_3 is rapidly quenched upon ozone exposure. However, upon irradiation, TiO_2 is active toward O_3 decomposition, and α-Al_2O_3 remains inactive. In the presence of relative humidity, ozone decay on α-Fe_2O_3 and α-FeOOH subject to irradiation or under dark conditions is found to decrease. In contrast, ozone decomposition is enhanced for irradiated TiO_2 as relative humidity initially increases but then begins to decrease at even higher relative humidity levels. A kinetic model was used

to obtain heterogeneous reaction rates for different homogeneous and heterogeneous reaction pathways taking place in the environmental aerosol chamber. Atmospheric implications of these results are discussed.

4.2 Introduction

It is estimated that between 1600 and 2000 Tg of mineral dust is uplifted into the atmosphere annually through wind action.[8] These emissions are likely to increase due to the predicted expansion of arid regions.[12] Transport of the smaller size fraction of mineral dust, consisting of particles with diameters of a few microns or less, over long distance raises the possibility that these mineral dust aerosols can alter atmospheric trace gas concentrations on a global scale.[18, 135]

One important heterogeneous reaction is the decomposition of ozone (O_3) on mineral dust surfaces. The reaction is of particular interest due to tropospheric ozone as a notable pollutant associated with health and environmental concerns.[136] Specifically, ozone is a greenhouse gas to trap heat in the atmosphere and a reactive oxidant to initiate chain reactions of atmospheric compounds. High levels of tropospheric ozone can irritate respiratory system, and reduce lung function.[136] Ground level ozone is not emitted directly into the atmosphere, but is formed through complex chemical reactions between precursor emissions of VOCs and NO_x under solar radiation.[1, 136] The concentration of ozone is therefore an air quality indicator that has been monitored at air monitoring sites. Ground-level ozone mixing ratios range from 20 to 60 ppb, but the peak value can exceed 100 ppb in some polluted areas.

Field observations of reduced ozone concentrations in air masses with high particulate concentrations have been interpreted as evidence of direct uptake of ozone on the dust particle surface.[137-140] For example, de Reus et al.[138] observed reduced O_3 mixing ratios over the North Atlantic Ocean in a dust layer originating from North Africa,

suggesting the loss of ozone on the dust surface. Bonasoni et al.[140] gave further evidence that a strong anti-correlation exists between the concentrations of coarse particles and ozone. They proposed that coarse mineral aerosol originating from the Saharan desert can remove atmospheric ozone more effectively than fine particles from industrialized regions.

Modeling studies also supported considerable perturbation of heterogeneous reactions on mineral dust surface to tropospheric chemistry. A global three-dimensional model of the troposphere was used to simulate the role of mineral dust on tropospheric chemistry by Dentener et al.[135] The modeling results indicate that ozone levels near a dust source could decrease up to 10% due to the heterogeneous reaction with mineral dust aerosol. Heterogeneous reactions were also incorporated into a Regional Air Quality Model System by Li et al. to investigate the impact of heterogeneous reactions on tropospheric chemistry in East Asia during the dust storm period in March 2006.[141] The modeling study predicted that O_3 concentration decreases 2.1% when heterogeneous reactions are taken into account. Direct ozone loss on aerosol surfaces is a key variable contributing to considerable uncertainties in atmospheric chemistry models.[135, 142]

Significant uptake of ozone on oxide components of mineral dust as well as authentic dust samples has been observed in laboratory studies.[42, 43, 143-148] For example, Hanisch and Crowley[145] reported an initial uptake coefficient of $\gamma_0 \approx 3 \times 10^{-5}$ for authentic Saharan dust exposed to 30 ppbv ozone, while complete passivation occurred at higher ozone concentrations. Previous research from our laboratory suggests that that hematite (α-Fe_2O_3) catalytically decomposes ozone while corundum (α-Al_2O_3) saturates at a lower, finite ozone surface coverage.[42] In addition, the uptake of ozone on either oxide was suppressed by increased relative humidity.

Previously reported laboratory experiments have been carried out under dark conditions. The influence of solar radiation on heterogeneous reactions of ozone with mineral dust has not been assessed to any great extent. Indeed, in addition to insulators

such as SiO_2 and Al_2O_3, mineral dust also typically contains various photoactive semiconductor metal oxides, such as TiO_2, ZnO and Fe_2O_3. The interaction of solar radiation with semiconductor metal oxides will likely initiate a number of photochemical processes, which could potentially alter the dark reaction mechanism, overall reaction kinetics, and final product partitioning for reactions involving trace atmospheric gases with these components of mineral dust aerosol.

In addition to aerosols, various surfaces in contact with the atmosphere potentially play a role in affecting the chemical balance of the atmosphere. A representative example is TiO_2 coating surface, which have been widely applied for building exteriors, cover glass for road lamps, airport roofs, and road bricks. The main reason for this is that TiO_2 coated surface can decompose organic pollutants adhering to the surface and maintain itself clean while exposure to irradiation.[149, 150] With the ongoing and continuous development of industry, the application of metal-containing coatings will continue to grow and expand, bringing more surface available for heterogeneous photoreactions of atmospheric trace gases.

In fact a photoenhancement of ozone uptake on TiO_2 has been reported in a recent study, which investigated ozone decomposition on TiO_2/SiO_2 mixtures.[148] The uptake coefficients under irradiation increased with increasing TiO_2 mass fraction in the mixtures, and the corresponding uptake coefficient based on the geometric surface ranged from 3×10^{-6} to 3×10^{-5}. They also observed a reduced ozone loss at relative humidity above 30%.

The current study involves employing an environmental aerosol chamber that incorporates a solar simulator to investigate the photo-induced decomposition of ozone on different mineral dust components, including three semiconductor metal oxides, TiO_2, α-FeOOH and α-Fe_2O_3, as well as an insulator oxide, α-Al_2O_3. In order to quantitatively assess the impact of irradiation and relative humidity on ozone decomposition, a box model using the Kinetic PreProcessor[151] (KPP) was developed to simulate reactions in the

environmental aerosol chamber. Using these model results, uptake capacities of ozone on the relevant oxides under dark and irradiated conditions are compared. The potential influence of solar radiation on the heterogeneous reactions of mineral dust with tropospheric ozone is discussed.

4.3 Experimental Methods

4.3.1 Experimental Apparatus and Procedures

The experimental apparatus and protocol have been described in detail in Chapter 2. Ozone is produced by flowing oxygen (Air products, USP grade) through an electric discharge generator (OREC, Model O3V5-O). In a typical experiment, dry air was flowed through the chamber overnight to achieve a clean and dry state. The chamber was evacuated to a base pressure (e.g. 680 Torr), back-filled with a nominal concentration of ozone, and finally brought up to near atmospheric pressure with purge gas air at a nominal RH. The ozone/air mixture was allowed to sit under dark conditions for approximately one hour for passivation and quantification of wall losses. A weighed amount of oxide powder sample was introduced into the chamber, as described above, to initiate the heterogeneous reactions with ozone. The powder was held under vacuum for several hours prior to introduction to remove residual water. For photochemical experiments, the solar simulator was turned on for 100 minutes prior to aerosol introduction to further quantify wall losses and to characterize any homogeneous photochemical pathways. The ozone mixing ratios, as well as RH, temperature and pressure of the chamber, were monitored throughout the entire experiment.

The partial pressure of water vapor, and hence the relative humidity, was determined using a Beer's law calibration. The ozone partial pressure was quantified from the peak IR absorbance at 1055 cm^{-1} using a previously reported cross-section.[152, 153] Commercially available hematite (α-Fe_2O_3; Aldrich), goethite (α-FeOOH; Alfa Aesar),

titanium oxide (TiO_2; Degussa) and aluminum oxide (α-Al_2O_3; Alfa Aesar) were used as received. The specific surface areas of the oxide samples were measured by BET analysis (Quantachrome Nova 4200) and the mineralogy was confirmed by powder X-ray diffraction. The source and relevant physical properties for each oxide sample are tabulated in Table 4.1. The mass loadings of the various oxide samples were adjusted to take into account the respective BET surface areas and make the total available surface area in each experiment roughly equivalent to 8 m^2.

Table 4.1 Commercial Sources and Physical Properties of the Oxide Powder Samples Used in the Current Study

Oxide	Source	Size (nm)	Surface Area (m^2 g^{-1})	Band Gap E_g (eV)	Threshold Wavelength λ_0 (nm)
α-Fe_2O_3	Aldrich	690 ± 150	2.8 ± 0.1	2.2	570
α-FeOOH	Alfa Aesar	L:490 ± 265 W: 67 ± 22	14.6 ± 0.2	2.2	570
TiO_2	Degussa	24 ± 6	51.2 ± 0.2	3.0	420
α-Al_2O_3	Alfa Aesar	260 ± 90	8.4 ± 0.1	9.0	138

4.3.2 Kinetic Analysis

Given that there is overlap between the absorption spectrum of ozone with the irradiance spectrum of the solar simulator as discussed below, observed decay of ozone in the presence of light involves two competing processes: heterogeneous decomposition and homogeneous photolysis. A computational model is therefore essential to differentiate ozone decay induced by heterogeneous decomposition from homogeneous photolysis and obtain the kinetic information of ozone loss on particle surfaces.

Reactions in the environmental aerosol chamber were simulated using a box model built with the Kinetic PreProcessor (KPP V2.1), where ordinary differential equations are integrated with a Rosenbrock solver.[151] The Kinetic PreProcessor (KPP) is a software package that generates computer-friendly versions of chemical mechanism for efficient integration (kpp file) and currently is used by many academic, research, and industry groups.[151] To create a KPP model, several input files in KPP language are needed, including an equation file to define the chemical mechanism with rate constants (with suffix .eqn), a species file to definite the component of each species involved (with suffix . spc), and a initiative file to define the initial concentrations, temperature, and timescale (with suffix .def). In addition, a KPP input file (with suffix .KPP) is also needed to specify the model, the target language, the precision, the integrator and the driver, etc. All of the four files in KPP language are given in the Appendix B. Homogeneous gas reaction mechanisms and the corresponding rate constants were taken from published sources.[127] The gas-phase mechanism involves 12 species and 26 reactions as tabulated in Table 4.2. Three photolytic pathways were considered,

$$H_2O_2 + h\nu \xrightarrow{j_{H_2O_2}} 2OH \quad (4\text{-}1)$$

$$O_3 + h\nu\,(\lambda < 310\ nm) \xrightarrow{j_{O_3,1}} O(^1D) + O_2 \quad (4\text{-}2)$$

$$O_3 + h\nu\,(\lambda > 310\ nm) \xrightarrow{j_{O_3,2}} O(^3P) + O_2 \quad (4\text{-}3)$$

The photolysis rate constants of H_2O_2 and O_3 were calculated using irradiance measurements of the solar simulator. Determination of the simulator irradiance has been reported in Chapter 2. The irradiance averaged over the diameter of the simulator beam is approximately 1.2 of air mass one (AM1) (an average of 1.1 kW m^{-2}), which is close to the irradiance at the top of the Earth's atmosphere. The absolute spectral irradiance from the solar simulator, as well as the adsorption cross-sections for gas phase O_3 and H_2O_2 are

plotted in Figure 4.1. The spectral actinic flux, *I(λ),* was calculated from the irradiance data according to the following equation,[1]

$$I(\lambda) = \frac{E(\lambda)}{E_{photon}(\lambda)} \tag{4-4}$$

where $I(\lambda)$ is expressed as photons cm^{-2} s^{-1} nm^{-1}, $E(\lambda)$ is the spectral irradiance in W cm^{-2} nm^{-1}, and $E_{photon}(\lambda)$ is the photon energy in J $photon^{-1}$. The resultant spectral actinic flux was used to determine the photolysis rate constants as follows,[1]

$$j_a = \int_{\lambda_1}^{\lambda_2} \sigma_a(\lambda) \cdot \Phi_a(\lambda) \cdot I(\lambda) d\lambda \tag{4-5}$$

where $\sigma_a(\lambda)$ is the absorption cross-section in cm^2 and $\Phi_a(\lambda)$ is the dimensionless quantum yield. The wavelength dependent absorption cross-sections and quantum yields for O_3 and H_2O_2 were also taken from previous published sources.[127] The photolysis rate constants were set to zero for simulations of dark reactions.

Ozone loss in the chamber involved homogeneous photochemical pathways, as well as heterogeneous decomposition on the chamber walls and, when present, the surface of the relevant oxides. The heterogeneous reactions were modeled as pseudo first-order kinetic processes,

$$O_3 + \text{wall} \xrightarrow{k_{wall}} 1.5O_2 + \text{wall} \tag{4-6}$$

$$O_3 + S \xrightarrow{k_s} 1.5O_2 + S \tag{4-7}$$

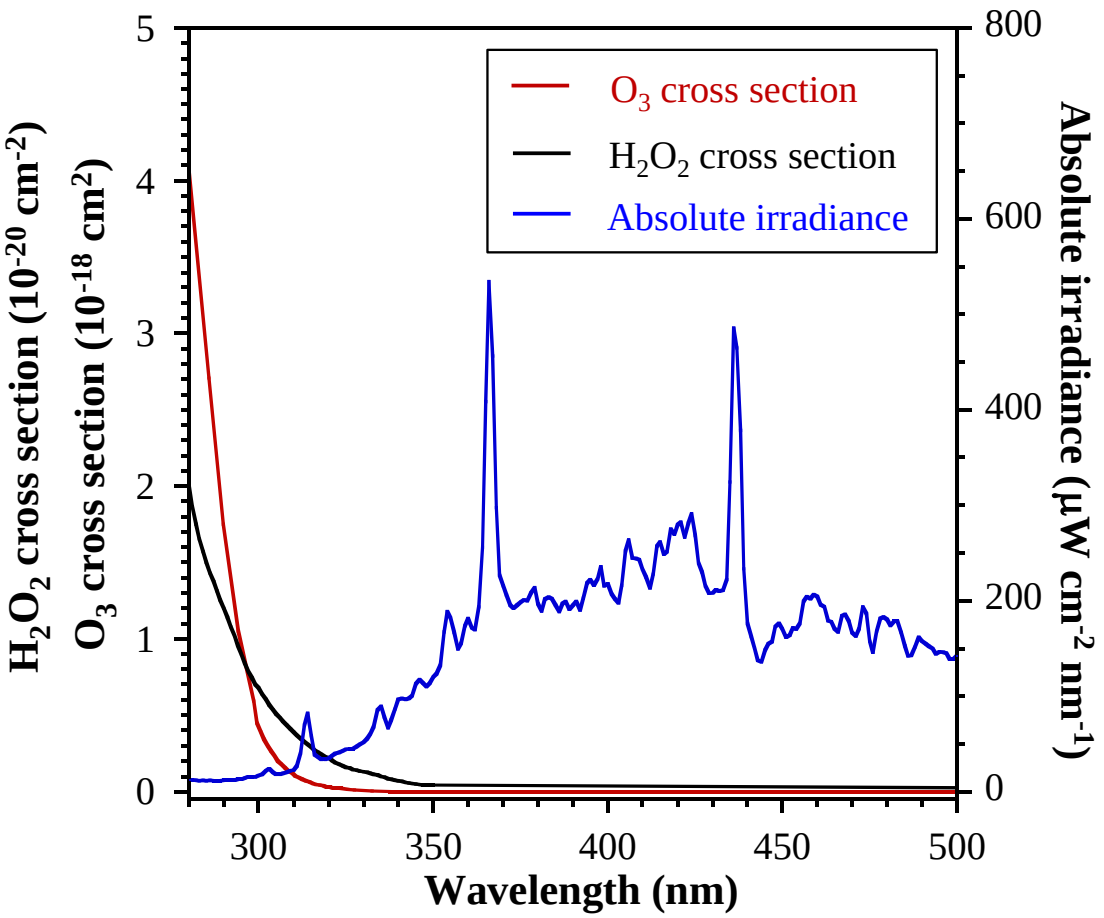

Figure 4.1 Solar simulator spectral irradiance (blue line) at the bottom of the environmental aerosol chamber compared to the absorption cross section of ozone (red line) and hydrogen peroxide (black line).

Table 4.2 Reactions and Their Corresponding Rate Constants Used in the KPP Modeling Simulation of Heterogeneous Photoreaction of Ozone with Oxides[127]

No.	Reaction	Rate Constant at 298 K (cm^3 $molecule^{-1}$ s^{-1})
1	$H_2O_2 \rightarrow 2HO$	1.1675×10^{-5}
2	$O_3 \rightarrow 0.6253O(^1D) + 0.3747O(^3P) + O_2$	1.106×10^{-3}
3	$O_3 + wall \rightarrow 1.5O_2 + wall$	-[a]
4	$O_3 + S \rightarrow 1.5O_2 + S$	-
5	$O(^3P) + O_2 + O_2 \rightarrow O_3 + O_2$	6.10×10^{-34}
6	$O(^3P) + O_2 + N_2 \rightarrow O_3 + N_2$	6.10×10^{-34}
7	$O(^3P) + O_3 \rightarrow 2O_2$	8.0×10^{-15}
8	$O(^1D) + O_2 \rightarrow O(^3P) + O_2$	3.95×10^{-11}
9	$O(^1D) + N_2 \rightarrow O(^3P) + N_2$	3.1×10^{-11}
10	$O(^1D) + O_3 \rightarrow O(^3P) + 1.5O_2$	2.40×10^{-10}
11	$H + HO_2 \rightarrow 1.788HO + 0.086H_2 + 0.086O_2 + 0.02H_2O + 0.02O(^3P)$	8.05×10^{-11}
12	$H + O_2 \xrightarrow{M} HO_2$	FALL(4.4E-32, 0E0, -1.3E0, 4.7E-11, 0, -0.2E0, 0.6E0)[b]
13	$O(^3P) + HO \rightarrow O_2 + H$	3.30×10^{-11}
14	$O(^3P) + HO_2 \rightarrow O_2 + HO$	5.90×10^{-11}
15	$O(^3P) + H_2O_2 \rightarrow HO_2 + HO$	1.70×10^{-15}
16	$O(^1D) + H_2 \rightarrow HO + H$	1.10×10^{-10}
17	$O(^1D) + H_2O \rightarrow 2HO$	2.00×10^{-10}
18	$HO + H_2 \rightarrow H_2O + H$	6.70×10^{-15}

19	$HO + HO \rightarrow H_2O + O(^3P)$	1.80×10^{-12}
20	$HO + HO \longrightarrow H_2O_2$	FALL(6.9E-31, 0E0, -1E0, 2.6E-11, 0, 0, 0.6E0)
21	$HO + HO_2 \rightarrow H_2O + O_2$	1.10×10^{-10}
22	$HO + H_2O_2 \rightarrow H_2O + HO$	1.80×10^{-12}
23	$HO + O_3 \rightarrow HO_2 + O$	7.30×10^{-14}
24	$HO_2 + HO_2 \rightarrow H_2O_2 + O_2$	1.50×10^{-12}
25	$HO_2 + HO_2 + O_2 \rightarrow H_2O_2 + O_2 + O_2$	4.90×10^{-32}
26	$HO_2 + HO_2 + N_2 \rightarrow H_2O_2 + O_2 + N_2$	4.90×10^{-32}
27	$HO_2 + O_3 \rightarrow HO + 2O_2$	1.90×10^{-15}
28	$H + O_3 \rightarrow HO + O_2$	2.90×10^{-11}
29	$O(^1D) + N_2 + O_2 \rightarrow N_2O + O_2$	2.82×10^{-36}
30	$O(^1D) + N_2 + N_2 \rightarrow N_2O + N_2$	2.82×10^{-36}

[a] See text for the determination of rate constants for wall losses and surface reactions;

[b] The definition of rate constants for termolecular reactions in the KPP model.

where S represents an surface active site, and k_{wall} and k_s are pseudo first-order rate constants for wall loss and oxide uptake, respectively. The wall loss constant, k_{wall}, was determined by fitting the observed ozone decay during the initial, one hour, dark passivation period (*vide supra*). The rate constants for the heterogeneous uptake on the various oxides, k_s, were extracted using the kinetic model, adjusting the value of k_s to best fit the measured ozone decay data in the presence of mineral dust. For simulation of reactions in the absence of aerosol, the k_s value was set to zero. The full reaction set used in the modeling is listed in Table 4.2.

The discrepancy between laboratory measurements and modeling calculations was defined as,

$$q = \frac{\sqrt{\sum_n (C_n - \overline{C_n})^2}}{n} \tag{4-8}$$

where C_n is the ozone concentration at each time point of the initial two hours determined by laboratory measurement, and $\overline{C_n}$ is the ozone concentrations at the corresponding time point obtained from KPP modeling calculation. The uptake rate constant, k_s, was evaluated by numerical iteration until q < 10^{14} molecule cm^{-3}, a detection limit of FTIR in the current study. The change of rate constant to get a q value around 2×10^{14} molecule cm^{-3} represents as the error of the rate constant.

Initial concentrations of O_3 and H_2O serving as model inputs were obtained from the experimental data. Initial concentrations of N_2 and O_2 were assumed to reflect atmospheric abundances. A temperature of 298 K was used in the kinetic simulation.

4.4 Results

4.4.1 Ozone Decomposition on Oxide Particle Surfaces

For all of the ozone uptake experiments, the FTIR data showed no evidence for the growth of new spectral features, indicating that any possible gaseous products are either IR inactive or formed in very low concentration. Figure 4.2 displays a comparison of ozone decay on oxides at <2% RH under dark and irradiated conditions. Under dark and dry (<2% RH) conditions, the ozone concentration exhibited a small decay prior to particle introduction on the timescale of the experiment due to wall losses. Subsequent irradiation enhances ozone loss. It is well established that ozone can photodissociate to yield ground and excited state oxygen atom products (equations (4-2) and (4-3)). The

oxygen atom generally quickly reforms O_3 in a three-body association reaction with O_2, but a small fraction of O atoms may be lost via wall collisions, leading to the enhanced ozone decay.

Rapid decay of ozone after the introduction of the hematite sample was observed, which is in accordance with our previous results.[42, 154] Hematite exhibits significant uptake capacity for ozone under both dark and irradiated conditions, irradiation slightly enhances the rate of ozone uptake (Figure 4.2a). In contrast, goethite shows a rapid ozone uptake in the dark but a slower uptake under irradiation conditions, indicating that light unexpectedly inhibits ozone loss on goethite surfaces (Figure 4.2b). Titanium oxide only shows ozone uptake upon irradiation (Figure 4.2c). The loss of ozone on aluminum oxide, the only insulator studied, is found to be negligible under both dark and irradiated conditions (Figure 4.2d).

Given the importance of water in atmospheric chemistry,[155] experiments to assess the effect of relative humidity on the ozone uptake process were also completed. Overall, the data showed clearly that relative humidity has a profound influence on ozone decay in the environmental aerosol chamber. The electronically excited oxygen atom produced in equation (4-2) can react with water to form hydroxyl radicals[1]

$$O(^1D) + H_2O \rightarrow 2OH \qquad (4\text{-}9)$$

enhancing ozone loss by competing with recombination with O_2. In addition, water can also adsorb onto the oxide surface, generally resulting in an inhibition of ozone uptake due to competition for active surface sites.[42] Given the complex interaction of water with reactive gas phase species (e.g. equation (4-9)) and through adsorption and reaction on oxide surfaces in the environmental aerosol chamber, it is necessary to incorporate a

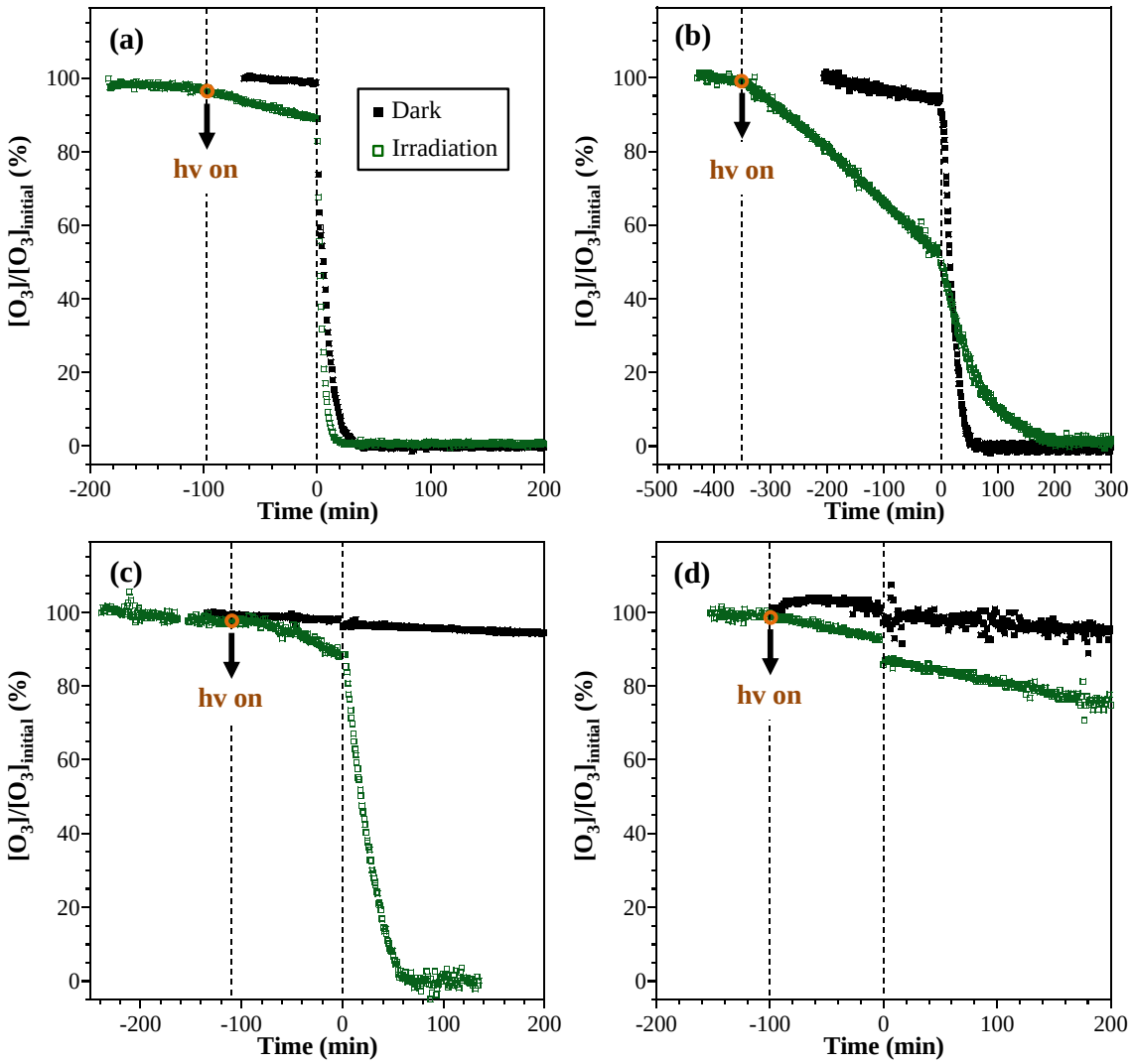

Figure 4.2 Ozone decay on oxides in the environmental aerosol chamber under dry, <2% RH, conditions for both dark and irradiation experiments: (a) α-Fe_2O_3, (b) α-FeOOH, (c) TiO_2 and (d) α-Al_2O_3. Aerosol introduction into the chamber occurred at time, t = 0 min. The effect of irradiation on the ozone uptake depends on the nature of the specific

kinetic model in data analysis to extract detailed kinetic information concerning the influence of oxide surfaces and radiation on ozone decay.

4.4.2 Kinetic Analysis

Control cases, consisting of ozone decay measurements in the presence of irradiation and RH but in the absence of aerosol, are first compared to simulations from the KPP model as a check of model accuracy. Comparisons between the laboratory data and model results for an experiment at 18% and 30% RH are plotted in Figure 4.3, displaying a good fit of the data, especially during the first 150 minutes. At longer reaction times, the modeling results deviate slightly from the laboratory data at both 18% and 30% RH, overestimating the ozone decay.

A first-order rate constant for the heterogeneous reaction of ozone with the oxide surface was then inputted into the kinetics model and adjusted to best fit the experimental data obtained in the presence of a dust sample. Figure 4.4 and Figure 4.5 displays the comparison between laboratory and model results for ozone decay with α-Fe_2O_3 and TiO_2 aerosol under a variety of conditions, respectively. In all cases, the model calculations agree well with the laboratory measurements throughout the entire time course of the experiments. The other oxide samples explored in this study similarly exhibited a good fit (not shown here). The resultant surface rate constants, k_s, obtained from the model calculations under various conditions are summarized in Table 4.3. Also shown in the table are uptake coefficients, γ, normalized to the specific surface areas. The heterogeneous uptake coefficient, which is defined as the fraction of gas-surface collisions that lead to gas loss, is determined from[42]

$$\gamma = \frac{4k_s}{\bar{c}S_{BET}[C_{mass}]} \qquad (4\text{-}10)$$

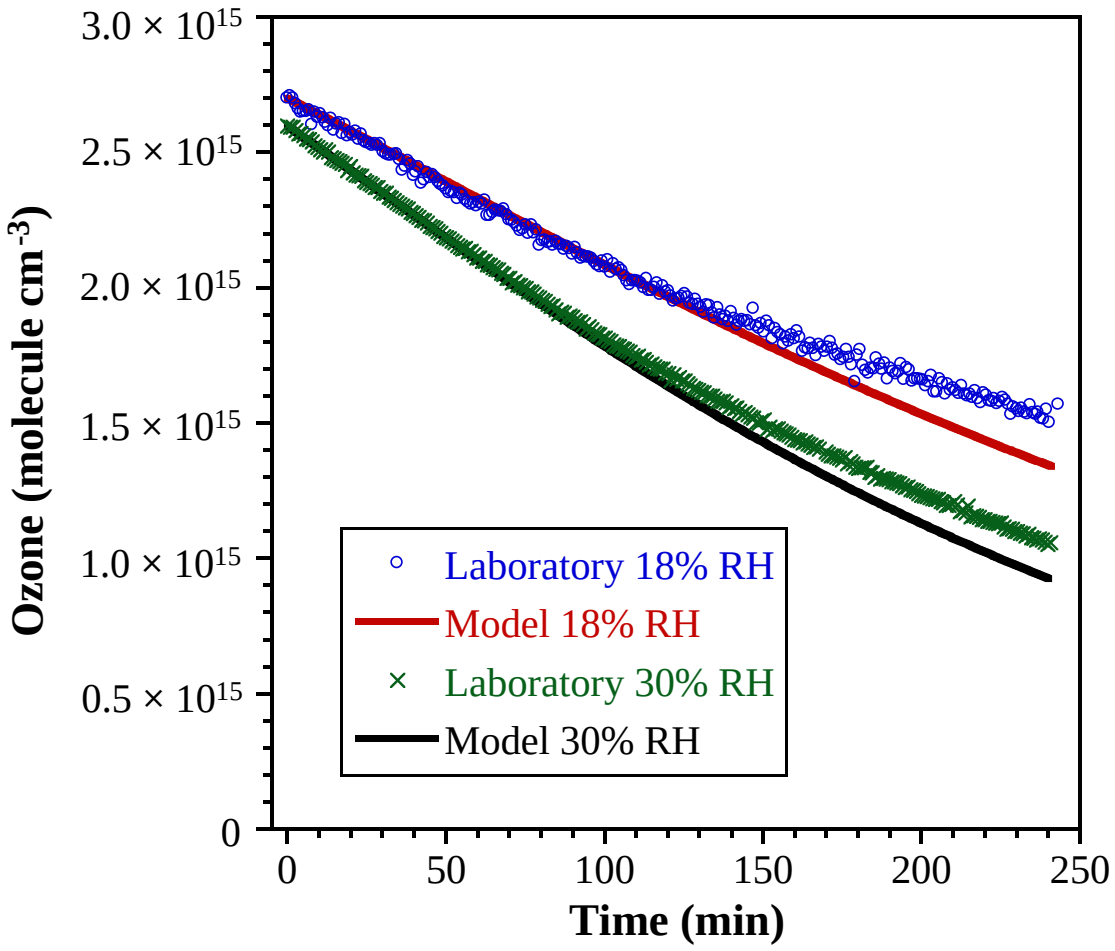

Figure 4.3 Comparison of ozone decay obtained from laboratory measurements and model calculations at 18% RH and 30% RH in the absence of oxides. Open symbols represent the experimental data, while the solid line depicts the results of the model calculation.

where $\bar{c}$ is the mean speed of ozone in m s^{-1}, S_{BET} is the specific surface area of the oxide in m^2 g^{-1}, and C_{mass} is the mass concentration of the oxide sample in the chamber in g m^{-3}.

As shown in Table 4.3, the measured uptake coefficients vary according to the oxide, the presence or absence of irradiation, and the RH level. These differences are discussed further, below. Dark uptake coefficients obtained from model calculations in the current study are in good agreement with the results of our previous study,[42] providing additional confidence in the integrity of the model employed.

4.5 Discussions

4.5.1 Comparison of Ozone Decomposition on Different Oxides under Dry Conditions

The uptake of ozone on oxide surfaces under dark conditions has been well studied.[42, 43, 116, 143, 144, 146-148, 156, 157] The reaction is postulated to proceed according to the following scheme,[156, 158]

$$O_3 + S \rightarrow O_2 + O - S \quad (4\text{-}11)$$

$$O_3 + O - S \rightarrow O_2 + O_2 - S \quad (4\text{-}12)$$

$$O_2 - S \rightarrow O_2 + S \quad (4\text{-}13)$$

$$O - S + O - S \rightarrow O_2 + 2S \quad (4\text{-}14)$$

where S represents an active site and S-O and S-O_2 are surface-bound oxide species. The formation of surface-bound oxide species has been previously reported.[156, 157, 159] The uptake of ozone on an active site to produce a surface-bound oxygen atom and a gaseous oxygen molecule (equation (4-11)) is fast relative to the subsequent rate-limiting

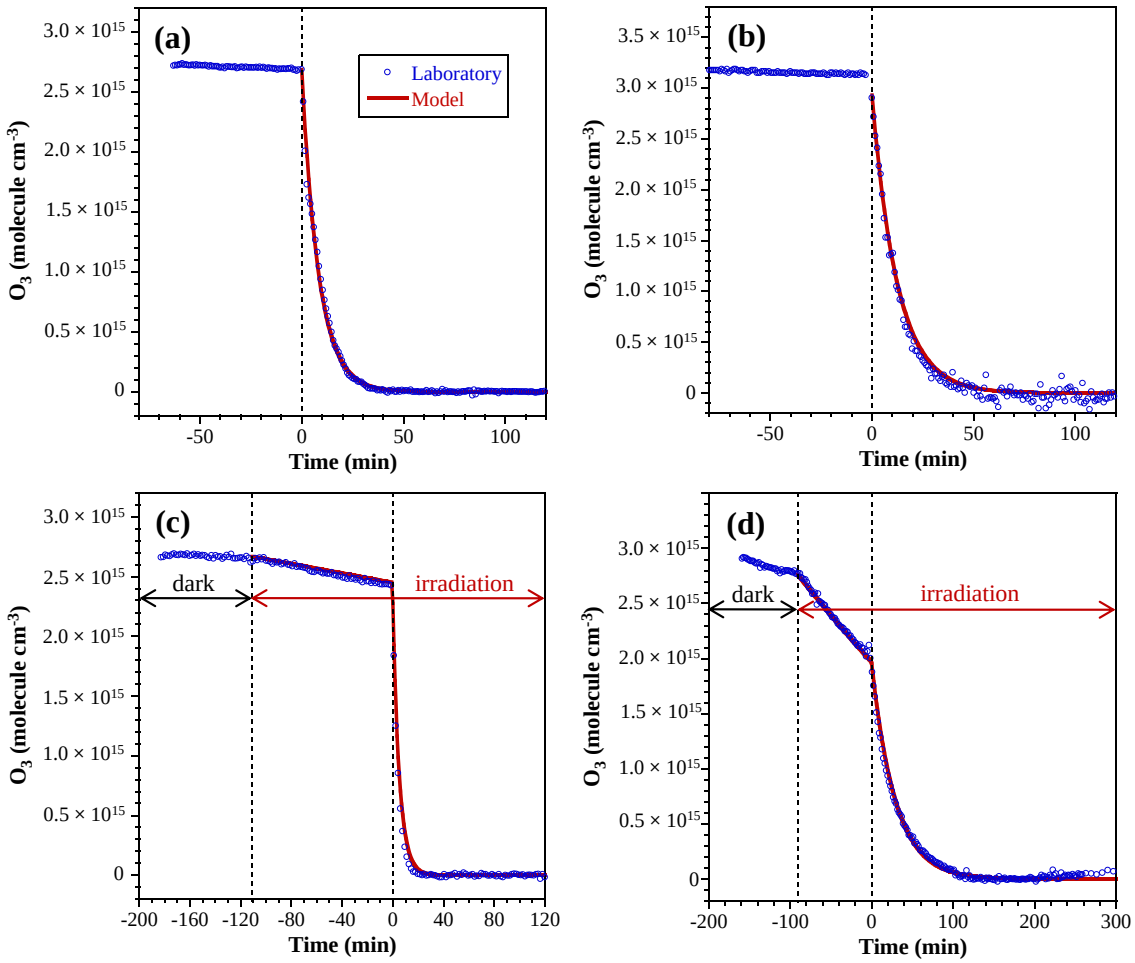

Figure 4.4 Comparison of ozone decay obtained from laboratory measurements and model calculations in the presence of α-Fe_2O_3 under a variety of conditions: (a) dark and dry, <2% RH, (b) dark and 21% RH, (c) irradiated and dry,<2% RH, and (c) irradiated and 25% RH. Open symbols represent the experimental data, while the solid line depicts the results of the model calculation. Aerosol introduction into the chamber occurred at time, t = 0 min.

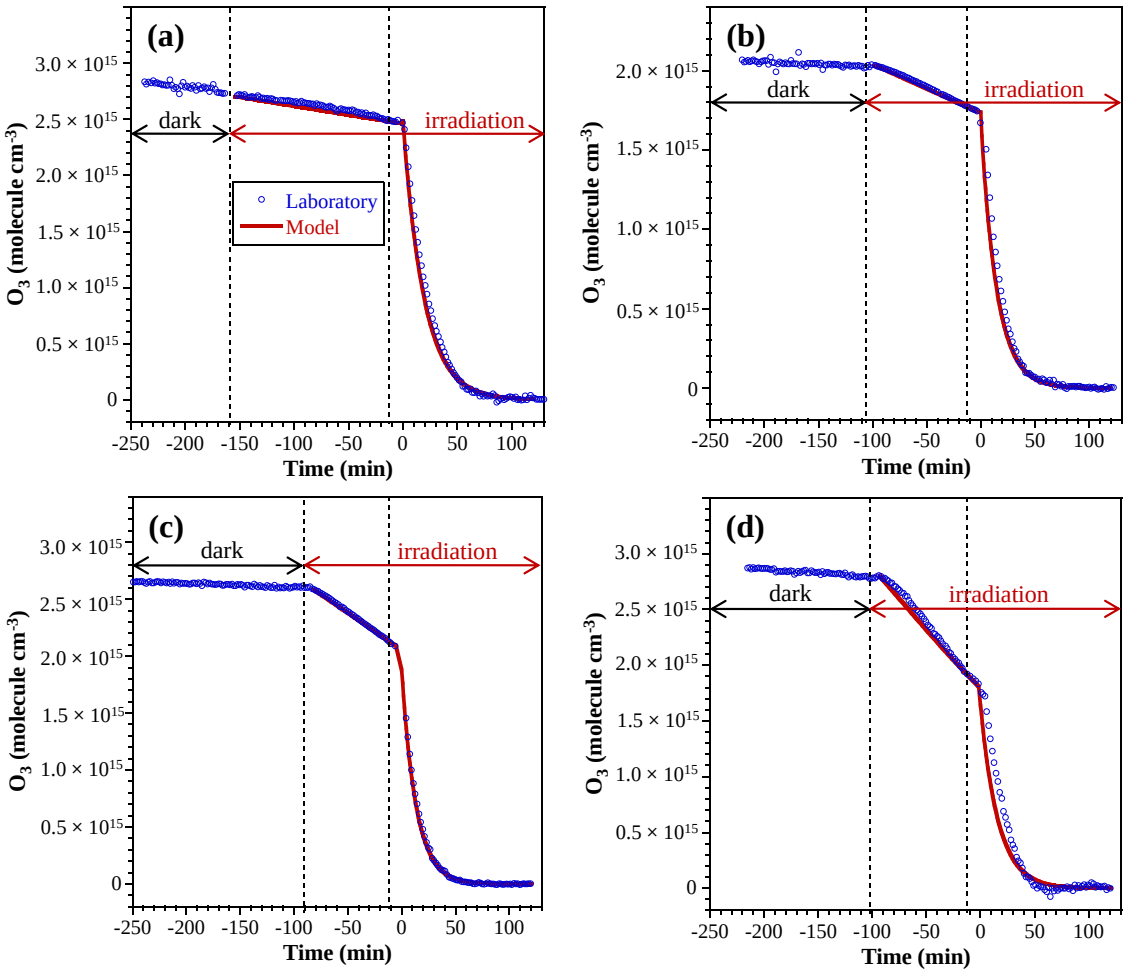

Figure 4.5 Comparison of ozone decay obtained from laboratory measurements and model calculations in the presence of TiO_2 under a variety of conditions: (a) irradiated and dry, <2% RH, (b) irradiated and 12% RH, (c) irradiated and 22% RH, and (c) irradiated and 39% RH. Open symbols represent the experimental data, while the solid line depicts the results of the model calculation. Aerosol introduction into the chamber occurred at time, t = 0 min.

Table 4.3 Surface Rate Constants and Uptake Coefficients for Ozone Uptake on Oxides Under a Variety of Conditions (%RH and Light)[a]

Oxide		RH (%)	Rate Constant (s^{-1})	Uptake Coefficient
α-Fe_2O_3	dark	<2	$(20 \pm 1) \times 10^{-4}$	$(4.1 \pm 0.2) \times 10^{-7}$
		21	$(13 \pm 1) \times 10^{-4}$	$(2.7 \pm 0.1) \times 10^{-7}$
	irradiation	<2	$(32 \pm 2) \times 10^{-4}$	$(6.6 \pm 0.3) \times 10^{-7}$
		12	$(27 \pm 1) \times 10^{-4}$	$(5.5 \pm 0.3) \times 10^{-7}$
		25	$(5.2 \pm 0.5) \times 10^{-4}$	$(1.1 \pm 0.1) \times 10^{-7}$
α-FeOOH	dark	<2	$(8.0 \pm 0.5) \times 10^{-4}$	$(1.6 \pm 0.1) \times 10^{-7}$
		18	-[b]	-
	irradiation	<2	$(2.3 \pm 0.5) \times 10^{-4}$	$(4.7 \pm 0.2) \times 10^{-8}$
		23	-	-
TiO_2	dark	<2	-	-
	irradiation	<2	$(9.8 \pm 0.5) \times 10^{-4}$	$(2.0 \pm 0.1) \times 10^{-7}$
		12	$(11 \pm 1) \times 10^{-4}$	$(2.2 \pm 0.1) \times 10^{-7}$
		22	$(12 \pm 1) \times 10^{-4}$	$(2.4 \pm 0.1) \times 10^{-7}$
		39	$(9.5 \pm 0.5) \times 10^{-4}$	$(1.9 \pm 0.1) \times 10^{-7}$
α-Al_2O_3	dark	<2	-	-
		19	-	-
	irradiation	<2	-	-
		21	-	-

[a] Errors in the reported rate constants and uptake coefficients are obtained from an error analysis of the KPP model;

[b] Indicates no significant uptake capability.

reactions. The regeneration of active sites via equations (4-13) and (4-14) makes the overall surface reaction catalytic. When the regeneration steps are much slower or otherwise inhibited on the timescale of the experiment, the oxide can exhibit surface saturation upon ozone exposure.

In the current study, aluminum oxide exhibits little or no uptake capacity for ozone under either dark or irradiated conditions (Figure 4.2d) and the surface becomes rapidly saturated. Similar behavior was observed for TiO_2 in the dark (Figure 4.2c). Both α-Al_2O_3 and TiO_2 have Lewis acid surface sites, which are proposed to be the most important active site for ozone decomposition.[159-161] The relatively large Lewis acid strength of sites on α-Al_2O_3 and TiO_2 may initially decompose ozone very efficiently via equation (4-11), but the resultant strong surface-oxygen bond may inhibit the subsequent surface site regeneration steps through dissociation and recombination, equations (4-13) and (4-14), respectively. Thus, these oxides might be expected to exhibit surface saturation.

In contrast to α-Al_2O_3 and TiO_2, the α-Fe_2O_3 and α-FeOOH surfaces are regarded to have weaker acid sites.[162] The consequently weaker surface-oxygen bonds formed upon ozone exposure may be more likely to facilitate dissociation and recombination, making the overall reaction catalytic. In addition, α-Fe_2O_3 exhibits a slightly larger uptake coefficient compared to α-FeOOH, which might be due to a faster regeneration of active sites on the experimental time scale.

The presence of irradiation significantly enhances ozone uptake on both α-Fe_2O_3 and TiO_2 surfaces under dry conditions, most likely due to their semiconductor nature. The uptake coefficient for α-Fe_2O_3 increases by approximately 60% in the presence of light. In the case of TiO_2, the ozone uptake is minimal under dark conditions but the uptake capacity increases greatly upon irradiation. The band gaps for bulk α-Fe_2O_3 and TiO_2 are 2.2 and 3.0 eV, corresponding to wavelength limits of 570 and 420 nm, respectively (Table 4.1).[163] The band gap energies are below the short-wavelength cutoff

of the solar simulator used in this study, representative of the solar actinic flux in the troposphere. Solar radiation of α-Fe_2O_3 and TiO_2 can, therefore, initiate photocatalytic processes, which enhance ozone decomposition. It is generally believed that semiconductor reactions proceed either through indirect reaction with photogenerated oxidizing or reducing chemical species, or direct reaction with the initially generated electron-hole pair.[164]

Indeed, hematite and titanium oxide are considered to be efficient photocatalysts for various redox reactions. Their photochemical activity has been extensively explored.[148, 165-169] For example, Toledano and Henrish[166] observed enhanced chemisorption of SO_2 onto single crystal Fe_2O_3(0001) subject to UV irradiation. The creation of a highly reactive transient Fe^{2+} cation by UV irradiation was proposed to be responsible for the enhanced adsorption. Ozone photodecomposition on dust samples prepared with trace TiO_2 in a matrix of SiO_2 was reported by Nicolas et al.[148] who observed an increase in the ozone uptake with an increase in the TiO_2 mass fraction. The photochemical reaction mechanism involving semiconductor TiO_2 is postulated to be,[148, 170]

$$TiO_2 + h\nu \rightarrow TiO_2\,(e^- + h^+) \quad (4\text{-}15)$$

$$O_3 + e^- \rightarrow O_3^- \quad (4\text{-}16)$$

$$O_2 + e^- \rightarrow O_2^- \quad (4\text{-}17)$$

$$O_2^- + O_3 \rightarrow O_3^- + O_2 \quad (4\text{-}18)$$

Ozone can be directly reduced by a photogenerated electron in equation (4-16), or indirectly through equations (4-17) and (4-18). The resultant ozonide anion radical can rapidly decompose to form molecular oxygen, O_2.

Irradiation of certain metal oxides opens the possibility for different reaction pathways compared to dark conditions. In the case of TiO_2, only light-induced ozone uptake is observed. In hematite, uptake of ozone occurs under both light and dark conditions although at different rates. A simple kinetic analysis of the ozone uptake on hematite is possible. It is assumed that the dark and irradiation uptake pathways occur in parallel and that the dark reaction is not affected by the presence of light. Since uptake coefficients were referenced to the same surface area, the light-induced ozone uptake coefficient is then calculated by subtracting the dark uptake coefficient from the uptake coefficient obtained under irradiation conditions. The resultant light-induced uptake coefficient for α-Fe_2O_3 is 2.5 ($\pm$ 0.5) $\times 10^{-7}$, which is slightly larger than that measured directly for TiO_2, 2.0 ($\pm$ 0.1) $\times 10^{-7}$. Previous studies of photocatalytic efficiency generally suggest that TiO_2 exhibits a higher efficiency towards the photodegradation of organic compounds than α-Fe_2O_3.[168, 171] The larger uptake coefficient for α-Fe_2O_3 observed in the current study can be partially rationalized by the larger number of photons available for absorption. As discussed above, hematite has a smaller band gap than that of TiO_2. Given the broadband irradiance provided by the solar simulator, there are more available photons to promote photocatalysis in α-Fe_2O_3 samples, perhaps yielding an efficiency for ozone photodecomposition that is at least as large as in TiO_2.

In contrast to the semiconductor metal oxides, the insulator oxide α-Al_2O_3 has a band gap of 9.0 eV (or 138 nm), obviously much larger than the cutoff of the solar simulator. Irradiation of α-Al_2O_3 has no discernible effect on the ozone uptake capacity in the experimental system used here, indicating the key role played by the semiconducting nature of the oxide samples.

Interestingly, the rate of ozone decomposition on α-FeOOH is unexpectedly lower under irradiation compared with reaction in the dark. Previous work has found smaller, but observable, photoactivity for α-FeOOH samples.[172, 173] It is possible that increased water adsorption on α-FeOOH suppresses its reactivity. Compared to hematite, goethite

has larger density number of surface hydroxyl groups, making its surface highly hydrophilic. Given the rise of wall temperature under irradiation, water desorbed from the walls and partitioning to the aerosol surface can effectively block surface active sites, suppressing its uptake capacity for ozone. The effect of water adsorption on ozone uptake is discussed in more detail below.

4.5.2 Effect of Relative Humidity on the Kinetics of Ozone Decomposition on Oxide Surfaces

Since water can adsorb strongly onto oxide surfaces, preferential adsorption of water at elevated RH levels can block active sites that would otherwise bind ozone, leading to an overall decrease in the ozone decay rate. Thus, consistent with a previous work,[42] it was observed an inhibition of the ozone uptake on α-Fe_2O_3 when the RH was increased under dark conditions (Table 4.3). The uptake coefficient at 21% RH decreased by approximately 30% compared to that under dry conditions. As the RH increases beyond 20%, multilayer water coverage can form on α-Fe_2O_3.[42, 174] The hematite sample does retain catalytic activity towards ozone decomposition and all O_3 in the chamber is eventually consumed, albeit at a slower rate than under dry conditions. This observation is not entirely consistent with a simple site-blocking argument, which would predict a significant decrease in ozone uptake once a water monolayer forms and all available surface sites are occupied by water.[42]

It is possible that water adsorption on α-Fe_2O_3 is not uniformly distributed and that water clusters form on the surface. This would leave some free surface area, and unblocked active sites, to react catalytically with ozone but with a reduced rate. An uneven distribution of adsorbed water on oxide surfaces has been reported in previous studies.[48, 175-177] A study of water adsorption on α-Al_2O_3 and SiO_2 using sum frequency generation spectroscopy, a surface specific technique for probing interfacial properties at the molecular level, suggested that isolated hydroxyl groups exist on the surface even at

relatively high RH levels.[175] Water uptake on another oxide, MgO, was also found to be non-uniform, proceeding through the formation of three-dimensional islands prior to coalescence and eventual surface saturation.[177] Another possible explanation is that water does not block all of the active surface sites on α-Fe_2O_3, perhaps leaving available less reactive sites, resulting ozone decomposition at a lower rate.

The inhibition of ozone uptake by water adsorption was much more significant on the α-FeOOH sample. It was observed a complete suppression, within the limits of detection of the apparatus, of ozone uptake at ≈ 20% RH. Given the greater tendency for water to adsorb onto the hydrophilic surface of α-FeOOH, it is likely that multilayer adsorption occurs at higher RH. If the resultant water layer is highly polarized and structured, perhaps even rigid, it may be that diffusion of ozone through the layer is slowed and that decomposition becomes negligible on the current experimental timescale. Finally, it may be that the active sites on the α-FeOOH surface are fundamentally different than on the other metal oxides and more easily deactivated by water adsorption.

The role of adsorbed water is complex on illuminated α-Fe_2O_3 and TiO_2 surfaces. In the case of hematite, irradiation actually decreases the uptake coefficient compared to dark conditions at similar RH levels. The overall uptake coefficient at 25% RH is, 1.1 ($\pm$ 0.1) $\times 10^{-7}$, in the irradiation experiment but is 2.7 ($\pm$ 0.1) $\times 10^{-7}$ under dark conditions at a similar RH, 21%. One hypothesis to interpret this behavior is that irradiation produces surfaces defects that can then become hydroxylated by water dissociation, forming a hydrophilic surface that enhances the affinity for water uptake.[178-180]

The photoactivity of illuminated TiO_2 exhibits a non-monotonic response to changes in RH. Initially, increasing the RH results in a faster ozone decay as the uptake coefficient increases from 2.0 ($\pm$ 0.1) $\times 10^{-7}$ at <2% RH to 2.4 ($\pm$ 0.1) $\times 10^{-7}$ at 22% RH. However, further increases in the RH yield a decreased uptake coefficient, manifesting a value 1.9 ($\pm$ 0.1) $\times 10^{-7}$ at 39% RH. Similar behavior has been reported in a previous study of TiO_2 photocatalytic activity.[148, 181, 182] It has been suggested that the ozonide

radical formed in equations (4-16) and (4-18) can rapidly reacted with water through the reactions,[178-180, 183]

$$O_3^- + H^+ \rightarrow HO_3 \quad (4\text{-}19)$$

$$HO_3 \rightarrow O_2 + OH \quad (4\text{-}20)$$

$$OH + O_3 \rightarrow O_2 + HO_2 \quad (4\text{-}21)$$

to generate hydroxyl radicals (equation (4-20)). The highly reactive hydroxyl radicals could then decompose O_3 via equation (4-21), accelerating ozone decomposition in the presence of water and irradiation. However, at RH levels above 20% RH, the resultant increase in surface hydroxyl groups, which have a greater affinity for water, will lead to enhanced water adsorption, blocking surface active sites and decreasing the photocatalytic capacity of TiO_2.[148, 181, 182]

Given the semiconductor nature of α-Fe_2O_3, one might expect a similar reaction sequence and an analogous RH dependence. However, the Lewis acid sites on hematite might have a higher affinity for adsorbed water, inhibiting O_3 uptake and masking the formation of hydroxyl radicals via equations (4-19) and (4-20) even at lower RH levels.

4.6 Conclusions and Atmospheric Implications

This study has focused on the heterogeneous photochemistry of ozone with typical oxide components of mineral dust aerosol, including α-Fe_2O_3, α-FeOOH, TiO_2 and α-Al_2O_3. It is shown that the activity toward O_3 decomposition depends greatly on the surface properties of the oxide, the presence of irradiation, and the relative humidity. The effect of RH on the ozone uptake rate depends strongly on specifics of the oxide surface, such as the type of active site and relative affinity for water. While hematite and

goethite can catalytically decompose O_3 in the dark, titanium oxide and aluminum oxide surfaces are deactivated by O_3 exposure. Under dark conditions, the presence of atmospheric water inhibits O_3 decomposition through the competitive adsorption of water molecules and ozone for active surface sites. In the presence of solar radiation under dry conditions, a photoenhancement in O_3 decomposition was observed for both α-Fe_2O_3 and TiO_2 due to their semiconducting properties with band gap energies in the solar spectrum. The presence of both water and solar radiation leads to more complicated behavior. Water adsorption may be enhanced on hematite surfaces due to the photoproduction of defect sites that promote surface hydroxylation, resulting in an anti-correlation between the ozone uptake coefficient and the RH level for α-Fe_2O_3 sample. More interestingly, irradiation of TiO_2 leads to an initial increase and a subsequent decease for ozone uptake coefficients as the RH is increased. Figure 4.6 is a schematic showing the daytime and nighttime chemistry of ozone on various atmospherically relevant oxides.

Mineral dust plays an important role in atmospheric chemistry, providing ample surface area for the adsorption and reaction of various atmospheric trace gas species.[18] In agreement with field observations,[137-140] This study confirmed that ozone can be effectively taken up on by oxide components of mineral dust. Given that mineral dust aerosol typically contains a number of semiconductor oxides, such as TiO_2, ZnO and Fe_2O_3, heterogeneous decomposition of O_3 induced by solar radiation may be an important sink for tropospheric ozone. In addition, the available surfaces on which such processes may occur extend beyond airborne particles and include soils, rock formations, and buildings. The relevant heterogeneous photochemical pathways might be widespread and influence global ozone concentrations. Modeling studies of atmospheric chemistry should take into account not only heterogeneous uptake of ozone on mineral dust but also include the effect of irradiation and relative humidity to further improve prediction accuracy.

This study has also demonstrated that the application of a simple box kinetic model to the environmental aerosol chamber results allows us to differentiate heterogeneous chemistry from homogeneous chemistry and extract valuable kinetic information. Finally, it should be noted that the concentrations of ozone and oxide particles in the environmental aerosol chamber used in the current work are considerably greater than those typical of the ambient troposphere. Experiments performed under more atmospherically relevant conditions will be a desirable goal for future research in this area.

4.7 Acknowledgements

This material is based upon work supported by the National Science Foundation under Grant No. CHE095260. Any opinions, findings, and conclusions or recommendations expressed in this material are those of the authors and do not necessarily reflect the views of the National Science Foundation. I would like to acknowledge Dr. Mark A. Young who gave enormous help and suggestions on the work. I would also like to thank Dr. Charles O. Stanier who gave me valuable advice for building the KPP model.

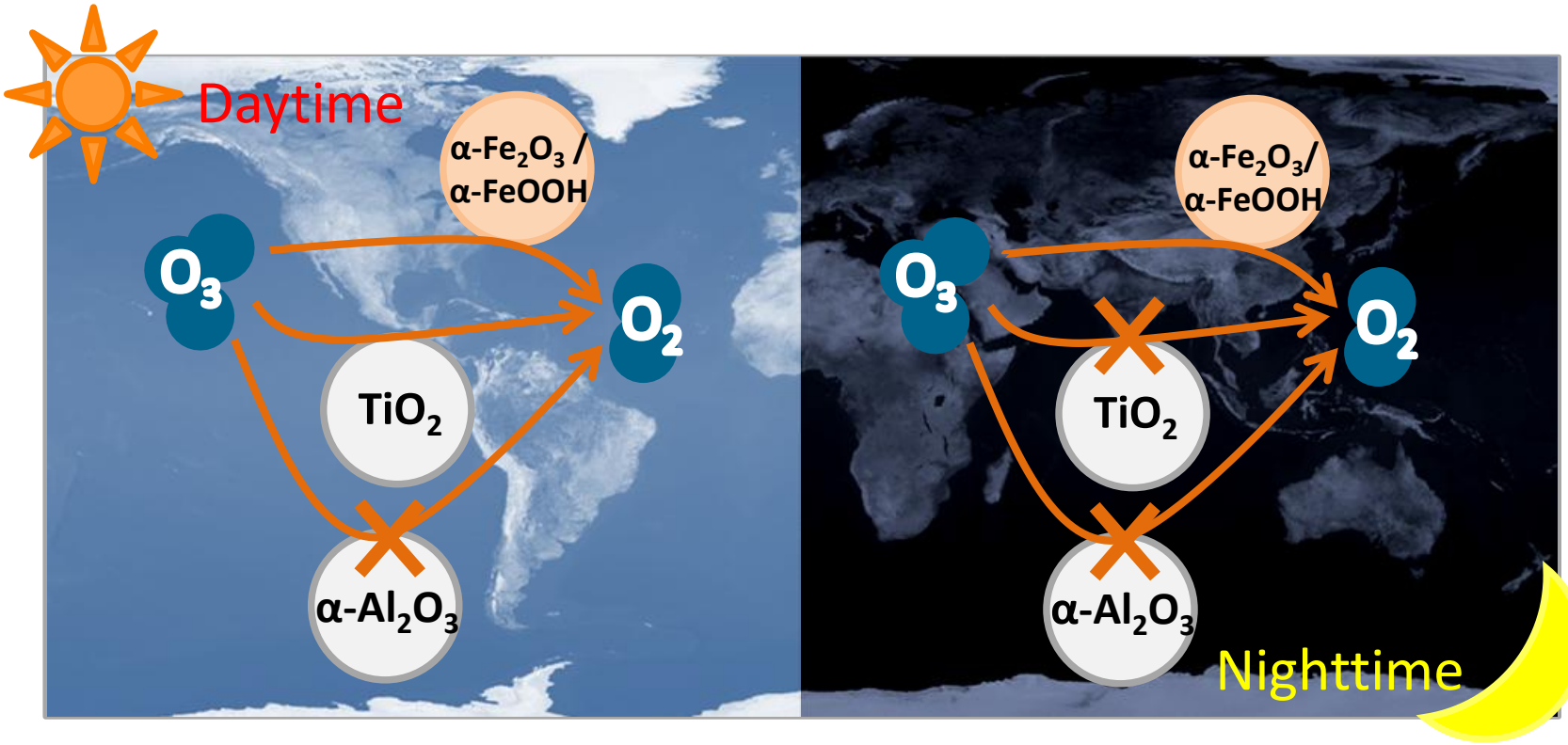

Figure 4.6 A schematic showing the comparison of daytime and nighttime chemistry of ozone on various atmospherically relevant oxides.

CHAPTER 5

CHARACTERIZATION OF ANTHROPOGENIC AEROSOLS AND IRON DISSOLUTION OF ANTHROPOGENIC AEROSOLS DURING SIMULATED ATMOSPHERIC PROCESSING

5.1 Abstract

Anthropogenic coal fly ash (FA) aerosols may represent a significant source of bioavailable iron in the open ocean. Few measurements have been made that compare the solubility of atmospheric iron from anthropogenic aerosols and other sources. This study reports an investigation of iron dissolution for three FA samples in acidic aqueous solutions and compare the solubilities with that of Arizona test dust (AZTD), a reference material for mineral dust. The effects of Fe speciation, pH, type of acid anion, simulated cloud processing, and solar radiation on iron solubility were explored. Similar to previously reported results on mineral dust, iron in aluminosilicate phases provides the predominant component of dissolved iron. Iron solubility of FA is substantially higher than of the crystalline minerals comprising AZTD. Simulated atmospheric processing elevates iron solubility due to significant changes in the morphology of aluminosilicate glass, a dominant material in FA particles. Iron is continuously released into the aqueous solution as FA particles break up into smaller fragments. Proton-promoted and ligand-promoted dissolutions are two main mechanisms in mobilizing iron under the current experimental conditions. Oxalate can form bidentate ligand with Lewis acid iron center, and therefore displayed the highest rate of iron dissolution. Solar irradiation shows a considerable enhancement on iron dissolution. The assessment of dissolved atmospheric iron deposition fluxes and their effect on the biogeochemistry at the ocean surface should be constrained by the source, environmental pH, type of acid anion, iron speciation, and solar radiation.

5.2 Introduction

Iron is an essential nutrient for marine organisms since it is required in various metabolic processes.[184-186] Biological primary productivity is limited by iron bioavailability in extensive regions of the ocean referred to as high nutrient low chlorophyll (HNLC) regions.[187-189] Mesoscale iron addition experiments from polar to tropical HNLC waters have demonstrated that iron enrichment leads to elevated phytoplankton biomass and rates of photosynthesis in surface water, eventually causing a potential feedback effect on the Earth's climate.[63-67]

It has been generally thought that soluble iron is mainly derived from the transport and deposition of mineral dust.[63, 68-71] While soils have relatively low iron solubility, the high solubility of atmospheric iron observed in field studies has been explained by the atmospheric chemical processing of dust particles during long-range transport.[69, 72-79, 190] Atmospheric chemical processing involves the reduction of Fe(III) to Fe(II), as well as the interaction with inorganic and organic acids, the exposure to sunlight, and cloud processing.[69, 72-79] Iron speciation in aerosol source material also plays a crucial role in controlling the solubility of aerosol iron.[83, 109, 191-194]

Recent evidence from field, modeling and laboratory studies, however, suggests that fly ash (FA) produced from fossil fuel combustion and biomass burning may also represent an important source of bioavailable iron.[70, 81-85, 193, 195-197] The high correlation between soluble iron and combustion-derived black carbon observed at Cheju, Korea[85] strongly suggested the importance of anthropogenic combustion sources. Spectro-microscopy analyses of individual particles collected at the Okinawa Island during an episode of a major outflow event from mainland China showed that the majority of the Fe-containing particles have the elemental signature of either biomass or coal combustion.[198] A modeling study by Luo[81] supported this hypothesis by predicting that combustion-derived aerosols supply a source of highly-soluble iron to the surface ocean. Although the source of bioavailable iron from combustion is not important globally

(<5%), combustion-derived aerosols could represent 50% of the total iron deposited in the ocean surrounding industrialized regions.[81]

Despite increasing evidence suggesting the importance of anthropogenic combustion-derived iron, the contribution of bioavailable iron from combustion emission relative to mineral dust is poorly understood. This study focuses on anthropogenic aerosols, via a series of characterization techniques and dissolution experiments, to better understand the impact of anthropogenic dust on providing soluble iron for marine ecosystem. Standard reference material fly ash particles were selected as the model of anthropogenic aerosol.

Typical environmental aerosols are diverse mixtures of different particles with a wide range of chemical composition, morphologies, sizes, as well as physical and chemical properties. Aerosols are additionally diverse in terms of their external mixing (ensembles of chemically different particles) and internal mixing (chemical heterogeneity within individual particles). Therefore, detailed multi-dimensional chemical characterization of particles during their lifetime in the environment is of critical importance for understanding their formation and reaction mechanisms, atmospheric history, evolution of their compositions and properties.[33]

Therefore traditional particle characterization techniques, such as SEM/EDX, CCSEM/EDX, BET, TEM and XPS, were used to fully characterize the particles used in the current study. In addition, a cross-sectioning technique using a dual focused ion beam coupled with secondary electron microscopy (FIB/SEM) was applied to FA particles to probe the interior structure of FA particles.

The microscopy technique is very powerful for particle characterization. Over the last decade, there has been a remarkable increase in developments and applications of novel microscopy and micro-spectroscopy techniques for chemical imaging analysis of environmental particles advancing fundamental understanding of particle interior and lateral chemical heterogeneity.[199-201] The qualitative and quantitative data obtained in

these studies are essential for evaluating hygroscopic and optical properties of particles, possible formation processes, atmospheric aging, and sources. Two requirements must be met for chemical imaging analysis: (i). the applied technique must have sufficient sensitivity to detect chemical differences on a nano scale, and (ii). either penetration volume of the probing technique must be controlled to interrogate particle interior, or it must include methods for controlled milling (depth profiling) of particle material. Capabilities of high resolution transmission electron microscopy (HRTEM) with coupled electron-beam based spectroscopy techniques, i.e. EELS – electron energy loss spectroscopy and mapping, EDX - energy dispersive X-rays spectroscopy, SAED - selected-area electron diffraction, as well as Z-contrast imaging, and ET – electron tomography, are commonly used for composition-specific chemical imaging, structural and elemental analysis of very small particles.[201] Methods of the HRTEM analysis work best for particles smaller than 100 nm which are sufficiently transparent to the electron beam. Interior of particles as large as a few microns in size can be probed by soft X-rays in the synchrotron-based scanning transmission X-ray microscopes (STXM).[200] HRTEM and STXM can probe sufficiently thin particles at lateral resolution of <1 nm and <50 nm, respectively. Analysis of larger, "non-transparent" particles by the same techniques requires milling of particles down to the thicknesses accessible by the selected technique. A convenient approach for preparation of thin samples for microscopy studies is a focused ion beam (FIB) technique that employs site-specific sputtering (milling) of specimen by energetic metal ions.[202] Advanced FIB instruments have an ion column interfaced with scanning electron microscope (SEM), energy dispersive microanalysis of X-rays (EDX), and mechanical accessories for nano-positioning and nano-manipulators assembled together into a multipurpose analytical platform called a dual-beam FIB/SEM. The FIB/SEM offers a distinct advantage in that it allows high-precision ion milling of specimen and revealing its interior structure that can be immediately imaged with nano-

scale resolution of SEM and its elemental composition can be probed with EDX microanalysis.

The dual beam FIB/SEM technique has been extensively used for broad applications in material science, including microscopic characterization of semi-conductors, circuit diagnostics and failure analysis, microstructural analysis of thin films and coatings, and many others.[203] However, applications of this technique in environmental sciences and particle analysis have been very limited so far and it's utility and limitations are yet to be explored. Examples of recent environmental applications include: site-specific milling, sample extraction and imaging of internal inclusions in mineral samples;[204] dissecting and interior analysis of pharmaceutical particles used for inhalation;[205] cross-sectioning and interior analysis of selected dust and fly-ash particles collected from an ambient air.[206, 207] The current study extends the application of FIB/SEM for systematic studies of internal composition of fly-ash particles with specific focus on the iron containing particles that may an important source of bioavailable iron in open ocean as discussed above.

Iron mobilization of mineral dust in aqueous solutions acidified by typical atmospheric inorganic acids, such as H_2SO_4 and HNO_3, has been extensively studied.[106, 208, 209] The effect of organic acids in iron dissolution, in addition, has not been assessed to any great extent. Indeed, a large number of organic acids such as acetic acid and oxalic acid have been identified in the atmosphere and in aerosol phase.[1, 210, 211] These organic acids mainly originate from both anthropogenic and biogenic sources. Low-molecular weight organic acids have also been verified as the major products during photo-degradation of various volatile organic compounds in the atmosphere.[1] Studies of precipitation chemistry have shown that organic acids account for a large fraction, up to 64%, of the total acidity in nonurban environments.[212] Due to their polar nature, these organic acids preferentially transfer into the aerosol phase,[211] potentially displaying different capacities in iron mobilization compared with inorganic acids.

Indeed, organic complexation has been suggested to play a role in promoting iron solubility from representative components of dust and authentic dusts.[196, 213-217] Field measurements showed a positive correlation between soluble iron and oxalate in collected samples of air mass over the North Atlantic region.[78, 218, 219] The positive correlation was probably due to the complexation of iron with oxalate, although the common origin of oxalate and aerosols of high soluble iron, like anthropogenic activities, may also play a role. A few laboratory experiments have suggested that organic acids have a great capacity in promoting iron dissolution from iron-containing minerals and authentic dusts.[196, 216, 217] Soluble iron increased from 0.0025% to 0.26% of total iron when oxalate was present.[217] A modeling study has also highlighted the role of organic acids in iron mobilization of atmospheric dust.[220] In the presence of solar radiation, photoreduced dissolutions of iron may occur, leading to a further enhancement.[220]

The overall objective of this study is to better understand the impact of anthropogenic dust on atmospheric iron cycling and marine ecosystems. Specifically, this study has examined the solubility of iron present in three types of coal fly ash (FA) particles and compared these results to Arizona test dust (AZTD), a commercially available reference material of mineral dust that has been previously characterized,[221] to explore the contribution of bioavailable iron from combustion emissions relative to mineral dust. Based on aqueous dissolution studies complemented by particle characterization techniques, this study explored the physicochemical factors, including composition, pH, solar radiation, atmospheric processing, iron speciation, and mineralogy, that influence the process of iron dissolution. Since an earlier modeling study[75] suggested that a deliquescent liquid layer with pH less than 2 can occur on particle surfaces, dissolution experiments were conducted to mimic aqueous environments at low pH associated with atmospheric aerosol under certain atmospheric conditions. This study also characterized individual particles of FA after processing for better understanding of how the simulated atmospheric processing modifies the

morphology, chemical compositions and element distributions of individual particles. These particle analysis data provide important insights on iron release behavior of fly ash particles during simulated atmospheric processing, and on the iron solubility trends of different particle source materials such as fly ash and mineral dust. Additionally, it is presented and discussed here an unconventional methodology of micro-positioning and cross sectioning of FA particles that utilizes their substantial electrostatic charges and tendency to form stable agglomerates of individual fly-ash spheres.

5.3 Experimental Methods

5.3.1 Reagents and Materials

All solutions were prepared using 18 MΩ Milli-Q water. Dissolution studies were conducted in aqueous solutions of H_2SO_4 (Fisher Inc.), acetic acid (Fisher Inc.), and oxalic acid (Fisher Inc.). For dissolved iron analysis 1,10-phenanthroline (Aldrich Inc.), hydroxylamine hydrochloride (Sigma Aldrich Inc.), ammonium acetate buffer (Sigma Aldrich Inc.) and ammonium fluoride (Aldrich Inc.) were used. Working standard solutions were prepared by diluting the calibrated stock standard solutions of Fe(II), Fe(III) or oxalate. The mobile phase used during HPLC analysis was prepared from H_2SO_4 (Fisher Inc.). FA standard reference material (SRMs 2689, 2690, and 2691; National Institute of Standards & Technology), and Arizona fine test dust (ISO 12103-1 A2 test dust; Power Technology Inc.) were used as received.

5.3.2 Traditional Characterization Methods

The morphology and composition of FA particles were examined using a Hitachi S-3400 N scanning electron microscopy (SEM) coupled with energy dispersive X-ray spectroscopy (EDX) system. SEM/EDX elemental maps were collected to examine the distribution of Fe in FA particles. Computer-controlled scanning electron microscopy

with energy dispersive X-ray analysis (CCSEM/EDX)[110] was applied to FA and AZTD particles before and after dissolution experiments to examine the effect of simulated atmospheric processing on the morphology, chemical composition, and element distribution within individual particles.

The surface composition of FA particles was measured using a custom-designed Kratos Axis Ultra X-ray photoelectron spectrometer with a monochromatic Al Ka X-ray source as previously described.[222] Since the intense carbon signal in EDX spectra are partly due to carbon tape used for sample mounting and the difficulty in obtaining quantitative data for low Z-elements, both SEM/EDX and XPS data exclude carbon and oxygen contents from quantitative analysis.

The iron content of AZTD was determined as described in previous study.[106] Surface area measurements for all samples used a seven-point N_2-BET adsorption isotherm that was acquired with a Quantachrome Nova 1200 surface area analyzer. The samples were evacuated overnight prior to measurements. ^{57}Fe Mössbauer spectra were collected as previously described.[106, 111] Briefly, ^{57}Fe Mössbauer spectra were collected on dry samples at T = 13 K, with an attempt made to randomly orient the powder prior to analysis. Spectral fitting was done using Recoil software (University of Ottawa; Ottawa, Canada) with Voigt-based modeling. Phase identification was done based on center shift, quadrupole splitting, hyperfine field values, and temperature-dependent magnetic ordering.

5.3.3 FIB/SEM Analysis

Particle samples for FIB/SEM analysis were prepared in the same manner for all tested particles. Dry particles were mechanically dispersed infront of the inlet of the Multi Orifice Uniform Deposition Impactor (MOUDI), model 110-R (MSP, Inc) and then were deposited onto TEM grids placed on the 5th stage (cut-off size, D_{50} = 1 μm) of the impactor.

A dual-beam FIB/SEM FEI Quanta instrument was used in this work. The instrument is equipped with an EDX spectrometer with a Si(Li) detector with an active area of 10 mm^2 and an ATW2 window. The instrument can be operated in computer-controlled (CC) SEM mode, enabling automated measurements of size and elemental composition for large populations of individual particles. In CCSEM/EDX operation mode, selected sample areas are imaged and particle features in the images are recognized by an increase of the detector signal above a pre-set threshold level. Then, X-ray spectra are acquired for all detected features. In this work, particles with an equivalent circle diameter within a range of 0.2-5 μm were measured. A magnification of ×2000-10000, a beam current of 400-600 pA, and an accelerating voltage of 20 kV were used, and X-ray spectra were acquired for 10 s. Additional details of the CCSEM/EDX analysis of particles can be found elsewhere.[110]

A focused Ga-ion beam was used to cross-section agglomerates of individual particle lifted from the substrate using an AutoProbe™ 300 nanomanipulator (Omniproble Inc.), as will be discussed in the results and discussion section of this chapter. During cross-sectioning of particles the ion beam energy and current were set at 30 kV and 3 nA, respectively, for initial milling, and then final cleaning was performed at 1 nA beam current. Cross sectioned particles were imaged by SEM from normal direction to the cross section plane. Additional ion-beam induced SEM images were acquired from direction parallel to the cross-section, using non-destructive ion beam current of 0.5 pA. Elemental mapping of sectioned particles was performed at the standard positioning geometry of the EDX detector at the takeoff angle of 45 °with respect to the cross-section plane, over the sample positioned at 10 mm working distance.

5.3.4 Dissolution Measurements

Dissolution measurements were carried out in a glass vessel containing an appropriate aqueous solution. Since minor variations in ionic strength did not

significantly influence the results of previous dissolution studies,[106] the ionic strength for these measurements was not controlled. All solutions were stirred under oxygen exposure and kept at 298 K using a water jacket integrated into the vessel. The solid loading was 2 g L^{-1}. Experiments were conducted in triplicate and results represent the average and standard deviation of three measurements. After addition of the particles into the solution, aliquots of suspension were periodically withdrawn for analyses of both dissolved Fe(II) and total dissolved Fe. The analysis method to determine iron concentrations is described in Chapter 2.

5.3.5 Simulated Cloud Processing with and without Solar Radiation

Cloud processing involves radical fluctuations in pH and has been suggested to increase the solubility of iron.[74, 77, 79, 107-109, 223] To determine the effect of varying pH cycles on iron solubility, solutions were cycled between highly and slightly acid conditions over periods of 24 hours in separate experiments to simulate cloud processing. Specifically, Milli-Q water was used instead of acidic media for simulated cloud processing experiments. After approximately 24 hours of dissolution the suspension was acidified with concentrated H_2SO_4 to pH ≈ 2, a pH value the deliquescent layer on the aerosol particle could have.[75] The system was allowed for dissolution for a further 24 hours before being restored to pH ≈ 5 with concentrated NH_4OH. The varying pH cycles were repeated up to three times. Sufficient aliquot amounts was periodically withdrawn for measurements of both Fe(II) and total dissolved Fe during the course of the experiment. To explore the effect of solar radiation during simulated cloud processing, a solar simulator with a 150 W xenon lamp (Oriel Corp.) was mounted on the top of the vessel to allow irradiated experiments. The sun-like spectrum provided by the xenon lamp ranges from 250 and 2400 nm, with maximum radiation in the region of 750 and 1000 nm. The vessel has a 5 mm thick quartz window mounted on top to allow

transmission of light. For reference, dissolution experiments under dark conditions were conducted with the vessel wrapped in aluminum foil.

5.4 Results and Discussions

5.4.1 Characteristics of Fly Ash and Arizona Test Dust

Measured specific surface areas of FA particles are tabulated in Table 5.1 as well as the total Fe content certified by NIST. The specific surface areas of three FA samples fall within the range of 0.8 to 3.8 $m^2 g^{-1}$, and the total Fe contents range from 4.42 to 9.32 wt %. FA 2689 exhibited the highest total Fe content (9.32 ± 0.06 wt %) but had the smallest surface area (0.8 ± 0.1 $m^2 g^{-1}$). FA 2690 had the highest specific surface area (3.8 ± 0.1 $m^2 g^{-1}$), but the lowest content of Fe (3.57 ± 0.06 wt %). The surface area and Fe content of AZTD were determined to be 4.2 ± 1.0 $m^2 g^{-1}$, and 1.98 ± 0.08 wt %, respectively.

The characteristic morphologies of FA particles are mainly spherical with smaller particles typically attached to larger ones, as demonstrated in the representative SEM image of FA particles shown in Figure 5.1. The particles ranged from less than 1 μm in size to greater than 50 μm, with the majority of the particles in the range of 1 to 10 μm. Agglomerated and irregularly shaped particles were also observed. Elemental maps show that Si and Al are relatively evenly distributed among the FA particles. In contrast, the uneven distribution of Fe is observed for all FA samples. Some particles were entirely free of Fe, whereas others exhibited elevated Fe content in localized regions or throughout the particle.

The bulk average composition of an ensemble of particles, determined by SEM/EDX is significantly different from that of the surface composition determined by XPS, as shown in Table 5.1. While Si, Al, Ca, Fe, Mg, and Na represented the major

Table 5.1 Physical Properties and Elemental Analysis of Fly Ash Particles Including FA 2689, 2690, and 2691

	S.A.[a]	%Fe[b]		Si	Al	Fe	Mg	Na	Ca	K	Ti	S	P	F
FA 2689	0.8 ± 0.1	9.32 ± 0.06	XPS[c]	43.8 ±1.5	19.7 ±0.5	8.7 ±0.8	2.5 ±0.8	1.5 ±0.6	6.0 ±0.1	1.9 ±1.0	n.d.[f]	15.9 ±0.2	n.d.	n.d.
			EDX[d]	44.6 ±4.0	30.9 ±3.0	6.9 ±1.1	2.0 ±0.5	1.0 ±0.3	5.8 ±3.1	5.4 ±2.1	1.4 ±0.5	1.5 ±1.0	0.5 ±0.3	n.d.
			Ratio[e]	1.0 ±0.1	0.6 ±0.1	1.3 ±0.2	1.3 ±0.5	1.5 ±0.8	1.0 ±0.6	0.4 ±0.2	-	10.6 ±7.1	-	-
FA 2690	3.8 ± 0.1	3.57 ± 0.06	XPS	34.2 ±1.0	18.7 ±0.3	7.3 ±0.4	16.4 ±0.4	3.8 ±0.1	8.1 ±0.1	2.0 ±1.0	n.d.	7.2 ±0.5	2.3 ±0.2	n.d.
			EDX	47.2 ±5.8	29.1 ±2.1	5.4 ±1.0	3.0 ±0.7	0.5 ±0.3	9.1±4.4	2.7 ±0.6	1.7 ±1.0	0.4 ±0.2	1.0 ±0.5	n.d.
			Ratio	0.7 ±0.1	0.6 ±0.1	1.4 ±0.3	5.5 ±1.3	7.6 ±4.6	0.9 ±0.4	0.7 ±0.4	-	18.0 ±9.1	2.3 ±1.2	-
FA 2691	2.2 ± 0.1	4.42 ± 0.03	XPS	19.6 ±0.2	8.3 ±0.8	3.7 ±0.8	9.2 ±0.4	8.8 ±1.0	23.2 ±0.1	3.7 ±1.1	n.d.	14.5 ±0.2	4.7 ±0.2	4.3 ±0.2
			EDX	27.9 ±10.1	18.7 ±7.3	6.0 ±1.1	5.4 ±2.4	2.5 ±1.0	32.0 ±9.4	1.8 ±1.0	2.8 ±0.9	2.7 ±0.9	1.9 ±0.8	n.d.
			Ratio	0.7 ±0.3	0.4 ±0.2	0.6 ±0.2	1.7 ±0.8	3.5 ±1.5	0.7 ±0.2	2.1 ±1.3	-	5.4 ±1.8	2.5 ±1.1	-

[a] Surface area in $m^2 g^{-1}$;

[b] Total iron content in wt %;

[c] Surface composition as determined by XPS;

[d] Composition as determined by EDX;

[e] High ratio of XPS/EDX indicates enrichment of element on the surface, while low ratio (<1) of XPS/EDX indicate enrichment of element in the inner core;

[f] n.d. = not detected.

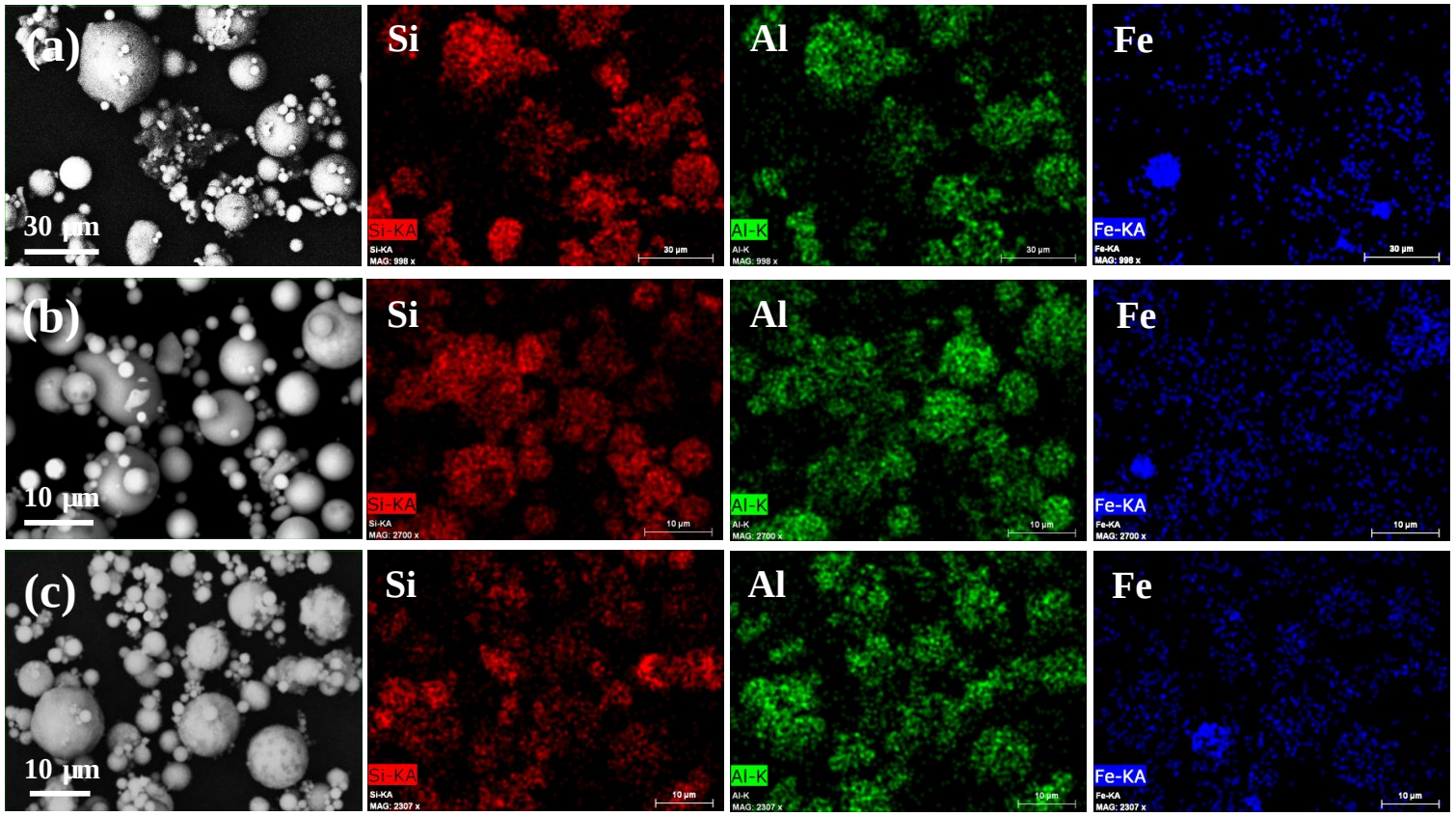

Figure 5.1 Representative secondary electron images and corresponding Al, Si, and Fe elemental maps obtained from SEM/EDX analyses of (a) fly ash SRM 2689, (b) fly ash SRM 2690, and (c) fly ash SRM 2691. The fly ash particles are mainly spherical with a heterogeneous distribution of iron.

elements for all samples, trace elements such as fluorine were also identified. Sulfur was present mainly on the surface for all FA samples. Phosphorus enrichment was found on the surface of FA 2690 and 2691. The distribution of other elements varied for the different samples. For example, iron in FA 2689 and 2690 is found to be enriched on the surface, but for FA 2691, iron on the surface is depleted with respect to the bulk. It is noteworthy that most FA particles are alkaline due to the presence of CaO and MgO. In agreement with the independent EDX characterization results discussed above, FA 2689 and 2691 are in fact low-calcium, American Society for Testing and Materials (ASTM) Class F FA particles, as certified by NIST. FA 2691 is an ASTM Class C FA with higher calcium content. The buffer capacity is likely to affect the dissolution behavior of iron from FA particles, as discussed in detail here.

Most interestingly, from the perspective of this study, is the observation of dark spherical FA particles that are seen to have bright aggregates attached to the surface as in SEM images. "Spot mode" EDX analyses showed that the bright aggregates on the surface contained significant higher content of Fe compared with the dark matrix material (data not shown). Similar Fe enrichment on the surface of FA particles was observed in previous work.[224, 225] It was proposed that the Fe-enriched aggregates were mainly composed with iron (oxyhydr)oxide, while iron in the matrix of FA particles was mainly in an aluminosilicate form.[224-226]

Mössbauer spectra collected at 13 K (Figure 5.2) provide information regarding the speciation of iron in FA particles. All spectra contain multiple ferric iron sextets (label (a) in Figure 5.2), revealing the presence of iron (oxyhydr)oxide phases such as hematite, goethite, ferrihydrite, and magnetite. Mössbauer spectra for three FA samples also show the Fe(III) doublet (label (b) in Figure 5.2) attributed to Fe(III) in an aluminosilicate phase based on the lack of magnetic ordering and the chemical shift (CS) and quadrupole splitting (QS) values.[227, 228] Since the three FA standard reference

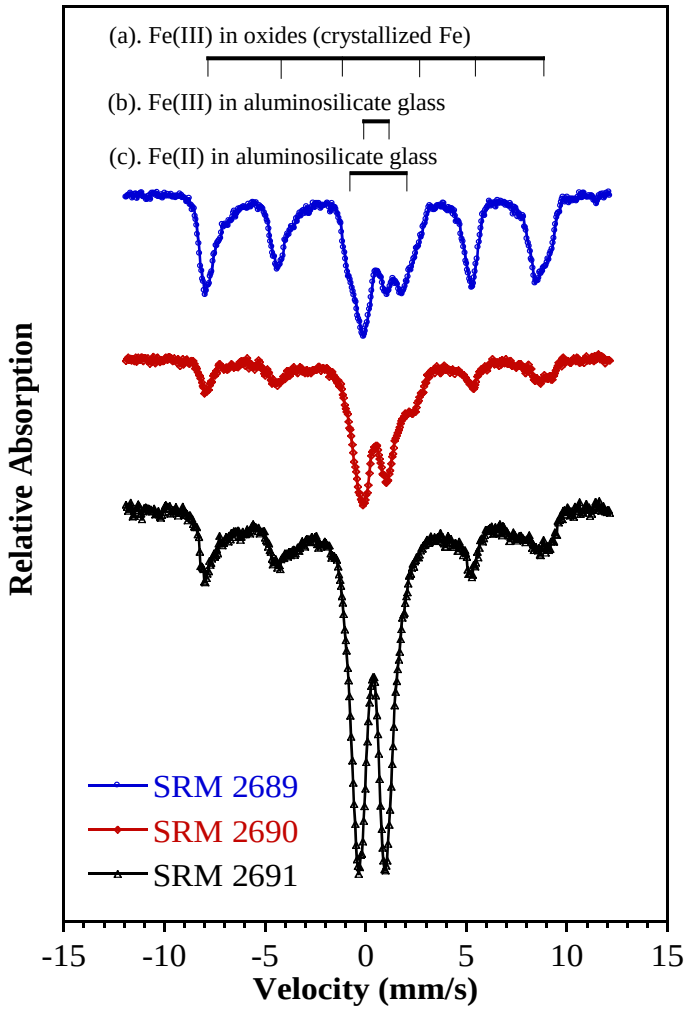

Figure 5.2 Mössbauer spectra of fly ash particles SRMs 2689, 2690, and 2691collected at 13 K. Each spectrum has been least-squares fitted to a model based on three distinct iron-bearing components, including Fe(III) in oxides (a), and Fe(III) (b) and Fe(II) (c) in aluminosilicate glass, respectively, as indicated by the line diagrams above the spectra.

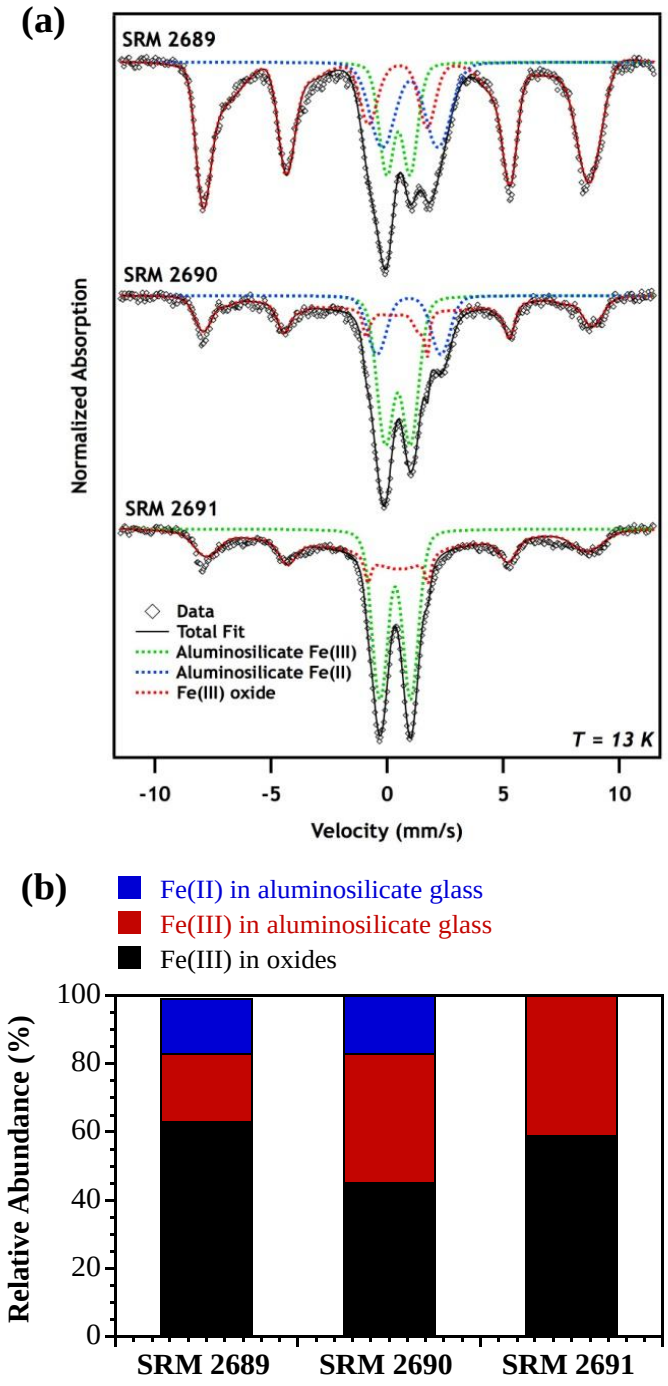

Figure 5.3 Fitting results of Mössbauer spectra of fly ash SRMs 2689, 2690, and 2691.(a) the fitting Mössbauer spectra; (b) the partitioning of iron speciation.

materials were previously characterized to be mainly glass, with much less amounts of quartz, hematite/magnetite and mullite,[229] here it is attributed the Fe(III) doublet to Fe(III) in aluminosilicate-glass phase. Similarly, Mössbauer spectra showed the Fe(II) doublet (label (c) in Figure 5.2) for FA 2689 and 2690, indicating the presence of Fe(II) in aluminosilicate glass. The partitioning of iron determined by spectral fitting varied among different FA particles as shown in Figure 5.3a. The fitting results are shown in Figure 5.3b displaying the percentages of different iron speciations for each FA sample. Iron in FA 2689 is mainly present as iron oxides, with a percentage of 63%, with less amounts of Fe(II) (16%) and Fe(III) (20%) in aluminosilicate glasses. FA 2690 contained 17% of Fe(II) and 38% of Fe(III) in aluminosilicate glasses, and 45% of Fe in oxides. FA 2691 contained 41% of Fe(III) but no Fe(II) in aluminosilicate glasses with the remaining iron (59%) as Fe(III) in oxides.

CCSEM/EDX analysis of individual particles also shows uneven distribution of Fe in FA 2689. Figure 5.4a shows the relative atomic ratios of Fe-Si-Al and Fe-Si-O elements in individual FA 2689 plotted in ternary diagrams. Each point illustrates the relative Fe-Al-Si and Fe-Si-O ratios determined for a single particle, and all particles were sorted into three groups according to size. The presence of aluminosilicates in FA 2689 particles is inferred from the ternary diagrams. Typical aluminosilicates come in compositional units of the following stoichiometry: $[AlSiO_4]^-$, $[AlSi_2O_6]^-$, $[AlSi_4O_{10}]^-$, $[Al_2Si_2O_8]^{2-}$, and $[Al_2Si_3O_{10}]^{2-}$.[230] This leads to a range of $1 < Si/Al < 4$ characteristic for aluminosilicates. A majority of the FA particles fall within this range. Particles with very high relative Fe content (>90%) and minimal Si and Al (<10%) were also observed. These data likely pertain to particles with Fe dominant in other forms, such as (oxyhydro)oxides (e.g., goethite, hematite or magnetite).

Ternary diagram of Fe-Si-O elements for FA 2689 particles in Figure 5.4a further confirms the unevenly distributions of Fe and Si. A large portion of the particles

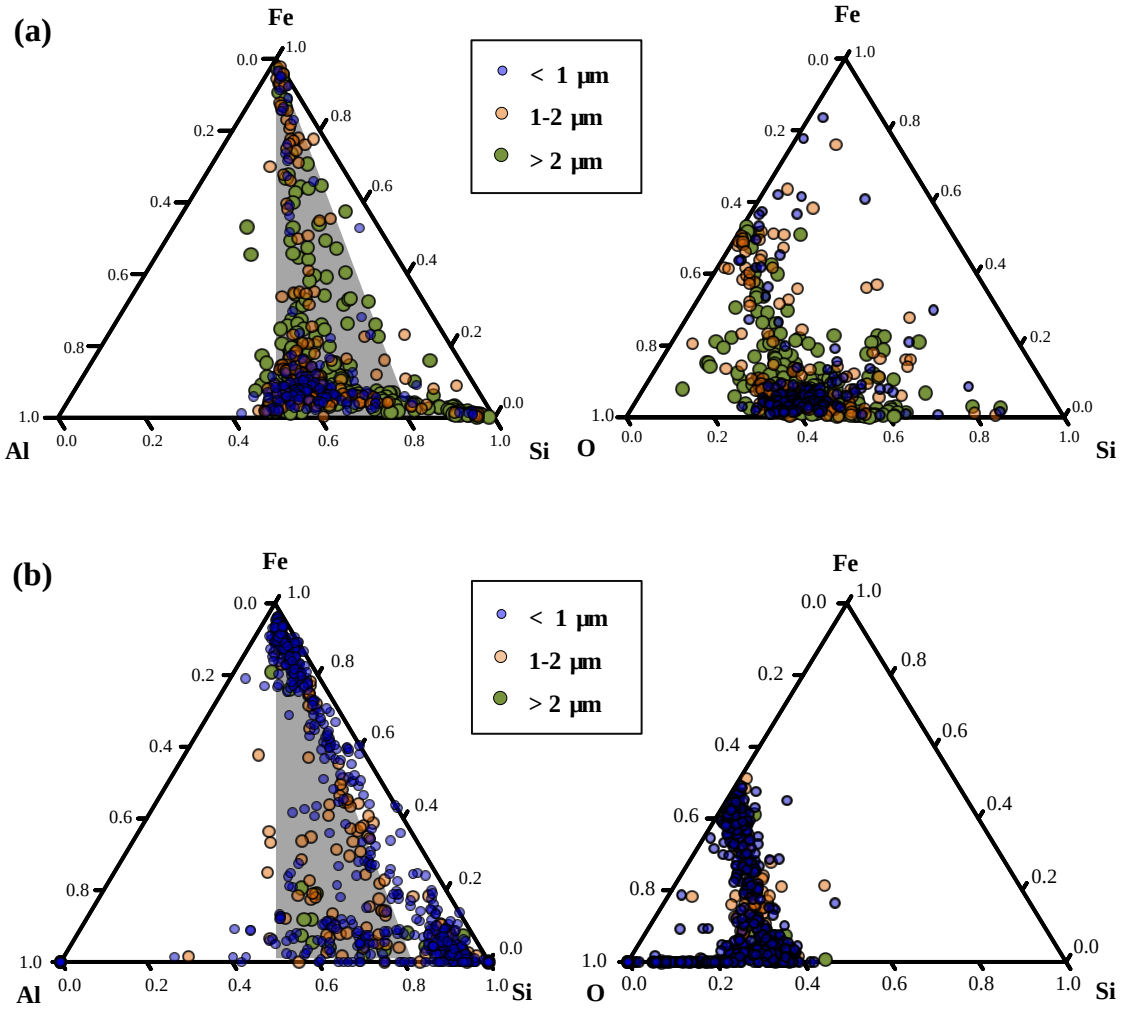

Figure 5.4 Ternary diagrams indicating the relative amounts of Fe-Si-Al and Fe-Si-O obtained by CCSEM/EDX analysis in (a) fresh fly ash SRM 2689 particles, and (b) processed fly ash SRM 2689 particles after dissolution in pH 2 H_2SO_4 for 50 hours.

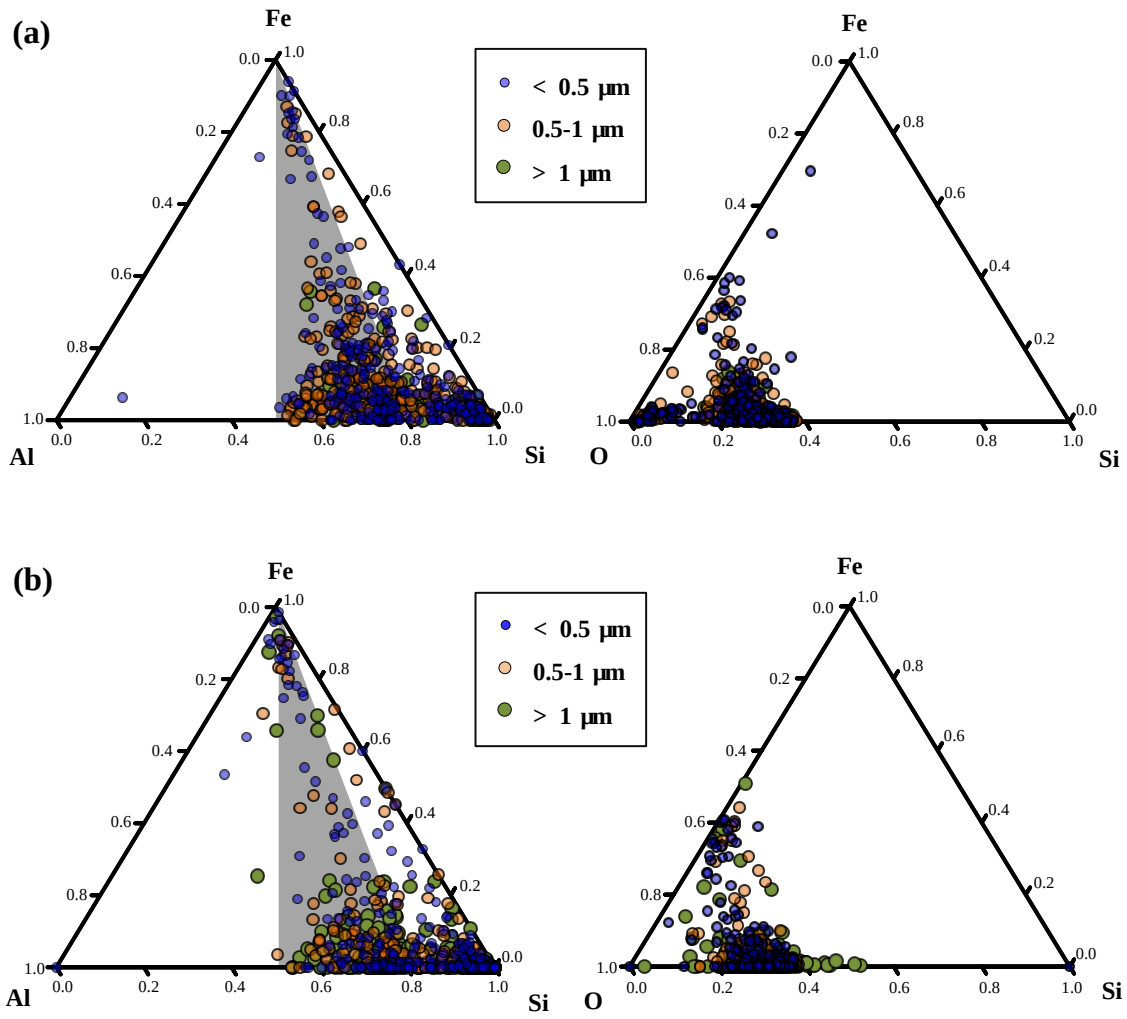

Figure 5.5 Ternary diagrams indicating the relative amounts of Fe-Si-Al and Fe-Si-O obtained by CCSEM/EDX analysis in (a) fresh Arizona test dust particles, and (b) processed Arizona test dust particles after dissolution in pH 2 H_2SO_4 for 50 hours.

exhibited high contents of Fe or Si with less content of O. Some particles contained high content of O indicating the presence of other metal particles within individual particles. More interestingly, particles with size smaller than 1 μm mostly exhibited high Si contents with low Fe contents. In contrast, particles with size larger than 1 μm contained relatively high contents of Fe.

In order to compare the compositional difference between FA and AZTD, CCSEM/EDX analysis was also performed for AZTD particles. The obtained results are plotted in ternary diagram in Figure 5.5a. Compared with FA 2689 (Figure 5.4a), which contains considerable particles with size >2 μm, AZTD particles have relatively smaller sizes. Most of AZTD particles are less than 1 μm in size. Although AZTD particles also mostly fall within the aluminosilicate regions, AZTD particles have relatively higher Si contents and lower Fe contents compared with FA 2689. Ternary diagram of Fe-Si-O elements for AZTD particles in Figure 5.5a indicates that the oxidation state of Fe-containing and Si-containing particles is relative stable. AZTD particles have relatively higher contents of O compared with FA 2689 in Figure 5.4a, which is in consistent with the AZTD as a highly weathered soil.

Although both FA and AZTD contain significant aluminosillicates, FA particles are dominantly Si-Al-Fe-Ca-K glassy spheres formed via high-temperature combustion followed by a fast cooling process.[229, 231, 232] AZTD and authentic dusts contain mainly aluminosilicate clay mineral,[106] which is more crystalline compared with aluminosilicate glass. The difference in chemical structure plays an important role in controlling the dissolution behavior of the particles, as discussed in detail below.

5.4.2 Interior Structure of Fly Ash SRM 2689 Particles

FIB/SEM studies were then applied to fresh FA particles to explore the particle interior. Consecutive SEM images illustrating the preparation process of cross-section FA particles are shown in Figure 5.6. The tungsten probe tip was firstly cut into scoop shape

with focused ion beam to facilitate lifting as shown in Figure 5.6a. Using the SE imaging normal to the grid, an agglomerate of FA particles deposited on the TEM grid was identified and selected for cross-sectioning. The scoop-shaped probe tip was then carefully operated to lift up the agglomerate (Figure 5.6b). Due to the attractive electrostatical effect of spherical FA particles, the agglomerate remained stable on the probe tip during the tip motion and FIB milling. Using the ion-beam induced SEM imaging that was acquired from direction parallel to the tip's cross section, focused Ion beam in a rectangular pattern was applied to the agglomerate for cross sectioning. It is noteworthy that the agglomerate would move or even fly off during the milling process, depending on the charge the agglomerate carried on. The probe tip can be rotated to an optimal degree for elemental mapping if the agglomerate stays on the tip. Otherwise, the lift-out process will be repeated. The side-view and top-view SEM images of the resultant cross-section particle cluster are shown in Figure 5.6c and Figure 5.6d, respectively. The edges of cross sections in the top view image (Figure 5.6d) are highlighted with open red circles for clarification. Some FA particles were cut in half, showing their cross sections, while others were left untreated.

Cross-sectioning of FA particles - Case I. The elemental maps of the cross-section particle agglomerate were collected overnight, and the results of elemental maps are shown in Figure 5.7. Most of the interested elements, including Si, Al, Fe, Ca, Mg, K, Na, C, P and S, were unevenly distributed among different FA particles. For example, silicon in one particle significantly enriched with less other metal elements present, indicating that it was mainly composed of silicon dioxide. The uneven distribution of iron was also found. Some particles contained significant higher contents of iron, while others showed moderate iron abundances. For individual particles, it can be clearly seen that C, P and S enriched on the surface. One particle in the agglomerate contained more Na in the inner core, while some particles exhibited the enrichment of Na on the surface.

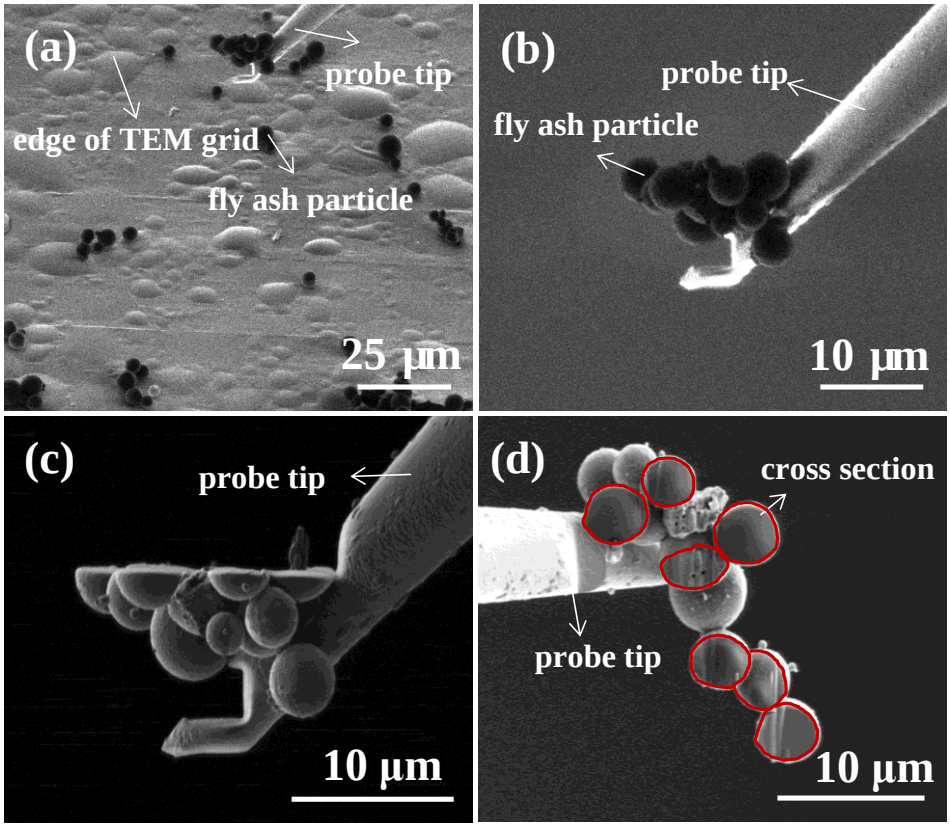

Figure 5.6 Preparation of a cross-section FA particles, (a) lift-out of particles from substrate; (b) a high-magnification view of a cluster of fly-ash particles electrostatically attached to the probe tip.

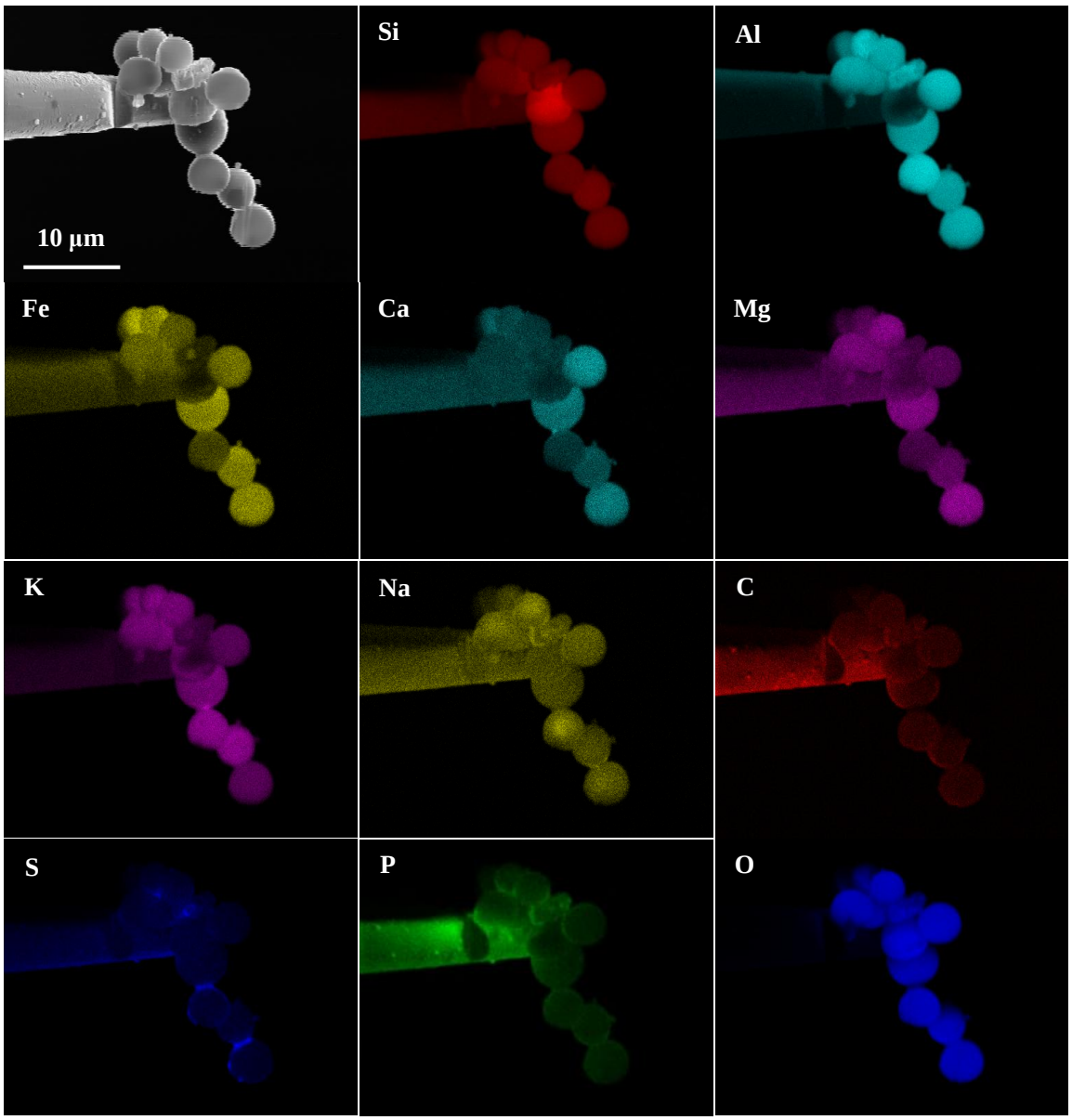

Figure 5.7 Elemental maps obtained from EDX analysis of the cross-section fly ash particles in Figure 5.6.

More interestingly, the un-sectioned particles in Figure 5.7 contained higher abundance of Fe compared with the ones sectioned by ion beam. One possible explanation is the enrichment of iron on the particle surface, which is consistent with the "spot mode" EDX analyses discussed above. The surface enrichment of iron will be further verified by other cases of FA cross-sectioning as discussed in detail below.

Cross-sectioning of FA particles - Case II. Shown in Figure 5.8 is another case of FA cross-sectioning. Three FA particles in the particle agglomerate had been cross sectioned as the edges of cross sectioned particles are highlighted with open red circles as shown in Figure 5.8b. Similarly, the uneven distribution of the interested elements, including Si, Al, Fe, Ca, Mg, K, Na, C, S and P, was observed. The contents of oxygen among different FA particles, however, are relative invariable. A small uncross sectioned FA particles contained significantly high content of Si with less other metal elements, and is attributed to silicon dioxide particles. The largest particle in Figure 5.8, though partially shadowed by the probe tip, contained significant higher content of Fe compared with other particles in the same agglomerate.

In order to closely explore the element distribution in individual particles, the particle cluster showed in Figure 5.8 was cut with Ga-ion beam at a lower level to make both of the cross section and the surface of the largest particle exposed in the top-view SEM image. Although a portion of the particle was still shadowed by the probe tip as shown in Figure 5.9, enrichment of Fe on the surface was evident. Both the "spot mode" EDX analysis as well as cross-sectioning and elemental mapping of FA particles supported that dark spherical FA particles commonly coated with bright fragments.[209] These Fe-enriched fragments were mainly composed with iron (oxyhydr)oxide, while Fe in the inner core of FA particles was mainly in aluminosilicate form. [224, 225] It is noteworthy that it was not observe surface enrichment of Fe from elemental maps of cross-section particles due to the thin and unevenly coating iron-rich fragments on the FA spheres.

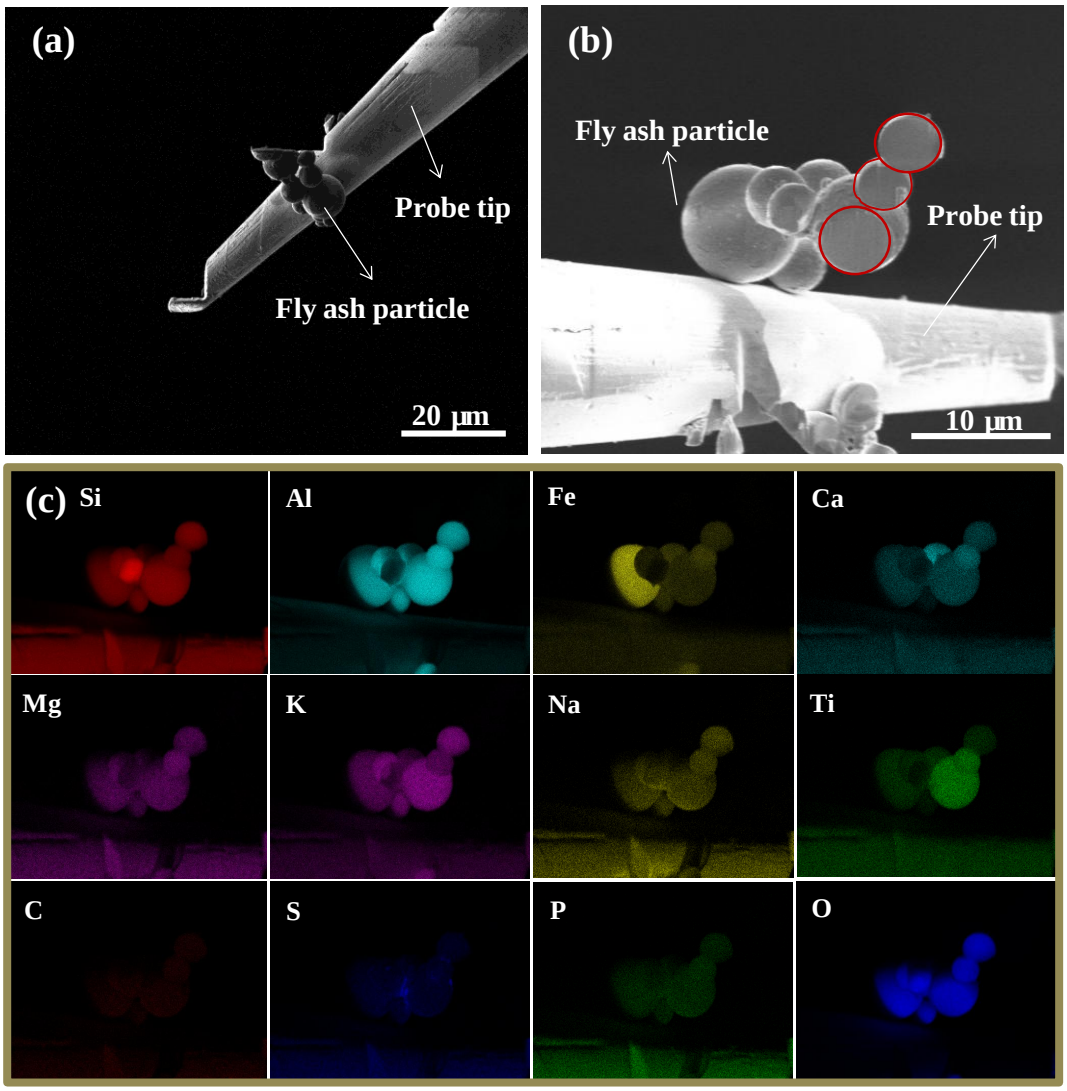

Figure 5.8 Side-view (a) and top-view (b) secondary electron images of fly ash particles cut by a 30-kV Ga focused ion beam across selected boundary. The cross sections are highlighted with open red circles in the top-view image. (c) Elemental maps obtained from EDX analysis of the cross-section fly ash particles in (b).

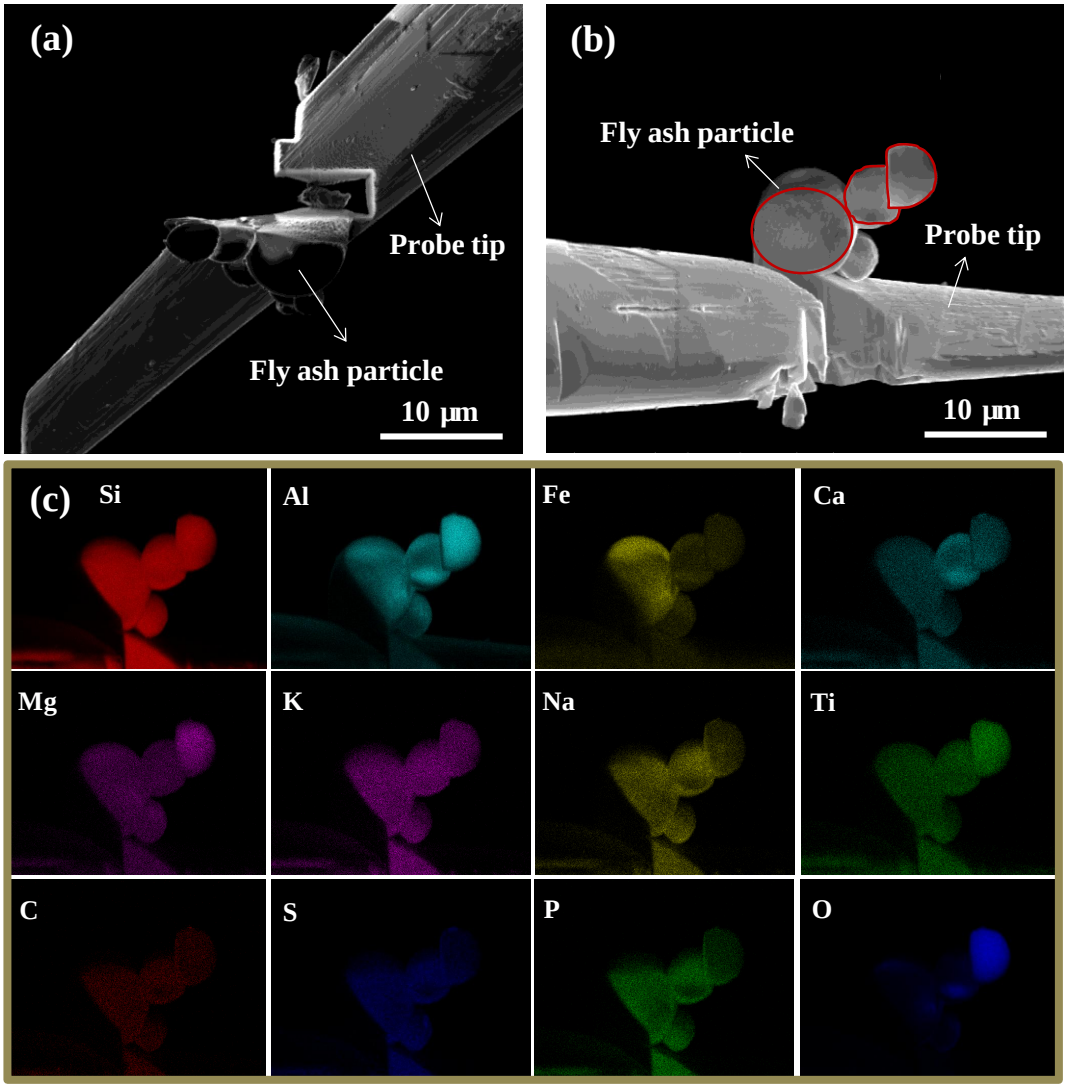

Figure 5.9 Side-view (a) and top-view (b) secondary electron images of fly ash particles cut by a 30-kV Ga focused ion beam across selected boundary. The cross sections are highlighted with open red circles in the top-view image. (c) Elemental maps obtained from EDX analysis of the cross-section fly ash particles in (b).

Cross-sectioning of FA particles - Case III. In another case of cross-sectioning of FA shown in Figure 5.10 an ellipse shaped particle contained significant higher Fe content, with less Al, Si and other metal elements present, indicating the presence of iron (oxyhydr)oxide in FA.

Cross-sectioning of FA particles - Case IV. Another case of cross-sectioning of FA is shown in Figure 5.11, in which only one particle was lift up and cut with Ga-ion beam. The particles displayed significant uneven distribution of elements, including Si, Al, K and Fe, within one single particle.

The characterization results suggest the inhomogeneity of FA particles, which reflects the complicated processes for FA formation. During high temperature combustion, the clay, carbonate, and sulfide minerals as well as other minor minerals are melted together with the formation of oxide phases.[233] When aluminosilicate glassy spheres are produced in the subsequent fast cooling process, iron may segregate and crystallize to form hematite and magnetite, which may then be present in, or condense on the surface of the FA particles. In some cases iron spinels form and make up an entire particle as evidence in Figure 5.11. Other minor elements, such as Ca, K, S and Zn, or their compounds can absorb, condense, or react onto the aluminosilicate FA particles,[233] resulting in the observed inhomogeneous distributions and surface enrichment of some elements. As shown in the dissolution experiment below, the particle chemical inhomogeneity is a critical factor controlling iron dissolution in these samples.

5.4.3 Comparing Iron Dissolution between FA and AZTD at Low pH

The kinetics of FA 2689 and AZTD dissolution in pH 1 and pH 2 H_2SO_4 are plotted in Figure 5.12. The dissolved Fe species, including Fe(II), Fe(III) and total dissolved Fe increased with time in both experiments, indicating that a great fraction of iron in FA and AZTD particles is soluble and bioavailable under these experimental

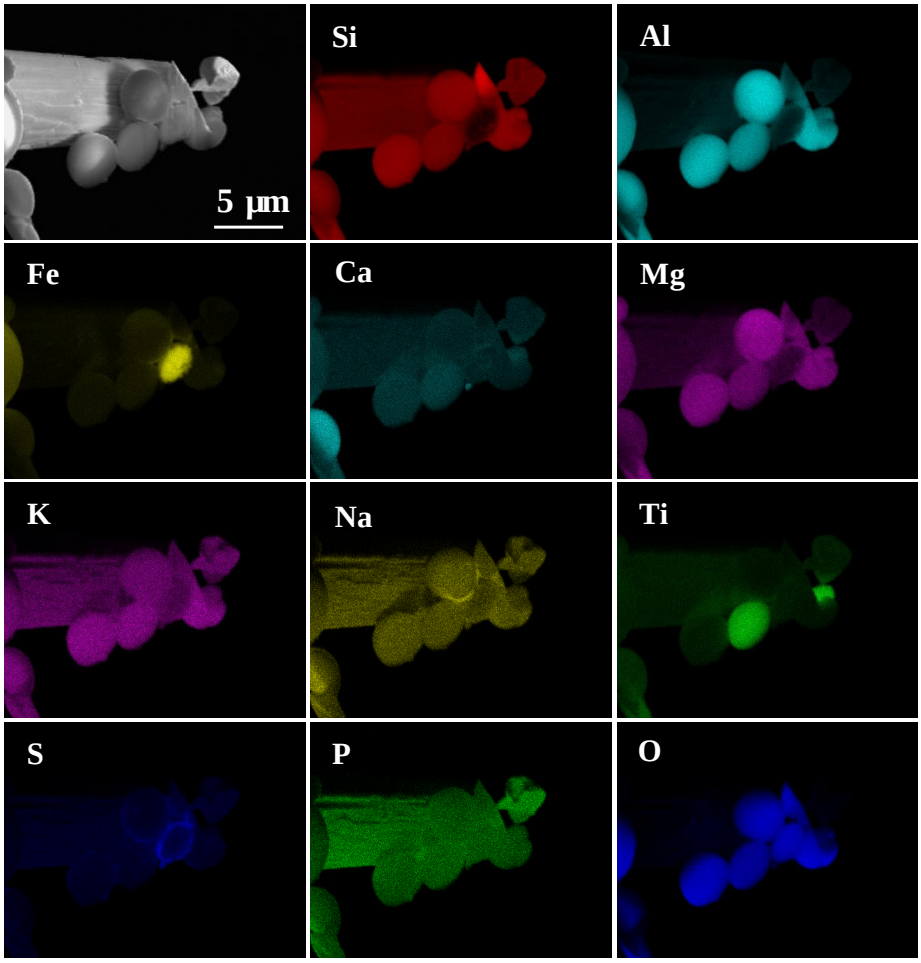

Figure 5.10 Secondary electron images and elemental maps of fly ash particles cut by a 30-kV Ga focused ion beam across selected boundary. Elemental maps were obtained from EDX analysis of the cross-section fly ash particles.

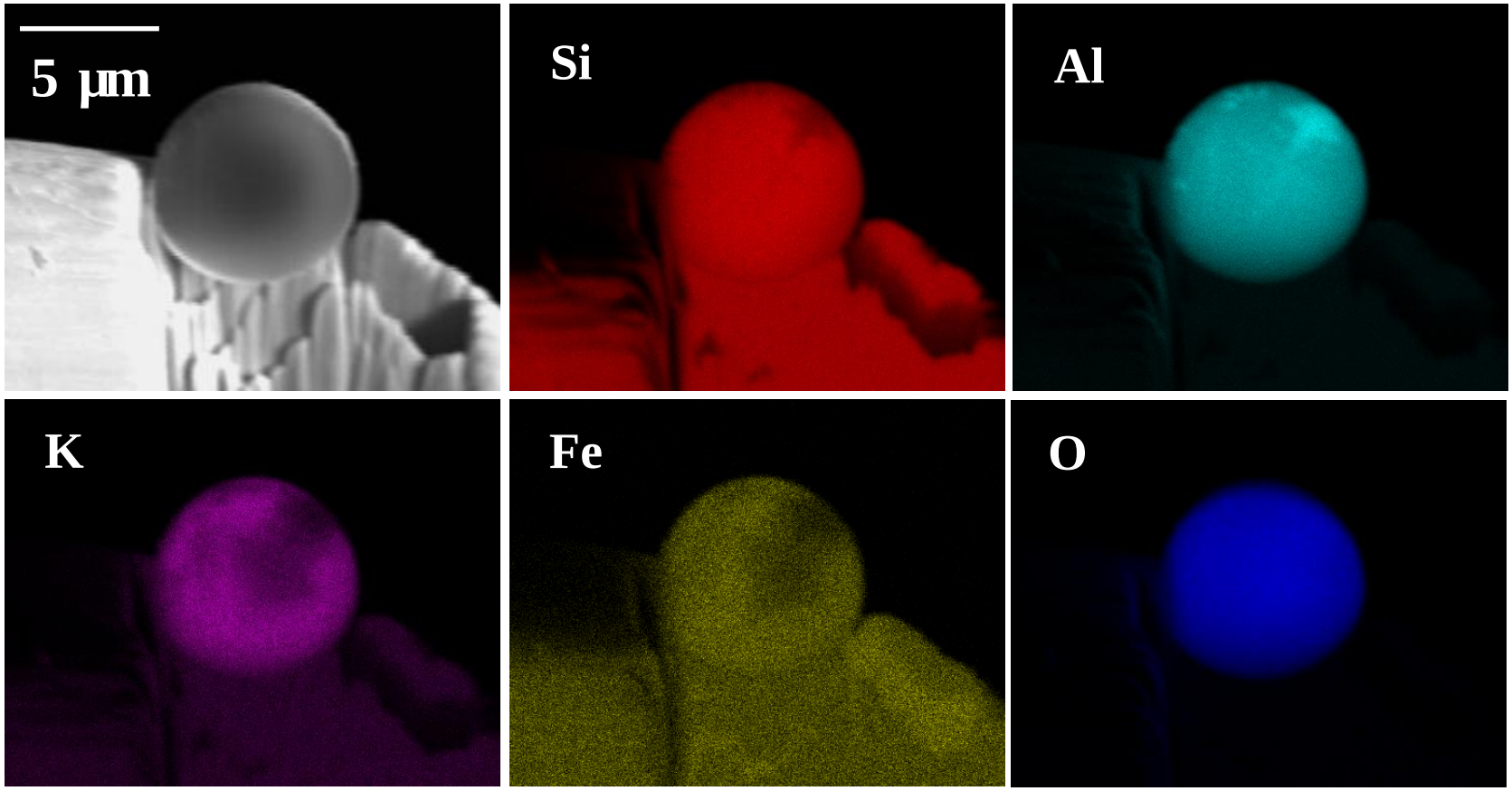

Figure 5.11 Secondary electron images and elemental maps of fly ash particles cut by a 30-kV Ga focused ion beam across selected boundary. Elemental maps were obtained from EDX analysis of the cross-section fly ash particles.

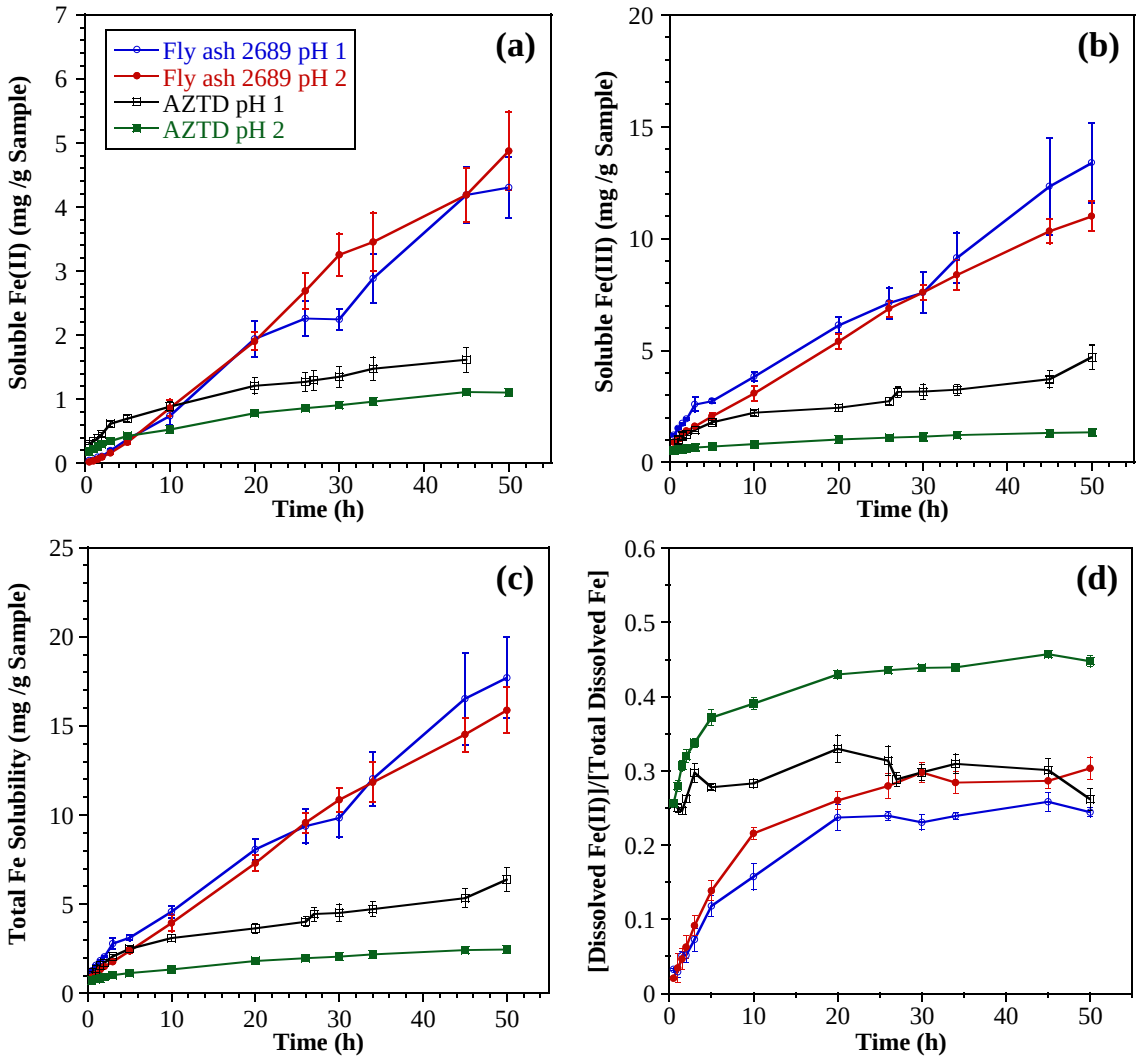

Figure 5.12 Dissolution of fly ash SRM 2689 and Arizona test dust in pH 1 and pH 2 H_2SO_4 over time. Calculated solubilities are shown for (a) dissolved Fe(II), (b) dissolved Fe(III), (c) total dissolved iron, and (d) the fraction of total dissolved Fe present as Fe(II) for each sample. Reactors contained a solids loading of 2 g L^{-1}. When present, uncertainties represent one standard deviation from triplicate experiments.

conditions. The FA samples released considerably higher dissolved Fe per unit mass of particles compared with AZTD. The yield of Fe per unit mass for FA 2689 was 2 and 7 times greater than that of AZTD at pH 1 and pH 2, respectively, after 50 hours of dissolution in acidic media. The generation of soluble Fe species from AZTD was greatest initially ($t < 10$ h), followed by a more gradual, yet steady, rate of change over longer time intervals. The initial rapid release of Fe from AZTD was likely linked to the highly soluble Fe in AZTD particles. As this portion of Fe dissolved, Fe dissolution proceeded at a much lower rate. In contrast, Fe species in FA continually dissolved into the solutions in relative constant rates without any plateau being reached on the timescale of measurements in this study. In addition, the Fe solubility of FA was less pH dependent compared with AZTD. Increasing pH from 1 to 2 resulted in a 50 ± 10 % decrease in total dissolved Fe (Fe_s) concentration for AZTD, whereas total dissolved Fe concentration for FA only decreased by 10 ± 3 %. In accord with previous studies on dissolution of dust materials,[77, 234, 235] proton-promoted dissolution is one of the primary routes for soluble iron production at low pH. At low pH, abundant protons attack iron oxides and even some aluminosilicate minerals to destabilize the Fe-O bond, leading to the release of Fe ions into the aqueous phase.[77, 106, 235]

Figure 5.12d displays the comparison of fractional Fe(II) ($Fe(II)/Fe_s$) between AZTD and FA 2689 as a function of time. The ratio of $Fe(II)/Fe_s$ increased with increasing pH in both experiments. Such changes in dissolved Fe speciation are due to the greater solubility of Fe(II) relative to Fe(III) in solution. Based on the reported solubility products for ferrous and ferric hydroxide, the maximum dissolved concentration of Fe(II) at pH 2 is orders of magnitude greater than that of Fe(III).[236]

The Fe(II) to total Fe ratio remained relatively stable for AZTD during the course of the dissolution measurement, especially when dissolved in pH 1 solution, indicating that likely ferrous and ferric iron distribute evenly among AZTD particles. The slight

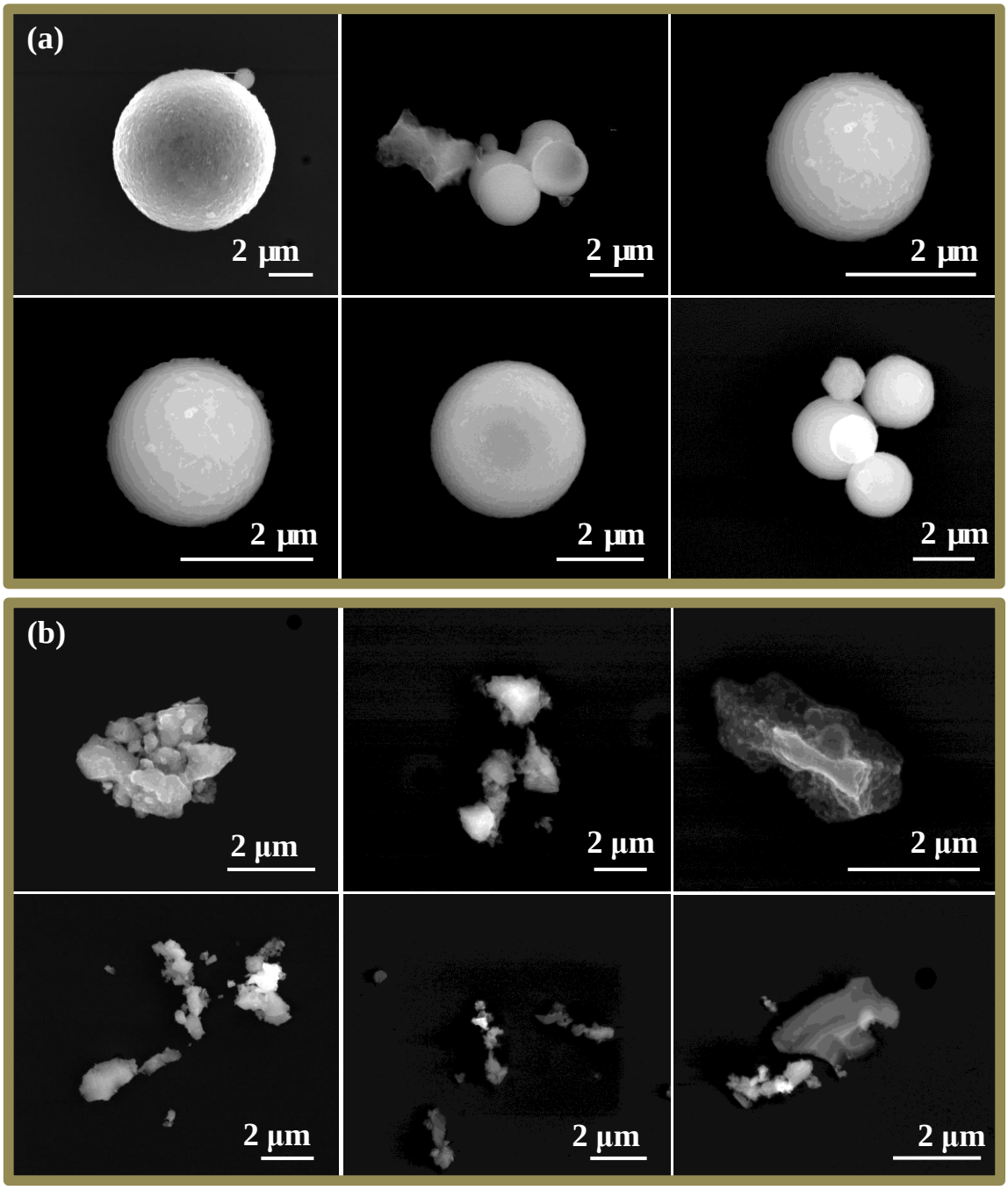

Figure 5.13 Representative secondary electron images of (a) fresh fly ash SRM 2689, and (b) processed fly ash SRM 2689 after dissolution in pH 2 H_2SO_4 for 50 hours.

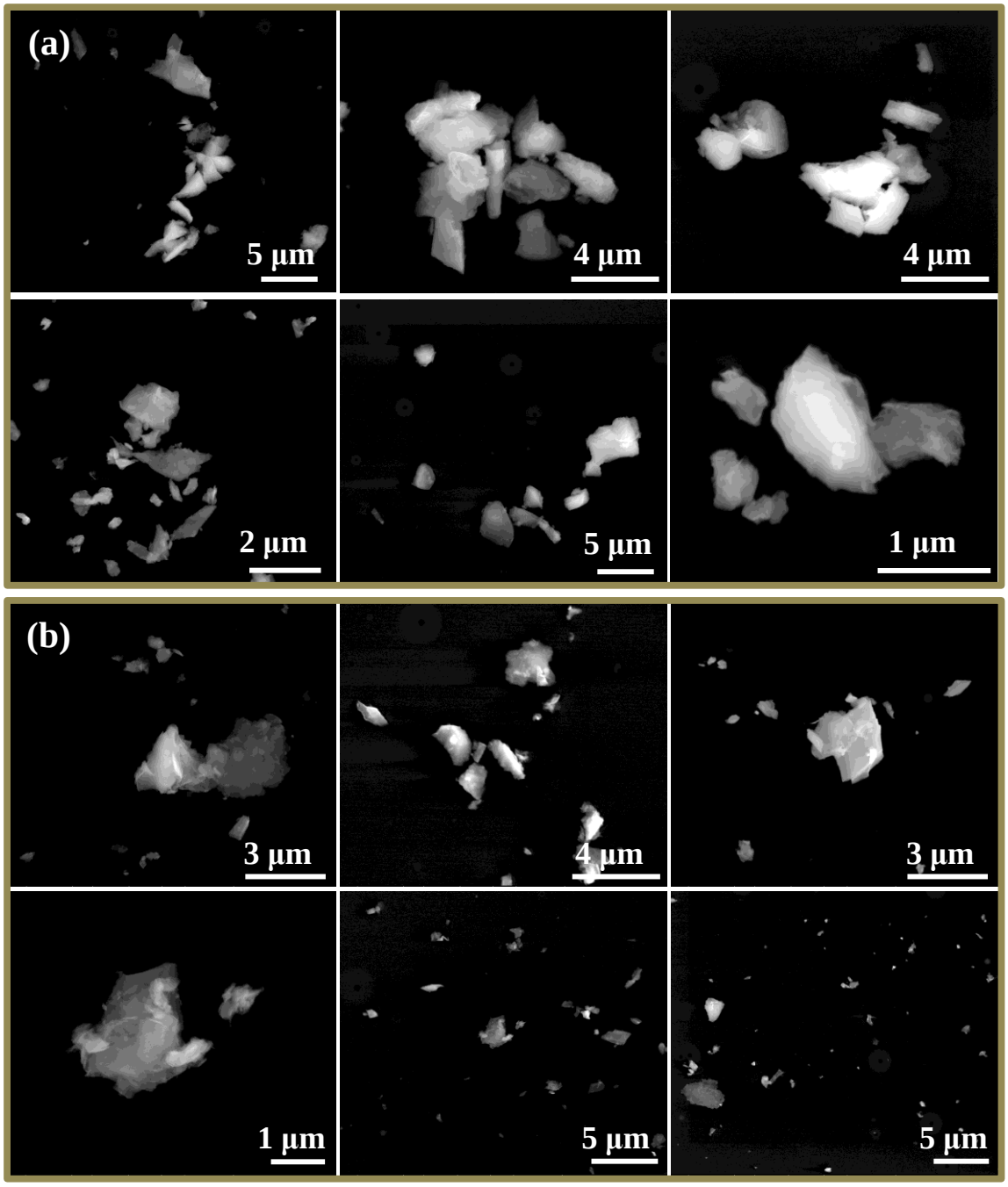

Figure 5.14 Representative secondary electron images of (a) fresh Arizona test dust, and (b) processed Arizona test dust after dissolution in pH 2 H_2SO_4 for 50 hours.

increase of Fe(II)/Fe_s for AZTD at pH 2 can be explained by the differences in the relative rate and extent of dissolution of the various Fe(II)- and Fe(III)-containing species in AZTD particles.[106] In contrast, the ratio of Fe(II)/Fe_s for FA 2689 shows more significant increase over time in both pH 1 and pH 2 solutions.

5.4.4 Morphology and Chemical Composition Change of Fly Ash and Arizona Test Dust during Simulated Atmospheric Processing

FA particles underwent significant morphology changes in the dissolution process as seen in SEM images shown in Figure 5.13. Compared with fresh FA particles as shown in Figure 5.13a, these processed FA particles collected after dissolution at pH 2 for 50 hours, as shown in Figure 5.13b, were found to produce smaller flaky precipitates with irregular shaped morphology as particles disintegrate. As discussed earlier, fresh FA spheres were attached with iron oxide aggregates, which first released from solid phase in the initial dissolution process. Ferrous iron in aluminosilicate glass was mainly present in the matrix of FA particles. As FA particles dissolve and break up into smaller fragments more ferrous iron comes in contact with the low pH solution and therefore can be released into the aqueous phase, displaying a progressive increase of Fe(II)/Fe_s as shown in Figure 5.12b. The disintegration of FA particles into smaller fragments also leads to a continuous and less pH-dependent release of iron compared with AZTD as shown in Figure 4a.

SEM images for fresh and processed AZTD particles were also collected as shown in Figure 5.14a and Figure 5.14b, respectively. Unlike FA particles, fresh AZTD particles exhibit irregular shape and a wide size distribution. In addition, the morphology of AZTD particles shows no significant change after simulated atmospheric processing.

The relative atomic ratios of Fe-Si-Al and Fe-Si-O elements in individual FA 2689 and AZTD particles after simulated atmospheric processing were also obtained by

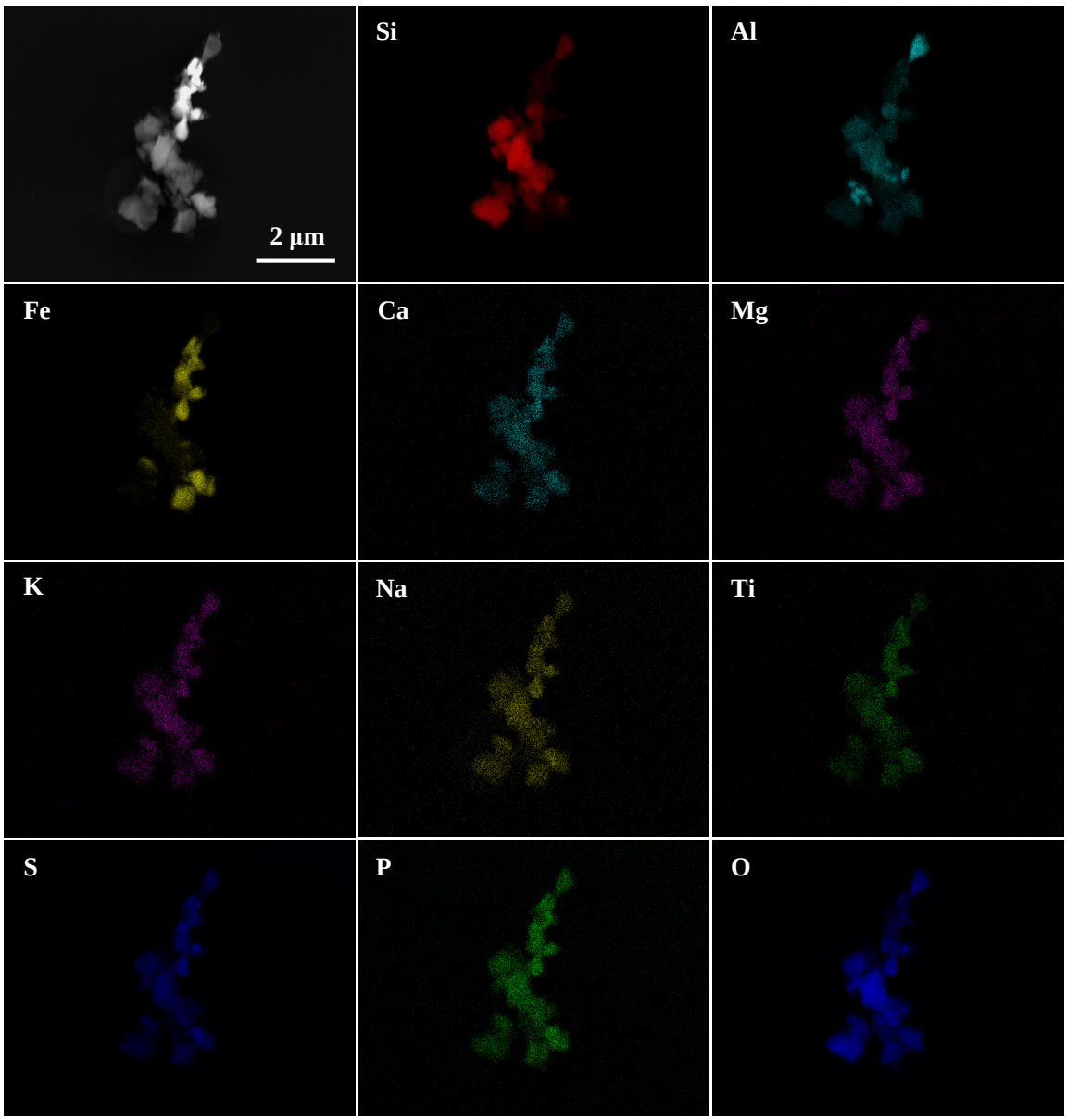

Figure 5.15 Elemental maps of processed fly ash SRM 2689 particles after dissolution in pH 2 H_2SO_4 for 50 hours. The Fe-rich and Si-rich particles are clearly distinguished, further verifying the enrichment of Fe or Si in individual particles.

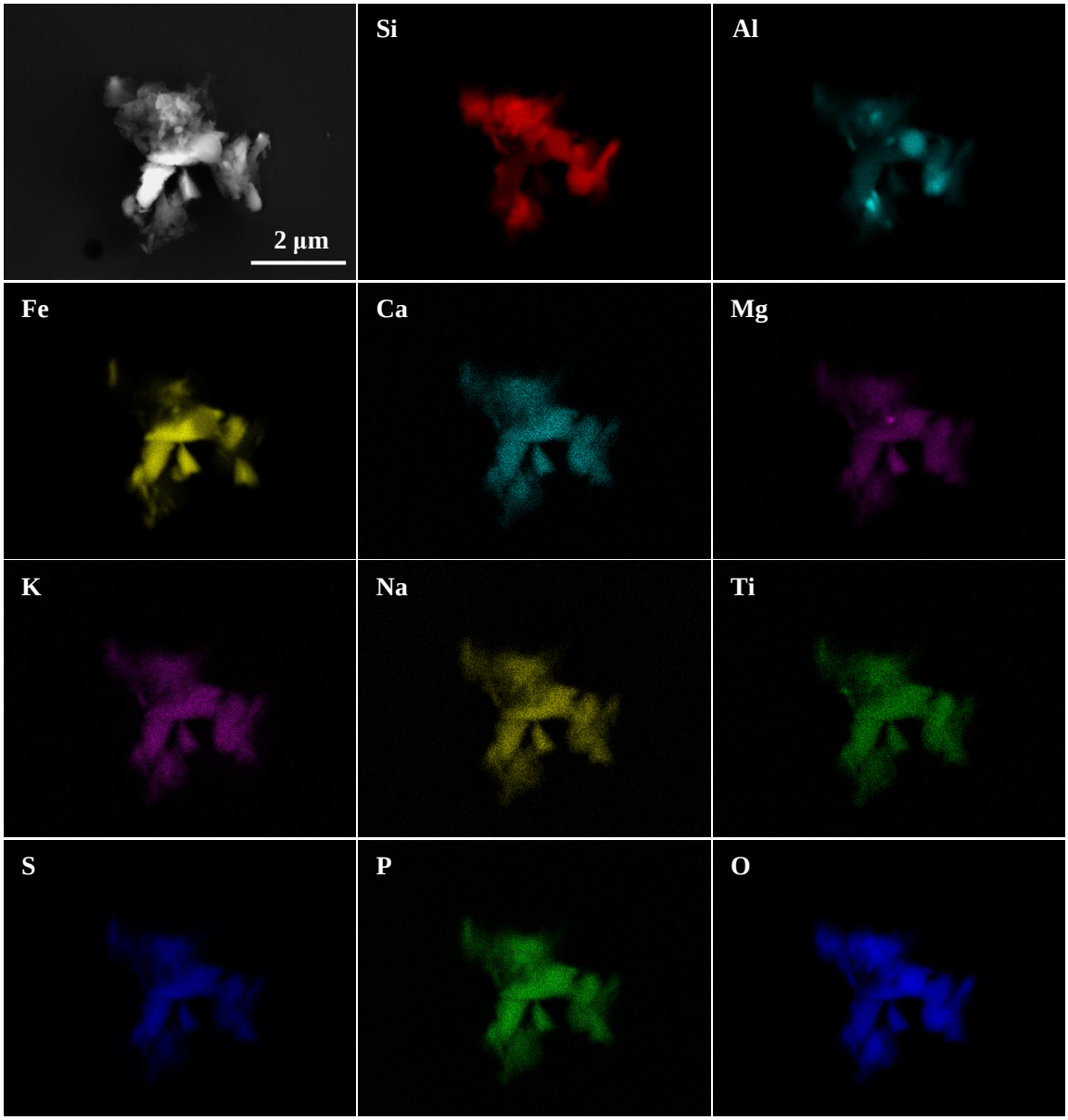

Figure 5.16 Elemental maps of processed fly ash SRM 2689 particles after dissolution in pH 2 H_2SO_4 for 50 hours. The Fe-rich and Si-rich particles are clearly distinguished, further verifying the enrichment of Fe or Si in individual particles.

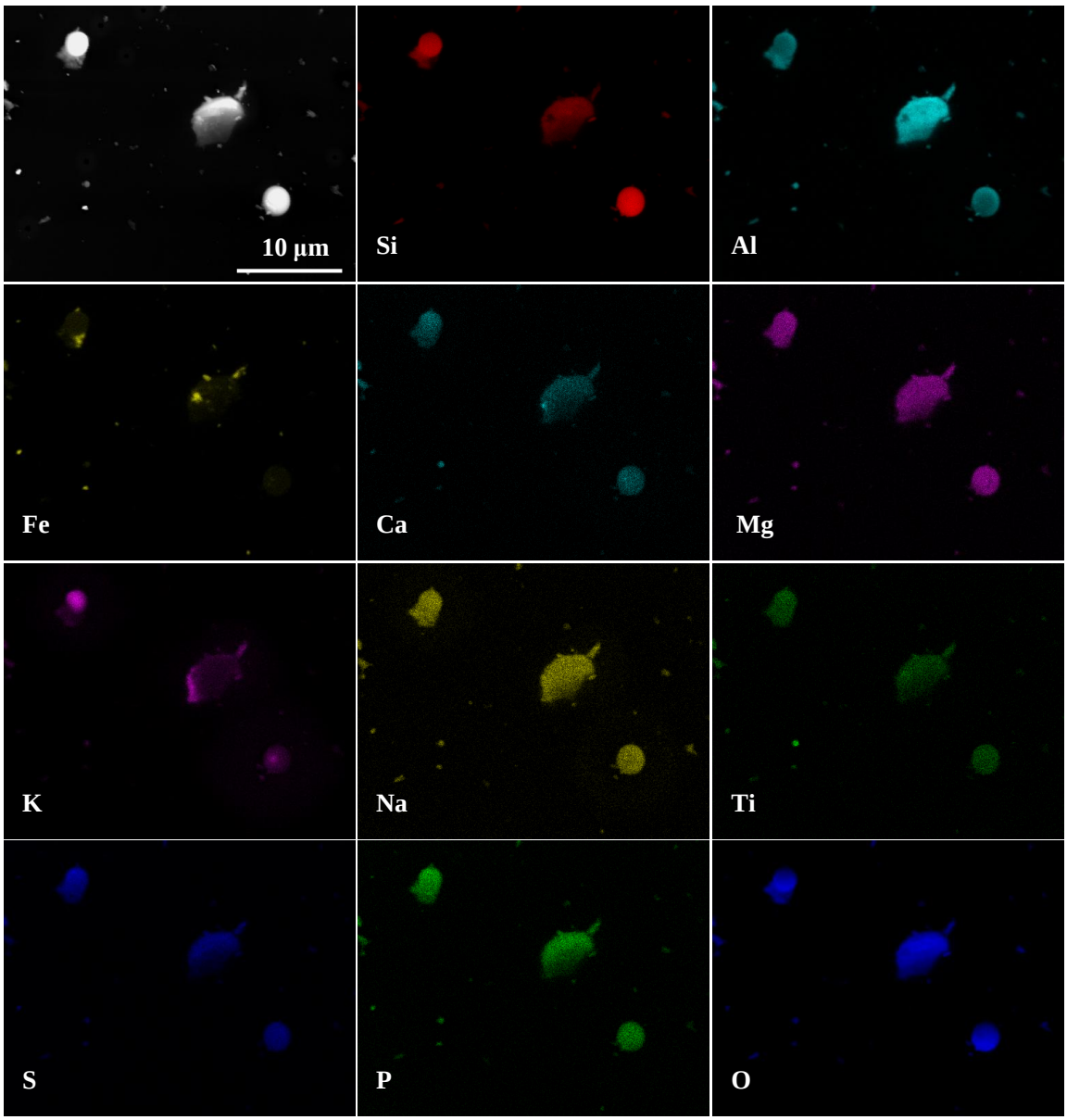

Figure 5.17 Elemental maps of processed fly ash SRM 2689 particles after dissolution in pH 2 H_2SO_4 for 50 hours.

CCSEM/EDX analysis and the results are plotted in Figure 5.4b and Figure 5.5b respectively. Compared with fresh FA particles, FA particles underwent simulated atmospheric processing in pH 2 H_2SO_4 solution for 50 hours were disintegrated into smaller fragments. A major of processed FA particles has size less than 1 μm. The disintegration of FA particles during simulated atmospheric processing is in good agreement with what is suggested from the SEM images of processed FA in Figure 5.13.

More interestingly, processed FA particles mostly had either high Fe or high Si contents, with fewer particles in the aluminosilicate region. The relative atomic ratios of Fe-Si-O elements for processed FA particles in Figure 5.4b indicate that both the Fe/O and Si/O ratios of processed FA particles are less variable compared with fresh ones. The Fe and Si containing species at low oxidation state, like Fe(II), either dissolved into the aqueous phase or transformed into species at high oxidation state. The residual particles are mainly composed of SiO_2, Fe_2O_3 or their mixture.

Elemental maps of processed FA 2689 particles are shown in Figure 5.15-5.17 for further verification of Fe or Si enrichments. The Fe-rich and Si-rich particles are clearly distinguishable from these elemental maps. Elemental maps of process FA particles shown in Figure 5.16 exhibit slightly correlations between Fe and sulfur/phosphorus, indicating the formation of Fe-sulfates/phosphates during simulated atmospheric processing. Processed FA particles that remained relative spherical were also selected for elemental mapping as shown in Figure 5.17. FA particles that showed no significant disintegration were mainly composed of aluminosilicate, with barely iron presents within the particles.

These data suggest that Fe-rich aggregates on the fresh FA surface tended to split off from the original FA spheres and that processed FA particles disintegrate during dissolution. Iron in the aluminosilicate-glass phases was present in the matrix of FA spheres, and kept dissolving into the solution. Meanwhile, given that chemical bonds in

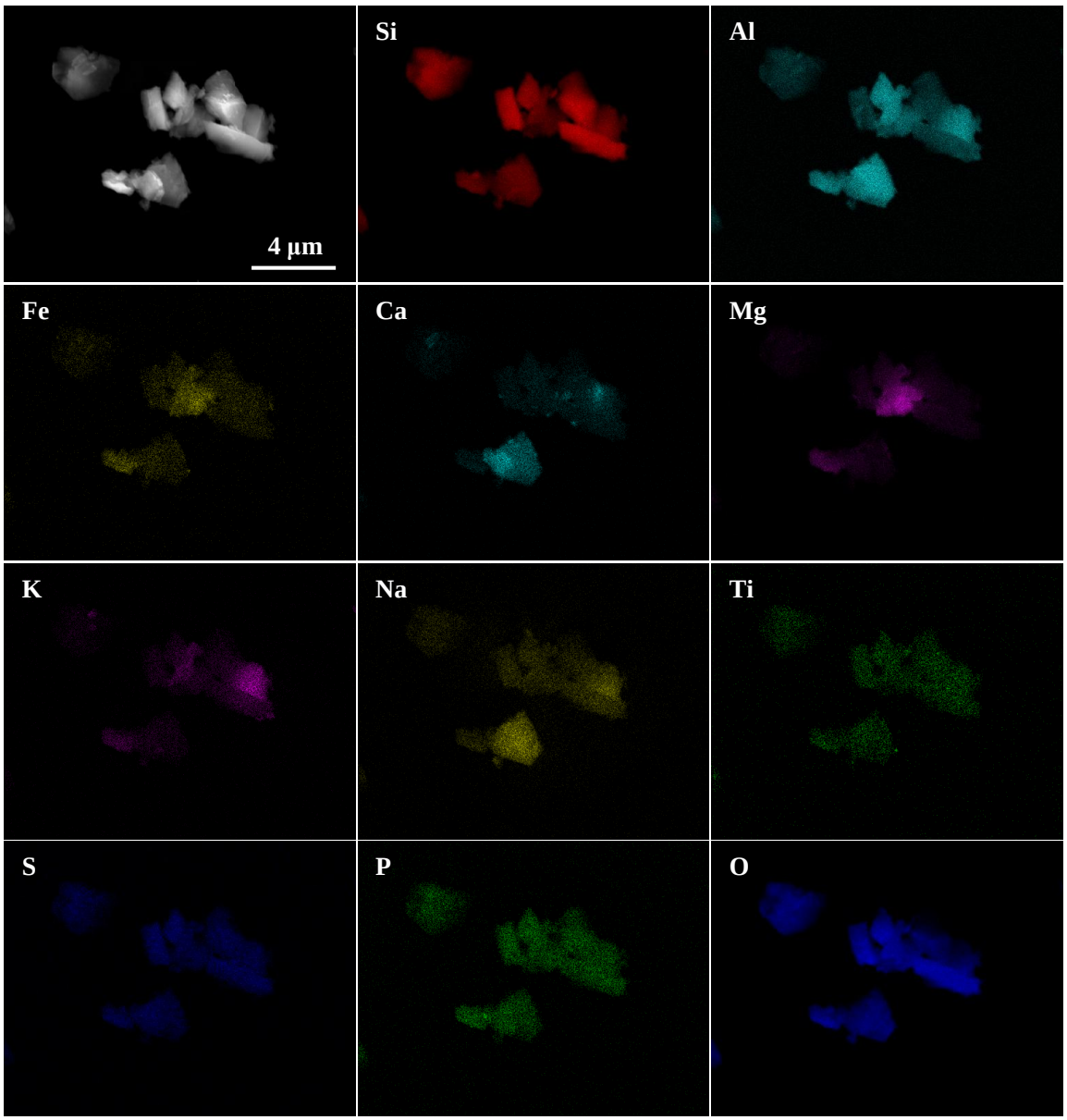

Figure 5.18 Elemental maps of fresh Arizona test dust particles.

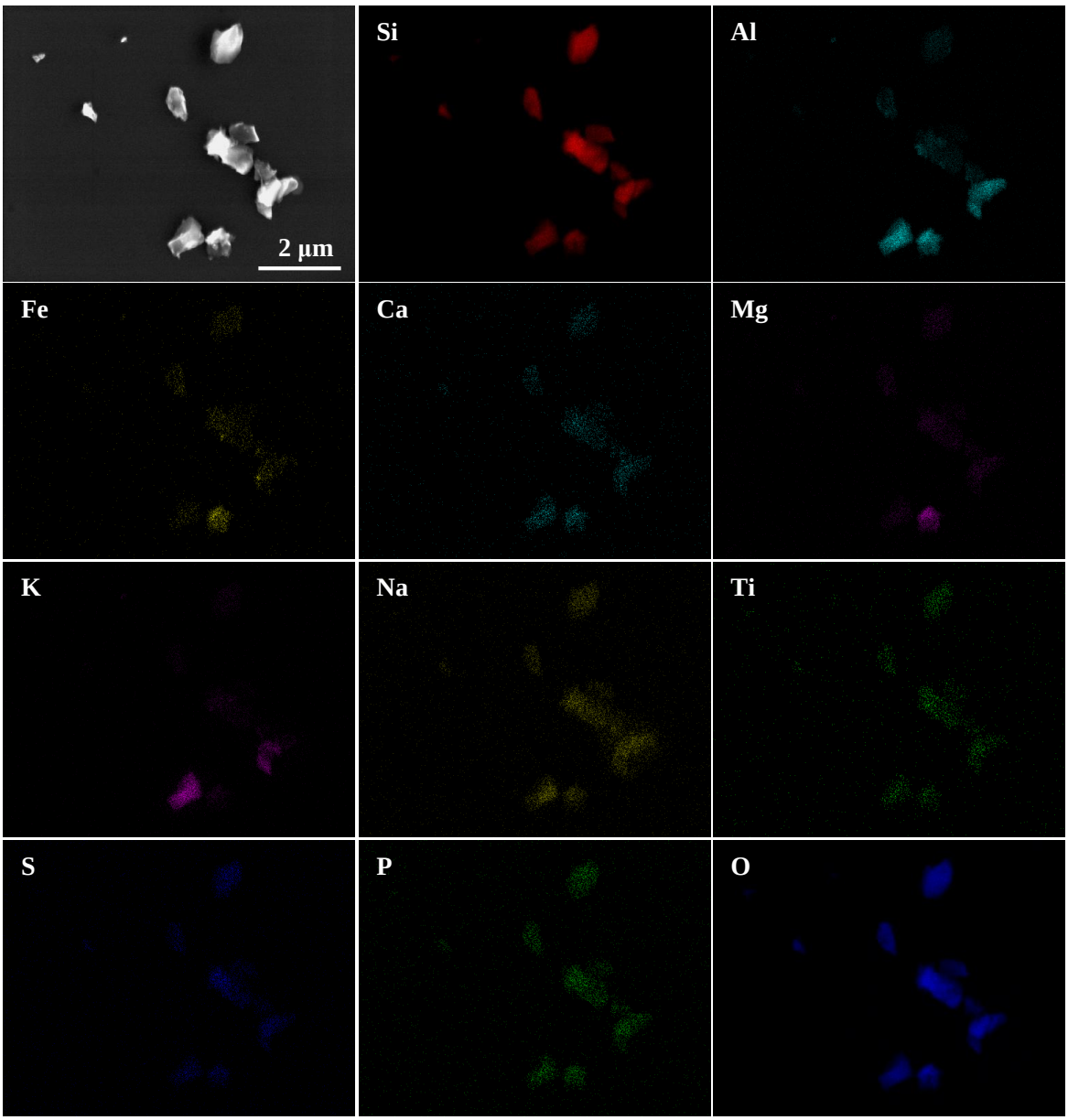

Figure 5.19 Elemental maps of processed Arizona test dust particles after dissolution in pH 2 H_2SO_4 for 50 hours.

aluminosilicate glass are weak and, thus, can easily be attacked and destabilized by protons, the mobilization of Al, K, and Na occur along with the disintegration of FA particles. Individual particle analyses by CCSEM/EDX, therefore, showed the enrichment of Fe or Si in individual particles. A portion of Si-rich particles were attributed to water-insoluble quartz present in fresh FA particles. Processed particles with moderate Si and Al contents were due to water-insoluble mullite or other aluminosilicate minerals present in fresh FA particles. Those aluminosilicate minerals are well crystalline and insoluble so that stay relative stable during simulated atmospheric processing. Therefore it was observed a small portion of spherical FA particles after simulated atmospheric processing as shown in Figure 5.17. Given that FA samples contain significant sulfur and phosphorus, and sulfuric acid was used as the acid media for iron dissolution, formation of Fe-sulfate/phosphates, and even other metal-sulfate/phosphate are plausible.

Unlike FA 2689, processed AZTD particles did not display significant change in the size distribution as shown the triplot diagram (Figure 5.5). Neither did AZTD show significant mobilization of aluminum. Aluminosilicate minerals, a major component of AZTD, is highly crystalline and more stable compared to aluminosilicate glass in FA. Disintegration and mobilization of AZTD occurs less readily than FA. Although a large portion of processed AZTD particles still lies in the marked aluminosilicate region, the relative atomic concentrations of Fe moderately decreased. Iron in aluminosilicate glass is more soluble and, thus, has a higher tendency to be mobilized in simulated atmospheric processing.[106, 192] Elemental maps of fresh and processed AZTD are shown in Figure 5.18 and Figure 5.19 respectively. The distribution of Si is relative evenly in AZTD particles. In contrast, the distribution of other metal, especially Al and Fe is variable among different AZTD particles. Unlike FA particles, the elemental distributions between fresh and processed AZTD particles exhibit no significant difference, further supporting the relative stability of well crystalline AZTD. The data presented here implies that the

heterogeneity and glassy nature of FA particles are critical and unique factors controlling its iron dissolution behavior.

In previous studies from our laboratory, iron dissolution from a variety of mineral dust source materials,[106] including Saudi beach sand, Inland Saudi sand, Saharan sand, and China loess, was investigated. A comparison with the current study shows that the iron solubility of FA is higher than the iron solubility of authentic mineral dusts. The soluble Fe(II) released from FA is also higher compared with mineral dusts, especially Saharan sand and Inland Saudi sand.

Schroth[83] reported that iron solubility of FA formed in oil combustion, in which iron is mainly present as ferric sulfate salt, is approximately 77-81%,which is higher than the solubility of coal FA obtained in this study (20-25%). The physicochemical properties are different between oil FA and coal FA. Coal FA has a crustal-like composition with a great amount of aluminosilicate glass,[237] whereas oil FA tends to be small, vesicular, carbon-rich spheres with high porous surface.[238] The matrix of amorphous carbonaceous material with high surface area to volume ratio makes iron in oil FA potentially more water soluble.

5.4.5 Simulated Cloud Processing of Iron Dissolution in FA

Simulated cloud processing experiments also were conducted for FA 2689 to investigate the role of cloud processing in mobilizing iron, as shown in Figure 5.20. With the addition of FA to water, a rapid increase of approximately 3 pH units was observed due to alkaline components (e.g. CaO and MgO) in FA particles. The suspension of FA was acidified to pH ≈ 2 after 24-hour dissolution, leading to a rapid release of dissolved iron. Increasing pH from 2 to 5 after a further 24-hour period resulted in rapid and almost complete removal of dissolved Fe(III) (Figure 5.20d). The rapid response of dissolved iron to a change in pH indicates that iron dissolution under pH cycling is reversible. The

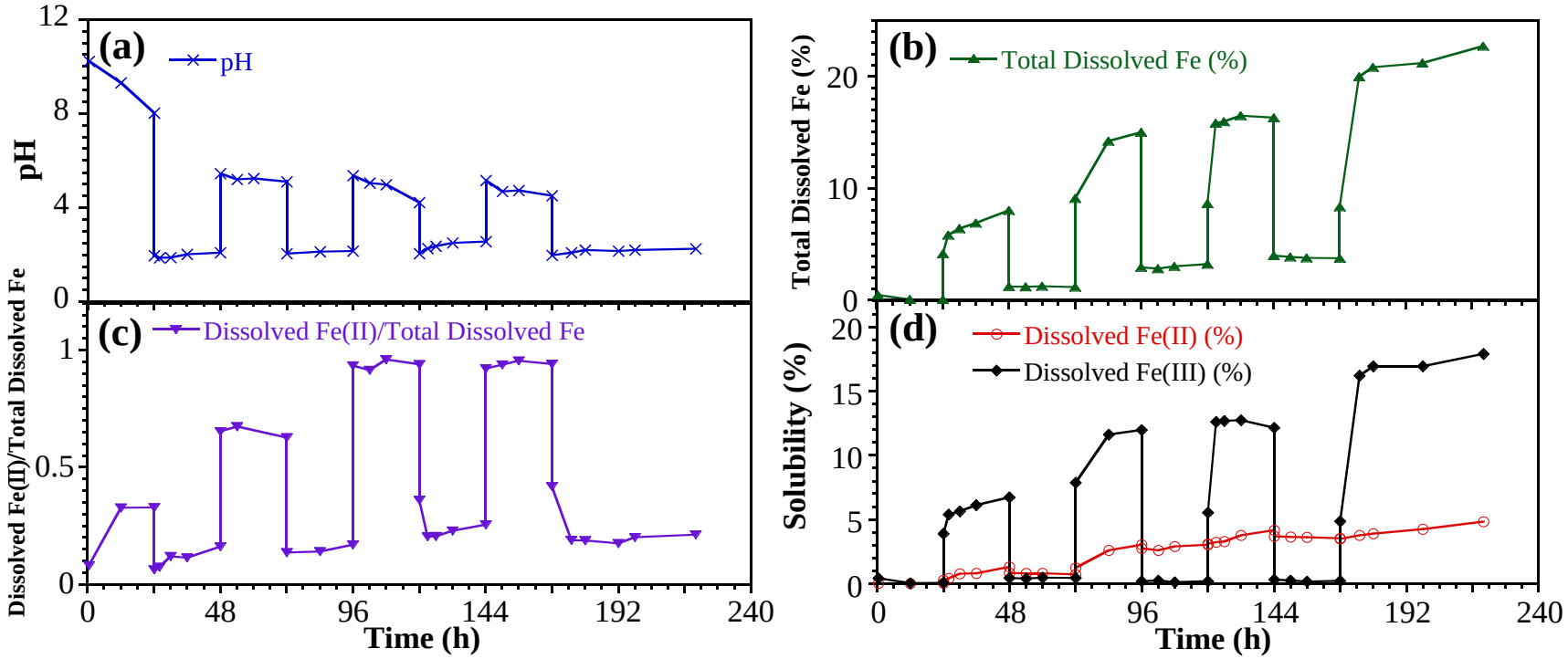

Figure 5.20 Dissolution of iron over time in simulated cloud processing of fly ash SRM 2689 particles: (a) the imposed pH cycle, (b) the corresponding total Fe solubility, (c) the fraction of total dissolved Fe present as Fe(II), and (d) the dissolved Fe(II) and Fe(III).

dissolution and precipitation of Fe(III) is directly driven by acid and circumneutral pH, respectively.

Unlike Fe(III), changing pH had a lesser effect on the dissolved Fe(II). The dissolved Fe(II) exhibited only a slight decrease under circumneutral conditions, resulting in dissolved iron mainly present as Fe(II) at pH ≈ 5. Under circumneutral conditions the slight decrease of Fe(II) was due to oxidation by O_2 to form Fe(III), which subsequently precipitated into the solid phase.[188, 239, 240]

The total Fe solubility increased with pH cycling: it is approximately 21% after three pH cycles, as compared to 8% after the first 24-hour low pH period. The concentration of dissolved Fe after each rapid release at pH 2 was even higher than the concentration before the solution being neutralized to pH 5, indicating that disintegration of FA particles occurred in both acid and circumneutral conditions. Disintegration of FA particles under circumneutral conditions produced highly dispersed Fe-bearing particles exposed to the aqueous phase, enhancing the availability of Fe-bearing species being attacked by protons. The results presented here indicate that cloud processing does play an important role in mobilizing iron from FA.

Spokes et al.[77] have investigated the dissolution of iron from field collected Saharan and urban aerosols under simulated cloud processing. Although they used HNO_3 rather than H_2SO_4 for acidification and the mass loading of particles was much lower compared with the current study, it is still informative to make a comparison. The Fe solubilities from Saharan and urban aerosols after three pH cycles were around 5% and 12%, respectively, which were much lower than the solubility of Fe from FA reported here. The pH cycling had a lesser effect (~1% increase) on the iron solubilities of Saharan and urban aerosols compared with FA. Desboeufs et al.[241] also reported that increasing the number of cloud processing cycles has negligible effect on the iron solubility profile of Saharan aerosol. The significant effect of cloud processing on FA reported here is due

to its glassy nature, a unique characteristic of FA not present in iron-containing dust from other sources.

Table 5.2 Correlation Coefficients between Different Parameters of Fly Ash SRMs 2689, 2690, and 2691

Correlation Parameter		Correlation Coefficient (r)[b]
$Fe(III)_s$	$Fe(III)_{total}$	0.97
	$Fe(III)_{oxides}$	-0.27
	$Fe(III)_{glass}$	0.95
$Fe(II)_s$	$Fe(II)_{glass}$	0.81
Fe_s	S.A.	0.60

[a] The fractions of dissolved iron after three cycle simulated cloud processing include Fe(II) ($Fe(II)_s$), Fe(III) ($Fe(III)_s$), and total dissolved Fe (Fe_s). The physicochemical parameters include the fractions of total Fe(III) ($Fe(III)_{total}$), Fe(III) in oxide ($Fe(III)_{oxides}$), Fe(III) in glass ($Fe(III)_{glass}$), and Fe(II) in glass ($Fe(II)_{glass}$) obtained from Mössbauer spectroscopy, as well as surface area (S.A.) obtained from BET measurements;

[b] Large coefficient means high correlation, while small or negative coefficient means insignificant or no correlation.

Simulated cloud processing experiments were also performed for FA 2690 and 2691 for comparison. Similar dissolution trends were observed for both FA 2690 and 2691 as shown in Figure 5.21 and 5.22. FA 2691 yielded the highest total iron solubility. Approximately 70% of the total iron in FA 2691 dissolved into the solution after three pH cycles, compared to 50% and 21% in FA 2690 and 2689, respectively, indicating that

iron mobilization is highly dependent on the physicochemical properties of the FA particles.

The coefficients of linear correlation between dissolved Fe fractions Fe(II), Fe(III) and total dissolved Fe, obtained from simulated cloud processing, and the physicochemical properties, obtained from particle characterization, of three FA samples were calculated as shown in Table 5.2. The dissolved Fe(II) fraction highly correlated (r = 0.81) to the total ferrous iron species present in the FA particles. No relationship was observed between dissolved Fe(III) and total Fe(III) in oxides, with a negative correlation coefficient of -0.27. In contrast, dissolved Fe(III) highly correlated (r = 0.95) to the Fe(III) species in aluminosilicate glass. The calculated coefficients indicate that iron solubility is closely linked to the Fe speciation of particles. Dissolved Fe was mainly released from aluminosilicate glass, supporting previous studies:[191, 192] they suggested that Fe solubility was lowest for the oxides with iron covalently bound in the crystalline lattice compared with iron presented as amorphous glass or in clay mineral.

Baker[242] suggested that surface area plays an important role in iron solubility. The coefficient of total dissolved Fe and the corresponding surface area of three FA particles was 0.60, indicating that surface area mildly affects iron solubility of FA particles. It is noteworthy that with the simulated cloud processing experiments, it is assumed that the alkali FA particles can be completely acidified to lower the surface pH to 2. The amount of acidic substances deposited/formed on the aerosol surface is dependent on the residence time of aerosol particle in the atmosphere and gas species in contact with aerosol during long-range transport. The FA 2691 contains significant higher contents of CaO and MgO, and thus need more acidic species for titration.

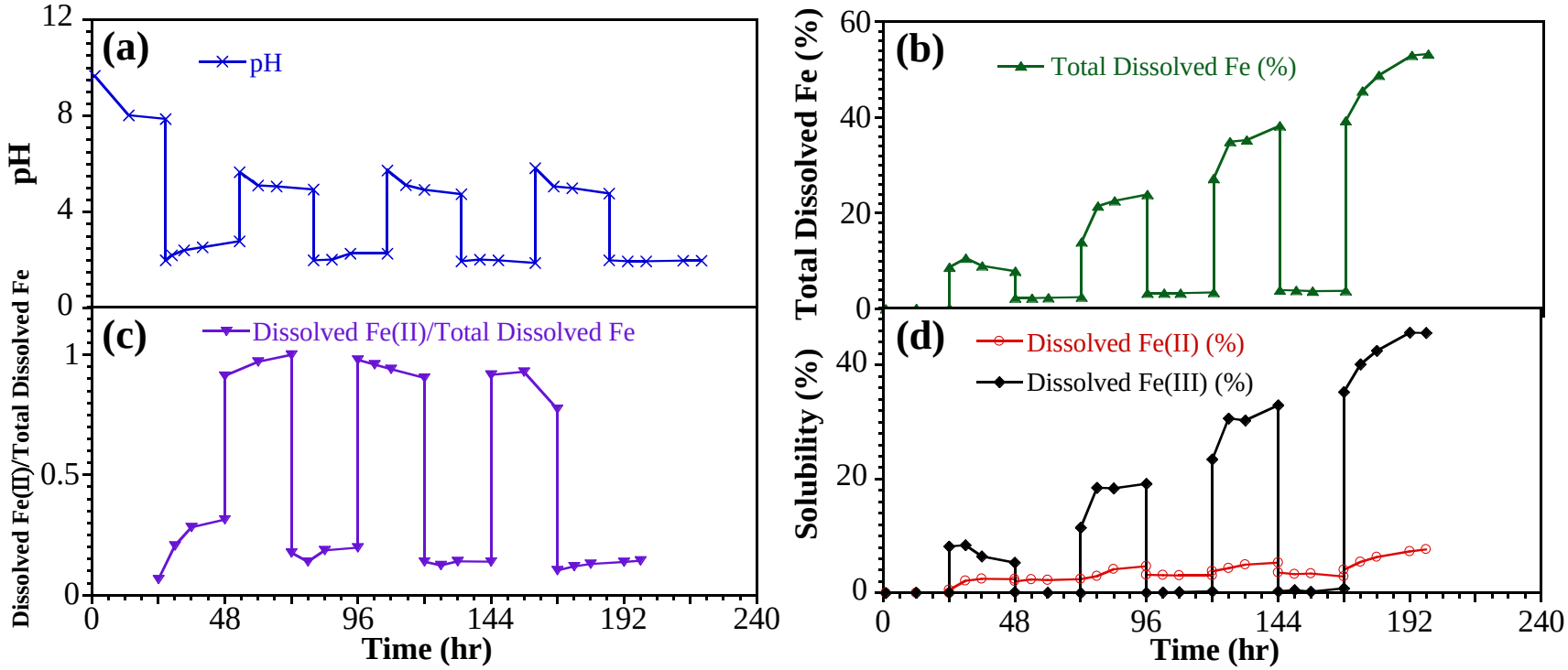

Figure 5.21 Dissolution of iron over time in simulated cloud processing of fly ash SRM 2690 particles: (a) the imposed pH cycle, (b) the corresponding total Fe solubility, (c) the fraction of total dissolved Fe present as Fe(II), and (d) the dissolved Fe(II) and Fe(III).

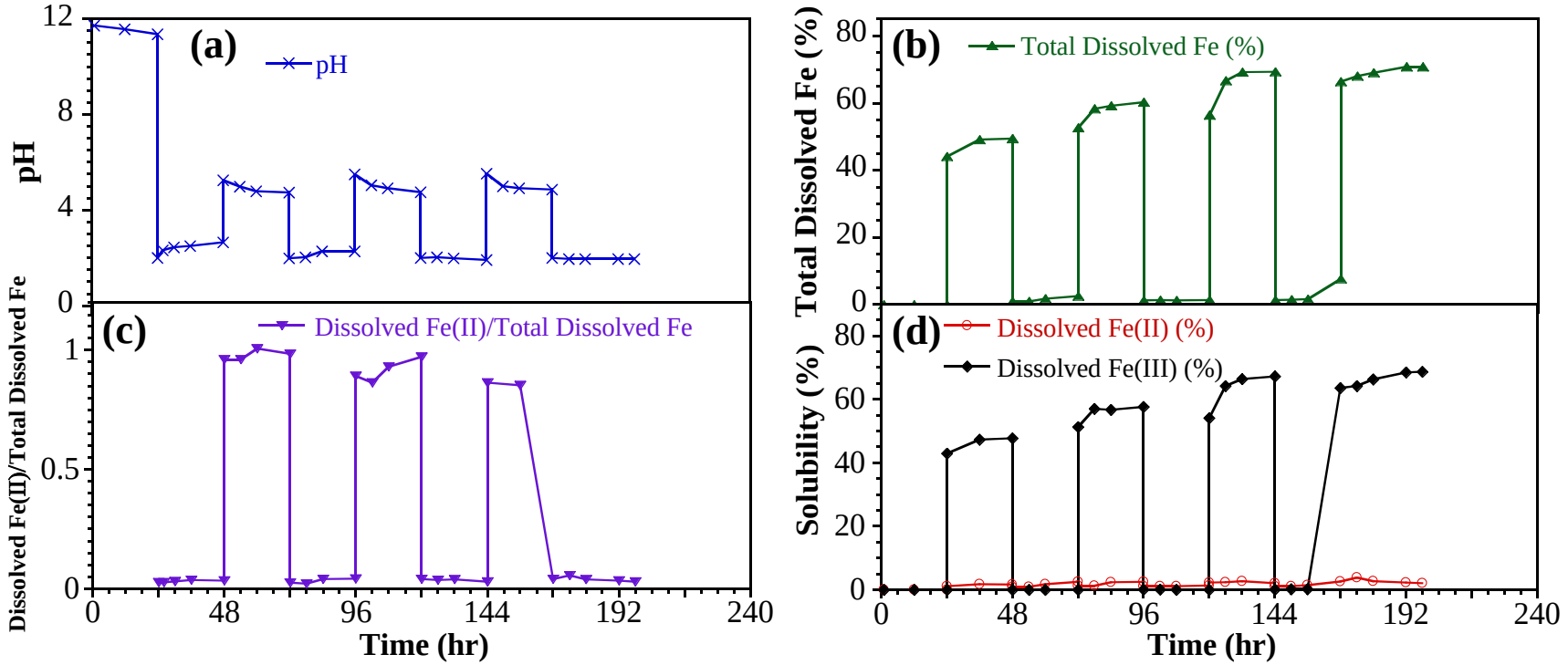

Figure 5.22 Dissolution of iron over time in simulated cloud processing of fly ash SRM 2691 particles: (a) the imposed pH cycle, (b) the corresponding total Fe solubility, (c) the fraction of total dissolved Fe present as Fe(II), and (d) the dissolved Fe(II) and Fe(III).

5.4.6 Solar Radiation Enhances Iron Dissolution during Simulated Cloud Processing.

Simulated cloud processing of FA 2689 under irradiation was also carried out to investigate the effect of solar radiation, as shown in Figure 5.23. Both the concentration of total dissolved Fe and the Fe(II)/Fe_s were markedly enhanced under irradiation. The enhanced Fe(II) production indicates that dissolution proceeded via a photochemical reduction mechanism.[74, 208, 243] The photolysis of surface hydroxyl groups can reduce Fe(III) surface atoms, producing surface-bound Fe(II) species that subsequently detach to yield dissolved Fe(II). A semiconductor mechanism is also plausible: reduced electron/hole pair generation in the iron oxide lattice with subsequent reduction of surface Fe(III) by photovoltaic electrons.[244]

5.4.7 Influence of Different Acids on Iron Dissolution

The effect of different atmospherically relevant acids on the generation of soluble iron species in FA 2689 suspension at pH 2 was investigated, and the results are shown in Figure 5.24. The dissolved iron species, including Fe(II), Fe(III) and therefore total dissolved iron (Fe_s) increased with time in all experiments, indicating that all of the atmospherically relevant acids investigated in this study can mobilize and release considerable iron from FA particles. The relative effectiveness of the acids in total iron solubility, as shown in Figure 5.24c, was in the order of oxalic acid > H_2SO_4 > acetic acid. Specifically, total iron solubilities were 44 $\pm$ 3 %, 16 $\pm$ 1 %, and 9 $\pm$ 1 % after 45 h of dissolution in pH 2 oxalic acid, H_2SO_4, and acetic acid, respectively. Oxalic acid displayed the highest capacity in mobilizing both Fe(II) and Fe(III) among the three acids.

As revealed in previous studies,[213, 215, 236, 245, 246] proton-promoted and ligand-promoted dissolution are two main mechanisms of iron dissolution from oxides and aluminosilicates. The dissolution reaction is critically dependent on the coordinative

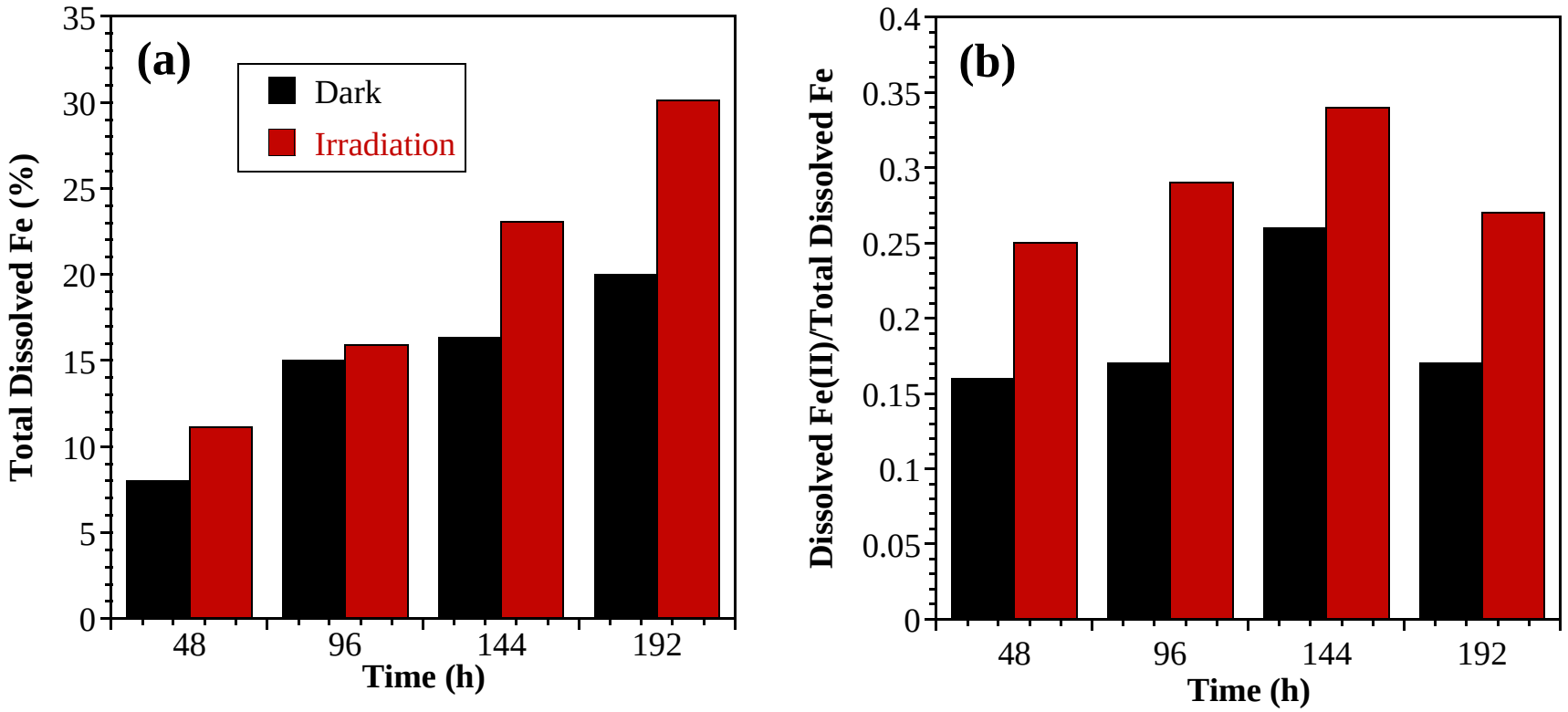

Figure 5.23 Comparison of iron dissolution under dark and irradiated conditions at different sampling points during the pH cycling from fly ash SRM 2689 particles. Irradiation enhances both the total dissolved Fe and the fraction of total dissolved Fe present as Fe(II).

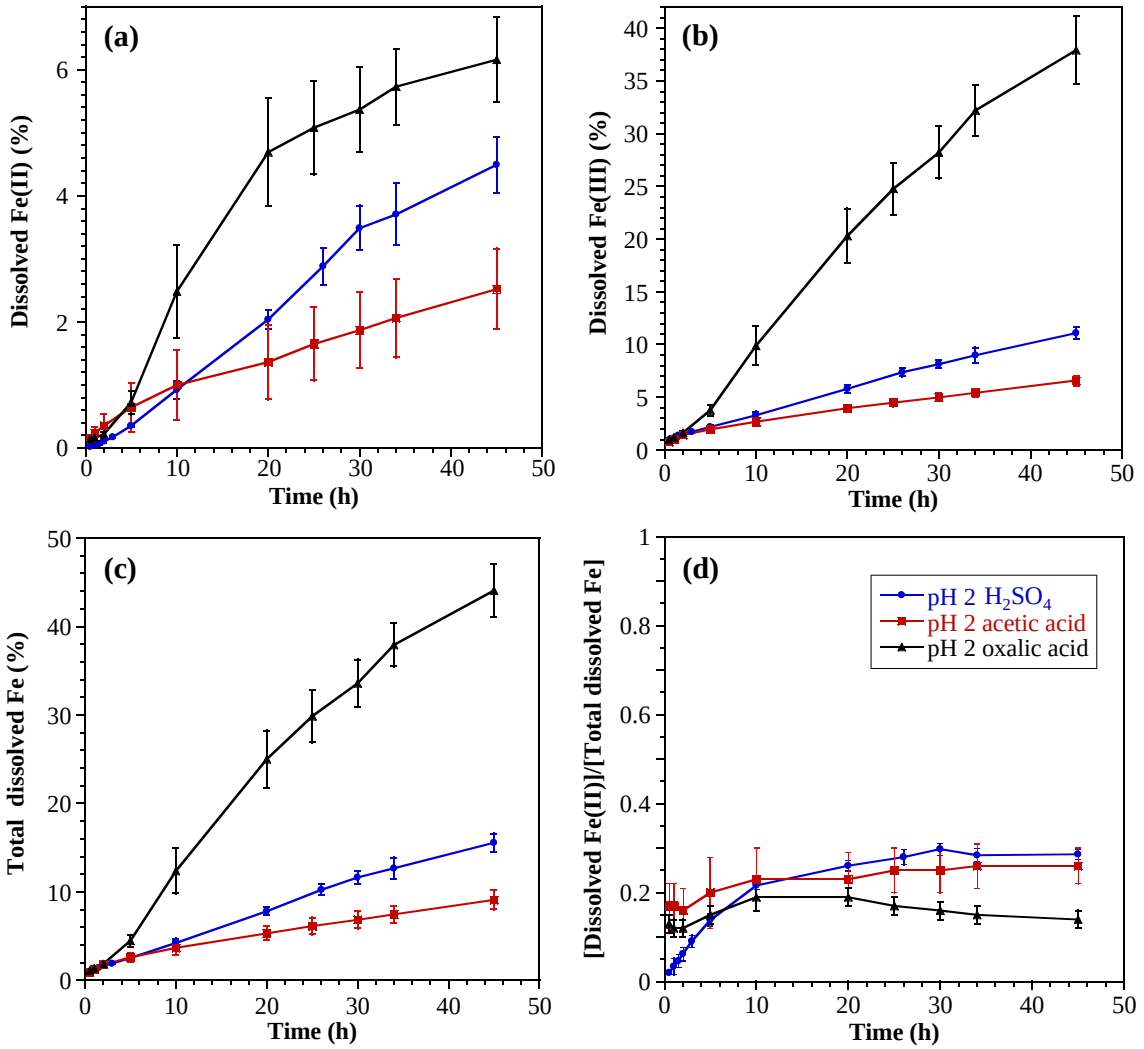

Figure 5.24 Dissolution of fly ash SRM 2689 as a function of time in pH 2 solutions acidified by H_2SO_4, acetic acid and oxalic acid, respectively. Measured dissolved iron is shown as (a) dissolved Fe(II), (b) dissolved Fe(III), (c) total dissolved iron, and (d) the fraction of total dissolved iron present as Fe(II). Reactors contained a solid loading of 2 g L^{-1}. When present, error bars represent one standard deviation from triplicate experiments.

interactions which take place on the surfaces.[213, 215, 247] Functional groups, such as H^+ and OH^- at the surface of particles are able to interact with H^+ ions and ligands to form surface complexes, resulting in the weakening of the bonds in the proximity of a surface iron center, and the slow detachment of surface iron species into the aqueous phase.[213, 215, 247]

If the H^+-ion activity alone influenced the iron solubility, all acidic medium at the same pH should have displayed similar capacities in mobilizing iron species. The different capacities of atmospherically relevant acids in iron mobilization showing here is due to different abilities of the corresponding anions to form soluble complexes with surface iron. oxalate, which can form bidentate ligand with Lewis acid iron center, brings electron density into the coordination sphere of the surface iron, labilizes the surface Fe-O bond, and eventually enhances the iron release into the adjacent solution.

Another plausible explanation for the highest capacity of oxalic acid in iron mobilization is reductive dissolution of Fe(III) in the Fe(II)-oxalate system. Although oxalate alone can promote iron dissolution at a considerable rate, the presence of Fe(II) significantly enhances the dissolution rate at the same concentration of oxalate.[214] The mechanism can be depicted as follows,[214]

$$>Fe^{III}-OH + HC_2O_4^- \longleftrightarrow >Fe^{III}-C_2O_4^- + H_2O \quad (5\text{-}1)$$

$$>Fe^{III}-C_2O_4^- + Fe^{2+} \longleftrightarrow >Fe^{III}-C_2O_4-Fe^{II+} \quad (5\text{-}2)$$

$$>Fe^{III}-C_2O_4-Fe^{II+} + HC_2O_4^- \longleftrightarrow >Fe^{III}-C_2O_4-Fe^{II}-C_2O_4^- + H^+ \quad (5\text{-}3)$$

$$>Fe^{III}-C_2O_4-Fe^{II}-C_2O_4^- \xleftrightarrow{\text{electron transfer}} >Fe^{II}-C_2O_4-Fe^{III}-C_2O_4^- \quad (5\text{-}4)$$

$$>Fe^{II}-C_2O_4-Fe^{III}-C_2O_4^- \longrightarrow >Fe^{II} + Fe^{III}(C_2O_4)_2^- \quad (5\text{-}5)$$

$$>Fe^{II} \longrightarrow >\ldots + Fe^{2+} \quad (5\text{-}6)$$

Oxalate can be adsorbed onto the surface through the complexation with surface iron, and act as an electron bridge to facilitate electron transfer between dissolved Fe(II) and surface Fe(III). Ferrous iron was suggested to be a catalyst so there is no net reduction in the speculated mechanism.[214]

In contrast, sulfuric acid only displayed moderate capacity in iron mobilization given that HSO_4^- and SO_4^{2-} can only form weak complexes with surface iron. The iron solubilities in acetic acid solution were lowest among the three acids investigated in this study, indicating that the monocarboxylic anion has negligible effect on iron mobilization. It has previously reported that dissolution of ripidolite by acetic acid appeared to be mainly related to a proton-promoted dissolution reaction, whereas H_2SO_4 and oxalic acid significantly increased the dissolution rate by forming metal-ligand complexes with framework metals.[248] The dissolution results indicate that ligand-promoted dissolution could be as important as acidic processing in controlling iron mobilization from atmospheric dust.

Figure 5.24d displays the comparison of fractional Fe(II) ($Fe(II)/Fe_s$) in aqueous solutions acidified by H_2SO_4, acetic acid, and oxalic acid, respectively, as a function of time. The $Fe(II)/Fe_s$ stayed relative constant at 27 ± 3 % after 10 h of dissolution in H_2SO_4 and acetic acid solutions, indicating that there was no redox reaction occurred in both systems under dark conditions. The dissolved Fe(II) and Fe(III) arose exclusively from the Fe(II)- and Fe(III)- containing species in the FA particles, respectively. The initial difference of $Fe(II)/Fe_s$ can be explained by the differences in the relative rate and extent of dissolution of the various Fe(II)- and Fe(III)- containing species in different acidic medium.

In contrast, the $Fe(II)/Fe_s$ in oxalic acid solution was lower, and displayed an initial increase followed by a slightly decrease with time. Comparison of the dissolution profile of Fe(II) and Fe(III) in oxalic acid solution with those in H_2SO_4 and acetic acid solutions suggests that the oxalic acid enhanced the formation of dissolved Fe(III) to a

greater extent compared with the formation of dissolved Fe(II), leading to a lower Fe(II)/Fe_s. Given that surface Fe(II)-O bond has larger lability than Fe(III)-O bond,[215] proton alone can effectively destabilize the Fe(II)-O bond with the detachment of iron ions from the surface into the aqueous phase. Ligand-promoted dissolution mechanism therefore displays lesser effect on the dissolution of Fe(II) compared with the dissolution of Fe(III). The catalytic dissolution of Fe(III) in oxalate-Fe(II) system discussed above (Eq. 1-6) can also contribute to the enhanced dissolution of Fe(III). In addition, oxidation of Fe(II) into Fe(III) by oxygen may occur in a considerable rate in aerated oxalic acid solution. Although the oxidation of Fe(II) by oxygen is very slow at pH less than 4 (e.g., $t_{1/2}$ ~ years in air-saturated water),[239] the presence of ligands can accelerate the rate of Fe(II) oxidation by complexation with Fe(II) to change the reduction potential of iron and create a labile coordination position capable of forming an inner-sphere complex with O_2.[247] Ferric iron therefore presented as the main dissolved iron species in oxalic acid solution.

Acid-promoted dissolution experiments were also performed for AZTD for comparison. Similar dissolution trends were observed for AZTD in H_2SO_4, acetic acid, and oxalic acid, respectively, as shown in Figure 5.25. The total dissolved iron in pH 2 oxalic acid solution was approximately 3.6 and 4.4 times greater than those in pH 2 H_2SO_4 and acetic acid solutions, respectively, after 45 h of dissolution in the corresponding acidic medium. Oxalic acid enhanced the dissolution of both Fe(II) and Fe(III) compared with H_2SO_4 and acetic acid. Unlike FA 2689, for which the total dissolved iron was lower than 1% after the initial 0.5 h of dissolution in all acidic medium, a rapid release of iron after the addition of AZTD particles into acidic medium was observed, reaching approximately 5% of total dissolved iron after 0.5 h of dissolution in all systems. The results indicate that a portion of iron species in AZTD particles is highly soluble so can be rapidly mobilized into the aqueous phase. In good

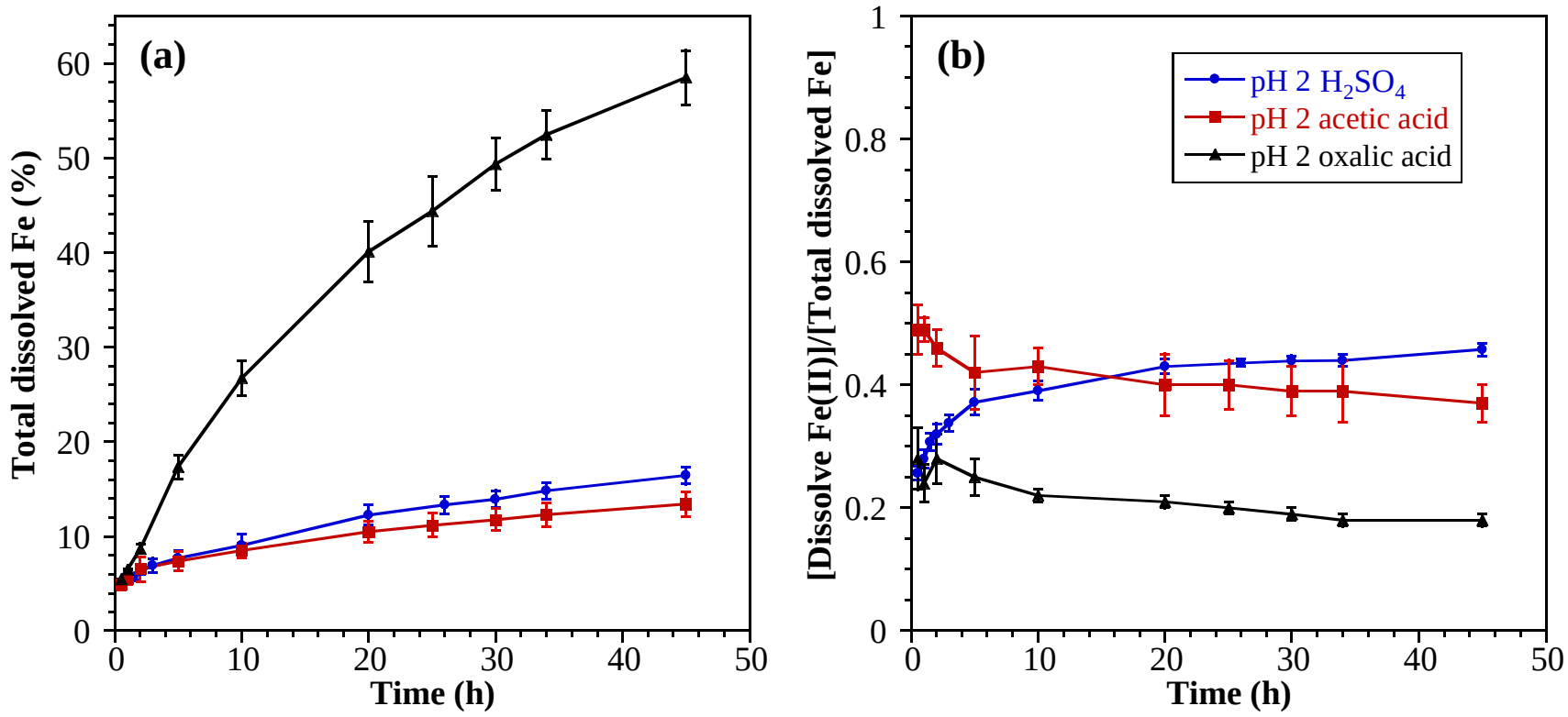

Figure 5.25 Dissolution of Arizona test dust as a function of time in pH 2 solutions acidified by H_2SO_4, acetic acid and oxalic acid, respectively. Measured dissolved iron is shown as (a) total dissolved iron and (b) the fraction of total dissolved iron present as Fe(II). Reactors contained a solid loading of 2 g L^{-1}. When present, error bars represent one standard deviation from triplicate experiments.

agreement with previous research,[106, 192, 209] iron speciation is a critical factor controlling the rate and extent of iron dissolution in aqueous solution.

Our previous research reported that compared with crystalline minerals comprising AZTD, FA particles can continually release dissolved iron into the aqueous solutions acidified by H_2SO_4 as FA particles break up into smaller fragments.[209] In the current study, iron species in FA particles continually dissolved into the aqueous solutions acidified by organic acids in relative constant rates without any plateau being reached on the time scale of the current measurements, indicating that the disintegration of FA particles also occurred in aqueous solutions acidified by organic acids.

5.4.8 Influence of pH of Organic Solution on Iron Dissolution and Dissolved Iron Speciation

Dissolution experiments were performed for FA 2689 in pH 3 acetic acid and oxalic acid solutions to investigate the influence of pH on iron dissolution. Figure 5.26 illustrates the evolution of total dissolved iron and the $Fe(II)/Fe_s$ as a function of time in these experimental systems. As anticipated from established dissolution trends for iron-containing atmospheric dust,[77, 106, 209, 235] increasing pH from 2 to 3 produced roughly 60% and 80% decrease in total dissolved iron concentrations in acetic acid and oxalic acid solutions, respectively. Compared with acetic acid, iron dissolution in oxalic acid showed a more significant decrease as the increase of pH. The concentration of oxalic acid in pH 2 and pH 3 is 1.18×10^{-2} and 9.68×10^{-4} M, respectively. Given that iron dissolution in oxalic acid solution is mainly driven by ligand complexation as discussed above, the drastic decrease of oxalate concentration significantly suppressed iron release from FA in oxalic acidic media at pH 3. The results are in good agreement with a recent laboratory measurement, in which a positive correlation between oxalate concentration and iron solubility from various dust sources was observed.[217] The solution pH could also

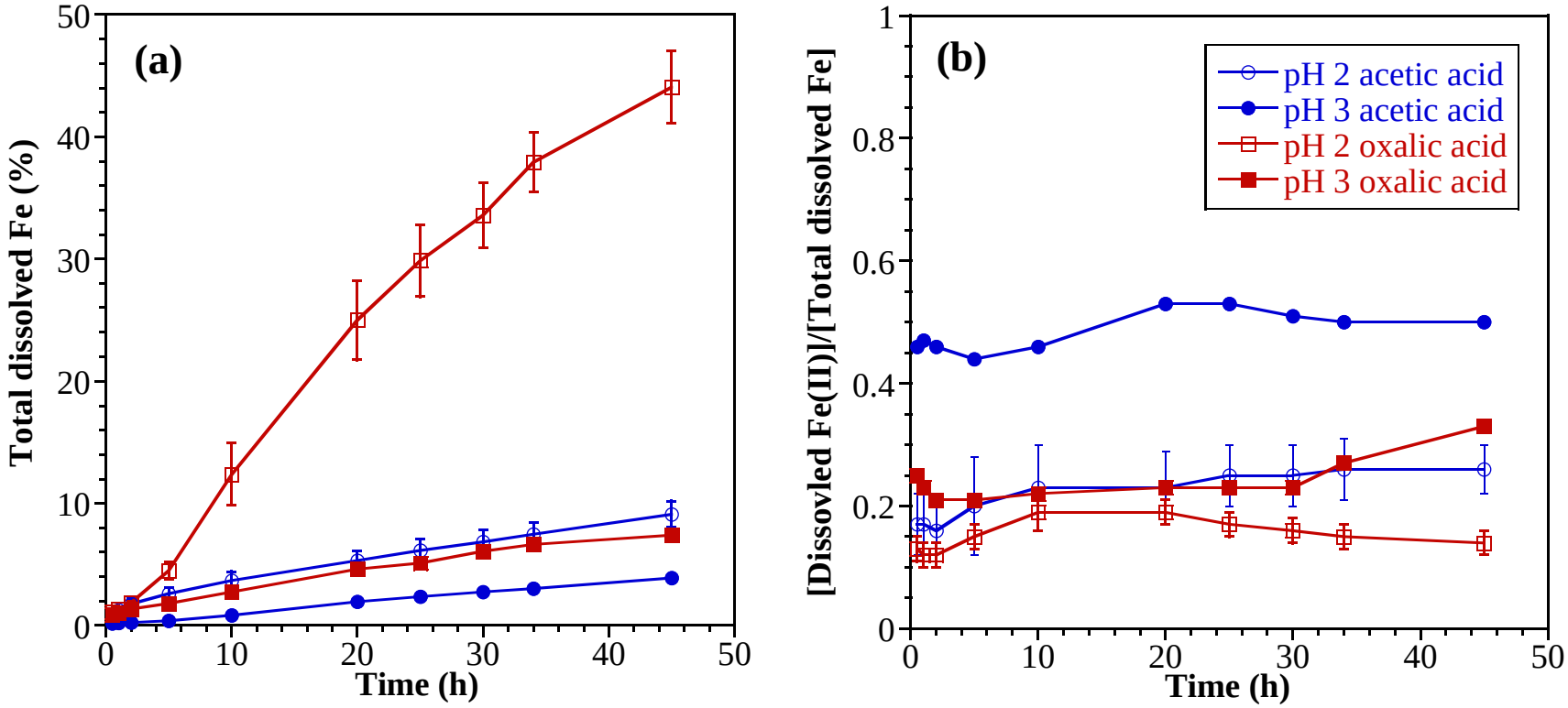

Figure 5.26 Influence of pH on iron dissolution of fly ash SRM 2689 at a function of time in solutions acidified by acetic acid and oxalic acid, respectively. Measure dissolved iron is shown as (a) total dissolved iron and (b) the fraction of total dissolved iron present as Fe(II). Reactors contained a solid loading of 2 g L^{-1}. When present, error bars represent one standard deviation from triplicate experiments.

influence surface complexation of oxalate with iron by controlling charge characteristics of both the surface and the ligand. Increasing pH makes the surface less positively charged, whereas the acid dissociates to become more negative, resulting in less likelihood of the acids to approach and bind to the surface.[249]

The Fe(II)/Fe_s increased with increasing pH in both experiments. Such changes in dissolved iron speciation are due to the greater solubility of Fe(II) relative to Fe(III) solution at high pH. Similar dissolution behavior of FA 2689 in H_2SO_4 solution has been reported in our previous work.[209]

5.4.9 Influence of Solar Radiation on Iron Dissolution and Dissolved Iron Speciation in Organic Solution

Dissolution experiments were also carried out under irradiation in pH 2 acetic acid and oxalic acid solutions, respectively, to investigate the effect of solar radiation on iron solubility, and the results are shown in Figure 5.27. Irradiation displayed significant effect on the iron dissolution in both acetic acid and oxalic acid-containing systems as discussed in detail below.

No discernible change in the concentration of total dissolved iron was observed for the irradiated acetic acid solution. The Fe(II)/Fe_s, however, showed a consistent decrease with time, with less than 5% of total dissolved iron present as Fe(II) after 45 h of dissolution. Comparison with the iron dissolution in the dark, in which the Fe(II)/Fe_s slightly increased with time and reached approximately 22% after 45 h, indicates that irradiation promotes the formation of dissolved Fe(III) in acetic acid solution. It has been well established[239,250,247] that Fe(II) can be oxidized into Fe(III) by active oxygen species like O_2^-/HO_2/H_2O_2 in irradiated aerate waters. Photoreduction of Fe(III) with the formation of Fe(II) could also occur while an electron-donating compound is present.[247, 250] Given that complexation of Fe(III) with acetic acid is negligible under the current

experimental conditions, the photochemically active species has been suggested to be hydrolytic iron,[250]

$$Fe(OH)^{2+} \xleftrightarrow{h\nu} Fe^{2+}OH\cdot \quad (5\text{-}7)$$

$$Fe^{2+}OH\cdot + CH_3COOH \longrightarrow Fe^{2+} + H_2O + CH_3COO\cdot \quad (5\text{-}8)$$

The iron redox cycling can eventually reach steady state , and the ratio of Fe(II)/Fe_s is dependent on rate constants of the reactions involved, solution pH, light intensity, as well as concentrations of iron species, acetic acid and dissolved oxygen. It is noteworthy that while large excess acetic acid was present in the current experiment system, no discernible changes of the concentration of acetic acid and pH were observed.

In the case of oxalic acid, a completely different dissolution kinetics under irradiation was observed. The total dissolved iron in irradiated oxalic acid solution as shown in Figure 5.27a initially increased followed by a rapid decrease, with more than 90% of iron presented as Fe(II) after 10 h of dissolution. In order to obtain detailed information on iron dissolution in irradiated oxalic acid system, a 10-h dissolution experiment under the same conditions was carried out, and oxalate content and pH were periodically determined as well as iron species. Figure 5.28 shows the solution pH, the concentration of oxalic acid, the total dissolved iron and the Fe(II)/Fe_s as a function of time. The concentration of oxalic acid (Figure 5.28b) showed a slight decrease in the initial 4 hours, and then a drastic decrease during 4 to 7 hours, followed by a slow decrease after 7 h of dissolution. The solution pH in the current experiment system was controlled by oxalic acid, and was therefore negatively correlated with the concentration of oxalic acid as shown in Figure 5.28a. While a controlled dissolution experiment showed that no significant decomposition of oxalic acid occurred in the absence of FA

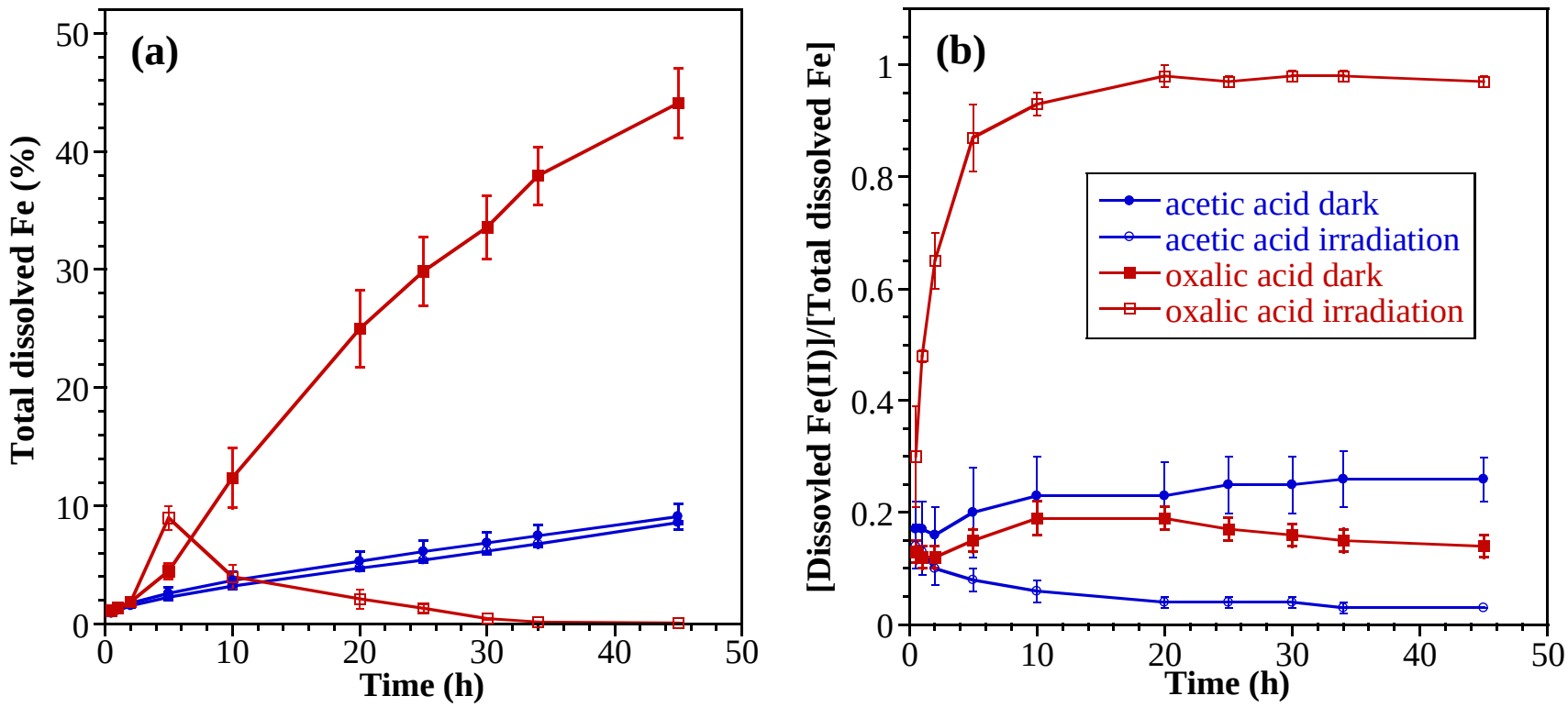

Figure 5.27 Influence of irradiation on iron dissolution of fly ash SRM 2689 at a function of time in solutions pacified by acetic acid and oxalic acid, respectively. Measure dissolved iron is shown as (a) total dissolved iron and (b) the fraction of total dissolved iron present as Fe(II). Reactors contained a solid loading of 2 g L^{-1}. When present, error bars represent one standard deviation from triplicate experiments.

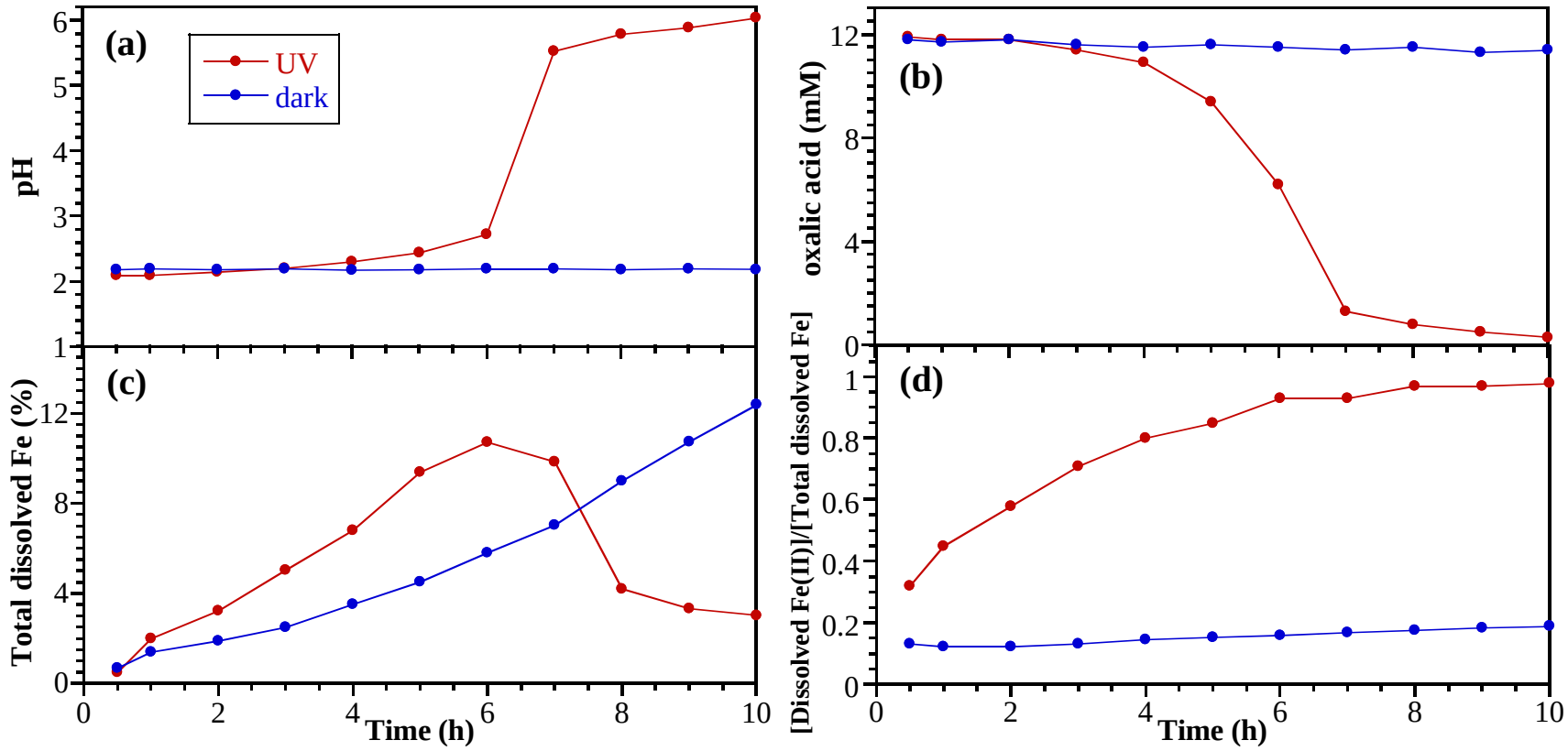

Figure 5.28 Dissolution profile of fly ash SRM 2689 as a function of time in pH 2 oxalic acid under dark and irradiation conditions, respectively. The results are showed the evolution of (a) pH, (b) the concentration of oxalic acid, (c) total dissolved iron, and (d) the fraction of total dissolved iron present as Fe(II).

particles (data not shown), the observed decrease of oxalic acid in FA-containing system was due to iron-catalyzed photodegradation of oxalate.

The first step in the slow process of oxalic acid decomposition during the initial 4 hours was attributed to the complexation of oxalic acid with surface iron, which promotes the detachment of both Fe(II) and Fe(III) from FA particles into the aqueous phase. Photodegradation of oxalate adsorbed on the FA surface could occur under irradiation according to the following mechanism,[251]

$$>Fe^{III}-C_2O_4^{-} \overset{h\nu}{\longleftrightarrow} >Fe^{II}C_2O_4^{-}\cdot \quad (5\text{-}9)$$

$$>Fe^{II}C_2O_4^{-}\cdot \longleftrightarrow >Fe^{II}+CO_2+CO_2^{-} \quad (5\text{-}10)$$

After formation of the Fe(III)-oxalate complex, ligand-to-metal electron transfer occurs under irradiation, resulting in the reduction of structural Fe(III) to Fe(II) and the oxidation of oxalate. The surface-associated Fe(II) can then detach from the surface to generate dissolved Fe(II). The photoexcitation of Fe(III)-oxalate complex through reaction 9 was probably a relative slow process and the rate-limiting step in controlling the photodegradation of oxalic acid, resulting in a slow decrease of oxalate during the initial 4 hours.

With the dissolution of iron species, photodegradation of oxalic acid can also occur in aqueous phase as follows,[250]

$$2[Fe^{3+}(C_2O_4^{-})_n]^{(3-2n)} \overset{h\nu}{\longleftrightarrow} 2Fe^{2+}+(2n-1)C_2O_4^{2-}+C_2O_4^{-}\cdot \quad (5\text{-}11)$$

$$C_2O_4^{-}\cdot + O_2 \longrightarrow O_2^{-}\cdot + 2CO_2 \quad (5\text{-}12)$$

$$HO_2\cdot/O_2^{-}\cdot + Fe^{2+} \longrightarrow H_2O_2 + Fe^{3+} \quad (5\text{-}13)$$

Photolysis of ferrioxalate yields Fe(II) and oxalate radical. The oxalate radical then interacts with oxygen to form superoxide ($O_2^{-}\cdot$) and its conjugated acid, hydroperoxide radicals ($HO_2\cdot$). The $HO_2\cdot/O_2^{-}\cdot$ is a strong oxidant and can rapidly reoxidize Fe(II) to Fe(III), leading to the formation of H_2O_2. With the accumulation of

dissolved iron species in the aqueous solution, the photodegradation of oxalic acid in aqueous phase appeared to be autocatalytic with time, and its concentration therefore displayed a drastic decrease during 4 to 7 hours of dissolutions.

With the increase of pH, ferric iron started to precipitate, displaying a rapid decrease of total dissolved iron and an increase of $Fe(II)/Fe_s$. Even though the fraction of the anionic form of oxalic acid increases at high pH, surface adsorption and complexation of oxalate on the particle surface is suppressed. [72,252] With the less likelihood of surface complexation of oxalate, and the decrease of dissolved Fe(III), photodegradation of oxalic acid was inhibited, leading to a slow decay of oxalic acid after 7 h of dissolution.

5.5 Atmospheric Implications

The source of bioavailable iron from anthropogenic FA has been suggested from recent studies, and this study confirms that coal FA releases larger amounts of iron into water system compared with AZTD and authentic dusts studied in previous works.[106, 197, 208] It is suggest that the disintegration of FA facilitates the mobilization of iron into the aqueous phase. Aluminosilicate glass, a dominant material in FA particles, has a disordered structure that can more easily be destabilized by protons, resulting in the disintegration of the particles. In contrast, mineral dust mainly consists of aluminosilicate minerals (clay) that are well crystallized and more stable. A schematic showing fly ash particles undergo atmospheric processing is shown in Figure 5.29.

Results in this study also suggest that cloud processing results in the disintegration of FA particles with production of soluble iron as the particles move

downwind during long-range transport in the atmosphere. This can at least partially explain the high solubility of iron from anthropogenic aerosols collected in field work.[82, 84] In addition, the slowly disintegration of FA particles can provide a constant release of iron to marine organisms while suspending and recirculating through the HNLC waters. Dissolved iron is mainly associated with the aluminosilicates rather than oxides. Photo-driven solubility of atmospheric iron is also suggested to be important environmental process.

Data reported here and in the literature[83, 106] show that iron solubility of different source materials is generally in the order of: oil FA > coal FA > mineral dust. Aerosol iron solubility is strongly influenced by the source material. Anticipated increases in energy production from fossil fuel and coal combustion have the potential to exert significant effects on the magnitude and spatial distribution of soluble iron deposition to the open ocean. Compared to the increased flux of windblown mineral dust caused by the global expansion of arid and semi-arid regions, increased industrialization, coal combustion, and biomass burning in developing countries (such as China and India) would play a more significant role in increasing soluble iron species to regions of the ocean. While the emission of FA coincides with the emission of trace acidic gases, such as SO_2 and NO_x, the interaction of FA with acidic gases would further enhance their iron solubility.

By comparing of iron dissolution from FA and AZTD particles in H_2SO_4, acetic acid and oxalic acid, it is suggested that proton-promoted and ligand-promoted dissolutions are two main mechanisms in mobilizing iron under the current experimental conditions. Oxalate can form bidentate ligand with Lewis acid iron center, and therefore displayed the highest rate of iron dissolution. Sulfuric acid only displayed moderate rate in releasing iron given that HSO_4^- and SO_4^{2-} can only form weak complexes with surface iron. The iron solubility in acetic acid solution was lowest, indicating that the monocarboxylic anion has negligible effect. Compared with acidic processing, ligand-

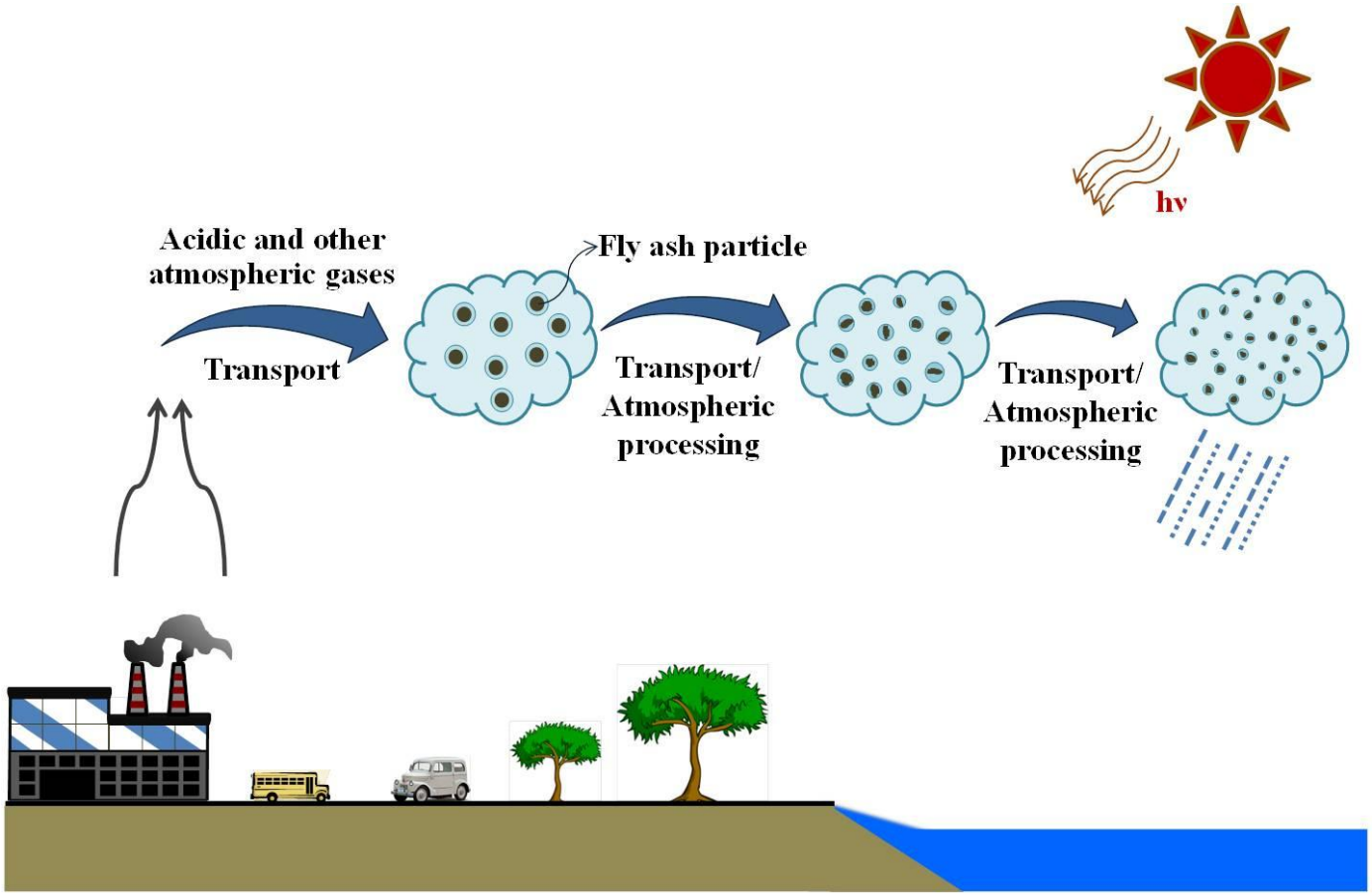

Figure 5.29 Schematic showing disintegration of spherical coal fly ash particles into small irregular fragments during atmospheric transport and processing.

promoted dissolution of iron may play a more important role in mobilizing iron from atmospheric dust. The capacity of organic species in iron mobilization is critically dependent on the ability of these anions to form complexes with surface iron. A ligand to form multiple bonds with surface iron, like oxalic acid investigated here can significantly enhance iron mobilization. In contrast, monodentate ligands, like acetic acid, which presumably can readily penetrate the surface structure, are believed to be less efficient for iron mobilization. When solar radiation is present, iron-catalyzed photodegradation of oxalic acid can lead to a decrease of oxalic acid available for surface complexation as well as an increase of solution pH, and eventually suppress dissolution of iron. In agreement with previous study,[217] photo-reduction of iron on aerosol surfaces is probably not as important as surface complexation in iron mobilization.

Current global-biogeochemical models have generally assumed that the fractional solubility of aerosol iron is constant at 1-2% because of the limitation of data available on iron solubility.[253-257] As indicated in the current study, the assumption was not sufficient to capture the iron distribution on a global scale. Given the potential disintegration of FA particles during long-range transport, the treatment of anthropogenic mode iron processing may in fact be different from dust mode processing. The assessment of dissolved atmospheric iron deposition fluxes and their effect on surface ocean biogeochemistry should be constrained by taking into account the source materials, environmental pH, Fe speciation, type of acidic media and solar radiation in future modeling efforts.

5.6 Acknowledgements

This material is based on upon work supported by the National Science foundation under Grant No. CHE1012037. Any opinions, findings, and conclusions or recommendations expressed in this material are those of the authors and do not reflect the

views of the National Science Foundation. The CCSEM/EDX analysis was performed at the William R. Wiley Environmental Molecular Sciences Laboratory, a national scientific user facility sponsored by the DOE's Office of Biological and Environmental Research and located at Pacific Northwest National Laboratory (PNNL). Pacific Northwest National Laboratory is operated for the U.S. Department of Energy by Battelle Memorial Institute under Contract No. DE-AC06-76RLO 1830. I would like to acknowledge Dr. Alex Laskin at PNNL who gave me enormous help and instruction on the operation of the FIB/SEM system. I would also like to thank Dr. Jonas Baltrusaitis, who helped me to collect and analyze the XPS data, as well as Professor Michelle M. Scherer and her graduate student Dr. Christopher A. Gorski, who helped me collect and analyze the Mössbauer data.

CHAPTER 6

HETEROGENEOUS CHEMISTYR OF NITROGEN DIOXIDE ON LEAD OXIDE PARTICLES AND ITS IMPACT ON LEAD DISSOLUTION

6.1 Abstract

Heterogeneous chemistry of nitrogen dioxide with lead-containing particles is investigated for better understanding heavy metal mobilization in the environment. In particular, PbO particles, a model lead-containing compound due to its wide spread presence as a component of lead paint and as a naturally occurring minerals, massicot and litharge, are exposed to nitrogen dioxide at different relative humidity. Exposed particles are found to increase the amount of lead that dissolves in aqueous suspensions at pH 7 threefold compared to unreacted particles. The surface coverage of adsorbed nitrate is relative humidity dependent. X-ray photoelectron spectroscopy shows that upon exposure to nitrogen dioxide, PbO surfaces form adsorbed nitrates with the surface coverage and extent of formation of adsorbed nitrate relative humidity dependent. Although powder X-ray diffraction analysis shows no bulk formation of $Pb(NO_3)_2$, surface adsorbed nitrate increases the amount of dissolved lead. These results point to the potential importance and impact that heterogeneous chemistry with trace gases can have on increasing solubility and therefore the mobilization of heavy metals such as lead in the environment. This study also shows that surface intermediates, such as adsorbed nitrates, that form can yield higher concentrations of dissolved lead in water systems including drinking water systems, ground water systems, estuaries and lakes.

6.2 Introduction

Due to the increased processing of lead (Pb) ore, the emission of Pb into the environment has drastically increased during the twentieth century. The introduction of tetraethyl Pb into gasoline as an antiknock additive in the 1920s contributed substantially

to increase airborne Pb concentrations. As shown in Figure 6.1, by 2008, Unite States (U.S.) Pb emissions totaled 1,016 tons per year, of which mobile contributed 58% of total Pb emissions, far exceeding emissions from stationary sources.[258] In addition, with the widely application of Pb containing materials, there is the potential for humans to be exposed to these harmful Pb containing materials in water, soil and food.

The adverse health effects of Pb containing materials were discovered shortly after the introduction of leaded gasoline.[259] With studies of decades, the adverse health effect of Pb has been well understood. Childhood lead poisoning remains a major environmental health problem. Research have demonstrated that children with high levels of lead in their bodies can suffer from damages to the brain and nervous system, and behavior and learning problems, such as hyperactivity, slowed growth, hearing problems, as well as headaches. Besides, lead is also harmful to adults, potentially causing reproductive problems, high blood pressure and hypertension, nerve disorders, memory and concentration problems, as well as muscle and joint pain. Since the United States Environmental Protection Agency (EPA) confirmed the health risks caused by exposure of Pb in particulate matters (MA), regulations were issued to protect human health. The legislation set a maximum limit on the Pb content of gasoline and initiated the phase-out of tetraethyl Pb in gasoline. Over the last few decades, lead emissions in developed countries decreased due to the use of the unleaded oil.[97] In spite of that, due to the widespread commercial use of Pb containing materials in batteries, metal alloys, solder, glass and ceramics, lead persists in daily use maintaining its presence and potential for toxic exposure.[260] The exposure of humans to lead is still one of the biggest environmental and occupational concern.[261]

Atmospheric transport and leaching are two primary pathways of environmental heavy metal mobilization.[262] Our interest in this study is related to natural and anthropogenic lead mobilization from stationary or airborne sources through atmospheric processing. Lead in stationary sources, including lead paint, pipes and lead-containing

minerals, are often exposed to trace atmospheric gases. The behavior of materials during atmospheric transport and processing depends on their physicochemical properties, particle size distributions and meteorological conditions. Trace elements associated with atmospheric aerosols can undergo either wet or dry deposition into terrestrial or aquatic environments. While in the atmosphere, atmospheric aerosols can undergo a variety of chemical and physical processing. A very strong relationship , for example, exists between acid rain and heavy metal concentrations for insoluble heavy metals associated with acidic precipitation and accumulation in soil.[263, 264] It is also related to the presence of gas phase NO_2 and SO_2, mainly from anthropogenic emissions like coal-fired power plants.[18]

A recent study showed that when exposed to nitrogen dioxide (NO_2) and ozone (O_3), lead-based paint granules became more available for subsequent transfer due to the reaction of these gases with polymeric binders in paint.[265] This may cause great risks of lead leaching and poisoning, particularly in rural areas where lead-based paints remain in old buildings and machinery. Thus reactions of atmospheric gases with Pb surfaces need to be investigated to provide a greater detail on possible enhancement of Pb leaching in rural and urban environments.

In this study, PbO, a model compound used in paints that also occurs as the minerals massicot and litharge in the environment, is exposed to nitrogen dioxide, a common pollutant in the atmosphere with expected increasing concentrations in the next two decades.[266] Following reactions at different relative humidity (RH), the concentrations of dissolved lead in aqueous suspensions at pH 7 were determined. The results show that lead solubility increases by approximately a factor of three after exposure to NO_2. X-ray photoelectron spectroscopy shows that the resulting surface adsorbed nitrates after exposure to NO_2 lead to the increase in solubility. The environmental and health implications of this work are discussed.

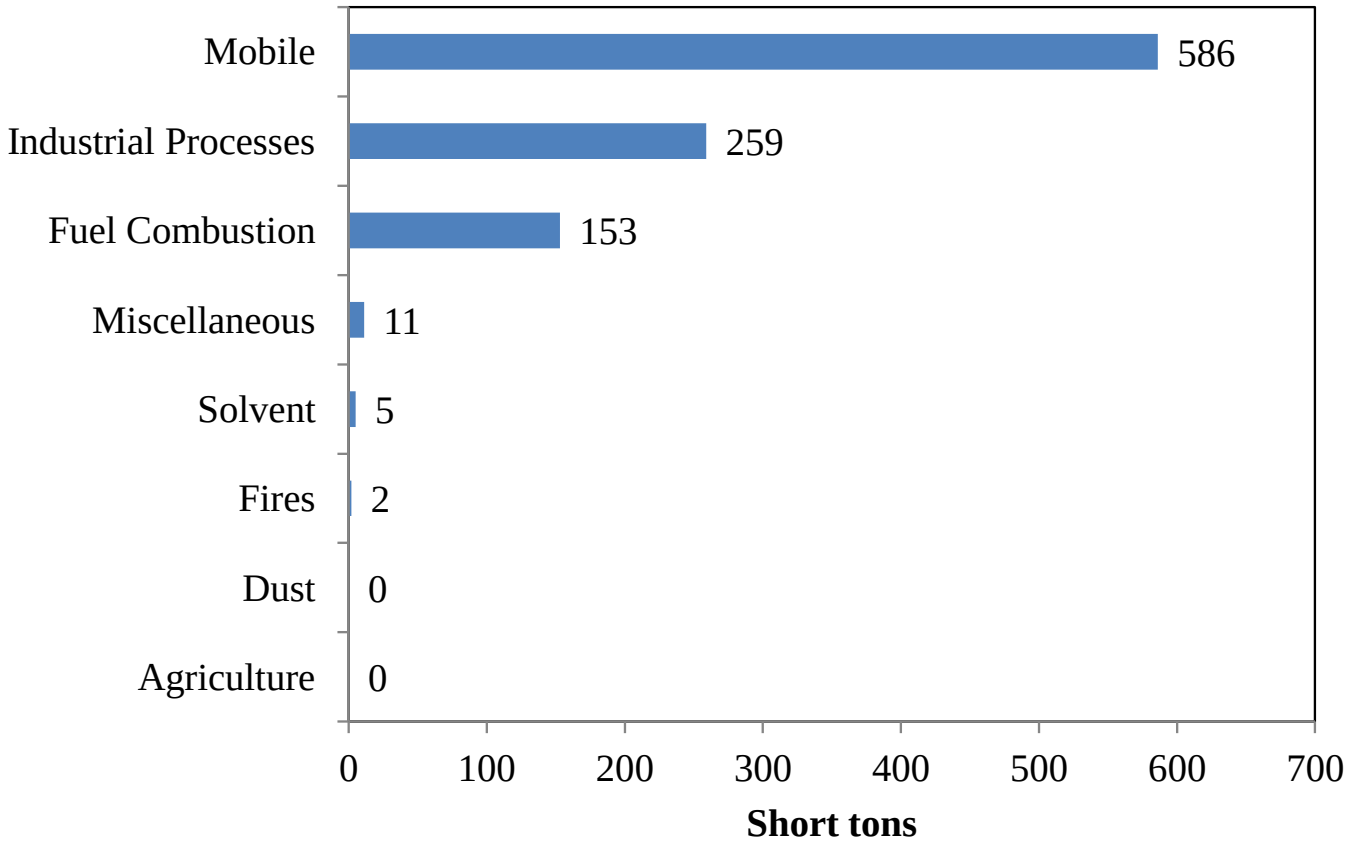

Figure 6.1 National inventory of lead emissions in U.S. in 2008[258]

6.3 Experimental Methods

6.3.1 Materials

Lead oxide, PbO (> 99.9%), and lead nitrate, $Pb(NO_3)_2$ (ACS grade), particles were purchased from Acros Organics. All particles were used as received. Nitrogen dioxide (NO_2, research grade) was purchased from Matheson and used as received. Distilled water (Optima grade from Fisher Scientific) was used for relative humidity studies. Prior to use, the distilled water was degassed several times with consecutive freeze-pump-thaw cycles.

6.3.2 Particle Characterization

BET area was determined using a seven-point Brunauer-Emmett-Teller (BET) technique on the analysis instrument of NOVA 4200e (Quantachrome instruments). Powder X-ray diffraction was performed using Rigaku MiniFlex II with a filtered cobalt source. SEM images were obtained using Hitachi S3400 with 20 kV accelerating voltage operating in variable pressure mode.

6.3.3 Dissolution Measurements

PbO dissolution experiments were performed in a glass reactor at room temperature. First, ex situ heterogeneous reaction of NO_2 with PbO was performed in an overnight evacuated cell with (a) 100 mTorr NO_2 and (b) 100 mTorr NO_2 and 8 Torr H_2O present to evaluate the effect of NO_2 and RH on a possible mobilization of lead. Reacted samples were then transferred into a solution reaction vessel described before.[267] Reacted particles were suspended and stirred in Mill-Q water for 24 hours. The mass loading was 50 g L^{-1}. Aliquot from the supernatant was then passed through a 0.2 μm PTFE filter to remove particles. The concentration of Pb ions was measured using Varian 720-ES inductively coupled plasma-optical emission spectrometer (ICP-OES). Dissolution of

fresh PbO was also conducted under the same conditions for comparison. All experiments were conducted in triplicate and result represents the average of three measurements and the standard deviation.

6.3.4 Surface Analysis

A custom-designed Kratos Axis Ultra X-ray photoelectron spectroscopy system was used to investigate the interaction of NO_2 with lead and lead oxide particle surfaces under different environmental conditions. In a typical experiment, lead oxide particle surfaces were exposed to gas-phase reactants in the reaction chamber in the following order: (1) NO_2 and (2) NO_2 and H_2O vapor at various RH, introducing NO_2 first followed by H_2O vapor. Thus, all the reaction experiments were performed consecutively, using the same sample. The time necessary for the introduction of each reactant was approximately 15 seconds. The resulting gas mixture was allowed to equilibrate with the sample for 30 min before evacuation. The sample holder with reacted samples was then transferred to the analysis chamber for XPS analysis.

6.4 Results and Discussions

6.4.1 Particle Characterization

SEM image and XRD pattern of PbO particles are shown in Figure 6.2. The PbO particles show platelet morphology with a particle size of ~5μm. The large particles observed in SEM image is in consistent with the small BET surface area of PbO, 0.4 ± 0.2 $m^2\ g^{-1}$, determined by BET surface area analysis. The XRD patterns of Pb-containing reference compounds and minerals, including PbO (massicot),[268] Pb metal,[269] PbO (litharge),[270] PbO_2 (plattnerite),[271] Pb_3O_4 (minium),[272] $PbCO_3$ (cerussite)[273] and $Pb_3(CO_3)_2(OH)_2$ (hydrocerussite), [274] are also shown in Figure 6.2 for comparison.

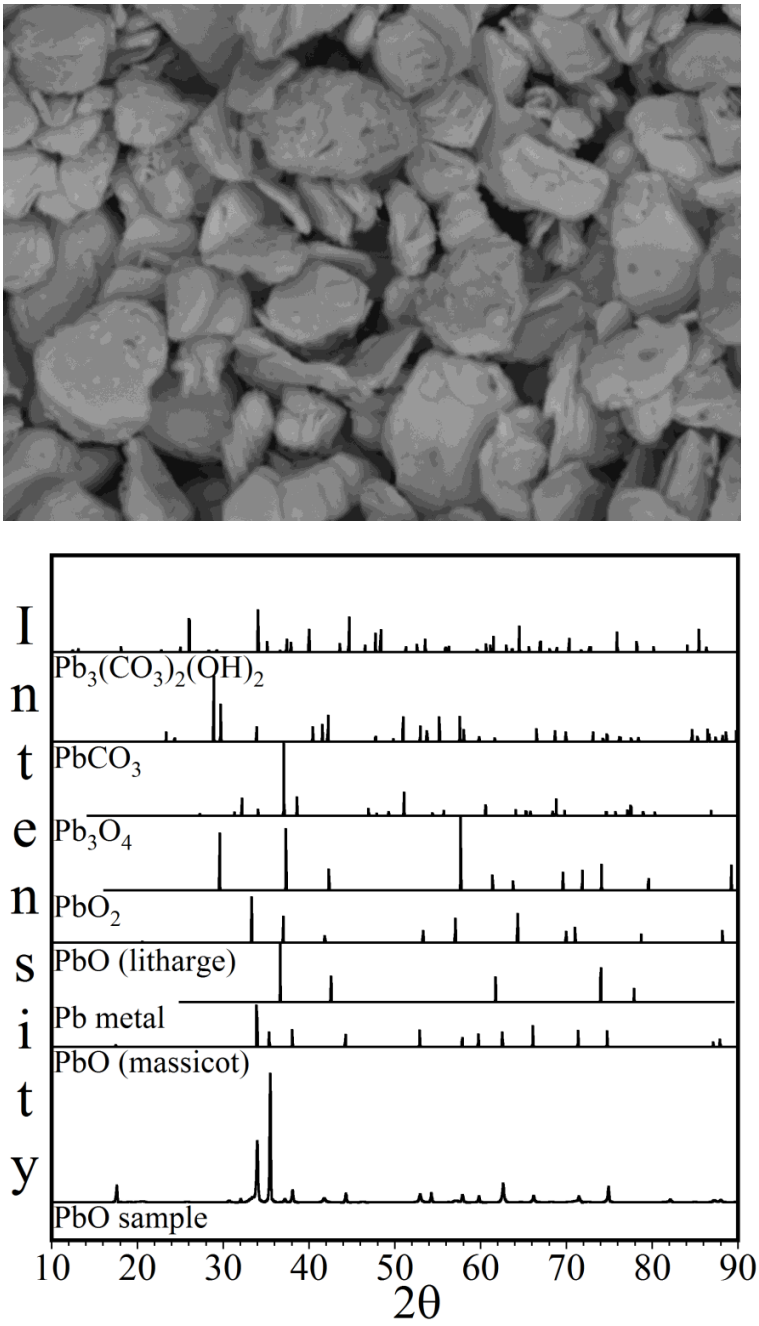

Figure 6.2 SEM image and XRD pattern PbO particles used in the current study. For comparison, XRD patterns of lead containing compounds and minerals, including PbO (massicot),[268] Pb metal,[269] PbO (litharge),[270] PbO_2 (plattnerite),[271] Pb_3O_4 (minium),[272] $PbCO_3$ (cerussite)[272] and $Pb_3(CO_3)_2(OH)_2$ (hydrocerussite)[274] are shown.

Orthorhombic PbO in the form of mineral massicot present as the major constituent (Figure 6.2).[268] Small amounts of other crystalline Pb-containing species were also observed. Indeed, a number of crystalline Pb-containing species are thermodynamically stable in the ambient environments. Formation enthalpies of massicot and litharge, for example, are -217.3 and -219.0 kJ mol^{-1}, respectively.[275] The formation enthalpy is higher for PbO_2, -277.4 kJ mol^{-1}.[275] Pb_3O_4 has highest enthalpy of formation, -718.4 kJ mol^{-1}, followed by $PbCO_3$, -699.1 kJ mol^{-1}.[275] $Pb(OH)_2$ has been reported to have -576 kJ mol^{-1}enthalpy of formation.[276] In addition, cerussite ($PbCO_3$), hydrocerussite ($Pb_3(CO_3)_2(OH)_2$), massicot (PbO) and elemental lead were previously detected via XRD analyses of weather materials of lead bullets collected in shooting ranges.[277] In the current study, reflections at 33 and 37 degrees in XRD pattern of PbO particles are assigned to tetragonal form of PbO, litharge.[270] Reflections at 30, 31, 46 and 82 degrees can be due to more complex phases of lead containing compounds, including cerussite ($PbCO_3$) and hydrocerussite ($Pb_3(CO_3)_2(OH)_2$).

The XRD data showing here indicated the formation of a complex slightly oxidized surface layer on PbO particles under the ambient conditions. The various oxidized Pb-containing species are form via reactions of fresh PbO samples with atmospheric oxygen and carbon dioxide under humid conditions, termed as “atmospheric aging” or “atmospheric processing” here. The reactions are thermochemically favorable, potentially affecting the capacity of lead mobilization for the PbO sample. These processes were further assessed using surface sensitive X-ray photoelectron spectroscopy as discussed below.

6.4.2 XPS Analysis of NO_2 Exposed PbO Particles under Various Environmental Conditions

XPS analysis was performed for unreacted, as well as NO_2 reacted PbO particles. Survey scans were acquired for unreacted PbO particles, as well as those reacted with

100 mTorr NO_2 for 30 min. The obtained XPS data are shown in Figure 6.3. Main peaks in XPS spectra are due to Pb4f, C1s, Pb4d, O1s, Pb4p, Pb4s and O KLL photoelectrons at around 137, 285, 411, 530, 641, 892 and 971 eV, respectively. Low intensity peak appeared at around 400 eV for reacted sample is due to nitrogen compounds indicating that the formation of surface adsorbed species on PbO particles.

To obtain detailed insight of the interaction of NO_2 with PbO particles, high resolution XPS spectra at O1s, N1s, C1s and Pb4f regions were collected as shown in Figure 6.4 with the corresponding binding energy values and their assignments tabulated in Table 6.1. Spectra are shown for unreacted PbO, reacted consecutively with 100 mTorr NO_2, 100 mTorr NO_2 and 1.9, 8 and 18 Torr H_2O for 30 min, corresponding to 9, 38 and 85 %RH. Given that metal oxides are known to form nitrates on the surface via NO_2 adsorption,[278] XPS spectra of $Pb(NO_3)_2$ were also collected and are shown in Figure 6.4 for comparison. $Pb(NO_3)_2$ has enthalpy of formation of -451.9 kJ mol^{-1},[275] indicating that its formation is thermodynamically favorable.

O1s region shows a primary peak at 528.9 eV for unreacted PbO particles due to Pb-O bonds. A peak at 531.1 is assigned to surface hydroxyl groups and/or carbonates.[279, 280] After reaction with 100 mTorr NO_2, the peak of Pb-O bonds at 528.9 eV shifted to 529.6 eV in conjunction with the shift observed in Pb4f region (*vide infra*). A new peak appeared at 533.2 eV due to the O atoms in surface nitrate, in agreement with $Pb(NO_3)_2$ reference O1s peak. This shift of peak due to Pb-O bonds suggests a distinct effect of adsorbed NO_2 product on the electronic structure of PbO. Shift towards higher binding energies can be related to the high electronegativity of nitrate, thus affecting the electronic structure of PbO on the surface. Finally, when the PbO sample was further reacted with 100 mTorr NO_2 and a series of increased RH, peak due to surface Pb-O bonds at 529.6 eV almost completely disappeared showing main surface species as $Pb(NO_3)_2$ (533.2 eV) and small amount of adsorbed hydroxyls/carbonates (531.8 eV). These data suggest that the outermost (~3 nm) layer of PbO particles were reactively

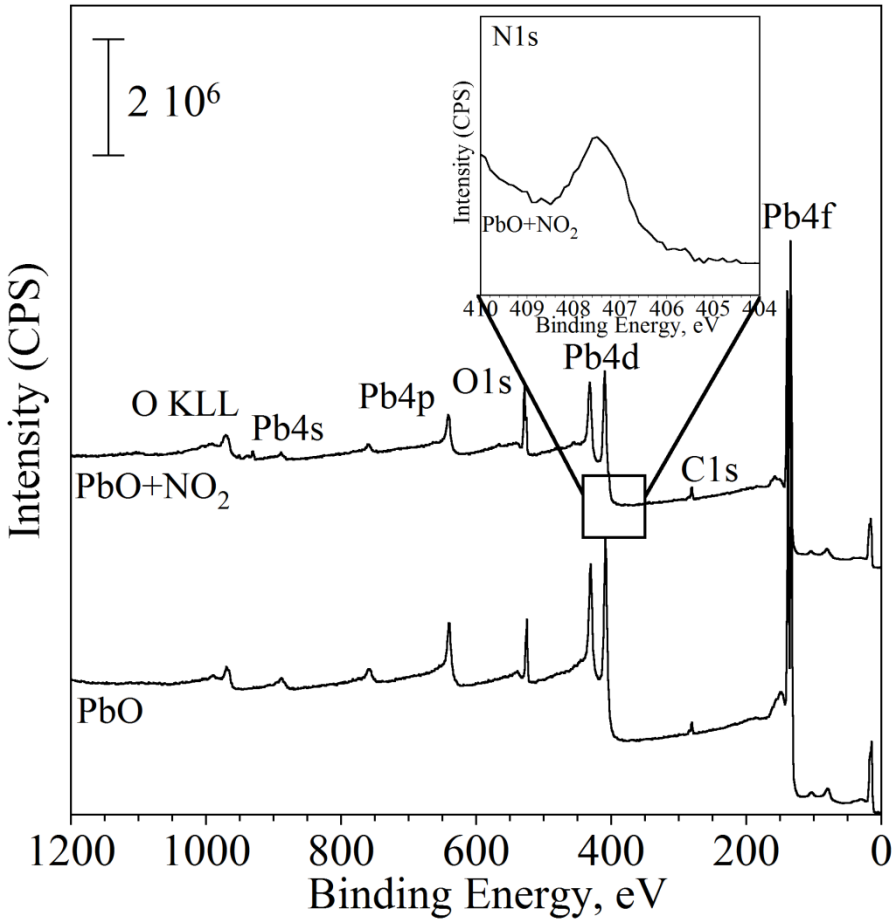

Figure 6.3 Survey spectra of unreacted PbO and after reactions with 100 mTorr NO_2. Inset: N1s region with a peak due to the adsorbed nitrate, NO_3^-, species. Standard deviation was calculated from three independent 30 min NO_2 adsorption experiments.

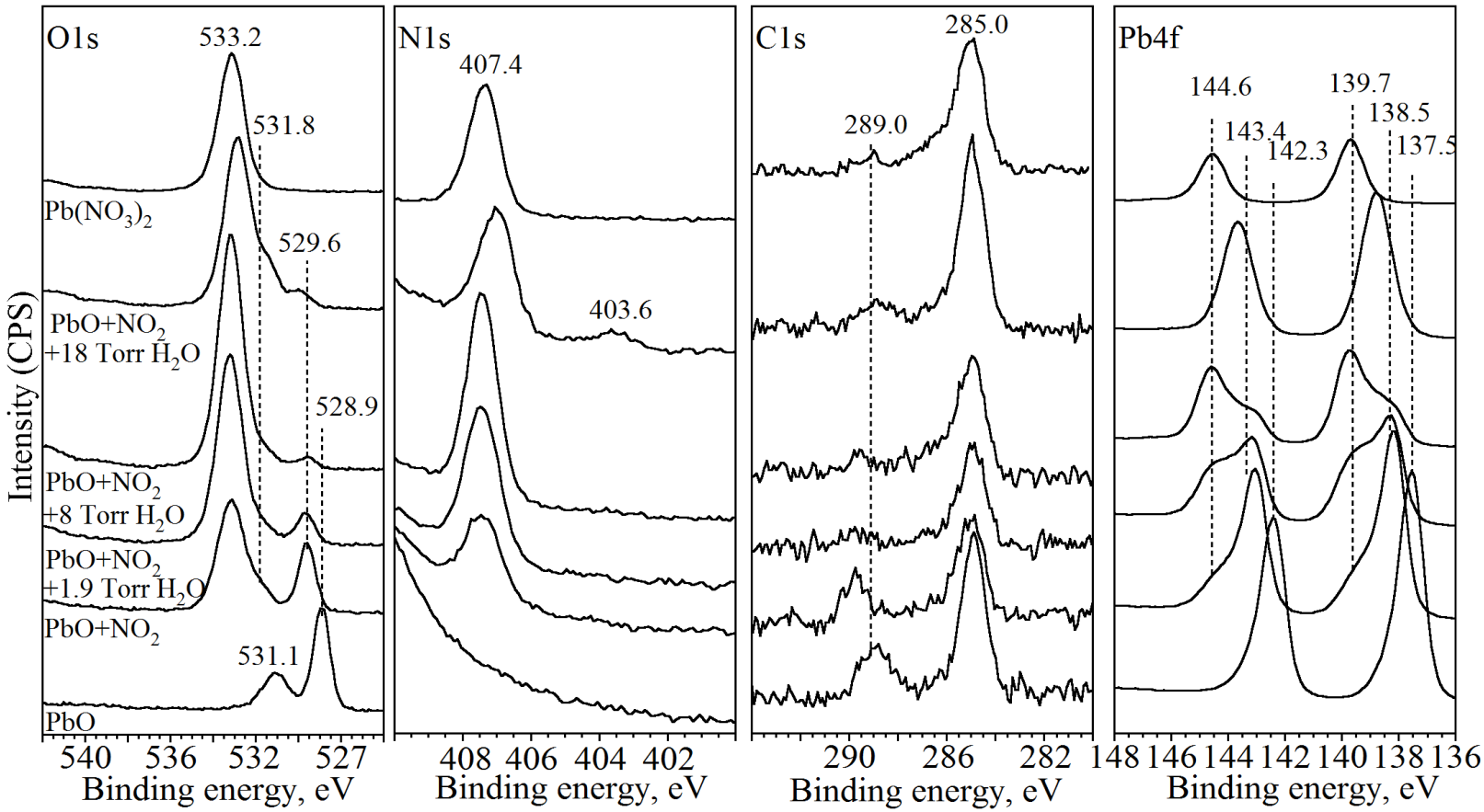

Figure 6.4 High resolution XPS O1s, N1s, C1s and Pb4f spectra of unreacted and reacted PbO under various environmental conditions, as well as $Pb(NO_3)_2$ standard.

Table 6.1 XPS Binding Energy Assignments

Region	Assigned Species	Binding Energy, eV	
		Current Work[a]	Reference
O1s	O^{2-} in Pb-O	528.9(529.6)	528.8 [281]
	OH^-; CO_3^{2-}	531.1(531.8)	531.2 [279, 280]
	NO_3^-	533.2	$Pb(NO_3)_2$ standard
N1s	NO_3^-	407.4	$Pb(NO_3)_2$ standard
C1s	C-C	285.0	285.0 [282]
	CO_3^{2-}	289.0	298.1 [283]
Pb4f	Pb^{2+} in Pb-O	137.5 (138.5)	137.1 [281]
	$Pb(NO_3)_2$	139.7	$Pb(NO_3)_2$ standard

[a] Calibrated to the C1s peak at 285.0 eV

converted into $Pb(NO_3)_2$ via heterogeneous reaction with NO_2 and water greatly enhances the extent of reaction.

The appearance of NO_3^- peak at 407.4 eV, in agreement with the nitrate N1s peak of the $Pb(NO_3)_2$, further confirms the formation of surface nitrate. This surface nitrate species can be formed through a two step reaction mechanism via NO_2 adsorption on surface sites followed by combination of two surface adsorbed NO_2 into surface adsorbed nitrate and gaseous NO.[284] (where ≡Pb represents surface Pb site)

$$\equiv Pb + NO_2(g) \rightarrow \equiv PbNO_2 \quad (6\text{-}1)$$

$$2 \equiv PbNO_2 \rightarrow \equiv PbNO_3 + NO(g) \quad (6\text{-}2)$$

This partitioning has previously been reported on TiO_2 surfaces with NO_3^- ion bound onto Ti^{4+} sites and NO^+ ion on O^{2-} sites.[285] Alternatively, as inferred from the peak shifts due to the electron delocalization in O1s region, surface oxygen atoms can be directly involved into reaction to form adsorbed nitrate via equation (6-3).

$$\equiv PbO + NO_2(g) \rightarrow \equiv PbNO_3 \qquad (6\text{-}3)$$

High resolution N1s spectrum of PbO_2 reacted with 18 Torr H_2O (85% RH) in Figure 6.4 exhibits nitrate peak at 407.1 eV, slightly shifted towards lower binding energies and an additional peak at 403.6 eV. This peak was only apparent at higher RH (85% RH) and can be assigned to several nitrogen containing species, with most likely due to that of surface nitrite, NO_2^-, as determined from analysis of well-defined $NaNO_2$ particles.[278]

Stable NO_2^- formation is possible via adsorption of NO_2 on PbO surface sites via O or N atoms with neighboring oxygen sites strongly hydroxylated and unavailable for further reaction

$$\equiv Pb + NO_2(g) \rightarrow \equiv Pb^+\text{-}NO_2^- \qquad (6\text{-}4)$$

$$\equiv Pb + NO_2(g) \rightarrow \equiv Pb^+\text{-}ONO^- \qquad (6\text{-}5)$$

or via hydroxyl bound complex disproportionation reaction (6-6) by analogy with the mechanisms previously observed on γ-Al_2O_3.[286]

$$2 \equiv Pb\text{-}OH + 2NO_2(g) \rightarrow 2 \equiv Pb\text{-}OH \cdot 2NO_2$$
$$\rightarrow \equiv Pb^+\text{-}NO_2^- + \equiv Pb^+\text{-}NO_3^- + H_2O \qquad (6\text{-}6)$$

At high RH water not only forms a film to protect surface from further reactions, but also affect the product partitioning by inducing the formation of surface adsorbed nitrite. It is noteworthy that PbO used in this work has a low BET surface area (0.4 ± 0.2 m^2 g^{-1}), indicating that the resulting adsorbed species has to be sufficient to generate signal for XPS analysis. It is therefore plausible that surface nitrite species was formed at RH lower than 85% but not sufficient to exhibit a distinct peak in the XPS spectrum.

C1s region for all of the particles showed a main peak at 285.0 eV due to the adventitious carbon, commonly used as a charge calibration reference. Notably, while this peak was present in all the samples, another peak at 289.0 eV was only present in the unreacted PbO implying that the underlying carbon species is consumed or displaced during the reaction with NO_2. This peak is due to the adsorbed carbonate species, $PbCO_3$, in support of the complex nature of PbO surface in the ambient environment as discussed in XPS data. Calculation of C1s:Pb4f ratio indicates about 20% of surface sites covered by adventitious carbon or carbonate for unreacted PbO.

Pb4f region showed doublets characteristic of $Pb4f_{7/2}$ and $Pb4f_{5/2}$ transitions. Pb4f peaks of unreacted PbO locate at 137.5 and 142.3 eV, consistent with previous literature values.[281] Upon reaction with 100 mTorr NO_2, both peaks shifted to higher binding energies by ~1 eV due to the increased surface electronegativity. New peak appear in Pb4f spectrum at 144.6 and 139.7 eV, in agreement with $Pb(NO_3)_2$. When reacted PbO was further exposed to 100 mTorr NO_2 and series of RH, peaks due to PbO disappeared, further confirming that all PbO within the surface depth investigated (~3 nm) was converted into $Pb(NO_3)_2$.

Relative humidity can change the speciation and the amount of adsorbed NO_2 product. To investigate RH effect, PbO sample was consecutively exposed to 100 mTorr NO_2 at different RH values. Resulting XPS spectra were used to quantify adsorbed nitrogen product on the sample surface in terms of N1s:Pb4f ratio as shown in Figure 6.5. The adsorbed nitrogen species increases with increasing RH up to ~30%, and then

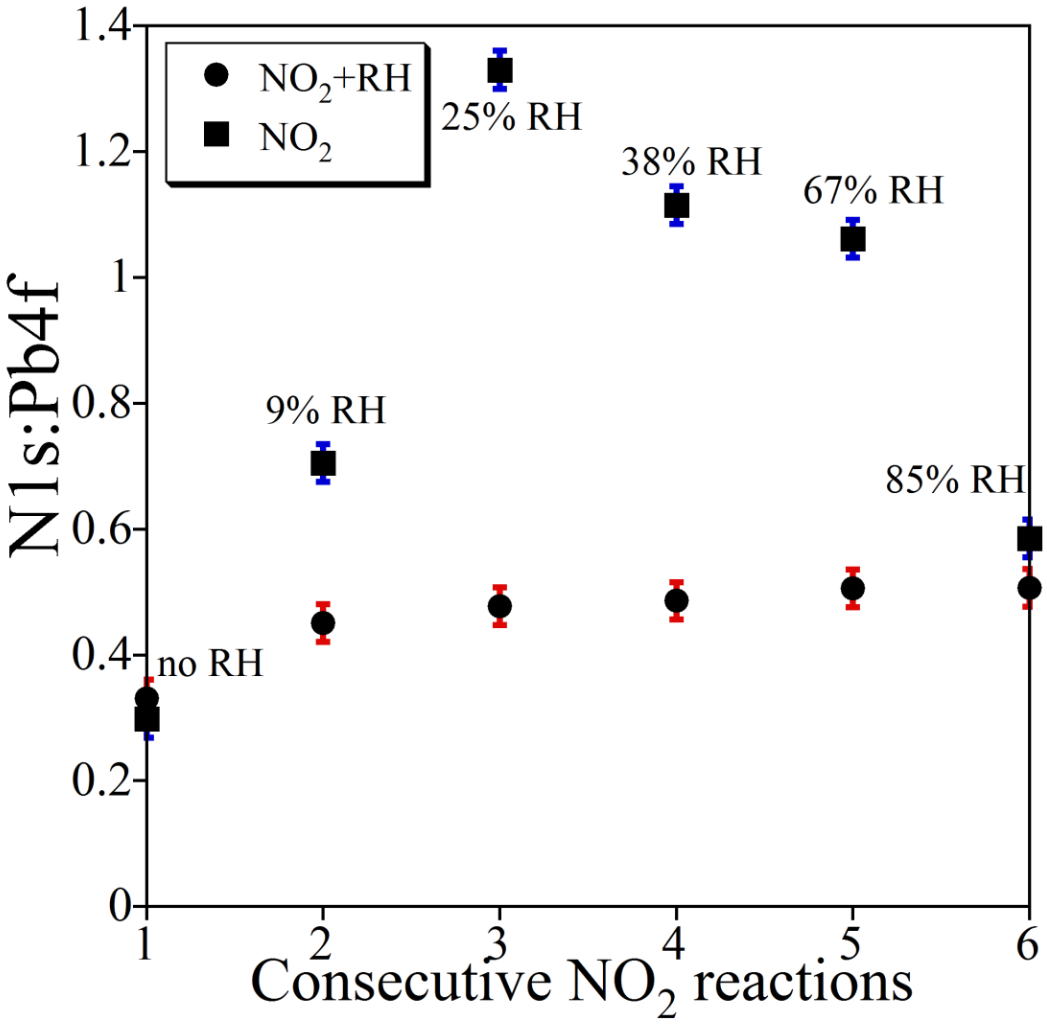

Figure 6.5 (Filled circles) Quantification of nitrogen reaction product adsorbed on PbO after six consecutive exposures to 100 mTorr NO_2 for 30 min. For comparison, separate set of data is shown in filled squares of consecutive 100 mTorr NO_2 exposures at various RH.

decreases at high RH. At 85% RH the amount of surface nitrogen species was close to that of 6th NO_2 exposure in the absence of RH. No increase in adsorbed nitrogen was observed when PbO was consecutively exposed to 100 mTorr NO_2 in the absence of RH. These data are consistent with previous observations of Tompkins *et al.*[287] via gravimetric measurements showing high growth rate of $Pb(NO_3)_2$ thin film on tin-lead alloy upon exposure to NO_2 at intermediate RH (20-40%) with a very slow growth rate at high RH. They postulated that at high RH adsorbed water exceeds a monolayer and unevenly spread out across the sample surface. This clustering, in turn, would result in decreased NO_2 reaction with lead surface sites. In our experiments, however, adsorbed nitrogen amount decreased with RH after 25% RH showing removal of surface nitrogen species back to gas phase.

6.4.3 Effect of NO_2 Exposure on the Dissolution of PbO Particles

Dissolution experiments were performed for unreacted PbO as well as on those reacted with NO_2 under various environmental conditions to investigate how mobility of PbO changes upon atmospheric aging in the presence of acidic gases. Data obtained is shown in Figure 6.6. It can be seen that compared with unreacted PbO both NO_2 and NO_2+RH reacted samples had increased dissolution of lead about two and three fold, respectively. To better understand the cause of the increased solubility of Pb and relative species involved, solubility product values for several relevant Pb-containing compounds are tabulated in Table 6.2. The lead oxide, hydroxide or carbonate compounds are insoluble in water, while $Pb(NO_3)_2$ is soluble (59.7 g/ 100 g H_2O at 25^{o}C). Lead nitrate formed on surface of PbO, thus, can be mobilized in aqueous solutions. XRD spectra obtained for the reacted PbO samples after the exposure to NO_2 and NO_2+RH didn't show any new peaks (data not shown), indicating that NO_2 adsorption is surface limited and reaction doesn't extend to the bulk of the particles. This agrees well with the low BET surface area of PbO. Notably, the presence of RH (8 Torr, ~38 % RH at room

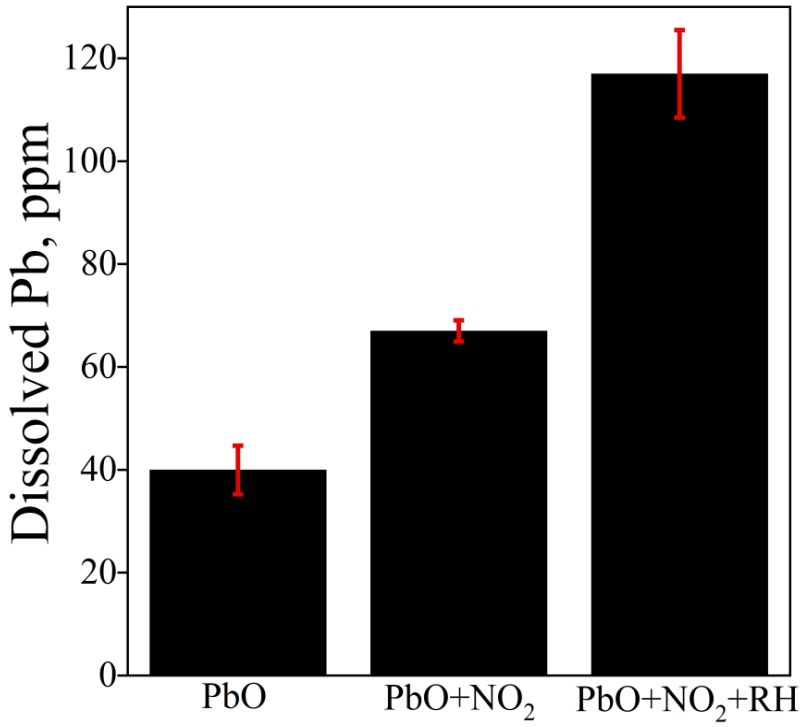

Figure 6.6 ICP-OES measured Pb amounts in solution from unreacted PbO and reacted with 100 mTorr NO_2 for 24 h, as well as 100 mTorr NO_2 and 8 Torr H_2O mixture for 24 h. Reactors contained a solids loading of 50 g L^{-1}. Uncertainties represent one standard deviation from triplicate experiments.

temperature) enhanced the mobility of Pb, indicating that the presence of RH lead to greater uptake of adsorbed nitrogen species. Similar enhancement was previously observed in spectroscopical studies of SO_2 adsorption on calcite.[222]

Table 6.2 Tabulated Solubility Products of Lead Compounds

Compound (mineral)	K_{sp}	Reference
PbO (litharge)	1.2×10^{-15}	288
PbO_2 (plattnerite)	3.2×10^{-66}	288
$Pb(OH)_2$	1.43×10^{-20}	275
$PbCO_3$ (cerussite)	7.4×10^{-14}	275
$Pb(NO_3)_2$	Soluble5 9.7 g/ 100 g H_2O at 25°C	275

[a] No solubility data for PbO (mineral massicot) was found

6.5 Environmental and Health Implications

Taken together, these data show that nitrogen dioxide can react with lead containing particles by forming adsorbed lead nitrates, which in turn can readily dissolve in solution and thus increase the mobilization of otherwise stationary Pb. Resulting lead nitrate layer is very mobile in the environment due to its enhanced solubility. The amount of dissolved lead is increased nearly three times following exposure to NO_2. To our knowledge, this is the first mechanistic study of the reactivity characterization of lead particles towards NO_2 under environmentally relevant conditions. Recent work by Edwards and co-workers showed increased Pb mobility after exposure to NO_2 and O_3 mixture while concluding that a reaction with polymer binder was major factor in Pb release.[265] It can be argued that an alternative mechanism for the formation of soluble Pb

salts in the environment and the release of Pb is through the heterogeneous reaction of NO_2 with lead oxide surfaces. In fact, this is the likely mechanism to release most lead into the environment as lead nitrate is soluble in water. Furthermore, lead nitrate films formed could easily react with organic compounds available in the environment such as carboxylic and humic acids in water[289] and isoprene and other higher hydrocarbons[3] yielding organonitrates, alternatively to the OH radical initiated mechanisms proposed recently.[290] These organic lead nitrate compounds due to their volatility and high solubility are much more readily mobilized that inorganic lead compounds and can have enhanced toxicity, with confirmed organolead poisoning of nervous system.[260] Yadav and Sharma showed that both 4.5% lead nitrate or lead acetate in diet of mice severely damaged heme synthesis.[291] Thus it is proposed that in order to fully understand the mobilization and toxicity of lead containing materials, adsorption assessment of model organic molecular compounds, such as formic, acetic and citric acid is needed.

6.6 Acknowledgments

This material is based on the work supported by the Environmental Health Sciences Research Center (EHSRC) at the University of Iowa pilot grant program funded by NIEHS NIH P30 ES05605. The work in this chapter is a collaboration study with Dr. Jonas Baltrusaitis, who helped me collect and analyze the XPS data. I would like to acknowledge Daniel Allman for help with XRD experiments, and Gayan Rubasinghege for help with reaction experiments of PbO with NO_2 for determination of Pb solubility.

CHAPTER 7

A COLLABORATIVE STUDY ON THE IMPACT OF IRON-CONTAINING PARTICLES ON HUMAN HEALTH

7.1 Abstract

Ambient air pollution contains particulate matter (PM), a complex mixture which is often rich in iron. Given the increased use of iron containing nanoparticles in a number of applications, understanding the mechanisms of iron-containing particle induced bacterial growth and virulence provides valuable knowledge in the development of future public health policies aimed at controlling not only ambient concentrations of PM, but also in understanding the physicochemical characteristics of particles that potentially can cause detrimental effects on human health. This is especially true for susceptible populations. Since iron concentrations are extremely low in body fluids, there is the potential that iron-containing particles will influence the ability of bacteria to scavenge iron for growth, and inhibit antimicrobial peptide (AMP) activity. Furthermore, the physicochemical characteristics and properties of these particles can play an important role in this activity. In this study, *Pseudomonas aeruginosa* (PAO1) was grown in the presence of iron oxide nanoparticles of different size and AMPs. It is reported here that PAO1 utilizes iron from particles for growth and inhibits AMPs. Furthermore, nanoparticle surface area and size correlate with bacteria growth.

7.2 Introduction

Iron-containing nanoparticles exhibit intrinsic qualities, and have been widely used in industry. For example, these materials are used in recording media because of their paramagnetic properties.[292] They have also been used as a catalyst in clean fuel synthesis.[292] Given that iron-containing nanoparticles are relatively inexpensive and

readily available, it is expected that their application will be potentially expanded in future industrial activities, partially replacing the usage of rare-earth containing materials.

Although the properties of iron nanoparticles prove beneficial in a wide-range of applications, little is known about the effects of iron-containing nanoparticles on bacterial pathogens. Through evolution, several organisms, including humans, have developed numerous mechanisms that limit iron bioavalability to microbial pathogens, keeping extremely low iron concentrations in various biological fluids (10^{-18} M).[293] Iron-containing nanoparticles can therefore act as an exogenous iron source for bacteria, potentially becoming deleterious to human health.

Metal oxide nanoparticles have been shown to alter the composition of the soil bacterial community by reducing both biomass and diversity.[294] Epidemiological studies have shown that exposure to ambient air pollution is associated with increased respiratory exacerbations,[295-298] pneumococcal infections,[299] otitis media,[300] and eye infections.[301] One significant component for ambient air pollution is particulate matter (PM), which is composed of particles of various compositions, morphologies, and sizes. Due to the increasing applications of iron-containing nanoparticles in industry, as well as its prominent natural occurrence, the potential for increased iron-containing particle exposure as particulate matter in the atmosphere is an environmental and public concern. Recent studies have shown that chemical and biological reactivity of iron-containing carbon nanoparticles is positively correlated with the surface area.[302]

Hematite (α-$Fe_2O_{3)}$ is one of the most abundant phase of iron oxides that has been detected in atmospheric dusts over a wide size range.[303] The aqueous phase dissolution of iron is controlled by the physicochemical properties of the particles, including particle size, morphology, composition, and crystalline structure. Aggregation of nanoparticles can impact both the dissolution rate and reactivity of the nanoparticles.[304] Previous study suggested that nanorods of α-FeOOH (goethite) have a higher iron dissolution capacity compared to microrods due to the greater surface area and chemical activity of nanorod

α-FeOOH.[305] Nanomaterial morphology and crystallinity can influence toxicological response due to large aspect ratio of irregular shapes or highly crystalline, and thus highly reactivity of metal oxide nanoparticles.[306] Aging of the nanoparticles in natural or biological relevant environment distinctly changes their physicochemical characteristics, reactivity and, thus, bioactivity.[307, 308] Given the potential size and surface area effect of nanoscale particles, nanoscale α-Fe_2O_3 potentially provide a source of iron to bacteria, and induce significant effect on bacterial growth and virulence.

In this study, *Pseudomonas aeruginosa* (PAO1) was grown in the presence of α-Fe_2O_3 nanoparticles of different size and antimicrobial peptides (AMPs). The obtained results demonstrate that α-Fe_2O_3 nanoparticles enhance bacterial growth with a strong dependence of bacterial growth on particle surface area and size. α-Fe_2O_3 nanoparticles inhibit AMP activity, one of the host first lines of defense against foreign invaders. Furthermore, α-Fe_2O_3 nanoparticles increase pathogenecity more than nanoparticles devoid of iron (e.g. aluminum oxide nanoparticles).

7.3 Experimental Methods

7.3.1 Synthesis of α-Fe_2O_3 Nanoparticles

Hematite particles used in the current study is either synthesized or commercially available. The smallest α-Fe_2O_3 nanoparticles investigated, 2 ± 1 nm in size, were prepared using a synthesis method similar to that used previously for other metal oxide nanoparticles reported earlier by Wu *et al*.[309] Briefly, 2.35 g (8.7 mmol) of iron chloride hexahydrate precursor was added to 40 ml methanol. The solution was refluxed for several minutes to dissolve the precursor and 3 ml of water was added to the resulting solution. In the next step, 30 ml of methanol solution containing 1.04 g (26.1 mmol) of NaOH was added drop-wise and refluxed. After 48 hours of reaction at reflux temperature, a brown-red precipitate was collected by centrifugation at 10,000 rpm for 30

minutes. The isolated precipitates were washed three times using a 1:1 ratio of ethanol/acetone and dried under vacuum for 24 hours. The weight of the α-Fe_2O_3 product from a 3 ml water addition reaction was 0.82 g corresponding to a 60 % yield based on the iron precursor reactant. Other nanoscale α-Fe_2O_3 samples were purchased from various sources including Nanostructured & Amorphous Materials, Alfa Aesar, Sigma Aldrich.

7.3.2 Characterization of α-Fe_2O_3 Nanoparticles

Morphology, composition, surface area and crystallinity properties of the synthesized and commercially purchased α-Fe_2O_3 nanoparticles were characterized by powder X-ray diffraction (XRD), transmission electron microscopy (TEM), BET surface area analysis, and X-ray photoelectron spectroscopy (XPS).

7.3.3 α-Fe_2O_3 Nanoparticle Bacterial Exposure Experiments

In order to determine the effects of nanoscale α-Fe_2O_3 on bacteria growth, *Pseudomonas aeruginosa* (PAO1), a known bacterial pathogen to humans,[310] animals[311] and plants,[311, 312] was grown overnight in an iron deficient media (M9) at pH 6.8 with 2.2 mM glucose, 0.002 M magnesium sulfate ($MgSO_4$), 0.001 M calcium chloride ($CaCl_2$) and 25mM sodium succinate. To test size-dependent effects of nanoscale α-Fe_2O_3 particles on bacteria growth, 10 μg/mL of four different size α-Fe_2O_3 particles (540, 85, 43 and 2 nm) were added to 3 hour sub-cultured PAO1 cultures and growth was determined by measuring OD_{600} at 37 ℃ for 9 hours while correcting for particle absorbance effects. 25μM iron chloride ($FeCl_3$), a soluble source of iron, and 10μg/mL aluminum oxide (γ-Al_2O_3), an iron-deficient control particle, were used as positive and negative controls respectively. Prior to conducting experiments, the presence of any bacterial contamination in α-Fe_2O_3 samples was determined by diluting and culturing them on chromagar plates. None of the α-Fe_2O_3 nanoparticle samples contained any

culturable bacteria (data not shown). Agglomeration of the nanoparticles in M9 media was monitored using dynamic light scattering (DLS) instrument from Beckman Coulter. All α-Fe_2O_3 nanoparticles used in this study formed larger aggregates in M9 media of approximately the same size, ~500 nm, as measured by DLS. Additionally, inductively coupled plasma-optical emission spectroscopy (ICP-OES) was performed using Varian 720-ES instrument to determine the extent of dissolution in the medium. Nanoscale α-Fe_2O_3 were suspended in 4mL of M9 media with 10 μg/mL concentration and incubated at pH 6.8 for 4 h at 37^{o}C while rotating at 300 rpm. Samples were then centrifuged at 2950 rpm for 8 min followed by filtering through 0.2 μm filter to remove undissolved particles. This process of removing undissolved particles worked well for all but the smallest particle size investigated. Thus for the smallest particle the amount of bioavailable iron is the sum of dissolved iron and extremely small nanoparticles. Three independent experiments were performed and represented by the standard deviation reported.

7.4 Results and Discussions

7.4.1 Characterization of Nanoscale α-Fe_2O_3

The properties of the particles used in this study, including TEM derived primary particle size, BET specific surface area and manufacturer information are provided in Table 7.1. Smallest (~2 nm) α-Fe_2O_3 nanoparticles was synthesized as previously described (see Wu *et al.*[309] and references therein). XRD spectrum of the synthesized α-Fe_2O_3 shown in Figure 7.1a exhibit the most intense peaks at 39 and 41 degrees due to the (104) and (110) reflections of hematite.[313] Small amount of amorphous nature of the synthesized α-Fe_2O_3 nanoparticles was also observed in the XRD spectrum, according to the underlying background. The amorphous iron oxides and hydroxides have been shown

Table 7.1 Summary of TEM Particle Size, BET and Manufacturer Data of α-Fe_2O_3 Nanoparticles Used

Sample	Source	Size[a] (nm)	Specific Surface Area (m^2 g^{-1})[b]
α-Fe_2O_3	Synthesized	2 ±1	220 ±10
α-Fe_2O_3	Nanostructured & Amorphous Materials	43 ±6	39 ±1
α-Fe_2O_3	Alfa Aesar	85 ±25	11 ±1
α-Fe_2O_3	Sigma Aldrich	540 ±90	2.5 ±0.1
γ-Al_2O_3 [c]	Degussa	16 ±5	101 ±4

[a] Particle diameter and standard deviation as determined from TEM images;

[b] Triplicate measurements;

[c] γ-Al_2O_3 was used as a control nanoparticle that did not contain iron.

to dissolve faster than their crystalline counterparts and may play a role in supplying dissolved iron to bacteria. Dissolution rate of Fe(III) has shown to depend on crystallinity, among other parameters, thus increasing the rate orders of magnitude for poorly crystalline nanoparticles.[314] Fe(III) extraction process with EDTA and ammonium oxalate from amorphous iron oxide, hematite and goethite mixture only dissolved amorphous fraction due to its high reactivity.[315] Wahid and Kamalam proposed that crystalline Fe(III) oxides have to be transformed into amorphous Fe(III) oxides via microbial processing or hydration before transformed into bioavailable Fe(II).[316] To explore the size effect of α-Fe_2O_3 nanoparticles on bacterial growth, 43, 85 and 540 nm particles from various commercial sources were also used in this study. XRD patterns for these nanoparticles are also shown in Figure 7.1. Major reflections in XRD due to the

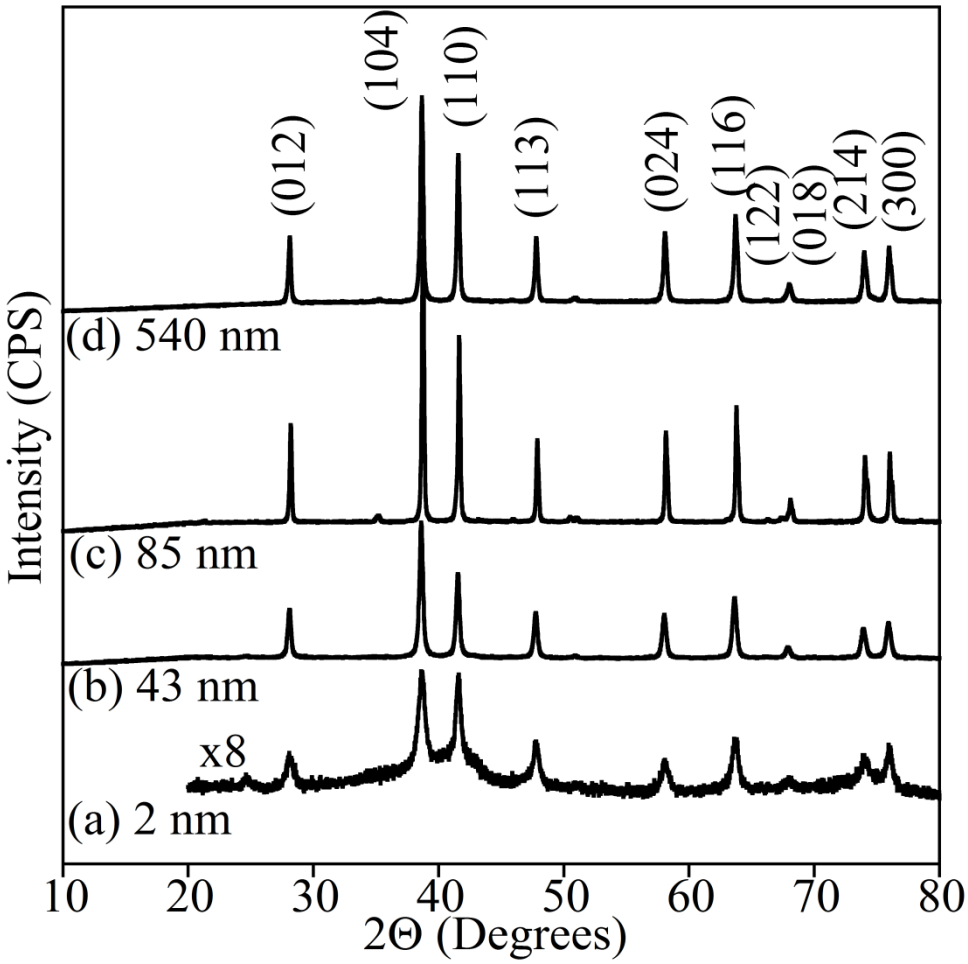

Figure 7.1 Powder X-ray diffraction (XRD) patterns of α-Fe_2O_3 nanoparticles used in this study.

hematite, α-Fe_2O_3, crystalline phase are observed in all of these different sized nanoparticles, while small peaks at 36 and 52 degrees are due to minor impurities of other iron oxide phases.[317] This information is important to fully understand the biological response, in this case the growth and pathogeneity (*vide infra*), as iron oxide and hydroxide nanoparticles can have different dissolution mechanisms depending on their crystallinity and chemistry.[318]

Representative TEM images of nanoscale α-Fe_2O_3 used in this work are shown in Figure 7.2. Particle samples show relatively narrow size distributions. 540 nm particles are irregular in shape, while other samples have morphologies best described as spherical or rhombohedral, as is typically seen for hematite.[319] As expected, measured BET surface areas increase with decreasing particle size with the smallest 2 ± 1 nm particles having the largest BET surface area of 220 ± 10 m^2 g^{-1}.

XPS was used to determine the composition of the nanoparticle surfaces. The high resolution spectra of Fe2p, O1s and C1s for nanoparticles used in this work are shown in Figure 7.3. These all have nearly the same spectral features showing very similar chemical composition of the surface. Namely, a doublet in Fe2p region with peaks at 710.8 and 724.4 eV are due to the $2p_{3/2}$ and $2p_{1/2}$ transitions in hematite.[320] O1s spectrum showed primary peak at 530.0 eV due to the surface Fe-O bonds and a broader feature at 531.7 eV which is due to the combination of lattice and adsorbed Fe-OH bonds.[320] Additionally, C1s spectrum showed a strong peak at 285.0 eV due to the adventitious carbon and 289.0 eV due to the O-C-O bonds.[321] Collectively, these data show surface species present on the hematite nanoparticles includes structural and adsorbed hydroxyl groups and some adventitious carbon material either left over from the synthesis or from ambient air contamination. To assess the relative abundance of each element and corresponding species within, quantification was performed based on XPS data. The calculated ratios are shown in Table 7.2. In particular, the O1s:Fe2p ratio shows a value of 1.40, close to the expected stoichiometric 1.5 in α-Fe_2O_3 particles in all

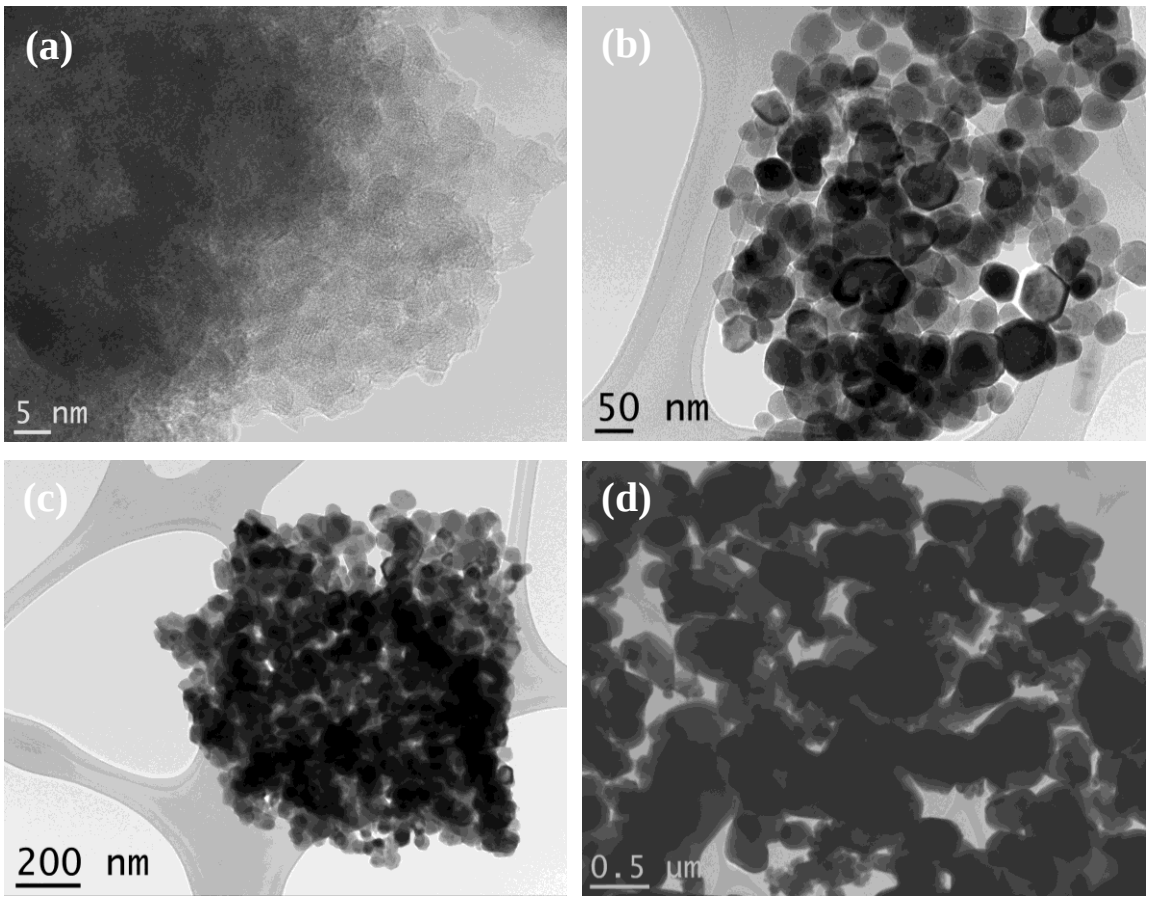

Figure 7.2 TEM images of α-Fe_2O_3 nanoparticles of different size. Analysis of over two hundred particles yield an average size of 2 ± 1, 43 ± 6, 85 ± 25, and 540 ± 90 nm for the four different samples used (see Table 7.1).

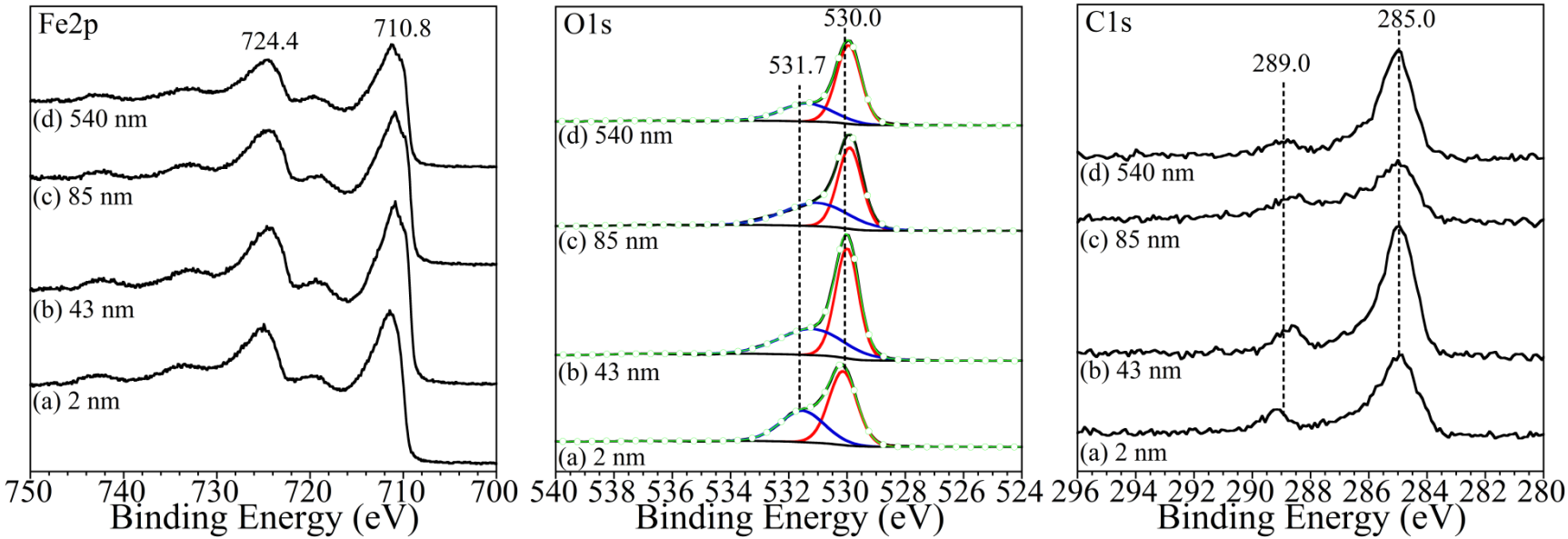

Figure 7.3 XPS high resolution spectra in the Fe2p, O1s and C1s regions for α-Fe_2O_3 nanoparticles. The O1s region was peak-fit using four Gaussian-Lorentzian synthetic components. The black solid line represents experimental data and the green line with circular markers represents the total calculated fit. The other curves represent components used to curve fit the spectra. Ratios for different peak areas are given in Table 7.2

Table 7.2 Elemental Composition of α-Fe_2O_3 Nanoparticles as Determined from XPS Analysis

Size (nm)	Quantification			
	O1s:Fe2p	C1s:Fe2p	O1s(Fe-O):O1s	O1s(Fe-OH):O1s
2 ± 1	1.23	0.25	0.60	0.40
43 ± 6	1.42	0.30	0.61	0.39
85 ± 25	1.45	0.29	0.57	0.43
540 ± 90	1.37	0.37	0.67	0.32

samples but the smallest 2 ± 1 nm one. For the smallest particles, the O1s:Fe2p ratio is found to be 1.23 suggesting a slightly reduced stoichiometry. It is possibly related to the fact that small metal oxide nanoparticles are prone to reduction in the XPS instrument under X-ray illumination in vacuum, as has been observed for 6 nm CuO particles.[322] C1s:Fe2p ratio in all samples was close to ~0.3 showing that just a little less than one-third of surface sites are covered with carbonaceous material. Two observed oxygen species with O1s region, Fe-O and Fe-OH accounted for 60% and 40% of total oxygen, respectively. This shows that hematite nanoparticle surface is terminated with hydroxyl groups which have been shown to be active sites for surface dissolution and adsorption.[319]

7.4.2 Growth and Pathogenicity of PAO1 in the Presence of α-Fe_2O_3 Nanoparticles

As shown in Figure 7.4, the smallest particles (2 ± 1 nm) induce the greatest amount of growth when compared to larger ones. The bacterial growth is positively

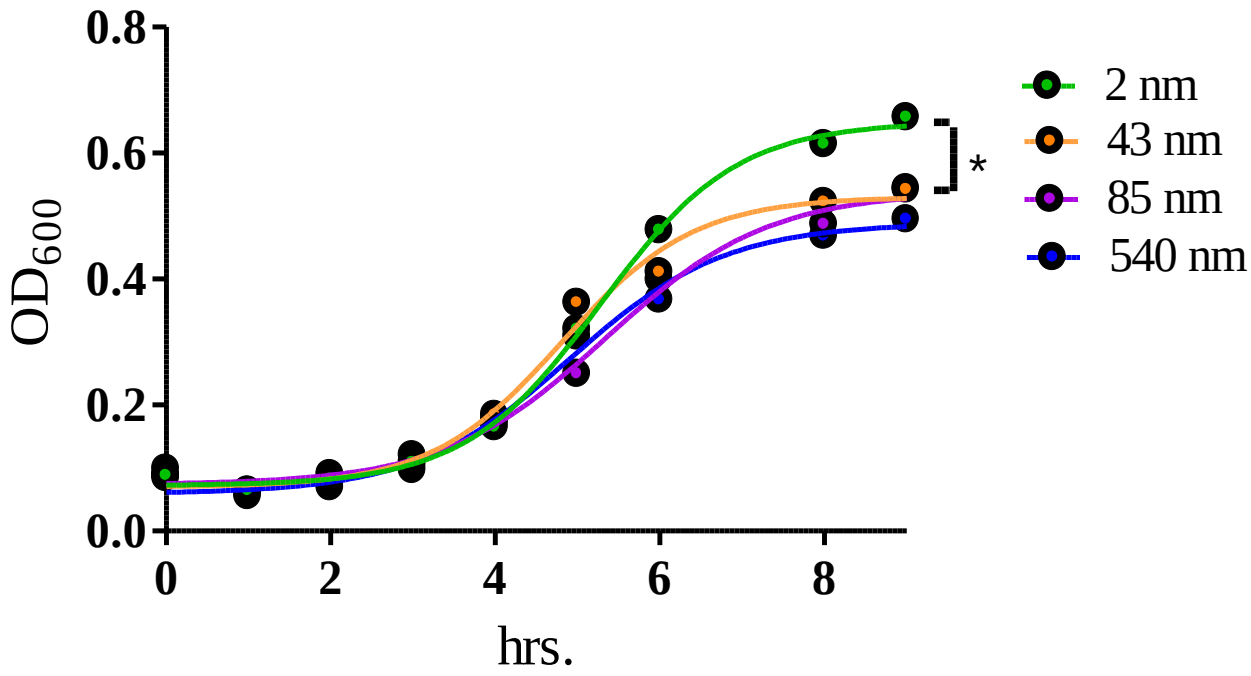

Figure 7.4 PAO1 grown overnight in M9 media were subcultured and exposed to four α-Fe_2O_3 particles (10 μg/mL) of different size and surface area (Table 7.1). Growth was recorded over nine hours. PAO1 exposed to the smaller particles with a larger surface area had the largest growth effect. Non-linear regression (curve-fit) with variable slope from three independent experiments was used for statistical analysis. Data were compared for all parameters of the growth curve using the extra sum of squares F-test to detect differences throughout the entire growth curve. n = 3 in triplicates. SEM reported * $p<0.0001$.

correlated to particle BET surface area (R^2 = 0.8153), although all of the α-Fe_2O_3 nanoparticles form larger aggregates in the M9 media, near 500 nm in size as measured by DLS. In order to determine whether this effect was due to different propensities of dissolved iron in the different samples, all four samples were incubated for 4 hours at 37 ℃ in M9 media and inductively coupled plasma optical emission spectrometer (ICP/OES) (Varian, 720-ES) was used to determine the concentrations of dissolved iron. Blank samples were also analyzed to ensure no other significant source of iron. Only 2 and 43 nm particles resulted in a measurable amount of bioavailable, 14.8 ± 1.5 and 5.1 ± 1.6 ppb of dissolved iron, respectively, at pH 6.8 in M9 media. The dissolved iron for 85 and 540 nm particle dissolution is under the detection limit of ICP/OES, indicating increased propensity of iron to dissolve and become bioavailable as decreased particle size. It is therefore expected that the 2 nm particle has an increased iron bioavailability for the PAO1. Since the optimal iron requirement for bacterial growth is 0.3-1.8 μM in vitro cultures,[323] the amount of iron in the media with the other iron oxide particles could be beyond the experimental detection limits but well within the range of iron requirement through other mechanisms such as direct iron-bacteria interactions. It is a potential reason that all α-Fe_2O_3 nanoparticles used in the current study play a role in bacterial growth although some samples shows no significant dissolution of iron in M9 media.

Bacteria not only exist in planktonic form, but frequently they form highly structured communities called biofilms that can coat the inside of tubes such as catheters or faucets or form dense communities in patients with cystic fibrosis or chronic obstructive pulmonary disease (COPD).[324] Previous study has shown that the presence of iron ($FeCl_3$) enhances biofilm formation.[325] Therefore, the effect of α-Fe_2O_3 nanoparticles on biofilm formation was assessed using the crystal violet method.[326] In the presence of 10 μg/mL α-Fe_2O_3 particles, biofilm formation was enhanced compared with control ($p < 0.0001$) and $FeCl_3$ ($p = 0.0269$) containing experiments. However, no significant size dependent effect was observed between 2 nm and 540 nm α-Fe_2O_3 particles(Figure 7.5).

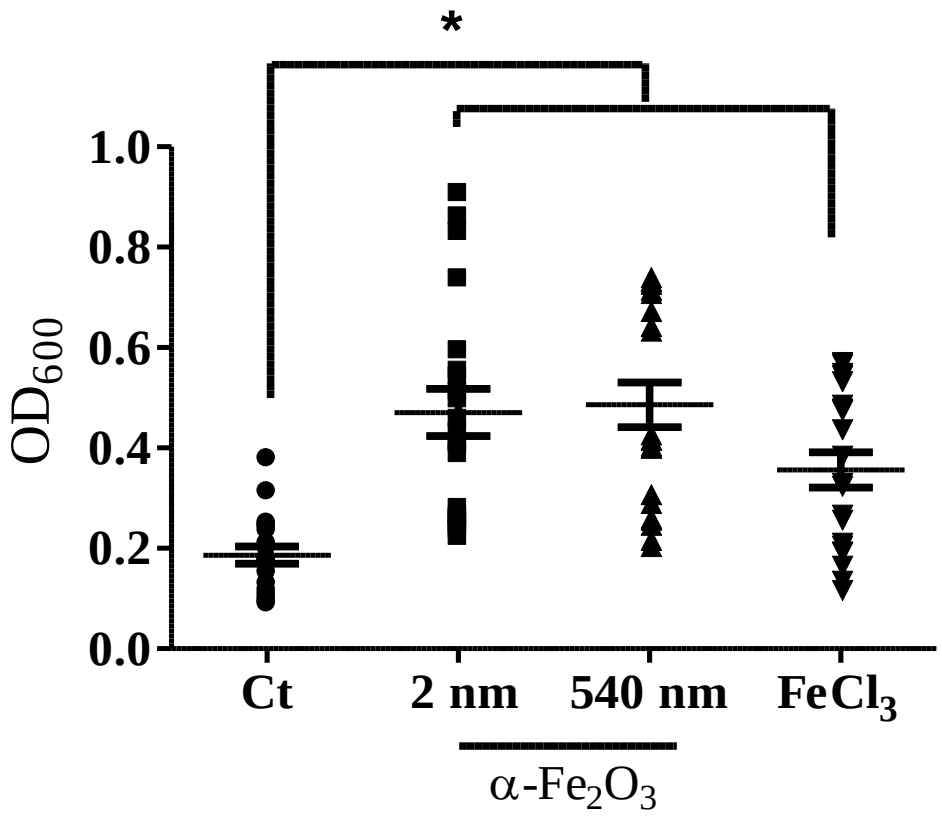

Figure 7.5 Iron oxide nanoparticles increase biofilm formation. PAO1 grown in the presence of 10µg/mL α-Fe_2O_3 (2 nm and 540 nm) or $FeCl_3$ for 24 hours and crystal violet staining was used to determine biofilm formation. 2 nm and 540 nm α-Fe_2O_3 as well as $FeCl_3$ increased biofilm formation more than control (*$p<0.0001$), however there were no differences between 2 nm and 540 nm biofilm formation. N=7 in triplicates. T-test used to compare 2 nm and 540 nm conditions. SEM reported.

The lack of size dependent effects in biofilm formation could be possibly due to similarity in their production of siderophores, which are well-known low molecular weight ligands and have a high affinity for iron. Indeed, bacteria has to produce siderophores to coordinate Fe (III) to acquire iron in any anaerobic environment.[327] Siderophore production is increased in order to increase iron bioavailability in low density populations.[328] Therefore, siderophore production could be more affected by the species of iron particle rather than size in the iron-deprived environment. The increase in biofilm formation in the presence of the α-Fe_2O_3 particles over $FeCl_3$ could be explained by the increased solubility of iron in $FeCl_3$ thus decreasing siderophore production and consequently biofilm formation.[328] However, the increased solubility of iron should be sufficient to overcome the reduced siderophore production.[329] A further examination of specific siderophore production would need to be conducted in order to understand the mechanism of biofilm formation in the current model which is beyond the scope of this current study. Although there was no size dependent effect, the direct increase of biofilm formation due to the presence of α-Fe_2O_3 nanoparticles could have dramatic effects in populations who are chronically colonized with biofilms of *Pseudomonas*.

The airway surface liquid (ASL) is comprised of a combination of proteins that prevent bacterial colonization, including lysozyme, lactoferrin and β-Defensins 1 & 2. These antimicrobial peptides (AMPs) are part of the host innate immunity. Each AMP has specific bactericidal activity and has been shown to have synergistic effects. Lysozyme is known to degrade the bacterial cell wall by muramidase activity and β-Defensins have broad antibacterial activity.[330] Lactoferrin is an iron-binding glycoprotein that sequesters iron thus inhibiting microbial respiration.[330] Not only does lactoferrin inhibit bacterial growth, but it has been shown to inhibit biofilm formation due to its ability to sequester iron.[331] In order to determine the effect of iron-containing particles on AMP activity, physiologically relevant concentrations of AMPs[332] and α-Fe_2O_3 particles were incubated and effects of bacterial killing were tested. Specifically, 600 μg/mL

lysozyme, 200 µg/mL lactoferrin and 100 ng/mL β-Defensins 1 & 2 were used in this mixture. PAO1 was grown overnight in M9 media, subcultured and $1.3e^4$ was used in the experiment. 10 µg/mL α-Fe_2O_3 particles were added with AMPs and PAO1 to a sodium phosphate buffer at pH 7.8 in a 96 deep well plate. Mixture was incubated for one hour at 37℃ and 300 rpm. ¼ diluted Luria Broth (LB) media was added and grown overnight. OD_{600} was measured to determine level of PAO1 growth (+AMP). In order to determine if the effects on AMP inhibition were due to direct AMP inhibition or PAO1 growth as seen in the previous experiments, particles were incubated with AMPs for one hour and then removed by centrifugation and filtration. After the AMPs were filtered, the experiment was conducted as stated above.

As shown in Figure 7.6a, $FeCl_3$ completely inhibited AMPs activity with and without pre-incubation. Conversely, smaller α-Fe_2O_3 particles (2 nm) inhibited AMP activity more effectively compared to the larger particles (540 nm) (Figure 7.6b, p=0.0061). The size dependent effect was lost when AMPs were pre-incubated for one hour with 10µg/mL α-Fe_2O_3 particles (Figure 7.6b, Inc.AMP). Therefore, this effect appears to be due to direct α-Fe_2O_3 particles AMP activity inhibition rather than merely increased growth in the 2 nm condition. This could be due to direct lysozyme inhibition as it has been shown that cations inhibit lysozyme activity.[333] Therefore, the observed inhibition of AMPs in current experiment could be due to the presence of Fe^{2+} interaction with lysozyme. In addition, the size related effects of AMP inhibition could be due to the increasing structural disorder of particles with decreasing size.[303] For example, in the presence of smaller α-Fe_2O_3 particles, more cations could be readily released, thus inhibiting AMPs. Overall, the attenuated AMP activity by α-Fe_2O_3 particles prevents the body's defense system from properly fighting foreign invaders.

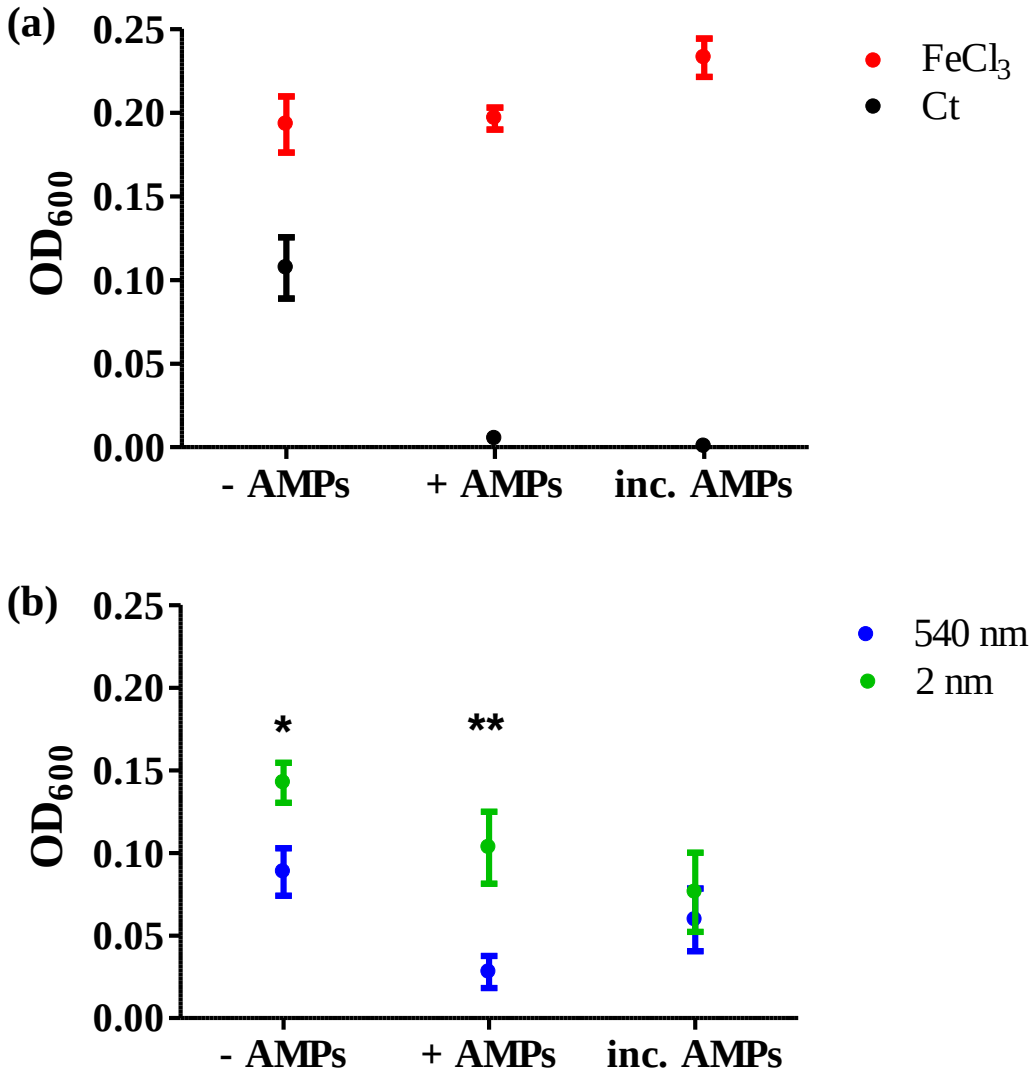

Figure 7.6 Iron oxide nanoparticles inhibit antimicrobial peptide activity. Panel a. PAO1 growth in the presence of $FeCl_3$ with and without AMP cocktail in sodium phosphate buffer. After eighteen hours, $FeCl_3$ increased PAO1 growth. (-AMP) In the presence of $FeCl_3$, AMPs (600 µg/mL Lysozyme, 200 µg/mL Lactoferrin and 100ng/mL β-Defensin 1&2) are inhibited with and without incubating for one hour. (+AMP and Inc. AMPs) Panel b. α-Fe_2O_3 particles (2 nm and 540 nm) were added to PAO1 culture in the presence and absence of AMPs. PAO1 growth in the presence of 2 nm induces more growth than 540 nm particles (-AMP) * p=0.011. 2 nm α-Fe_2O_3 appears to inhibit AMP activity (+AMP) when compared with 540 nm **p=0.0061. When particles are removed after incubating with AMPs for one hour, the size dependent effect of AMP inhibition is lost (Inc. AMPs). N=3 in triplicates. T-test used to compare 2 nm and 540 nm conditions. SEM reported.

7.5 Conclusions

The results demonstrate that one mechanism of iron containing particle induced PAO1 growth is linked to particle size and surface area, likely explained by the increased propensity of large surface area iron particles to have a greater amount of iron dissolution and the ability of small particles to get into bacteria. Although this is true while the bacteria exist in planktonic form, the size dependent effect on growth does not translate to increased biofilm formation. Another finding of this work is that α-Fe_2O_3 particles are able to inhibit AMP activity, thus impairing the ability of a body to respond to foreign invaders such as PAO1. Overall, size and surface area of iron nanoparticles seem to be a factor in playing a role to the effects of bacteria growth, pathogenicity, and impairing the AMP activity.

Although recent studies of hematite nanoparticles greater than 90 nm do not show signs of toxicity in macrophages and lung epithelial cells,[334] nanoparticles, especially the smaller particles with large surface areas, may be harmful to human health as it relates to individuals susceptible to bacterial infections and/or colonization. In the era of nanotechnologies continued promise and growth, understanding the mechanisms of nanoparticle induced bacterial growth and virulence is important for the development of future public health policies aimed at controlling, not only PM concentrations in the environment, but at potential regulations for materials with properties that can cause detrimental effects in healthy and ill subjects.

7.6 Acknowledgements

This publication was made possible by Grant Number UL1RR024979 from the National Center for Research Resources (NCRR), a part of the National Institutes of Health (NIH). Its contents are solely the responsibility of the authors and do not necessarily represent the official views of the CTSA or NIH. This publication was also

supported by Center for Health Effects of Environmental Contamination (CHEEC) Seed Grants: FY 2010 and NIH Grant: KO1HL080966. The work in this chapter is a collaboration work with Dr. Alejandro P. Commellas research group. The biological response data were collected by Jennifer Borcherding. The 2 ± 1 α-Fe_2O_3 was synthesized by Chia-Ming Wu. The XPS data was collected and analyzed by Dr. Jonas Baltrusaitis. The DLS data was collected and analyzed by Larissa Stebounova. I would like to acknowledge all of them for their cooperation and help to make this work accomplished.

CHAPTER 8

CONCLUSIONS AND FUTURE WORK

Atmospheric aerosols greatly influence the chemical balance of the atmosphere, biogeochemical cycles, the Earth's climate and human health. Although extensive studies have been carried out to explore these effects, there is still considerable uncertainty. Studies in this thesis aim to evaluate better the global impacts of metal-containing aerosols in the atmosphere via a series of laboratory experiments.

Although heterogeneous reactions of atmospheric trace gases, such as SO_2, NO_x, HNO_3, O_3 and volatile organic compounds, on aerosols under dark conditions have been well understood after extensive studies in the last two decades, the effect of solar radiation on these heterogeneous reactions has not yet been explored to any great extent. In order to better understand difference between daytime and nighttime chemistry, heterogeneous photochemistry of HNO_3 and O_3, two common atmospheric pollutants, on typical components of metal-containing aerosols was explored using an environmental aerosol chamber that has incorporated with a solar simulator. Heterogeneous photoreaction of HNO_3 on Al_2O_3 shows the formation of gas phase NO_x via the adsorption of HNO_3 on Al_2O_3 to form nitrate followed by the photodecomposition of nitrate to produce NO_x that are released back into the gas phase. It was displayed a dynamic balance between surface adsorbed nitrate, and gaseous HNO_3, NO_2 and NO under irradiation. The work confirms that nitrate is not the end product but the reservoir for nitrogen oxides in the atmosphere. This is consistent with previous field studies showing the release of NO_x from Antarctic and Greenland snow packs,[52, 53] and laboratory experiments showing the formation and release of NO_x from amorphous carbon after exposure to HNO_3.[123] The presence of water has significant effects on the reaction extent, the uptake of HNO_3, and even the reaction mechanism.

Heterogeneous photochemistry of ozone on α-Fe_2O_3, α-FeOOH, TiO_2 and Al_2O_3 was also explored using the environmental aerosol chamber. Experiments show that Al_2O_3, the only insulator used in this study, exhibits no significant activity toward ozone decomposition under either dark or irradiated conditions. α-Fe_2O_3 and α-FeOOH show great capacities in decomposing ozone under both dark and irradiated conditions. More interestingly, TiO_2 only decomposes ozone in the presence of irradiation. The effect of relative humidity on the ozone uptake rate depends strongly on specifics of the oxide surface, such as the type of active site and relative affinity for water. The rate of ozone decay on α-Fe_2O_3 decreases with increasing relative humidity under both dark and irradiated conditions due to the competitive adsorption of water and ozone on surface active sites. Increasing relative humidity for TiO_2-O_3-irradiation system initially shows an enhancement on ozone decay. But at high relative humidity the ozone decomposition is inhibited. It was explained by the combination effects of the formation of surface hydroxyl groups, a highly active oxidant, at low relative humidity and the coverage of water film on TiO_2 surface to block surface active sites at high relative humidity.

The studies on heterogeneous photochemistry of atmospheric trace gases in this thesis indicate that daytime chemistry differs from nighttime chemistry, and plays an important role in regulating the chemical balance of the atmosphere. Heterogeneous photoreactions of atmospheric trace gases may change the reaction mechanism, kinetics, and even products and product partitioning compared with reactions in the dark. Since the surfaces on which such processes may occur include not only airborne particles but also soils, rock formations, buildings, and vegetation, the relevant heterogeneous photoreactions might be widespread and globally impact the chemical state of the troposphere. Modeling studies of atmospheric chemistry should take into account heterogeneous photochemistry of aerosols for better evaluation of aerosol effects and better prediction of atmospheric chemistry.

Given that heterogeneous photochemistry of aerosols has not been fully understood, future works are needed. Some future directions include,

1. Heterogeneous photochemistry of other atmospheric trace gases such as NO_x, and reactive volatile organic compounds is important to pursue to fully understand the fate of atmospheric trace gases.

2. Heterogeneous photochemistry of other typical components of aerosols, such as ZnO, seasalt and soot needs to be explored to fully understand heterogeneous photochemistry of aerosols.

3. Due to the expanding application of metal containing materials in the industry, such as sunscreen and cosmetic using nanoscale TiO_2 and ZnO as constituents, as well as the coating of TiO_2 or TiO_2 containing materials on building exterior, road lamps, and car mirrors, the effects of other surfaces in contact with the atmosphere, besides aerosol, are needed to be explored.

4. The effect of physicochemical properties of aerosol components, including size, shape, ad surface properties (like defect and crystalline face) needs to be examined.

5. The effect of external/internal mixing of two or more metal containing components on their photochemistry is important to peruse.

6. Reactions under more atmospherically relevant conditions should be explored. e.g. reactant gas concentrations at ppb/ppt levels; particle concentrations close to atmospheric levels.

7. The effect of irradiation at different wavelengths is important to be explored.

For the impact of aerosols on biogeochemical cycles, laboratory experiments were performed to better understand the role of anthropogenic aerosols in supplying soluble iron into the open ocean. Aerosols, especially mineral dust, are considered to be the main source of soluble iron in open ocean water. The transport and deposition of aerosols on the ocean water can cause a release of iron. Given that iron is a limiting nutrient for ocean organism in extensive regions of the ocean referred to as high nutrient low chlorophyll

regions,[187-189] the release of iron leads to elevated phytoplankton biomass and rates of photosynthesis in surface water, eventually causing a potential feedback effect on the Earth's climate.[63-67] While recent evidence suggests anthropogenic aerosols to be more important than mineral dust in supplying bioavailable iron, few measurements have been made to compare the iron solubilities between them. In this thesis, coal fly ash was selected as the model of anthropogenic aerosols to investigate iron mobilization of anthropogenic aerosols. Through a variety of characterization techniques coupled with dissolution experiments, it was found that aluminosilicate glass, a major component of coal fly ash, disintegrates into fragments during simulated atmospheric processing, causing an enhancement of iron mobilization. In contrast, Arizona test dust, a proxy of mineral dust used in this study, is mainly composed of aluminosilicate mineral, which is well crystallized and stays relatively stable without significant morphology change during simulated atmospheric processing. Research indicates that anthropogenic aerosols have different chemical structures compared with mineral dust, and therefore exhibit different iron mobilization abilities. Iron mobilization from aerosols is strongly dependent on the source material, atmospheric acid processing, atmospheric cloud processing, surface pH, type of acidic media and solar radiation. These factors should be taken into account in assessing the soluble and bioavailable iron provided by the transport and deposition of aerosols.

Since the effect of anthropogenic aerosols on providing soluble and bioavailable iron into the open ocean waters remain uncertainty, further studies are desirable. Some future directions include,

1. Given that coal fly ash is the only model of anthropogenic aerosols used in this study, further laboratory studies are needed to investigate iron mobilization of other kinds of anthropogenic aerosols, such as engineering iron-containing particles, and biomass burning aerosols to fully understand the impact of anthropogenic aerosols on biogeochemical cycles.

2. Dissolution experiments should be performed at high pH in future work to better simulate atmospheric processing. Specially, the effect of pH in the range of 3-6 is important to be closely examined given that iron solubilities of oxides and minerals change dramatically in the pH range of 3-6.[236]

3. Field studies should be performed to investigate potential changes of morphology and chemistry of fly ash particles during atmospheric transport as suggested in the laboratory study here.

For health effect of heavy metal containing species, PbO was selected to investigate lead mobilization. The effect of atmospheric processing, i.e. reaction with NO_2, on Pb mobilization has also been investigated. Experiments show that PbO can effectively react with NO_2 to form surface adsorbed nitrate. At high relative humidity, surface nitrite was also observed. The formation of surface Pb-NO_3 and Pb-NO_2 species greatly enhances Pb mobilization, potentially causing more mobile Pb entering the environment. These results point to the potential importance and impact that heterogeneous chemistry with trace gases can have on increasing solubility and therefore the mobilization of heavy metals such as lead in the environment. This study also shows that surface intermediates, such as adsorbed nitrates, can yield higher concentrations of dissolved lead in water systems including drinking water systems, ground water systems, estuaries and lakes. Some future studies include,

1. The heterogeneous reactions of other atmospheric trace gases, including NO, HNO_3, SO_2, and organic acids with Pb-containing materials are desirable to better assess the effect of atmospheric trace gases on lead dissolution.

2. The current work should be expanded to other Pb-containing materials, such as PbO_2, Pb_3O_4 and elemental Pb to further understand Pb mobilization in the environment.

Iron is the most abundant transition metal in the troposphere. As a transition metal, it is capable of generating reactive oxygen species (ROS) and contributing to oxidative stress. In collaboration with Dr. Alejandro Comellas' laboratory in the

Department of Internal Medicine, biological response of iron-containing particles was investigated. Specifically, *pseudomonas aeruginosa* (PAO1) was grown in the presence of α-Fe_2O_3 nanoparticles of different size and antimicrobial peptides (AMPs). Results demonstrate that one mechanism of iron containing particles induced PAO1 growth is linked to particle size and surface area, likely explained by the increased propensity of large surface area iron particles to have a greater amount of iron dissolution and the ability of small particles to get into bacteria. Although this is true while the bacteria exist in planktonic form, the size dependent effect on growth does not translate to increased biofilm formation. In addition, α-Fe_2O_3 particles are able to inhibit AMP activity, thus impairing the ability of a body to respond to foreign invaders such as PAO1. This study suggests that size and surface area of iron nanoparticles seem to be a factor in playing a role to the effects of bacteria growth, pathogenicity, and impairing the AMP activity.

This study highlights that nanoparticles, especially the smaller particles with large surface areas, may be harmful to human health as it relates to individuals susceptible to bacterial infections and/or colonization. In the era of nanotechnologies continued promise and growth, understanding the mechanisms of nanoparticle induced bacterial growth and virulence is important for the development of future public health policies aimed at controlling, not only PM concentrations in the environment, but at potential regulations for materials with properties that can cause detrimental effects in healthy and ill subjects. In order to better understand the potential effect of iron-containing particulate matter on human health, some future studies include,

1. Other iron containing materials including goethite and Fe nanoparticles should be explored.

2. The role of physicochemical properties of iron containing particles, such as size and shape, plays in controlling the detrimental effects in human health is needed to be explored.

3. Atmospheric processing can cause changes of physicochemical properties of iron containing particles. For example, particle surface can be covered with nitrate/sulfate/organic acids. How atmospheric processing influences the detrimental effect of iron-containing particles is interesting to be pursued.

In conclusion, the work reported in this thesis helps to further understand the impacts of aerosols on the chemical state of the atmosphere, biogeochemical cycles, the Earth's climate and human health. The knowledge gained here can be combined into future atmospheric modeling studies to better evaluate of the global impacts of aerosols and accurately predict atmospheric chemistry as well as global climate change. Regulations should be made in future to restraint the release of atmospheric aerosols, especially metal-containing particles, in order to protect public and environmental health.

APPENDIX A

WINFIRST MACROS USED FOR INFRARED SPECTRAL COLLECTION AND ANALYSIS

The following macro programs were used for infrared spectral collection and analysis. The generalized programs are given while the individual collection intervals, integration region, peak height, reference spectrum etc. were changed accordingly dependent upon the experiment or analysis being conducted.

Macro 1: Used to collect a serious of infrared spectra continuously

```
pause "press enter when ready"
verbose "on"
sleep 15
verbose "off"

for x=1 to 300 step 1
begin
bench:scan
end

for x=1 to 300 step 1
begin
bench:scan
sleep 150
end
```

Macro 2: Used to ratio all single beam spectra (*.sbm) to absorbance spectra (*.abs)

```
cd C:\VMS\033107
S = findFirstFile "cVMS0*.sbm"
A = stringLength S
if (A > 0)
{
while (A > 0)
{
        B = load S
        ratio "cVMS0001.sbm"
        ras2abs
        SAVE
        S = findNextFile
        A = stringLength S
    }
}
```

Macro 3: Used to integrate a specific set of absorbance bands

```
cd c:\praveen
S = findFirstFile "5ja05*.abs"
A = stringLength S
verbose "on"
if (A > 0)
{
    while (A > 0)
    {
        B = load S
        A = integrate 680 807
        A = integrate 807 940
        A = integrate 1152 1272
        A = integrate 1272 1383
        A = integrate 3490 3603
        S = findNextFile
        A = stringLength S
    }
}
```

Macro 4: Used to obtain the peak height (net absorbance) of a specific absorbance feature

```
cd c:\amp\feb2002\feb06
S = findFirstFile "2fe06*.abs"
A = stringLength S
if (A > 0)
{
    while (A > 0)
    {
        B = load S
        A = neta 1197.58 1700.0819 2120.36
        SAVE
        S = findNextFile
        A = stringLength S
    }
}
```

Macro 5: Use to subtract out gas phase water contributions

```
cd c:\vms\022007
S = findFirstFile "Cvms0*.abs"
A = stringLength S
if (A > 0)
{
    while (A > 0)
    {
        B = load S
        C = integrate 1300 1235
        load "c:\vms\subtract\Water40.abs"
        E = integrate 1300 1235
        F = C/E
        B = load S
        loadRef "c:\vms\subtract\Water40.abs"
        subtract F
        save
        S = findNextFile
        A = stringLength S
    }
}
```

APPENDIX B

INPUT FOR KINETIC PREPROCESSER

The following files were used as input of Kinetic PreProcesser to define the chemical mechanism with reaction constants, the formula of each species involved in, the initial conditions, the numerical integrator, and the output language.

(I) aerosol_ozone.eqn: The equation file, used to define the reaction mechanism with reaction constants.

#Equations

{Constant need to qualify}

{R32} H2O2 = 2HO:	*1.1675E-5;*	
{R12} O3 = 0.63O1D + 0.37O3P + O2:	*1.1060E-3;*	{photolysis of ozone}
{Rwallloss} O3 + wall = 1.5O2 + wall:	*4.2485E-6;*	
{Rsuface} O3 + FeS = 1.5O2 + FeS:	*0;*	
{R1_1} O3P + O2 + O2 = O3 + O2:	*ARR(6.0E-34, 0.00E0, -2.40E0);*	
{R1_2} O3P + O2 + N2 = O3 + N2:	*ARR(6.0E-34, 0.00E0, -2.40E0);*	
{R2} O3P + O3 = 2O2:	*ARR(8.0e-12, 2060.0e0, 0.0e0);*	
{R3} O1D + O2 = O3P + O2:	*ARR(3.3e-11, -55.0e0, 0.0e0);*	
{R3_2} O1D + N2 = O3P + N2:	*ARR(2.15e-11, -110.0e0, 0.0e0);*	
{R4} O1D + O3 = 1.5O2 + O3P:	*2.40E-10;*	
{R13} H + HO2 = 1.788HO + 0.086H2: + 0.086O2 + 0.02H2O + 0.02O3P	*7.95E-11;*	
{R14_1} H + O2 + O2 = HO2 + O2:	*FALL(4.40E-32, 0.00E0, -1.30E0, 4.70E-11, 0.00E0, -0.20E0, 0.60E0);*	
{R14_2} H + O2 + N2 = HO2 + N2:	*FALL(4.40E-32, 0.00E0, -1.30E0, 4.70E-11, 0.00E0, -0.20E0, 0.60E0);*	
{R15} O3P + HO = O2 + H :	*ARR(2.20E-11, -120.00E0, 0.0E0);*	

{R16} O3P + HO2 = HO + O2:	*ARR(3.00E-11, -200.00E0, 0.0E0);*
{R17} O3P + H2O2 = HO + HO2:	*ARR(1.40E-12, 2.0E3, 0.0E0);*
{R18} O1D + H2 = HO + H:	*1.10E-10;*
{R19} O1D + H2O =2HO :	*ARR(1.63E-10, -60.0E0, 0.0E0);*
{R20} HO + H2 = H2O + H:	*ARR(2.80E-12, 1.80E3, 0.0E0);*
{R21} HO + HO = H2O + O3P:	*1.80E-12;*
{R22_1} HO + HO + O2 = H2O2 + O2:	*FALL(6.90E-31, 0.00E0, -1.00E0, 2.60E-11, 0.00E0, 0.00E0, 0.60E0);*
{R22_2} HO + HO + N2 = H2O2 + N2:	*FALL(6.90E-31, 0.00E0, -1.00E0, 2.60E-11, 0.00E0, 0.00E0, 0.60E0);*
{R23} HO + HO2 = H2O + O2:	*ARR(4.80E-11, -250.00E0, 0.0E0);*
{R24} HO + H2O2 = H2O + HO2:	*1.80E-12;*
{R25} HO + O3 = HO2 + O2:	*ARR(1.70E-12, 940.00E0, 0.0E0);*
{R26] HO2 + HO2 = H2O2 + O2:	*ARR(3.50E-13, -430.00E0, 0.0E0);*
{R27_1} HO2 + HO2 + O2 = H2O2 + O2 + O2:	*ARR(1.70E-33, -1000.00E0, 0.0E0);*
{R27_2} HO2 + HO2 + N2 = H2O2 + O2 + N2:	*ARR(1.70E-33, -1000.00E0, 0.0E0);*
{R28} HO2 + O3 = HO + 2O2:	*ARR(1.00E-14, 490.00E0, 0.0E0);*
{R29} H + O3 = HO + O2:	*ARR(1.40E-10, 470.00E0, 0.0E0);*
{R30} O1D + N2 + O2 = N2O + O2:	*ARR(2.80E-36, 0.00E0, -0.9E0);*
{R31} O1D + N2 + N2 = N2O + N2:	*ARR(2.80E-36, 0.00E0, -0.9E0);*

aerosol_ozone.spc: The species file, used to specify the formula of each species involved in the reactions.

include atoms

#DEFVAR {define variable species}

O3P = O;

O1D = O;

O3 = 3O;

O2 = O + O;

HO = H + O;

H2O = H + H + O;

H2O2 = 2H + 2O;

H2 = 2H;

H = H;

HO2 = H + 2O;

N2O = 2N + O;

#DEFFIX {define fixed species, the formulas of wall and surface active site are ignored}

N2 = N + N;

wall = IGNORE;

FeS = IGNORE;

aerosol_ozone.def: The initiative file, used to define the initial conditions

```
#include aerosol_ozone.spc

#include aerosol_ozone.eqn

 //#LANGUAGE Fortran90              {Output Language}

//#DOUBLE ON                        {Double Precision}

//#JACOBIAN SPARSE_LU_ROW           {Use Sparse DATA STRUCTURES}

 //#INTEGRATOR rodas3               {Specify the numerical integrator used}

//#DRIVER general

#LOOKATALL                         {File Output}

#MONITOR O3;H2O;                   {Monitor the concentrations of O3 and H2O}

#INITVALUES                        {Initial Values}


      CFACTOR = 1;                 {Conversion Factor}

      O2 = 5.168e+18;              {Initial concentration of O2}

      N2 = 1.944e+19;

      O3 = 2.9155e+15;

      H2O = 0.1984E+17;

      wall = 1;

      FeS = 0;                     {FeS represents the surface active sites of hematite, set
                                      to 0 when aerosol is absence}


#INLINE F90_INIT                   {Define the integration step}

      TSTART = 12.0d0*3600.0d0

      TEND = TSTART + 10.0d0*3600.0d0

      DT = 0.01d0*3600.d0

      TEMP = 298.0d0               {Define the reaction temperature}

#ENDINLINE
```

aerosol_ozone.kpp: The KPP input file, used to generate KPP file

```
#MODEL          aerosol_ozone
#INTEGRATOR     rosenbrock
#LANGUAGE       Fortran90
#DRIVER         general
#HESSIAN        ON
#STOICMAT       ON
#DOUBLE         ON
```

REFERENCES

1. Seinfeld, J. H.; Pandis, S. N., *Atmospheric Chemistry and Physics: From Air Pollution to Climate Change*. 2 ed.; John Wiley: New York, 2006.

2. Calvert, J. G. Hydrocarbon involvement in photochemical smog formation in Los Angeles atmosphere. *Environmental Science & Technology* **1976,** *10*(*3*), 256-262.

3. Chameides, W. L.; Lindsay, R. W.; Richardson, J.; Kiang, C. S. The role of biogenic hydrocarbons in urban photochemical smog: Atlanta as a case study. *Science* **1988,** *241*(*4872*), 1473-1475.

4. Bell, M. L.; Davis, D. L. Reassessment of the lethal London Fog of 1952: Novel indicators of acute and chronic consequences of acute exposure to air pollution. *Environmental Health Perspectives* **2001,** *109*(*3*), 389-394.

5. Davis, A.; Ruby, M. V.; Bergstrom, P. D. Bioavailability of arsenic and lead in soils from the Butte, Montana, mining district. *Environmental Science & Technology* **1992,** *26*(*3*), 461-468.

6. Monks, P. S.; Granier, C.; Fuzzi, S.; Stohl, A.; Williams, M. L.; Akimoto, H.; Amann, M.; Baklanov, A.; Baltensperger, U.; Bey, I.; Blake, N.; Blake, R. S.; Carslaw, K.; Cooper, O. R.; Dentener, F.; Fowler, D.; Fragkou, E.; Frost, G. J.; Generoso, S.; Ginoux, P.; Grewe, V.; Guenther, A.; Hansson, H. C.; Henne, S.; Hjorth, J.; Hofzumahaus, A.; Huntrieser, H.; Isaksen, I. S. A.; Jenkin, M. E.; Kaiser, J.; Kanakidou, M.; Klimont, Z.; Kulmala, M.; Laj, P.; Lawrence, M. G.; Lee, J. D.; Liousse, C.; Maione, M.; McFiggans, G.; Metzger, A.; Mieville, A.; Moussiopoulos, N.; Orlando, J. J.; O'Dowd, C. D.; Palmer, P. I.; Parrish, D. D.; Petzold, A.; Platt, U.; Pöschl, U.; Prévôt, A. S. H.; Reeves, C. E.; Reimann, S.; Rudich, Y.; Sellegri, K.; Steinbrecher, R.; Simpson, D.; ten Brink, H.; Theloke, J.; van der Werf, G. R.; Vautard, R.; Vestreng, V.; Vlachokostas, C.; von Glasow, R. Atmospheric composition change - global and regional air quality. *Atmospheric Environment* **2009,** *43*(*33*), 5268-5350.

7. Mahowald, N.; Ward, D. S.; Kloster, S.; Flanner, M. G.; Heald, C. L.; Heavens, N. G.; Hess, P. G.; Lamarque, J.-F.; Chuang, P. Y. Aerosol impacts on climate and biogeochemistry. *Annual Review of Environment and Resources* **2011,** *36*(*1*), 45-74.

8. Ginoux, P.; Chin, M.; Tegen, I.; Prospero, J. M.; Holben, B.; Dubovik, O.; Lin, S. J. Sources and distributions of dust aerosols simulated with the GOCART model. *Journal of Geophysical Research-Atmospheres* **2001,** *106*(*D17*), 20255-20273.

9. Prospero, J. M.; Ginoux, P.; Torres, O.; Nicholson, S. E.; Gill, T. E. Environmental characterization of global sources of atmospheric soil dust identified with the NIMBUS 7 Total Ozone Mapping Spectrometer (TOMS) absorbing aerosol product. *Reviews of Geophysics* **2002,** *40*(*1*), 1002.

10. Tegen, I.; Fung, I. Modeling of mineral dust in the atmosphere: Sources, transport, and optical thickness. *Journal Geophysical Research* **1994,** *99*(*D11*), 22897-22914.

11. Sokolik, I. N.; Toon, O. B. Direct radiative forcing by anthropogenic airborne mineral aerosols. *Nature* **1996,** *381*(*6584*), 681-683.

12. Sheehy, D. P. A perspective on desertification of grazing-land ecosystems in North China. *Ambio* **1992,** *21*(*4*), 303-307.

13. Husar, R. B.; Tratt, D. M.; Schichtel, B. A.; Falke, S. R.; Li, F.; Jaffe, D.; Gass, S.; Gill, T.; Laulainen, N. S.; Lu, F.; Reheis, M. C.; Chun, Y.; Westphal, D.; Holben, B. N.; Gueymard, C.; McKendry, I.; Kuring, N.; Feldman, G. C.; McClain, C.; Frouin, R. J.; Merrill, J.; DuBois, D.; Vignola, F.; Murayama, T.; Nickovic, S.; Wilson, W. E.; Sassen, K.; Sugimoto, N.; Malm, W. C. Asian dust events of April 1998. *Journal of Geophysical Research* **2001,** *106*(*D16*), 18317-18330.

14. Gong, S. L.; Zhang, X. Y.; Zhao, T. L.; McKendry, I. G.; Jaffe, D. A.; Lu, N. M. Characterization of soil dust aerosol in China and its transport and distribution during 2001 ACE-Asia: 2. Model simulation and validation. *Journal Geophysical Research* **2003,** *108*(*D9*), 4262.

15. Jaffe, D.; Anderson, T.; Covert, D.; Kotchenruther, R.; Trost, B.; Danielson, J.; Simpson, W.; Berntsen, T.; Karlsdottir, S.; Blake, D.; Harris, J.; Carmichael, G.; Uno, I. Transport of Asian air pollution to North America. *Geophysical Research Letters* **1999,** *26*(*6*), 711-714.

16. VanCuren, R. A.; Cahill, T. A. Asian aerosols in North America: Frequency and concentration of fine dust. *Journal Geophysical Research* **2002,** *107*(*D24*), 4804.

17. McKendry, I. G.; Hacker, J. P.; Stull, R.; Sakiyama, S.; Mignacca, D.; Reid, K. Long-range transport of Asian dust to the Lower Fraser Valley, British Columbia, Canada. *Journal of Geophysical Research* **2001,** *106*(*D16*), 18361-18370.

18. Usher, C. R.; Michel, A. E.; Grassian, V. H. Reactions on mineral dust. *Chemical Reviews* **2003,** *103*(*12*), 4883-4939.

19. Gomes, L.; Gillette, D. A. A comparison of characteristics of aerosol from dust storms in Central Asia with soil-derived dust from other regions. *Atmospheric Environment. Part A. General Topics* **1993,** *27*(*16*), 2539-2544.

20. Nakajima, T.; Higurashi, A.; Kawamoto, K.; Penner, J. E. A possible correlation between satellite-derived cloud and aerosol microphysical parameters. *Geophysical Research Letters* **2001,** *28*(*7*), 1171-1174.

21. Sekiguchi, M.; Nakajima, T.; Suzuki, K.; Kawamoto, K.; Higurashi, A.; Rosenfeld, D.; Sano, I.; Mukai, S. A study of the direct and indirect effects of aerosols using global satellite data sets of aerosol and cloud parameters. *Journal of Geophysical Research-Atmospheres* **2003,** *108*(*D22*), 15.

22. Penner, J. E.; Andreae, M. O.; Annegarn, H.; Barrie, L.; Feichter, J.; Hegg, D.; Jayaraman, A.; Leaitch, R.; Murphy, D.; Nganga, J.; Pitari, G., Climate Change 2001: The Scientific Basis. Contribution of Working Group I to the Third Assessment Report of the Intergovernmental Panel on Climate Change. Cambridge University Press: Cambridge, UK, and New York, NY, USA, 2001.

23. Haywood, J.; Boucher, O. Estimates of the direct and indirect radiative forcing due to tropospheric aerosols: A review. *Reviews of Geophysics* **2000,** *38*(*4*), 513-543.

24. Lighty, J. S.; Veranth, J. M.; Sarofim, A. F. Combustion aerosols: Factors governing their size and composition and implications to human health. *Journal of the Air & Waste Management Association* **2000,** *50*(*9*), 1565-1618.

25. Chen, Y. Z.; Shah, N.; Huggins, F. E.; Huffman, G. P. Transmission electron microscopy investigation of ultrafine coal fly ash particles. *Environmental Science & Technology* **2005,** *39*(*4*), 1144-1151.

26. Bang, J. J.; Murr, L. E. Atmospheric nanoparticles: Preliminary studies and potential respiratory health risks for emerging nanotechnologies. *Journal of Materials Science Letters* **2002,** *21*(*5*), 361-366.

27. Zhiqiang, Q.; Siegmann, K.; Keller, A.; Matter, U.; Scherrer, L.; Siegmann, H. C. Nanoparticle air pollution in major cities and its origin. *Atmospheric Environment* **2000,** *34*(*3*), 443-451.

28. Oberdörster, G.; Oberdörster, E.; Oberdörster, J. Nanotoxicology: An emerging discipline evolving from studies of ultrafine particles. *Environmental Health Perspectives* **2005,** *113*(*7*), 823-829.

29. Nowack, B.; Bucheli, T. D. Occurrence, behavior and effects of nanoparticles in the environment. *Environmental Pollution* **2007,** *150*(*1*), 5-22.

30. Morawska, L.; Wang, H.; Ristovski, Z.; Jayaratne, E. R.; Johnson, G.; Cheung, H. C.; Ling, X.; He, C. JEM Spotlight: Environmental monitoring of airborne nanoparticles. *Journal of Environmental Monitoring* **2009,** *11*(*10*), 1758-1773.

31. Öktem, B.; Tolocka, M. P.; Johnston, M. V. On-line analysis of organic components in fine and ultrafine particles by photoionization aerosol mass spectrometry. *Analytical Chemistry* **2003,** *76*(*2*), 253-261.

32. Wang, S.; Zordan, C. A.; Johnston, M. V. Chemical characterization of individual, airborne sub-10-nm particles and molecules. *Analytical Chemistry* **2006,** *78*(*6*), 1750-1754.

33. Prather, K. A.; Hatch, C. D.; Grassian, V. H. Analysis of atmospheric aerosols. *Annual Review of Analytical Chemistry* **2008,** *1*, 485-514.

34. Kumar, P.; Nenes, A.; Sokolik, I. N. Importance of adsorption for CCN activity and hygroscopic properties of mineral dust aerosol. *Geophysical Research Letters* **2009,** *36*, L24804.

35. McNaughton, C. S.; Clarke, A. D.; Kapustin, V.; Shinozuka, Y.; Howell, S. G.; Anderson, B. E.; Winstead, E.; Dibb, J.; Scheuer, E.; Cohen, R. C.; Wooldridge, P.; Perring, A.; Huey, L. G.; Kim, S.; Jimenez, J. L.; Dunlea, E. J.; DeCarlo, P. F.; Wennberg, P. O.; Crounse, J. D.; Weinheimer, A. J.; Flocke, F. Observations of heterogeneous reactions between Asian pollution and mineral dust over the Eastern North Pacific during INTEX-B. *Atmospheric Chemistry and Physics* **2009,** *9*(*21*), 8283-8308.

36. Finlayson-Pitts, B. J.; Ezell, M. J.; Pitts, J. N. Formation of chemically active chlorine compounds by reactions of atmospheric NaCl particles with gaseous N_2O_5 and $ClONO_2$. *Nature* **1989,** *337*(*6204*), 241-244.

37. Behnke, W.; George, C.; Scheer, V.; Zetzsch, C. Production and decay of $ClNO_2$ from the reaction of gaseous N_2O_5 with NaCl solution: Bulk and aerosol experiments. *Journal Geophysical Research* **1997,** *102*(*D3*), 3795-3804.

38. Davies, J. A.; Cox, R. A. Kinetics of the heterogeneous reaction of HNO_3 with NaCl: Effect of water vapor. *The Journal of Physical Chemistry A* **1998,** *102*(*39*), 7631-7642.

39. Vogt, R.; Crutzen, P. J.; Sander, R. A mechanism for halogen release from sea-salt aerosol in the remote marine boundary layer. *Nature* **1996,** *383*(*6598*), 327-330.

40. Abbatt, J. P. D.; Waschewsky, G. C. G. Heterogeneous interactions of HOBr, HNO_3, O_3, and NO_2 with deliquescent NaCl aerosols at room temperature. *The Journal of Physical Chemistry A* **1998,** *102*(*21*), 3719-3725.

41. Goodman, A. L.; Bernard, E. T.; Grassian, V. H. Spectroscopic study of nitric acid and water adsorption on oxide particles: Enhanced nitric acid uptake kinetics in the presence of adsorbed water. *Journal of Physical Chemistry A* **2001,** *105*(*26*), 6443-6457.

42. Mogili, P. K.; Kleiber, P. D.; Young, M. A.; Grassian, V. H. Heterogeneous uptake of ozone on reactive components of mineral dust aerosol: An environmental aerosol reaction chamber study. *Journal of Physical Chemistry A* **2006,** *110*(*51*), 13799-13807.

43. Sullivan, R. C.; Thornberry, T.; Abbatt, J. P. D. Ozone decomposition kinetics on alumina: Effects of ozone partial pressure, relative humidity and repeated oxidation cycles. *Atmospheric Chemistry and Physics* **2004,** *4*, 1301-1310.

44. Parmon, V. N.; Zakharenko, V. S. Photocatalysis and photosorption in the Earth's atmosphere. *Cattech* **2001,** *5*(*2*), 96-115.

45. Ketteler, G.; Yamamoto, S.; Bluhm, H.; Andersson, K.; Starr, D. E.; Ogletree, D. F.; Ogasawara, H.; Nilsson, A.; Salmeron, M. The Nature of Water Nucleation Sites on TiO_2(110) Surfaces Revealed by Ambient Pressure X-ray Photoelectron Spectroscopy. *The Journal of Physical Chemistry C* **2007,** *111*(*23*), 8278-8282.

46. Yamamoto, S.; Bluhm, H.; Andersson, K.; Ketteler, G.; Ogasawara, H.; Salmeron, M.; Nilsson, A. In situ X-ray photoelectron spectroscopy studies of water on metals and oxides at ambient conditions. *Journal of Physics-Condensed Matter* **2008,** *20*(*18*), 184025.

47. Al-Abadleh, H. A.; Grassian, V. H. Oxide surfaces as environmental interfaces. *Surface Science Reports* **2003,** *52*(*3-4*), 63-161.

48. Grassian, V. H. Surface science of complex environmental interfaces: Oxide and carbonate surfaces in dynamic equilibrium with water vapor. *Surface Science* **2008,** *602*(*18*), 2955-2962.

49. Zhuang, H.; Chan, C. K.; Fang, M.; Wexler, A. S. Formation of nitrate and non-sea-salt sulfate on coarse particles. *Atmospheric Environment* **1999,** *33*(*26*), 4223-4233.

50. Wu, P. M.; Okada, K. Nature of coarse nitrate particles in the atmosphere - A single, particle approach. *Atmospheric Environment* **1994,** *28*(*12*), 2053-2060.

51. Lee, S. H.; Murphy, D. M.; Thomson, D. S.; Middlebrook, A. M. Chemical components of single particles measured with Particle Analysis by Laser Mass Spectrometry (PALMS) during the Atlanta SuperSite Project: Focus on organic/sulfate, lead, soot, and mineral particles. *Journal of Geophysical Research-Atmospheres* **2002,** *107*(*D1-D2*), 4003.

52. Honrath, R. E.; Peterson, M. C.; Guo, S.; Dibb, J. E.; Shepson, P. B.; Campbell, B. Evidence of NO_x production within or upon ice particles in the Greenland snowpack. *Geophysical Research Letters* **1999,** *26*(*6*), 695-698.

53. Jones, A. E.; Weller, R.; Wolff, E. W.; Jacobi, H. W. Speciation and rate of photochemical NO and NO_2 production in Antarctic snow. *Geophysical Research Letters* **2000,** *27*(*3*), 345-348.

54. Ramazan, K. A.; Wingen, L. M.; Miller, Y.; Chaban, G. M.; Gerber, R. B.; Xantheas, S. S.; Finlayson-Pitts, B. J. New experimental and theoretical approach to the heterogeneous hydrolysis of NO_2: Key role of molecular nitric acid and its complexes. *Journal of Physical Chemistry A* **2006,** *110*(*21*), 6886-6897.

55. Rivera-Figueroa, A. M.; Sumner, A. L.; Finlayson-Pitts, B. J. Laboratory studies of potential mechanisms of renoxification of tropospheric nitric acid. *Environmental Science & Technology* **2003,** *37*(*3*), 548-554.

56. Zhou, X. L.; Gao, H. L.; He, Y.; Huang, G.; Bertman, S. B.; Civerolo, K.; Schwab, J. Nitric acid photolysis on surfaces in low-NO_x environments: Significant atmospheric implications. *Geophysical Research Letters* **2003,** *30*(*23*), 2217.

57. Zhou, X. L.; He, Y.; Huang, G.; Thornberry, T. D.; Carroll, M. A.; Bertman, S. B. Photochemical production of nitrous acid on glass sample manifold surface. *Geophysical Research Letters* **2002,** *29*(*14*), 1681.

58. Rubasinghege, G.; Grassian, V. H. Photochemistry of adsorbed nitrate on aluminum oxide particle surfaces. *Journal of Physical Chemistry A* **2009,** *113*(*27*), 7818-7825.

59. Schuttlefield, J.; Rubasinghege, G.; El-Maazawi, M.; Bone, J.; Grassian, V. H. Photochemistry of adsorbed nitrate. *Journal of the American Chemical Society* **2008,** *130*(*37*), 12210-12211.

60. Bauer, S. E.; Koch, D.; Unger, N.; Metzger, S. M.; Shindell, D. T.; Streets, D. G. Nitrate aerosols today and in 2030: A global simulation including aerosols and tropospheric ozone. *Atmospheric Chemistry and Physics* **2007,** *7*(*19*), 5043-5059.

61. Pandis, S. N.; Wexler, A. S.; Seinfeld, J. H. Dynamics of tropospheric aerosols. *Journal of Physical Chemistry* **1995,** *99*(*24*), 9646-9659.

62. ICPP *Climate change 2007: The physical science basis. Contribution of working group I to the fourth assessment report of the intergovernmental panel on climate change*; Cambridge University Press: Cambridge, United Kingdom and New York, NY, USA, 2007.

63. Jickells, T. D.; An, Z. S.; Andersen, K. K.; Baker, A. R.; Bergametti, G.; Brooks, N.; Cao, J. J.; Boyd, P. W.; Duce, R. A.; Hunter, K. A.; Kawahata, H.; Kubilay, N.; laRoche, J.; Liss, P. S.; Mahowald, N.; Prospero, J. M.; Ridgwell, A. J.; Tegen, I.; Torres, R. Global iron connections between desert dust, ocean biogeochemistry, and climate. *Science* **2005,** *308*(*5718*), 67-71.

64. Boyd, P. W.; Jickells, T.; Law, C. S.; Blain, S.; Boyle, E. A.; Buesseler, K. O.; Coale, K. H.; Cullen, J. J.; de Baar, H. J. W.; Follows, M.; Harvey, M.; Lancelot, C.; Levasseur, M.; Owens, N. P. J.; Pollard, R.; Rivkin, R. B.; Sarmiento, J.; Schoemann, V.; Smetacek, V.; Takeda, S.; Tsuda, A.; Turner, S.; Watson, A. J. Mesoscale iron enrichment experiments 1993-2005: Synthesis and future directions. *Science* **2007,** *315*(*5812*), 612-617.

65. Cooper, D. J.; Watson, A. J.; Nightingale, P. D. Large decrease in ocean-surface CO_2 fugacity in response to in situ iron fertilization. *Nature* **1996,** *383*(*6600*), 511-513.

66. Coale, K. H.; Johnson, K. S.; Fitzwater, S. E.; Gordon, R. M.; Tanner, S.; Chavez, F. P.; Ferioli, L.; Sakamoto, C.; Rogers, P.; Millero, F.; Steinberg, P.; Nightingale, P.; Cooper, D.; Cochlan, W. P.; Landry, M. R.; Constantinou, J.; Rollwagen, G.; Trasvina, A.; Kudela, R. A massive phytoplankton bloom induced by an ecosystem-scale iron fertilization experiment in the equatorial Pacific Ocean. *Nature* **1996,** *383*(*6600*), 495-501.

67. Boyd, P. W.; Watson, A. J.; Law, C. S.; Abraham, E. R.; Trull, T.; Murdoch, R.; Bakker, D. C. E.; Bowie, A. R.; Buesseler, K. O.; Chang, H.; Charette, M.; Croot, P.; Downing, K.; Frew, R.; Gall, M.; Hadfield, M.; Hall, J.; Harvey, M.; Jameson, G.; LaRoche, J.; Liddicoat, M.; Ling, R.; Maldonado, M. T.; McKay, R. M.; Nodder, S.; Pickmere, S.; Pridmore, R.; Rintoul, S.; Safi, K.; Sutton, P.; Strzepek, R.; Tanneberger, K.; Turner, S.; Waite, A.; Zeldis, J. A mesoscale phytoplankton bloom in the polar Southern Ocean stimulated by iron fertilization. *Nature* **2000,** *407*(*6805*), 695-702.

68. Fung, I. Y.; Meyn, S. K.; Tegen, I.; Doney, S. C.; John, J. G.; Bishop, J. K. B. Iron supply and demand in the upper ocean. *Global Biogeochemical Cycles* **2000,** *14*(*1*), 281-295.

69. Mahowald, N. M.; Baker, A. R.; Bergametti, G.; Brooks, N.; Duce, R. A.; Jickells, T. D.; Kubilay, N.; Prospero, J. M.; Tegen, I. Atmospheric global dust cycle and iron inputs to the ocean. *Global Biogeochemical Cycles* **2005,** *19*(*4*), GB4025.

70. Mahowald, N. M.; Engelstaedter, S.; Luo, C.; Sealy, A.; Artaxo, P.; Benitez-Nelson, C.; Bonnet, S.; Chen, Y.; Chuang, P. Y.; Cohen, D. D.; Dulac, F.; Herut, B.; Johansen, A. M.; Kubilay, N.; Losno, R.; Maenhaut, W.; Paytan, A.; Prospero, J. A.; Shank, L. M.; Siefert, R. L. Atmospheric iron deposition: Global distribution, variability, and human perturbations. *Annual Review of Marine Science* **2009,** *1*, 245-278.

71. Duce, R. A.; Tindale, N. W. Atmospheric transport of iron and its deposition in the ocean. *Limnology and Oceanography* **1991,** *36*(*8*), 1715-1726.

72. Pehkonen, S. O.; Siefert, R.; Erel, Y.; Webb, S.; Hoffmann, M. R. Photoreduction of iron oxyhydroxides in the presence of important atmospheric organic-compounds. *Environmental Science & Technology* **1993,** *27*(*10*), 2056-2062.

73. Zhu, X. R.; Prospero, J. M.; Millero, F. J. Diel variability of soluble Fe(II) and soluble total Fe in North African dust in the trade winds at Barbados. *Journal of Geophysical Research-Atmospheres* **1997,** *102*(*D17*), 21297-21305.

74. Zhuang, G. S.; Yi, Z.; Duce, R. A.; Brown, P. R. Link between iron and sulfur cycles suggested by detection of Fe(II) in remote marine aerosols. *Nature* **1992,** *355*(*6360*), 537-539.

75. Meskhidze, N.; Chameides, W. L.; Nenes, A.; Chen, G. Iron mobilization in mineral dust: Can anthropogenic SO_2 emissions affect ocean productivity? *Geophysical Research Letters* **2003,** *30*(*21*), 2085.

76. Zhu, X.; Prospero, J. M.; Savoie, D. L.; Millero, F. J.; Zika, R. G.; Saltzman, E. S. Photoreduction of iron(III) in marine mineral aerosol solutions. *Journal of Geophysical Research-Atmospheres* **1993,** *98*(*D5*), 9039-9046.

77. Spokes, L. J.; Jickells, T. D.; Lim, B. Solubilization of aerosol trace-metals by cloud processing - A laboratory study. *Geochimica Et Cosmochimica Acta* **1994,** *58*(*15*), 3281-3287.

78. Johansen, A. M.; Siefert, R. L.; Hoffmann, M. R. Chemical composition of aerosols collected over the tropical North Atlantic Ocean. *Journal of Geophysical Research-Atmospheres* **2000,** *105*(*D12*), 15277-15312.

79. Solmon, F.; Chuang, P. Y.; Meskhidze, N.; Chen, Y. Acidic processing of mineral dust iron by anthropogenic compounds over the north Pacific Ocean. *Journal of Geophysical Research-Atmospheres* **2009,** *114*, D02305.

80. Baker, A. R.; French, M.; Linge, K. L. Trends in aerosol nutrient solubility along a west-east transect of the Saharan dust plume. *Geophysical Research Letters* **2006,** *33*(*7*).

81. Luo, C.; Mahowald, N.; Bond, T.; Chuang, P. Y.; Artaxo, P.; Siefert, R.; Chen, Y.; Schauer, J. Combustion iron distribution and deposition. *Global Biogeochemical Cycles* **2008,** *22*(*1*), GB1012.

82. Sholkovitz, E. R.; Sedwick, P. N.; Church, T. M. Influence of anthropogenic combustion emissions on the deposition of soluble aerosol iron to the ocean: Empirical estimates for island sites in the North Atlantic. *Geochimica Et Cosmochimica Acta* **2009,** *73*(*14*), 3981-4003.

83. Schroth, A. W.; Crusius, J.; Sholkovitz, E. R.; Bostick, B. C. Iron solubility driven by speciation in dust sources to the ocean. *Nature Geoscience* **2009,** *2*(*5*), 337-340.

84. Sedwick, P. N.; Sholkovitz, E. R.; Church, T. M. Impact of anthropogenic combustion emissions on the fractional solubility of aerosol iron: Evidence from the Sargasso Sea. *Geochemistry Geophysics Geosystems* **2007,** *8*, Q10Q06.

85. Chuang, P. Y.; Duvall, R. M.; Shafer, M. M.; Schauer, J. J. The origin of water soluble particulate iron in the Asian atmospheric outflow. *Geophysical Research Letters* **2005,** *32*(*7*), L07813.

86. Richards, R. What effects do mineral particles have in the lung? *Mineralogical Magazine* **2003,** *67*(*2*), 129-139.

87. Lippmann, M. 1989 Hamilton, Alice Lecture. 1.- Lead and human health - back ground and recent findings. *Environmental Research* **1990,** *51*(*1*), 1-24.

88. Schlesinger, R. B. The health impact of common inorganic components of fine particulate matter (PM2.5) in ambient air: A critical review. *Inhalation Toxicology* **2007,** *19*(*10*), 811-832.

89. Pöschl, U. Atmospheric aerosols: Composition, transformation, climate and health effects. *Angewandte Chemie International Edition* **2005,** *44*(*46*), 7520-7540.

90. Savolainen, K.; Alenius, H.; Norppa, H.; Pylkkänen, L.; Tuomi, T.; Kasper, G. Risk assessment of engineered nanomaterials and nanotechnologies - A review. *Toxicology* **2010,** *269*(*2-3*), 92-104.

91. Lioy, P. J.; Weisel, C. P.; Millette, J. R.; Eisenreich, S.; Vallero, D.; Offenberg, J.; Buckley, B.; Turpin, B.; Zhong, M.; Cohen, M. D.; Prophete, C.; Yang, I.; Stiles, R.; Chee, G.; Johnson, W.; Porcja, R.; Alimokhtari, S.; Hale, R. C.; Weschler, C.; Chen, L. C. Characterization of the dust/smoke aerosol that settled east of the World Trade Center (WTC) in lower Manhattan after the collapse of the WTC 11 september 2001. *Environmental Health Perspectives* **2002,** *110*(*7*), 703-714.

92. Offenberg, J. H.; Eisenreich, S. J.; Chen, L. C.; Cohen, M. D.; Chee, G.; Prophete, C.; Weisel, C.; Lioy, P. J. Persistent organic pollutants in the dusts that settled across lower Manhattan after september 11, 2001. *Environmental Science & Technology* **2002,** *37*(*3*), 502-508.

93. Herbert, R.; Moline, J.; Skloot, G.; Metzger, K.; Baron, S.; Luft, B.; Markowitz, S.; Udasin, I.; Harrison, D.; Stein, D.; Todd, A.; Enright, P.; Stellman, J. M.; Landrigan, P. J.; Levin, S. M. The World Trade Center disaster and the health of workers: Five-year assessment of a unique medical screening program. *Environmental Health Perspectives* **2006,** *114*(*12*), 1853-1858.

94. Landrigan, P. J.; Lioy, P. J.; Thurston, G.; Berkowitz, G.; Chen, L. C.; Chillrud, S. N.; Gavett, S. H.; Georgopoulos, P. G.; Alison, S. G.; Levin, S.; Perera, F.; Rappaport, S. M.; Small, C.; Group", T. N. W. T. C. W. Health and environmental consequences of the world trade center disaster. *Environmental Health Perspectives* **2004,** *112*(*6*), 731-739.

95. Guzmán, K. A. D.; Taylor, M. R.; Banfield, J. F. Environmental risks of nanotechnology: National nanotechnology initiative funding, 2000-2004. *Environmental Science & Technology* **2006,** *40*(*5*), 1401-1407.

96. Kreyling, W.; Semmler-Behnke, M.; Möller, W. Health implications of nanoparticles. *Journal of Nanoparticle Research* **2006,** *8*(*5*), 543-562.

97. Jarup, L. Hazards of heavy metal contamination. *British Medical Bulletin* **2003,** *68*(*1*), 167-182.

98. Zevenhoven, R.; Kilpinen, P., Trace elements, alkali metals. In *Control of pollutants in flue gases and fuel gases*, 2nd Ed. 2005.

99. Needleman, H. L.; Bellinger, D. The health-effects of low-level exposure to lead. *Annual Review of Public Health* **1991,** *12*, 111-140.

100. Ruby, M. V.; Davis, A.; Kempton, J. H.; Drexler, J. W.; Bergstrom, P. D. Lead bioavailability - Dissolution kinetics under simulated gastric conditions. *Environmental Science & Technology* **1992,** *26*(*6*), 1242-1248.

101. Ruby, M. V.; Davis, A.; Nicholson, A. In situ formation of lead phosphates in soils as a method to immobilize lead. *Environmental Science & Technology* **1994,** *28*(*4*), 646-654.

102. Ruby, M. V.; Davis, A.; Schoof, R.; Eberle, S.; Sellstone, C. M. Estimation of lead and arsenic bioavailability using a physiologically based extraction test. *Environmental Science & Technology* **1996,** *30*(*2*), 422-430.

103. Prince, A. M. P. Invesigations into the heterogeneous atmospheric intereactionsof ioslated metal oxide, carbonate and soot aerosols. Ph.D. Dessertation, The University of Iowa, Iowa City, IA, 2003.

104. Mogili, P. K. Heterogeneous chemistry and extinction measurements of mineral dust components. Ph.D. Dessertation, the University of Iowa, IA, Iowa City, IA, 2007.

105. Chen, H.; Navea, J. G.; Young, M. A.; Grassian, V. H. Heterogeneous photochemistry of trace atmospheric gases with components of mineral dust aerosol. *The Journal of Physical Chemistry A* **2011,** *115*(*4*), 490-499.

106. Cwiertny, D. M.; Baltrusaitis, J.; Hunter, G. J.; Laskin, A.; Scherer, M. M.; Grassian, V. H. Characterization and acid-mobilization study of iron-containing mineral dust source materials. *Journal of Geophysical Research-Atmospheres* **2008,** *113*, D05202.

107. Pruppacher, H. R.; Jaenicke, R. The processing of water vapor and aerosols by atmospheric clouds, a global estimate. *Atmospheric Research* **1995,** *38*(*1-4*), 283-295.

108. Mackie, D. S.; Boyd, P. W.; Hunter, K. A.; McTainsh, G. H. Simulating the cloud processing of iron in Australian dust: pH and dust concentration. *Geophysical Research Letters* **2005,** *32*(*6*), L06809.

109. Shi, Z.; Bonneville, S.; Krom, M. D.; Carslaw, K. S.; Jickells, T. D.; Baker, A. R.; Benning, L. G. Iron dissolution kinetics of mineral dust at low pH during simulated atmospheric processing. *Atmospheric Chemistry and Physics* **2011,** *11*(*3*), 995-1007.

110. Laskin, A.; Cowin, J. P.; Iedema, M. J. Analysis of individual environmental particles using modern methods of electron microscopy and X-ray microanalysis. *Journal of Electron Spectroscopy and Related Phenomena* **2006,** *150*(*2-3*), 260-274.

111. Rancourt, D. G.; Ping, J. Y. Voigt-based methods for arbitrary-shape static hyperfine parameter distributions in Mössbauer spectroscopy. *Nuclear Instruments and Methods in Physics Research Section B: Beam Interactions with Materials and Atoms* **1991,** *58*(*1*), 85-97.

112. Houghton, J. T.; Meira Filho, L. G.; Bruce, J.; Lee, H.; Callander, B. A.; Haites, E.; Harris, N.; Maskell, K., *Climate Change 1994: Radiative Forcing of Climate Change and an Evaluation of the IPCC IS92 Emission Scenarios*. Cambridge University Press: Cambridge, 1995; p 127-162.

113. Charlson, R. J.; Schwartz, S. E.; Hales, J. M.; Cess, R. D.; Coakley, J. A.; Hansen, J. E.; Hofmann, D. J. Climate forcing by anthropogenic aerosols. *Science* **1992,** *255*(*5043*), 423-430.

114. Haagen-Smit, A. J. Chemistry and physiology of Los Angeles smog. *Industrial & Engineering Chemistry* **1952,** *44*(*6*), 1342-1346.

115. Mamane, Y.; Gottlieb, J. Nitrate formation on sea-salt and mineral particles - A single-particle approach. *Atmospheric Environment Part A-General Topics* **1992,** *26*(*9*), 1763-1769.

116. Underwood, G. M.; Li, P.; Al-Abadleh, H.; Grassian, V. H. A Knudsen cell study of the heterogeneous reactivity of nitric acid on oxide and mineral dust particles. *Journal of Physical Chemistry A* **2001,** *105*(*27*), 6609-6620.

117. Underwood, G. M.; Song, C. H.; Phadnis, M.; Carmichael, G. R.; Grassian, V. H. Heterogeneous reactions of NO_2 and HNO_3 on oxides and mineral dust: A combined laboratory and modeling study. *Journal of Geophysical Research-Atmospheres* **2001,** *106*(*D16*), 18055-18066.

118. Hanisch, F.; Crowley, J. N. Heterogeneous reactivity of gaseous nitric acid on Al_2O_3, $CaCO_3$, and atmospheric dust samples: A Knudsen cell study. *Journal of Physical Chemistry A* **2001,** *105*(*13*), 3096-3106.

119. Hanisch, F.; Crowley, J. N. The heterogeneous reactivity of gaseous nitric acid on authentic mineral dust samples, and on individual mineral and clay mineral components. *Physical Chemistry Chemical Physics* **2001,** *3*(*12*), 2474-2482.

120. Grassian, V. H. Chemical reactions of nitrogen oxides on the surface of oxide, carbonate, soot, and mineral dust particles: Implications for the chemical balance of the troposphere. *Journal of Physical Chemistry A* **2002,** *106*(*6*), 860-877.

121. Zhu, C.; Xiang, B.; Chu, L. T.; Zhu, L. 308 nm photolysis of nitric acid in the gas phase, on aluminum surfaces, and on ice films. *The Journal of Physical Chemistry A* **2010,** *114*(*7*), 2561-2568.

122. Chatfield, R. B. Anomalous HNO_3/NO_x ratio of remote tropospheric air: Conversion of nitric acid to formic acid and NO_x ? *Geophysical Research Letters* **1994,** *21*(*24*), 2705-2708.

123. Rogaski, C. A.; Golden, D. M.; Williams, L. R. Reactive uptake and hydration experiments on amorphous carbon treated with NO_2, SO_2, O_3, HNO_3, and H_2SO_4. *Geophysical Research Letters* **1997,** *24*(*4*), 381-384.

124. Prince, A. P.; Wade, J. L.; Grassian, V. H.; Kleiber, P. D.; Young, M. A. Heterogeneous reactions of soot aerosols with nitrogen dioxide and nitric acid: atmospheric chamber and Knudsen cell studies. *Atmospheric Environment* **2002,** *36*(*36-37*), 5729-5740.

125. Baltrusaitis, J.; Schuttlefield, J.; Jensen, J. H.; Grassian, V. H. FTIR spectroscopy combined with quantum chemical calculations to investigate adsorbed nitrate on aluminium oxide surfaces in the presence and absence of co-adsorbed water. *Physical Chemistry Chemical Physics* **2007,** *9*(*36*), 4970-4980.

126. Prince, A. P. Investigations into the heterogeneous atmospheric interactions of isolated metal oxide, carbonate anf soot aerosols. University of Iowa, Iowa City, 2003.

127. Sander, S. P.; Friedl, R. R.; Golden, D. M.; Kurylo, M. J.; Moortgat, G. K.; Wine, P. H.; Ravishankara, A. R.; Kolb, C. E.; Molina, M. J.; Finlayson-Pitts, B. J.; Huie, R. E., *Chemial Kinetics and Photochemical Data for Use in Atmospheric Studies Evaluation No. 15*. Jet Propulsion Laboratory: Pasadena, 2006; Vol. 06-2.

128. Atkinson, R.; Baulch, D. L.; Cox, R. A.; Crowley, J. N.; Hampson, R. F.; Hynes, R. G.; Jenkin, M. E.; Rossi, M. J.; Troe, J. Evaluated kinetic and photochemical data for atmospheric chemistry: Volume I - gas phase reactions of O_x, HO_x, NO_x and SO_x species. *Atmospheric Chemistry and Physics* **2004,** *4*, 1461-1738.

129. Saliba, N. A.; Yang, H.; Finlayson-Pitts, B. J. Reaction of gaseous nitric oxide with nitric acid on silica surfaces in the presence of water at room temperature. *Journal of Physical Chemistry A* **2001,** *105*(*45*), 10339-10346.

130. Mack, J.; Bolton, J. R. Photochemistry of nitrite and nitrate in aqueous solution: a review. *Journal of Photochemistry and Photobiology A: Chemistry* **1999,** *128*(*1-3*), 1-13.

131. Goodman, A. L.; Underwood, G. M.; Grassian, V. H. Heterogeneous reaction of NO_2: Characterization of gas-phase and adsorbed products from the reaction, $2NO_2(g) + H_2O(a) \rightarrow HONO(g) + HNO_3(a)$ on hydrated silica particles. *Journal of Physical Chemistry A* **1999,** *103*(*36*), 7217-7223.

132. Akimoto, H.; Takagi, H.; Sakamaki, F. Photoenhancement of the nitrous-acid formation in the surface-reaction of nitrogen-dioxide and water-vapor-extra radical source in smog chamber experiments. *International Journal of Chemical Kinetics* **1987,** *19*(*6*), 539-551.

133. Ramazan, K. A.; Syomin, D.; Finlayson-Pitts, B. J. The photochemical production of HONO during the heterogeneous hydrolysis of NO_2. *Physical Chemistry Chemical Physics* **2004,** *6*(*14*), 3836-3843.

134. Syomin, D. A.; Finlayson-Pitts, B. J. HONO decomposition on borosilicate glass surfaces: Implications for environmental chamber studies and field experiments. *Physical Chemistry Chemical Physics* **2003,** *5*(*23*), 5236-5242.

135. Dentener, F. J.; Carmichael, G. R.; Zhang, Y.; Lelieveld, J.; Crutzen, P. J. Role of mineral aerosol as a reactive surface in the global troposphere. *Journal of Geophysical Research-Atmospheres* **1996,** *101*(*D17*), 22869-22889.

136. Finlayson-Pitts, B. J.; Pitts, J. N. Tropospheric air pollution: Ozone, airborne toxics, polycyclic aromatic hydrocarbons, and particles. *Science* **1997,** *276*(*5315*), 1045-1051.

137. Prospero, J. M.; Schmitt, R.; Cuevas, E.; Savoie, D. L.; Graustein, W. C.; Turekian, K. K.; Volzthomas, A.; Diaz, A.; Oltmans, S. J.; Levy, H. Temporal variability of summer-time ozone and aerosols in the free troposphere over the eastern North Atlantic. *Geophysical Research Letters* **1995,** *22*(*21*), 2925-2928.

138. de Reus, M.; Dentener, F.; Thomas, A.; Borrmann, S.; Strom, J.; Lelieveld, J. Airborne observations of dust aerosol over the North Atlantic Ocean during ACE 2: Indications for heterogeneous ozone destruction. *Journal of Geophysical Research-Atmospheres* **2000,** *105*(*D12*), 15263-15275.

139. Berkowitz, C. M.; Zaveri, R. A.; Bian, X. D.; Zhong, S. Y.; Disselkamp, R. S.; Laulainen, N. S.; Chapman, E. G. Aircraft observations of aerosols, O_3 and NO_y in a nighttime urban plume. *Atmospheric Environment* **2001,** *35*(*13*), 2395-2404.

140. Bonasoni, P.; Cristofanelli, P.; Calzolari, F.; Bonafe, U.; Evangelisti, F.; Stohl, A.; Sajani, S. Z.; van Dingenen, R.; Colombo, T.; Balkanski, Y. Aerosol-ozone correlations during dust transport episodes. *Atmospheric Chemistry and Physics* **2004,** *4*, 1201-1215.

141. Li, J.; Han, Z. A modeling study of the impact of heterogeneous reactions on mineral aerosol surfaces on tropospheric chemistry over East Asia. *Particuology* **2010,** *8*(*5*), 433-441.

142. Deng, J. J.; Wang, T. J.; Liu, L.; Jiang, F. Modeling heterogeneous chemical processes on aerosol surface. *Particuology* **2010,** *8*(*4*), 308-318.

143. Hanning-Lee, M. A.; Brady, B. B.; Martin, L. R.; Syage, J. A. Ozone decomposition on alumina: Implications for solid rocket motor exhaust. *Geophysical Research Letters* **1996,** *23*(*15*), 1961-1964.

144. Michel, A. E.; Usher, C. R.; Grassian, V. H. Heterogeneous and catalytic uptake of ozone on mineral oxides and dusts: A Knudsen cell investigation. *Geophysical Research Letters* **2002,** *29*(*14*), 1665.

145. Hanisch, F.; Crowley, J. N. Ozone decomposition on Saharan dust: An experimental investigation. *Atmospheric Chemistry and Physics* **2003,** *3*, 119-130.

146. Usher, C. R.; Michel, A. E.; Stec, D.; Grassian, V. H. Laboratory studies of ozone uptake on processed mineral dust. *Atmospheric Environment* **2003,** *37*(*38*), 5337-5347.

147. Michel, A. E.; Usher, C. R.; Grassian, V. H. Reactive uptake of ozone on mineral oxides and mineral dusts. *Atmospheric Environment* **2003,** *37*(*23*), 3201-3211.

148. Nicolas, M.; Ndour, M.; Ka, O.; D'Anna, B.; George, C. Photochemistry of atmospheric dust: Ozone decomposition on illuminated titanium dioxide. *Environmental Science & Technology* **2009,** *43*(*19*), 7437-7442.

149. Parkin, I. P.; Palgrave, R. G. Self-cleaning coatings. *Journal of Materials Chemistry* **2005,** *15*(*17*), 1689-1695.

150. Fujishima, A.; Zhang, X.; Tryk, D. A. TiO_2 photocatalysis and related surface phenomena. *Surface Science Reports* **2008,** *63*(*12*), 515-582.

151. Sandu, A.; Sander, R. Technical note: Simulating chemical systems in Fortran90 and Matlab with the Kinetic PreProcessor KPP-2.1. *Atmospheric Chemistry and Physics* **2006,** *6*, 187-195.

152. Hanst, P. L.; Stephens, E. R.; Scott, W. E.; Doerr, R. C. Absorptivities for the infrared determination of trace amounts of ozone. *Analytical Chemistry* **1961,** *33*(*8*), 1113-1115.

153. McAfee, J. M.; Stephens, E. R.; Fitz, D. R.; Pitts, J. N. Infrared absorptivity of the 9.6 μm ozone band as a function of spectral resolution and abundance. *Journal of Quantitative Spectroscopy and Radiative Transfer* **1976,** *16*(*10*), 829-837.

154. Navea, J. G.; Xu, S. H.; Stanier, C. O.; Young, M. A.; Grassian, V. H. Heterogeneous uptake of octamethylcyclotetrasiloxane (D-4) and decamethylcyclopentasiloxane (D-5) onto mineral dust aerosol under variable RH conditions. *Atmospheric Environment* **2009,** *43*(*26*), 4060-4069.

155. Vaida, V. Perspective: Water cluster mediated atmospheric chemistry. *Journal of Chemical Physics* **2011,** *135*(*2*), 020901.

156. Li, W.; Gibbs, G. V.; Oyama, S. T. Mechanism of ozone decomposition on a manganese oxide catalyst. 1. In situ Raman spectroscopy and Ab initio molecular orbital calculations. *Journal of the American Chemical Society* **1998,** *120*(*35*), 9041-9046.

157. Li, W.; Oyama, S. T. Mechanism of ozone decomposition on a manganese oxide catalyst. 2. Steady-state and transient kinetic studies. *Journal of the American Chemical Society* **1998,** *120*(*35*), 9047-9052.

158. Oyama, S. T. Chemical and catalytic properties of ozone. *Catalysis Reviews-Science and Engineering* **2000,** *42*(*3*), 279-322.

159. Roscoe, J. M.; Abbatt, J. P. D. Diffuse reflectance FTIR study of the interaction of alumina surfaces with ozone and water vapor. *Journal of Physical Chemistry A* **2005,** *109*(*40*), 9028-9034.

160. Qi, F.; Chen, Z. L.; Xu, B. B.; Shen, J. M.; Ma, J.; Joll, C.; Heitz, A. Influence of surface texture and acid-base properties on ozone decomposition catalyzed by aluminum (hydroxyl) oxides. *Applied Catalysis B: Environmental* **2008,** *84*(*3-4*), 684-690.

161. Yang, L.; Hu, C.; Nie, Y. L.; Qu, J. H. Surface acidity and reactivity of β-$FeOOH/Al_2O_3$ for pharmaceuticals degradation with ozone: In situ ATR-FTIR studies. *Applied Catalysis B: Environmental* **2010,** *97*(*3-4*), 340-346.

162. Domka, F.; Basinska, A.; Przystajko, W.; Fiedorow, R. Surface chemistry of Fe_2O_3-Cr_2O_3 and Fe_2O_3 catalysts. *Surface Technology* **1984,** *21*(*2*), 101-108.

163. Xu, Y.; Schoonen, M. A. A. The absolute energy positions of conduction and valence bands of selected semiconducting minerals. *American Mineralogist* **2000,** *85*(*3-4*), 543-556.

164. Hoffmann, M. R.; Martin, S. T.; Choi, W.; Bahnemann, D. W. Environmental applications of semiconductor photocatalysis. *Chemical Reviews* **1995,** *95*(*1*), 69-96.

165. Toledano, D. S.; Dufresne, E. R.; Henrich, V. E. Photoexcited Fe_2O_3 surfaces: Properties and chemisorption. *Journal of Vacuum Science & Technology a-Vacuum Surfaces and Films* **1998,** *16*(*3*), 1050-1054.

166. Toledano, D. S.; Henrich, V. E. Kinetics of SO_2 adsorption on photoexcited α-Fe_2O_3. *Journal of Physical Chemistry B* **2001,** *105*(*18*), 3872-3877.

167. Kim, H. J.; Shul, Y. G.; Han, H. S. Photocatalytic properties of silica-supported TiO_2. *Topics in Catalysis* **2005,** *35*(*3-4*), 287-293.

168. Kormann, C.; Bahnemann, D. W.; Hoffmann, M. R. Environmental photochemistry: Is iron oxide (hematite) an active photocatalyst? A comparative study: α-Fe_2O_3, ZnO, TiO_2. *Journal of Photochemistry and Photobiology A: Chemistry* **1989,** *48*(*1*), 161-169.

169. Zhang, H. J.; Chen, G. H.; Bahnemann, D. W. Photoelectrocatalytic materials for environmental applications. *Journal of Materials Chemistry* **2009,** *19*(*29*), 5089-5121.

170. Ohtani, B.; Zhang, S. W.; Nishimoto, S.; Kagiya, T. Catalytic and photocatalytic decomposition of ozone at room temperature over titanium(IV) oxide. *Journal of the Chemical Society-Faraday Transactions* **1992,** *88*(*7*), 1049-1053.

171. Litter, M. I.; Navio, J. A. Comparison of the photocatalytic efficiency of TiO_2, iron oxides and mixed Ti(IV)---Fe(III) oxides:

Photodegradation of oligocarboxylic acids. *Journal of Photochemistry and Photobiology A: Chemistry* **1994,** *84*(*2*), 183-193.

172. Leland, J. K.; Bard, A. J. Photochemistry of colloidal semiconducting iron oxide polymorphs. *The Journal of Physical Chemistry* **1987,** *91*(*19*), 5076-5083.

173. Feng, W.; Nansheng, D. Photochemistry of hydrolytic iron (III) species and photoinduced degradation of organic compounds. A minireview. *Chemosphere* **2000,** *41*(*8*), 1137-1147.

174. Clarke, N. S.; Hall, P. G. Adsorption of water-vapor by iron-oxides. 2. Water isotherms and X-ray photoelectron spectroscopy. *Langmuir* **1991,** *7*(*4*), 678-682.

175. Liu, D. F.; Ma, G.; Xu, M.; Allen, H. C. Adsorption of ethylene glycol vapor on α-Al_2O_3(0001) and amorphous SiO_2 surfaces: Observation of molecular orientation and surface hydroxyl groups as sorption sites. *Environmental Science & Technology* **2005,** *39*(*1*), 206-212.

176. Ewing, G. E. Ambient thin film water on insulator surfaces. *Chemical Reviews* **2006,** *106*(*4*), 1511-1526.

177. Foster, M.; D'Agostino, M.; Passno, D. Water on MgO(100) - An infrared study at ambient temperatures. *Surface Science* **2005,** *590*(*1*), 31-41.

178. Guan, K. H. Relationship between photocatalytic activity, hydrophilicity and self-cleaning effect of TiO_2/SiO_2 films. *Surface & Coatings Technology* **2005,** *191*(*2-3*), 155-160.

179. Wang, R.; Hashimoto, K.; Fujishima, A.; Chikuni, M.; Kojima, E.; Kitamura, A.; Shimohigoshi, M.; Watanabe, T. Light-induced amphiphilic surfaces. *Nature* **1997,** *388*(*6641*), 431-432.

180. Watanabe, T.; Nakajima, A.; Wang, R.; Minabe, M.; Koizumi, S.; Fujishima, A.; Hashimoto, K. Photocatalytic activity and photoinduced hydrophilicity of titanium dioxide coated glass. *Thin Solid Films* **1999,** *351*(*1-2*), 260-263.

181. Obee, T. N.; Brown, R. T. TiO_2 photocatalysis for indoor air applications: Effects of humidity and trace contaminant levels on the oxidation rates of formaldehyde, toluene, and 1,3-butadiene. *Environmental Science & Technology* **1995,** *29*(*5*), 1223-1231.

182. Sassine, M.; Burel, L.; D'Anna, B.; George, C. Kinetics of the tropospheric formaldehyde loss onto mineral dust and urban surfaces. *Atmospheric Environment* **2010,** *44*(*40*), 5468-5475.

183. Cernigoj, U.; Stangar, U. L.; Trebse, P. Degradation of neonicotinoid insecticides by different advanced oxidation processes and studying the effect of ozone on TiO_2 photocatalysis. *Applied Catalysis B: Environmental* **2007,** *75*(*3-4*), 229-238.

184. Martin, J. H.; Gordon, R. M.; Fitzwater, S. E. The case for iron. *Limnology and Oceanography* **1991,** *36*(*8*), 1793-1802.

185. Falkowski, P. G.; Barber, R. T.; Smetacek, V. Biogeochemical controls and feedbacks on ocean primary production. *Science* **1998,** *281*(*5374*), 200-206.

186. Morel, F. M. M.; Price, N. M. The biogeochemical cycles of trace metals in the oceans. *Science* **2003,** *300*(*5621*), 944-947.

187. Martin, J. H. Glacial-interglacial CO_2 change: The iron hypothesis. *Paleoceanography* **1990,** *5*(*1*), 1-13.

188. Martin, J. H.; Coale, K. H.; Johnson, K. S.; Fitzwater, S. E.; Gordon, R. M.; Tanner, S. J.; Hunter, C. N.; Elrod, V. A.; Nowicki, J. L.; Coley, T. L.; Barber, R. T.; Lindley, S.; Watson, A. J.; Vanscoy, K.; Law, C. S.; Liddicoat, M. I.; Ling, R.; Stanton, T.; Stockel, J.; Collins, C.; Anderson, A.; Bidigare, R.; Ondrusek, M.; Latasa, M.; Millero, F. J.; Lee, K.; Yao, W.; Zhang, J. Z.; Friederich, G.; Sakamoto, C.; Chavez, F.; Buck, K.; Kolber, Z.; Greene, R.; Falkowski, P.; Chisholm, S. W.; Hoge, F.; Swift, R.; Yungel, J.; Turner, S.; Nightingale, P.; Hatton, A.; Liss, P.; Tindale, N. W. Testing the iron hypothesis in ecosystems of the equatorial pacific-ocean. *Nature* **1994,** *371*(*6493*), 123-129.

189. Moore, J. K.; Doney, S. C.; Glover, D. M.; Fung, I. Y. Iron cycling and nutrient-limitation patterns in surface waters of the World Ocean. *Deep-Sea Research Part Ii-Topical Studies in Oceanography* **2002,** *49*(*1-3*), 463-507.

190. Shi, Z.; Krom, M. D.; Bonneville, S.; Baker, A. R.; Jickells, T. D.; Benning, L. G. Formation of iron nanoparticles and increase in iron reactivity in mineral dust during simulated cloud processing. *Environmental Science & Technology* **2009,** *43*(*17*), 6592-6596.

191. Veranth, J. M.; Smith, K. R.; Huggins, F.; Hu, A. A.; Lighty, J. S.; Aust, A. E. Mössbauer spectroscopy indicates that iron in an aluminosilicate glass phase is the source of the bioavailable iron from coal fly ash. *Chemical Research in Toxicology* **2000,** *13*(*3*), 161-164.

192. Journet, E.; Desboeufs, K. V.; Caquineau, S.; Colin, J. L. Mineralogy as a critical factor of dust iron solubility. *Geophysical Research Letters* **2008,** *35*(*7*), L07805.

193. Trapp, J. M.; Millero, F. J.; Prospero, J. M. Trends in the solubility of iron in dust-dominated aerosols in the equatorial Atlantic trade winds: Importance of iron speciation and sources. *Geochemistry Geophysics Geosystems* **2010,** *11*(*3*), Q03014.

194. Shi, Z. B.; Krom, M. D.; Bonneville, S.; Baker, A. R.; Bristow, C.; Drake, N.; Mann, G.; Carslaw, K.; McQuaid, J. B.; Jickells, T.; Benning, L. G. Influence of chemical weathering and aging of iron oxides on the potential iron solubility of Saharan dust during simulated atmospheric processing. *Global Biogeochemical Cycles* **2011,** *25*, GB2010.

195. Kumar, A.; Sarin, M. M.; Srinivas, B. Aerosol iron solubility over Bay of Bengal: Role of anthropogenic sources and chemical processing. *Marine Chemistry* **2010,** *121*(*1-4*), 167-175.

196. Upadhyay, N.; Majestic, B. J.; Herckes, P. Solubility and speciation of atmospheric iron in buffer systems simulating cloud conditions. *Atmospheric Environment* **2011,** *45*(*10*), 1858-1866.

197. Furutani, H.; Jung, J.; Miura, K.; Takami, A.; Kato, S.; Kajii, Y.; Uematsu, M. Single-particle chemical characterization and source apportionment of iron-containing atmospheric aerosols in Asian outflow. *Journal Geophysical Research* **2011,** *116*(*D18*), D18204.

198. Moffet, R. C.; Furutani, H.; Rödel, T. C.; Henn, T. R.; Sprau, P. O.; Prakash, S.; Laskin, A.; Uematsu, M.; Gilles, M. K. Iron speciation and mixing in single aerosol particles from the Asian continental outflow. *Journal of Geophysical Research-Atmospheres* **2012,** *117*, D07204.

199. Laskin, A., Electron Beam Analysis and Microscopy of Individual Particles. In *Fundamentals and Applications in Aerosol Spectroscopy*, Signorell, R.; Reid, J. P., Taylor and Francis Books, Inc: 2010; pp 463-491.

200. Moffet, R. C.; Tivanski, A. V.; Gilles, M. K., Scanning X-ray Transmission Microscopy: Applications in Atmospheric Aerosol Research. In *Fundamentals and Applications in Aerosol Spectroscopy*, Signorell, R.; Reid, J. P., Taylor and Francis Books, Inc: 2010; pp 419-462.

201. Posfai, M.; Buseck, P. R., Nature and Climate Effects of Individual Tropospheric Aerosol Particles. In *Annual Review of Earth and Planetary Sciences, Vol 38*, Jeanloz, R.; Freeman, K. H., 2010; Vol. 38, pp 17-43.

202. Stevie, F. A.; Vartuli, C. B.; Giannuzzi, L. A.; Shofner, T. L.; Brown, S. R.; Rossie, B.; Hillion, F.; Mills, R. H.; Antonell, M.; Irwin, R. B.; Purcell, B. M. Application of focused ion beam lift-out specimen preparation to TEM, SEM, STEM, AES and SIMS analysis. *Surface and Interface Analysis* **2001,** *31*(*5*), 345-351.

203. Munroe, P. R. The application of focused ion beam microscopy in the material sciences. *Materials Characterization* **2009,** *60*(*1*), 2-13.

204. Heaney, P. J.; Vicenzi, E. P.; Giannuzzi, L. A.; Livi, K. J. T. Focused ion beam milling: A method of site-specific sample extraction for microanalysis of Earth and planetary materials. *American Mineralogist* **2001,** *86*(*9*), 1094-1099.

205. Heng, D.; Tang, P.; Cairney, J. M.; Chan, H.-K.; Cutler, D. J.; Salama, R.; Yun, J. Focused-ion-beam milling: A novel approach to probing the interior of particles used for inhalation aerosols. *Pharmaceutical Research* **2007,** *24*(*9*), 1608-1617.

206. Kaegi, R.; Gasser, P. Application of the focused ion beam technique in aerosol science: detailed investigation of selected, airborne particles. *Journal of Microscopy-Oxford* **2006,** *224*(*2*), 140-145.

207. Conny, J. M.; Norris, G. A. Scanning electron microanalysis and analytical challenges of mapping elements in urban atmospheric particles. *Environmental Science & Technology* **2011,** *45*(*17*), 7380-7386.

208. Fu, H.; Cwiertny, D. M.; Carmichael, G. R.; Scherer, M. M.; Grassian, V. H. Photoreductive dissolution of Fe-containing mineral dust particles in acidic media. *Journal Geophysical Research* **2010,** *115*(*D11*), D11304.

209. Chen, H.; Laskin, A.; Baltrusaitis, J.; Gorski, C. A.; Scherer, M. M.; Grassian, V. H. Coal fly ash as a source of iron in atmospheric dust. *Environmental Science & Technology* **2012,** *46*(*4*), 2112-2120.

210. Kawamura, K.; Ng, L. L.; Kaplan, I. R. Determination of organic acids (C1-C10) in the atmosphere, motor exhausts, and engine oils. *Environmental Science & Technology* **1985,** *19*(*11*), 1082-1086.

211. Falkovich, A. H.; Graber, E. R.; Schkolnik, G.; Rudich, Y.; Maenhaut, W.; Artaxo, P. Low molecular weight organic acids in aerosol particles from Rondonia, Brazil, during the biomass-burning, transition and wet periods. *Atmospheric Chemistry and Physics* **2005,** *5*, 781-797.

212. Keene, W. C.; Galloway, J. N.; Holden, J. D., Jr. Measurement of weak organic acidity in precipitation from remote areas of the world. *Journal of Geophysical Research* **1983,** *88*(*C9*), 5122-5130.

213. Zinder, B.; Furrer, G.; Stumm, W. The coordination chemistry of weathering: II. Dissolution of Fe(III) oxides. *Geochimica Et Cosmochimica Acta* **1986,** *50*(*9*), 1861-1869.

214. Suter, D.; Siffert, C.; Sulzberger, B.; Stumm, W. Catalytic dissolution of iron(III)(hydr)oxides by oxalic acid in the presence of Fe(II). *Naturwissenschaften* **1988,** *75*(*11*), 571-573.

215. Sulzberger, B.; Suter, D.; Siffert, C.; Banwart, S.; Stumm, W. Dissolution of Fe(III)(hydr)oxides in natural waters; Laboratory assessment on the kinetics controlled by surface coordination. *Marine Chemistry* **1989,** *28*(*1-3*), 127-144.

216. Cwiertny, D. M.; Hunter, G. J.; Pettibone, J. M.; Scherer, M. M.; Grassian, V. H. Surface chemistry and dissolution of α-FeOOH nanorods and microrods: Environmental implications of size-dependent interactions with oxalate. *Journal of Physical Chemistry C* **2009,** *113*(*6*), 2175-2186.

217. Paris, R.; Desboeufs, K. V.; Journet, E. Variability of dust iron solubility in atmospheric waters: Investigation of the role of oxalate organic complexation. *Atmospheric Environment* **2011,** *45*(*36*), 6510-6517.

218. Chen, Y.; Siefert, R. L. Seasonal and spatial distributions and dry deposition fluxes of atmospheric total and labile iron over the tropical and subtropical North Atlantic Ocean. *Journal of Geophysical Research* **2004,** *109*(*D9*), D09305.

219. Xia, L.; Gao, Y. Chemical composition and size distributions of coastal aerosols observed on the US East Coast. *Marine Chemistry* **2010,** *119*(*1-4*), 77-90.

220. Johnson, M. S.; Meskhidze, N., Updated dust-iron dissolution mechanism: Effects of organic acids, photolysis, and dust mineralogy. In *2011 Fall Meeting*, San Fransico, CA USA, 2011.

221. Vlasenko, A.; Sjögren, S.; Weingartner, E.; Gäggeler, H. W.; Ammann, M. Generation of submicron Arizona Test dust aerosol: Chemical and hygroscopic properties. *Aerosol Science and Technology* **2005,** *39*(*5*), 452-460.

222. Baltrusaitis, J.; Usher, C. R.; Grassian, V. H. Reactions of sulfur dioxide on calcium carbonate single crystal and particle surfaces at the adsorbed water carbonate interface. *Physical Chemistry Chemical Physics* **2007,** *9*(*23*), 3011-3024.

223. Spokes, L. J.; Jickells, T. D. Factors controlling the solubility of aerosol trace metals in the atmosphere and on mixing into seawater. *Aquatic Geochemistry* **1995,** *1*(*4*), 355-374.

224. Norton, G. A.; Markuszewski, R.; Shanks, H. R. Morphological and chemical characterization of iron-rich fly ash fractions. *Environmental Science & Technology* **1986,** *20*(*4*), 409-413.

225. Kutchko, B. G.; Kim, A. G. Fly ash characterization by SEM-EDS. *Fuel* **2006,** *85*(*17-18*), 2537-2544.

226. Hansen, L. D.; Silberman, D.; Fisher, G. L.; Eatough, D. J. Chemical speciation of elements in stack-collected, respirable-size, coal fly ash. *Environmental Science & Technology* **1984,** *18*(*3*), 181-186.

227. Dyar, M. D. A review of Mössbauer data on trioctahedral micas - Evidence fortetrahedral Fe^{3+} and cation ordering. *American Mineralogist* **1987,** *72*(*1-2*), 102-112.

228. Dyar, M. D.; Agresti, D. G.; Schaefer, M. W.; Grant, C. A.; Sklute, E. C. Mössbauer spectroscopy of Earth and planetary materials. *Annual Review of Earth and Planetary Sciences* **2006,** *34*(*1*), 83-125.

229. Winburn, R. S.; Grier, D. G.; McCarthy, G. J.; Peterson, R. B. Rietveld quantitative X-ray diffraction analysis of NIST fly ash standard reference materials. *Powder Diffraction* **2000,** *15*(*3*), 163-172.

230. McBride, M. B., *Environmental Chemistry of Soils*. Oxford University Press: New York, 1994.

231. Gieré, R.; Carleton, L. E.; Lumpkin, G. R. Micro- and nanochemistry of fly ash from a coal-fired power plant. *American Mineralogist* **2003,** *88*(*11-12*), 1853-1865.

232. Gieré, R.; Blackford, M.; Smith, K. TEM study of $PM_{2.5}$ emitted from coal and tire combustion in a thermal power station. *Environmental Science & Technology* **2006,** *40*(*20*), 6235-6240.

233. Davison, R. L.; Natusch, D. F. S.; Wallace, J. R.; Evans, C. A. Trace elements in fly ash. Dependence of concentration on particle size. *Environmental Science & Technology* **1974,** *8*(*13*), 1107-1113.

234. Zhu, X. R.; Prospero, J. M.; Millero, F. J.; Savoie, D. L.; Brass, G. W. The solubility of ferric iron in marine mineral aerosol solutions at ambient relative humidities. *Marine Chemistry* **1992,** *38*(*1-2*), 91-107.

235. Desboeufs, K. V.; Losno, R.; Vimeux, F.; Cholbi, S. The pH-dependent dissolution of wind-transported Saharan dust. *Journal of Geophysical Research-Atmospheres* **1999,** *104*(*D17*), 21287-21299.

236. Stumm, W.; Morgan, J. J., *Aquatic chemistry: chemical equilibria and rates in natural waters*. 3rd ed.; John Wiley & Sons: New York, 1996.

237. Vassilev, S. V.; Menendez, R.; Borrego, A. G.; Diaz-Somoano, M.; Rosa Martinez-Tarazona, M. Phase-mineral and chemical composition of coal fly ashes as a basis for their multicomponent utilization. 3. Characterization of magnetic and char concentrates. *Fuel* **2004,** *83*(*11-12*), 1563-1583.

238. Bacci, P.; Del Monte, M.; Longhetto, A.; Piano, A.; Prodi, F.; Redaelli, P.; Sabbioni, C.; Ventura, A. Characterization of the particulate emission by a large oil fuel fired power plant. *Journal of Aerosol Science* **1983,** *14*(*4*), 557-572.

239. Stumm, W.; Lee, G. F. Oxygenation of ferrous iron. *Industrial & Engineering Chemistry* **1961,** *53*(*2*), 143-146.

240. Millero, F. J.; Sotolongo, S.; Izaguirre, M. The oxidation-kinetics of Fe(II) in seawater. *Geochimica Et Cosmochimica Acta* **1987,** *51*(*4*), 793-801.

241. Desboeufs, K. V.; Losno, R.; Colin, J. L. Factors influencing aerosol solubility during cloud processes. *Atmospheric Environment* **2001,** *35*(*20*), 3529-3537.

242. Baker, A. R.; Jickells, T. D. Mineral particle size as a control on aerosol iron solubility. *Geophysical Research Letters* **2006,** *33*(*17*), L17608.

243. Miller, W. L.; King, D. W.; Lin, J.; Kester, D. R. Photochemical redox cycling o iron in coastal seawater. *Marine Chemistry* **1995,** *50*(*1-4*), 63-77.

244. Cunningham, K. M.; Goldberg, M. C.; Weiner, E. R. Mechanisms for aqueous photolysis of adsorbed benzoate, oxalate, and succinate on iron oxyhydroxide (goethite) surfaces. *Environmental Science & Technology* **1988,** *22*(*9*), 1090-1097.

245. Kalinowski, B. E.; Schweda, P. Kinetics of muscovite, phlogopite, and biotite dissolution and alteration at pH 1-4, room temperature. *Geochimica Et Cosmochimica Acta* **1996,** *60*(*3*), 367-385.

246. Werner, S. Reactivity at the mineral-water interface: Dissolution and inhibition. *Colloids and Surfaces A: Physicochemical and Engineering Aspects* **1997,** *120*(*1-3*), 143-166.

247. Remucal Christina, K.; Sedlak David, L., The role of iron coordination in the production of reactive oxidants from ferrous iron oxidation by oxygen and hydrogen peroxide. In *Aquatic Redox Chemistry*, Tratnyek, P. G.; Grundl, T. J.; Haderlein, S. B., American Chemical Society: 2011; Vol. 1071, p 177.

248. Hamer, M.; Graham, R. C.; Amrhein, C.; Bozhilov, K. N. Dissolution of ripidolite (Mg, Fe-Chlorite) in organic and inorganic acid solutions. *Soil Science Society of America Journal* **2003,** *67*(*2*), 654-661.

249. Miller, W. P.; Zelazny, L. W.; Martens, D. C. Dissolution of synthetic crystalline and noncrystalline iron oxides by organic acids. *Geoderma* **1986,** *37*(*1*), 1-13.

250. Zuo, Y. G. Kinetics of photochemiscal chemical cycling of iron coupled with organic-substances in clound and fog droplets. *Geochimica Et Cosmochimica Acta* **1995,** *59*(*15*), 3123-3130.

251. Sulzberger, B.; Laubscher, H. Reactivity of various types of iron(III) (hydr)oxides towards light-induced dissolution. *Marine Chemistry* **1995,** *50*(*1-4*), 103-115.

252. Zhang, Y.; Kallay, N.; Matijevic, E. Interaction of metal hydrous oxides with chelating agents. 7. Hematite-oxalic acid and -citric acid systems. *Langmuir* **1985,** *1*(*2*), 201-206.

253. Archer, D. E.; Johnson, K. A model of the iron cycle in the ocean. *Global Biogeochemical Cycles* **2000,** *14*(*1*), 269-279.

254. Aumont, O.; Maier-Reimer, E.; Blain, S.; Monfray, P. An ecosystem model of the global ocean including Fe, Si, P colimitations. *Global Biogeochemical Cycles* **2003,** *17*(*2*), 1060.

255. Gregg, W. W.; Ginoux, P.; Schopf, P. S.; Casey, N. W. Phytoplankton and iron: validation of a global three-dimensional ocean biogeochemical model. *Deep Sea Research Part II: Topical Studies in Oceanography* **2003,** *50*(*22-26*), 3143-3169.

256. Moore, J. K.; Doney, S. C.; Lindsay, K. Upper ocean ecosystem dynamics and iron cycling in a global three-dimensional model. *Global Biogeochemical Cycles* **2004,** *18*(*4*), GB4028.

257. Moore, J. K.; Doney, S. C. Iron availability limits the ocean nitrogen inventory stabilizing feedbacks between marine denitrification and nitrogen fixation. *Global Biogeochemical Cycles* **2007,** *21*(*2*), GB2001.

258. U.S. Environmental Potection Agency. National Summary of Lead Emissions. http://www.epa.gov/cgi-n/broker?polchoice=Pb&_debug=0&_service=data&_program=dataprog.national_1.sas (accessed May 16, 2012).

259. Shrader, J. H. Tetra-ethyl lead and the public health. *American Journal of Public Health* **1925,** *15*(*3*), 213-216.

260. Kosnett, M. J., Heavy Metal Intoxication & Chelators. In *Basic & Clinical Pharmacology*, Katzung, B. G.; Masters, S. B.; Trevor, A. J., 12 Ed. McGraw-Hill: New York, 2012.

261. Nriagu, J. O. A history of global metal pollution. *Science* **1996,** *272*(*5259*), 223-224.

262. Friedman, J. R.; Ashton, W. B.; Rapoport, R. D. *A review of the global emissions, transport and effects of heavy metals in the environment*; Pacific Northwest Laboratory, Richland, WA, USA.: 1993; p 34.

263. Ruehling, A.; Tyler, G. Heavy metal pollution and decomposition of spruce needle litter. *Oikos* **1973,** *24*, 402-416.

264. Nouri, P. A.; Reddy, G. B. Influence of acid rain and ozone on soil heavy metals under loblolly pine trees: a field study. *Plant Soil* **1995,** *171*, 59-62.

265. Edwards, R. D.; Lam, N. L.; Zhang, L.; Johnson, M. A.; Kleinman, M. T. Nitrogen dioxide and ozone as factors in the availability of lead from lead-based paints. *Environmental Science and Technology* **2009,** *43*(*22*), 8516-8521.

266. Keuken, M.; Roemer, M.; van den Elshout, S. Trend analysis of urban NO_2 concentrations and the importance of direct NO_2 emissions versus ozone/NO_x equilibrium. *Atmospheric Environment* **2009,** *43*(*31*), 4780-4783.

267. Cwiertny, D. M.; Hunter, G. J.; Pettibone, J. M.; Scherer, M. M.; Grassian, V. H. Surface chemistry and dissolution of α-FeOOH nanorods and microrods: Environmental implications of size-dependent interactions with oxalate. *Journal of Physical Chemistry C* **2008,** *113*(*6*), 2175-2186.

268. Hill, R. J. Refinement of the structure of orthorhombic lead oxide (massicot) by Rietveld analysis of neutron powder diffraction data. *Acta Crystallographica, Section C Crystal Structure Communications* **1985,** *C41*(*9*), 1281-1284.

269. Davey, W. P. Precision measurements of the lattice constants of twelve common metals. *Physical Review* **1925,** *25*(*6*), 753-761.

270. Dickinson, R. G.; Friauf, J. B. The crystal structure of tetragonal lead monoxide. *Journal of the American Chemical Society* **1924,** *46*(*11*), 2457-2263.

271. Baur, W. H.; Khan, A. A. Rutile-type compounds. IV. SiO_2, GeO_2, and a comparison with other rutile-type structures. *Acta Crystallographica, Section B Structural Crystallography and Crystal Chemistry* **1971,** *27*(*11*), 2133-2139.

272. Dinnebier, R. E.; Carlson, S.; Hanfland, M.; Jansen, M. Bulk moduli and high-pressure crystal structures of minium, Pb_3O_4, determined by X-ray powder diffraction. *American Mineralogist* **2003,** *88*(*7*), 996-1002.

273. Chevrier, G.; Giester, G.; Heger, G.; Jarosch, D.; Wildner, M.; Zemann, J. Neutron single-crystal refinement of cerussite, $PbCO_3$, and comparison with other aragonite-type carbonates. *Zeitschrift fur Kristallograhie* **1992,** *199*(*1-2*), 67-74.

274. Cowley, J. M. Electron-diffraction study of the structure of basic lead carbonate, $2PbCO_3.Pb(OH)_2$. *Acta Crystallographica* **1956,** *9*(*4*), 391-396.

275. Haynes, W. M., *CRC Handbook of Chemistry and Physics, 91st ed. (Internet Version)*. CRC Press/Taylor and Francis, Boca Raton, FL: 2011.

276. Washburn, E. W., International Critical Tables of Numerical Data, Physics, Chemistry and Technology (1st Electronic Edition). Knovel: 1926 - 1930;2003.

277. Chen, M.; Daroub, S. H.; Ma, L. Q.; Harris, W. G.; Cao, X. Characterization of lead in soils of a rifle/pistol shooting range in central Florida, USA. *Soil and Sediment Contamination: An International Journal* **2002,** *11*(*1*), 1-17.

278. Baltrusaitis, J.; Jayaweera, P. M.; Grassian, V. H. XPS study of nitrogen dioxide adsorption on metal oxide particle surfaces under different environmental conditions. *Physical Chemistry Chemical Physics* **2009,** *11*(*37*), 8295-8305.

279. Wagner, C. D.; Zatko, D. A.; Raymond, R. H. Use of the oxygen KLL Auger lines in identification of surface chemical states by electron spectroscopy for chemical analysis. *Analytical Chemistry* **1980,** *52*(*9*), 1445-1451.

280. Chernyshova, I. V.; Andreev, S. I. Spectroscopic study of galena surface oxidation in aqueous solutions I. Identification of surface species by XPS and ATR/FTIR spectroscopy. *Applied Surface Science* **1997,** *108*(*2*), 225-236.

281. Payne, D. J.; Egdell, R. G.; Law, D. S. L.; Glans, P.-A.; Learmonth, T.; Smith, K. E.; Guo, J.; Walsh, A.; Watson, G. W. Experimental and theoretical study of the electronic structures of α-PbO and β-PbO_2. *Journal of Materials Chemistry* **2007,** *17*(*3*), 267-277.

282. Beamson, G.; Briggs, D., *High resolution XPS of organic polymers: the Scienta ESCA300 database*. Wiley: London, 1992.

283. Taylor, J. A.; Perry, D. L. An X-ray photoelectron and electron energy loss study of the oxidation of lead. *Journal of Vacuum Science and Technology A* **1984,** *2*(*2*), 771-774.

284. Underwood, G. M.; Miller, T. M.; Grassian, V. H. Transmission FT-IR and Knudsen cell study of the heterogeneous reactivity of gaseous nitrogen dioxide on mineral oxide particles. *Journal of Physical Chemistry A* **1999,** *103*(*31*), 6184-6190.

285. Hadjiivanov, K.; Bushev, V.; Kantcheva, M.; Klissurski, D. Infrared spectroscopy study of the species arising during nitrogen dioxide adsorption on titania (anatase). *Langmuir* **1994,** *10*(*2*), 464-471.

286. Börensen, C.; Kirchner, U.; Scheer, V.; Vogt, R.; Zellner, R. Mechanism and kinetics of the reactions of NO_2 or HNO_3 with alumina as a mineral dust model compound. *Journal of Physical Chemistry A* **2000,** *104*(*21*), 5036-5045.

287. Tompkins, H. G. Interaction of NO_2 with a tin-lead alloy. *Surface Science* **1972,** *32*(*2*), 269-277.

288. Graedel, T. E. Chemical mechanisms for the atmospheric corrosion of lead. *Journal of the Electrochemical Society* **1994,** *141*(*4*), 922-927.

289. Matilainen, A.; Lindqvist, N.; Korhonen, S.; Tuhkanen, T. Removal of NOM in the different stages of the water treatment process. *Environment International* **2002,** *28*(*6*), 457-465.

290. Matsunaga, A.; Ziemann, P. J. Yields of β-hydroxynitrates, dihydroxynitrates, and trihydroxynitrates formed from OH radical-initiated reactions of 2-methyl-1-alkenes. *Proceeding of the National Academy of Sciences of the United States of America* **2010,** *107*(*15*), 6664-6669.

291. Yadav, S.; Sharma, V. Lead induced alterations in hemoglobin content during gestation and lactation in Swiss albino mice. *Pharmacologyonline* **2011,** *3*, 44-47.

292. Huber, D. L. Synthesis, properties, and applications of iron nanoparticles. *Small* **2005,** *1*(*5*), 482-501.

293. Bullen, J. J.; Rogers, H. J.; Spalding, P. B.; Ward, C. G. Iron and infection: the heart of the matter. *FEMS Immunology and Medical Microbiology* **2005,** *43*(*3*), 325-330.

294. Ge, Y.; Schimel, J. P.; Holden, P. A. Evidence for Negative Effects of TiO_2 and ZnO Nanoparticles on Soil Bacterial Communities. *Environmental Science & Technology* **2011,** *45*(*4*), 1659-1664.

295. Goss, C. H.; Newsom, S. A.; Schildcrout, J. S.; Sheppard, L.; Kaufman, J. D. Effect of ambient air pollution on pulmonary exacerbations and lung function in cystic fibrosis. *American Journal of Respiratory and Critical Care Medicine* **2004,** *169*(*7*), 816-821.

296. Arbex, M. A.; de Souza Conceicao, G. M.; Cendon, S. P.; Arbex, F. F.; Lopes, A. C.; Moyses, E. P.; Santiago, S. L.; Saldiva, P. H.; Pereira, L. A.; Braga, A. L. Urban air pollution and chronic obstructive pulmonary disease-related emergency department visits. *Journal of Epidemiology and Community Health* **2009,** *63*(*10*), 777-783.

297. Larrieu, S.; Lefranc, A.; Gault, G.; Chatignoux, E.; Couvy, F.; Jouves, B.; Filleul, L. Are the short-term effects of air pollution restricted to cardiorespiratory diseases? *American Journal of Epidemiology* **2009,** *169*(*10*), 1201-1208.

298. Ling, S. H.; van Eeden, S. F. Particulate matter air pollution exposure: role in the development and exacerbation of chronic obstructive pulmonary disease. *International Journal of Chronic Obstructive Pulmonary Disease* **2009,** *4*, 233-243.

299. Kelly, F. J.; Fussell, J. C. Air pollution and airway disease. *Clinical and Experimental Allergy* **2011,** *41*(*8*), 1059-1071.

300. MacIntyre, E. A.; Karr, C. J.; Koehoorn, M.; Demers, P. A.; Tamburic, L.; Lencar, C.; Brauer, M. Residential air pollution and otitis media during the first two years of life. *Epidemiology* **2011,** *22*(*1*), 81-89.

301. Saxena, R.; Srivastava, S.; Trivedi, D.; Anand, E.; Joshi, S.; Gupta, S. K. Impact of environmental pollution on the eye. *Acta Ophthalmologica Scandinavica* **2003,** *81*(*5*), 491-494.

302. Waldman, W. J.; Kristovich, R.; Knight, D. A.; Dutta, P. K. Inflammatory Properties of Iron-Containing Carbon Nanoparticles. *Chemical Research in Toxicology* **2007,** *20*(*8*), 1149-1154.

303. Hochella, M. F., Jr.; Lower, S. K.; Maurice, P. A.; Penn, R. L.; Sahai, N.; Sparks, D. L.; Twining, B. S. Nanominerals, mineral nanoparticles, and Earth systems. *Science* **2008,** *319*(*5870*), 1631-1635.

304. Wiesner, M. R.; Lowry, G. V.; Casman, E.; Bertsch, P. M.; Matson, C. W.; Di Giulio, R. T.; Liu, J.; Hochella, M. F. Meditations on the Ubiquity and Mutability of Nano-Sized Materials in the Environment. *ACS Nano* **2011,** *5*(*11*), 8466-8470.

305. Rubasinghege, G.; Lentz, R. W.; Scherer, M. M.; Grassian, V. H. Simulated atmospheric processing of iron oxyhydroxide minerals at low pH: roles of particle size and acid anion in iron dissolution. *Proceedings of the National Academy of Sciences of the United States of America* **2010,** *107*(*15*), 6628-6633.

306. Sayes, C. M.; Warheit, D. B., Criteria and Implementation of Physical and Chemical Characteristics of Nanomaterials for Human Health Effects and Ecological Toxicity Studies. In *Nanotoxicity*, John Wiley & Sons, Ltd: 2009; pp 29-39.

307. Mudunkotuwa, I. A.; Grassian, V. H. The devil is in the details (or the surface): impact of surface structure and surface energetics on understanding the behavior of nanomaterials in the environment. *Journal of Environmental Monitoring* **2011,** *13*(*5*), 1135-1144.

308. Mudunkotuwa, I. A.; Pettibone, J. M.; Grassian, V. H. Environmental Implications of Nanoparticle Aging in the Processing and Fate of Copper-Based Nanomaterials. *Environmental Science & Technology* **2012**.

309. Wu, C.-M.; Baltrusaitis, J.; Gillan, E. G.; Grassian, V. H. Sulfur dioxide adsorption on ZnO nanoparticles and nanorods. *Journal of Physical Chemistry C* **2011,** *115*(*20*), 10164-10172.

310. Govan, J. R.; Deretic, V. Microbial pathogenesis in cystic fibrosis: mucoid Pseudomonas aeruginosa and Burkholderia cepacia. *Microbiological Reviews* **1996,** *60*(*3*), 539-574.

311. Rahme, L. G.; Stevens, E. J.; Wolfort, S. F.; Shao, J.; Tompkins, R. G.; Ausubel, F. M. Common virulence factors for bacterial pathogenicity in plants and animals. *Science* **1995,** *268*(*5219*), 1899-1902.

312. Walker, T. S.; Bais, H. P.; Deziel, E.; Schweizer, H. P.; Rahme, L. G.; Fall, R.; Vivanco, J. M. Pseudomonas aeruginosa-plant root interactions. Pathogenicity, biofilm formation, and root exudation. *Plant Physiology* **2004,** *134*(*1*), 320-331.

313. Blake, R. L.; Hessevick, R. E.; Zoltai, T.; Finger, L. W. Refinement of the hematite structure. *American Mineralogist* **1966,** *51*, 123-129.

314. Schwertmann, U. Solubility and dissolution of iron oxides. *Plant and Soil* **1991,** *130*(*1*), 1-25.

315. Borggaard, O. K. Selective extraction of amorphous iron oxide by EDTA from a mixture of amorphous iron oxide, goethite and hematite. *Journal of Soil Science* **1976,** *27*(*4*), 478-486.

316. Wahid, P. A.; Kamalam, N. V. Reductive dissolution of crystalline and amorphous Fe(III) oxides by microorganisms in submerged soil. *Biology and Fertility of Soils* **1993,** *15*(*2*), 144-148.

317. Schimanke, G.; Martin, M. In situ XRD study of the phase transition of nanocrystalline maghemite (γ-Fe_2O_3) to hematite (α-Fe_2O_3). *Solid State Ionics* **2000,** *136–137*(*0*), 1235-1240.

318. Waychunas, G. A.; Kim, C. S.; Banfield, J. F. Nanoparticulate iron oxide minerals in soils and sediments: unique properties and contaminant scavenging mechanisms. *Journal of Nanoparticle Research* **2005,** *7*(*4*), 409-433.

319. Cornell, R. M.; Schwertmann, U., *The Iron Oxides: Structure, Properties, Reactions, Occurences and Uses, 2nd edition*. 2003.

320. Baltrusaitis, J.; Cwiertny, D. M.; Grassian, V. H. Adsorption of sulfur dioxide on hematite and goethite particle surfaces. *Physical Chemistry Chemical Physics* **2007,** *9*(*41*), 5542-5554.

321. Briggs, D.; Grant, J. T., *Surface Analysis by Auger and X-Ray Photoelectron Spectroscopy*. 2003; p 899.

322. Wu, C.-K.; Yin, M.; O'Brien, S.; Koberstein, J. T. Quantitative analysis of copper oxide nanoparticle composition and structure by X-ray photoelectron spectroscopy. *Chemistry of Materials* **2006,** *18*(*25*), 6054-6058.

323. Kim, B. J.; Park, J. H.; Park, T. H.; Bronstein, P. A.; Schneider, D. J.; Cartinhour, S. W.; Shuler, M. L. Effect of iron concentration on the growth rate of Pseudomonas syringae and the expression of virulence factors in hrp-inducing minimal medium. *Applied and Environmental Microbiology* **2009,** *75*(*9*), 2720-2726.

324. Prince, A. S. Biofilms, antimicrobial resistance, and airway infection. *New England Journal of Medicine* **2002,** *347*(*14*), 1110-1111.

325. Patriquin, G. M.; Banin, E.; Gilmour, C.; Tuchman, R.; Greenberg, E. P.; Poole, K. Influence of quorum sensing and iron on twitching motility and biofilm formation in Pseudomonas aeruginosa. *Journal of Bacteriology* **2008,** *190*(*2*), 662-671.

326. Friedman, L.; Kolter, R. Genes involved in matrix formation in Pseudomonas aeruginosa PA14 biofilms. *Molecular Microbiology* **2004,** *51*, 675-690.

327. Butler, A.; Theisen, R. M. Iron(III)–siderophore coordination chemistry: Reactivity of marine siderophores. *Coordination Chemistry Reviews* **2010,** *254*(*3–4*), 288-296.

328. Kraemer, S. M. Iron oxide dissolution and solubility in the presence of siderophores. *Aquatic Sciences* **2004,** *66*(*1*), 3-18.

329. Banin, E.; Vasil, M. L.; Greenberg, E. P. Iron and Pseudomonas aeruginosa biofilm formation. *Proceedings of the National Academy of Sciences of the United States of America* **2005,** *102*(*31*), 11076-11081.

330. Wiesner, J.; Vilcinskas, A. Antimicrobail peptides: The ancient arm of the human immune system. *Virulence* **2010,** *1*(*5*), 440-464.

331. Singh, P. K.; Parsek, M. R.; Greenberg, E. P.; Welsh, M. J. A component of innate immunity prevents bacterial biofilm development. *Nature* **2002,** *417*(*6888*), 552-555.

332. Ganz, T. Antimicrobial polypeptides in host defense of the respiratory tract. *Journal of Clinical Investigation* **2002,** *109*(*6*), 693-697.

333. Boland, J. S.; Davidson, P. M.; Bruce, B.; Weiss, J. Cations reduce antimicrobial efficacy of lysozyme-chelator combinations. *Journal of Food Protection* **2004,** *67*(*2*), 285-294.

334. Freyria, F. S.; Bonelli, B.; Tomatis, M.; Ghiazza, M.; Gazzano, E.; Ghigo, D.; Garrone, E.; Fubini, B. Hematite nanoparticles larger than 90 nm show no sign of toxicity in terms of lactate dehydrogenase release, nitric oxide generation, apoptosis, and comet assay in murine alveolar macrophages and human lung epithelial cells. *Chemical Research in Toxicology* **2012,** *25*(*4*), 850-861.